THE EFFECTS OF CORROSION, COLD EXPANSION AND INTERFERENCE FIT ON THE FATIGUE OF ALUMINIUM ALLOY SPECIMENS CONTAINING FASTENER HOLES

ALEXEY NESTEROV

A thesis submitted in partial fulfilment of the requirements of Kingston University for the degree of Doctor of Philosophy

This research programme was carried out in collaboration with QinetiQ, Farnborough

February 2006

The following figures have not been digitised at the request of the university:

Figure 1.2.1 p.20

Figure 1.2.2 p.21

Figure 1.2.3 p.22

Figure 1.2.4 p.22

Figure 1.2.5 p.22

Figure 1.2.6 p.23

Figure 1.2.7 p.23

Figure 1.2.8 p.25

Figure 1.3.1 p.27

Figure 1.3.2 p.28

Figure 1.3.3 p.32

Figure 1.3.4 p.32

Figure 1.4.1 p.37

Figure 1.4.2 p.39

Figure 1.4.3 p.39

Figure 1.4.4 p.40

Figure 1.4.9 p.48

Figure 1.5.5 p.53

Figure 1.5.8 p.56

Figure 1.5.10 p.57

Figure 1.5.14 p.63

Figure 1.5.17 p.64

Figure 1.6.1 p.65

Figure 1.8.4 p.92

Figure 1.9.1 p.109

ABSTRACT

One of the most vulnerable areas for the initiation and propagation of fatigue cracks in aircraft structures is in the region of fastener holes. To reduce the incidence of fatigue cracking a number of methods have been developed which introduce residual stresses or induced stress fields at the fastener holes. Of these methods, two of the most widely used in the aerospace industry involve the use of interference-fit fasteners or a procedure for cold working the fastener holes. This investigation studies the effect of these two technologies on the fatigue performance of specimens manufactured from 2024-T351 aluminium alloy. The effect of exposure of the specimens to corrosion damage was also investigated.

Fatigue tests were carried out on flat plate specimens containing open plain holes and open cold worked holes as well as on plain hole and cold worked hole specimens containing interference fit pins. The fatigue crack growth in the specimens was investigated under constant amplitude sinusoidal loading at a stress ratio of R=0.1 and a frequency of 10 Hz. A proportion of the specimens were subjected to controlled corrosion exposure prior to testing.

Crack Growth Rate (CGR) diagrams were constructed from these experimental results and an analysis made of crack initiation, crack propagation rate and total life.

Crack Growth Rate models were developed based on the assumption that the dependence of CGR vs effective Stress Intensity Factor (SIF) for this material are not affected by residual stresses in the material. Crack opening stress distributions were derived from experimental crack growth rate data which were also confirmed by experimental data obtained by other investigators previously.

The beneficial effects of cold expansion and interference fit on fatigue performance were confirmed in plain and corroded specimens. Cold expansion treatment combined with the use of an interference fit fastener gave the greatest benefits in fatigue performance for the specimens tested including improvements in both crack initiation and propagation stages and in the total fatigue life. The effect of corrosion was found to be detrimental for both cold worked and plain specimens but was less severe for cold worked samples in comparison with plain untreated specimens.

KINGSTON UNIVERSITY

FACULTY OF ENGIGEERING

PHILOSOPHICAL DOCTORATE THESIS

ACADEMIC YEARS 2002-2005

ALEXEY NESTEROV

THE EFFECTS OF SURFACE CORROSION ON THE FATIGUE BEHAVIOUR OF ALUMINIUM ALLOY SPECIMENS CONTAINING COLD EXPANDED HOLES

ACADEMIC SUPERVISOR PAUL G. WAGSTAFF
KINGSTON UNIVERSITY UK

INDUSTRIAL SUPERVISOR KEN BROWN –QINETIQ UK

FEBRUARY 2006

This thesis is submitted in partial fulfilment of the requirements for the Degree of Doctor of Philosophy

Acknowledgements

First and foremost I would like to thank our God who allowed and helped me successfully to pass through this "piece of life" that included not only academic experience. Also, I would like to thank the following people who have somehow concern to the project and who someways or other help me to finish the project in spite of many obstacles we encountered through the duration of this project.

- My academic supervisor and part-time English father in one Paul Wagstaff who was always available for support, guidance, and friendship for the time of our working on the research project.
- My industrial supervisor Ken Brown for his support, guidance, kindness, great patience and indulgence to my academic writing.
- Technician of Civil Engineering Lab in Sopwith Building Colin Bradsell for his constructive help immediately in the fatigue tests, his patience and warmth all the way through the project.
- Technicians in Roehampton Vale Mike Varley, Bill Prophet and all staff from the workshop for their timely help and response to my current needs and requirements with the testing programs.
- Bill Edwards for his natural patience and helpfulness
- Adam Brown for repairing the Mayes Machine during emergencies.
- My part-time English second mother Shirley Trevena for remaining sweet, warmth and once in a while patient with me.
- John Garcia, Sergio Ferraris, and all my research room mates for sharing my office, helping me with computer questions, supporting me when the research was difficult, and for all the great laughs we had.

I would also like to thank especially the following persons who helped in life, aid me practically and morally during my staying in the UK:

Paula and Jack Wallas, Shirley and Dave Trevena, Ms. Shah and her family for their friendship, kindness and care during all my time staying in Kingston.

My parents, Viatcheslav and Ludmila for their moral support and great care.

I would like to express my especial gratitude to my first scientific teacher and supervisor Prof. Veniamin Raikher, who devolved knowledge of metal fatigue and aviation safety to me and brought me up as a scientist.

My close Russian friends Dmitry, Nikolay and Elena Dmtrievyh, Dmitry and Irina Savel'evyh, Dmitry Ivonin, Svetlana Vladimirova, Elena Zagorulkinna, Elena and

Matvey Chernikovyh, for their support, cordiality and encouragement from overseas. Mikhail and Julia Samartsevyh and Olga Elkins for their hospitality in England.
My new English Keith and Pari Barbour, French Raphael Rant'er and Spanish Fernando Cabero friends for their friendship, kindness and for a lot of really good time spent together in the mountains and pubs.
Eventually, I would like cordially to thank this country Great Britain generally and particularly England, Wales, Scotland where I spent possibly the best time in my life for the true hospitality, pleasant staying and travelling and that experience which I have taken for living here. During all that time I liked this country and regard it as my second homeland, though I still have to obtain a visa to visit it:-).

Nomenclature

a	bore crack length
c_1	Entrance surface crack length
c_2	exit surface crack length
c	Maximal of c_1 or c_2 surface crack length
N	Fatigue life
r	Radius of the hole
D	Diameter of the hole
t	Thickness of the specimen
2W	Specimen width
σ	Remote stress
σ_{app}	Applied Stress
σ_{net}	Net stress
σ_l	Local stress
σ_{res}	Residual stress
σ_{max}	Maximum stress
σ_{min}	Minimum stress
σ_{op}	Opening stress
σ_{eff}	Effective stress
σ_y	Yield stress
σ_{prt}	Pretention stress
R	Stress ratio
$K,\ K_{\max}, K_{\min}, \Delta K$	Stress Intensity Factor, maximal and minimal values and iys range
K_{op}	Opening Stress Intensity Factor
$K_{eff}, \Delta K_{eff}$	Effective Stress Intensity Factor and its range
$\Delta K_{\exp}$	Range of Stress Intensity Factor from Experiment
$F_{ThroughCrack}, F_{CornerCrack}$	Calibration functions for though and corner cracks

C, m C_{eff} m_{eff}	Crack Growth Rate Diagram Parameters and parameters of effective CGR diagram
ϕ	Parametric angle
E	Elastic modulus
ν	Poisson's ratio
CX, CW	Cold expanded, Cold Worked
COR	Corroded specimen
Pl	Plain Specimen
Inter Fit	Interference Fit
SIF	Stress Intensity Factor
CGR	Crack Growth Rate

Contents

INTRODUCTION

The structures of modern aircraft are very complex assemblies of the most up-to-date technologies, materials and design details. During its life it experiences an extremely complex set of different influences: gust, manoeuvre, landing, taxiing, acoustic loadings, extremes of temperatures, and a frequently hostile corrosive environment. Moreover it must fly for many years in a condition which can be proven to be safe to the airworthiness authorities. Weight is of paramount importance in the design of a new aircraft as it determines the future balance between economic benefits and safety. Hence the designer must aim to achieve the most optimal solution. The structure must be light and at the same time as strong as possible.

Designing an aircraft for unlimited life i.e. keeping design stresses below the fatigue limit leads to a severe weight penalty with subsequent considerable economic losses. This encourages the design of structures which work under the highest stresses possible, which may often lead to fatigue problems from the dynamic loading the aircraft experiences in service. In fact nearly all civil transport aircraft currently in service have developed some fatigue problems.

The National Research Council of Canada performed a study in 1984 on the fatigue initiation sites for fixed wing aircraft accidents [1]. The percentage occurrence of fatigue at different types of initiation site is shown in Table 1. The main initiation sites were found to be ***threaded fasteners such as a bolt, stud or screw and holes such as those for other fasteners***.

Table 1 Initiation Sites for Fixed Wing Accidents.

Initiation Site	**%**
Bolt, stud or screw	24
Fastener hole or other hole	16
Fillet, radius or sharp notch	13
Weld	12
Corrosion	10
Thread (other than bolt or stud)	7
Manufacturing defect	6
Scratch, nick or dent	6
Fretting	3
Others	3

From the foregoing one may conclude that fatigue considerations play a very large role in the design and operation of aircraft structures.

To avoid catastrophic failure and to predict fatigue life reliably there are special design philosophies: Safe Life Design, Damage Tolerant Design and its subpart Fail Safe Design.

The fatigue process may be characterized by the curve of crack length versus number of cycle, shown in the Figure 1. Three stages of behaviour are depicted. In the first, the repeated loadings cause an accumulation of damage leading to the initiation of a fatigue crack. In the second, the fatigue crack propagates at a steadily increasing rate, finally, catastrophic fracture occurs when the crack has grown to the size that is "critical" for the final applied load.

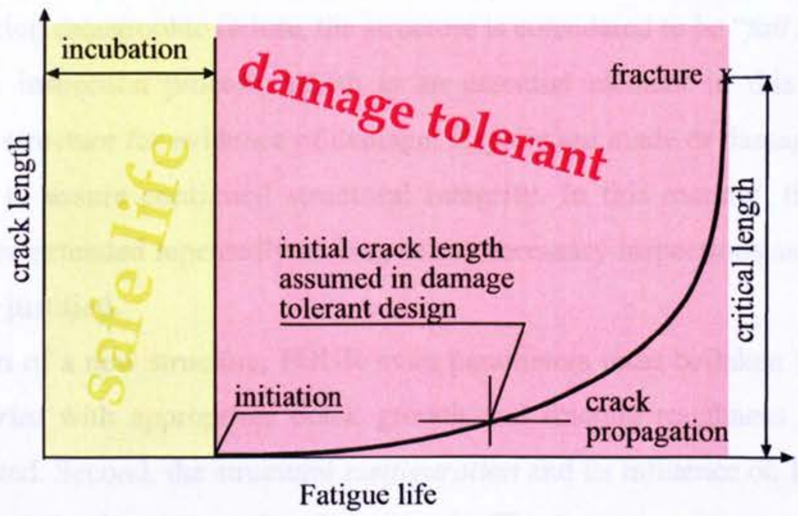

Figure 1 The Fatigue process

For structures designed in accordance with *Safe Life Design* principles, it is expected that there will not be any failures or cracks which can reduce the strength of the structure below a required minimum during a pre-determined operating time. This method permits operation of the structure without inspections. Normally, it is applied in those cases where fatigue damage to some primary structural parts can lead to the crash of an aircraft, but where this cannot be detected by periodical inspections during operation. Thus, this design approach implies operation mostly during the incubation period shown in the Figure 1. The decision about allowable operating time is determined by life calculations based on the usual S-N curves and statistical analysis.

The failure rate established is usually not greater than one per 1000.

Normally, manufacturers are required to test representative structures to four times the expected service life to demonstrate adequate fatigue life.

In the damage tolerant design philosophy, one or more significant flaws are assumed to exist in the structure (see Figure 1). Such flaws have been known to escape detection during manufacture. They might be introduced by inadvertent damage during service, or they might result from fatigue or stress corrosion. It is expected to limit the rate of crack propagation so that the largest flaw missed at one inspection will not cause catastrophic failure before one or more subsequent inspections are conducted. This design approach includes the selection of materials and adjustment of operating stress levels to achieve slow rates of crack growth. The analysis procedures depend heavily on fracture mechanics considerations for predictions of crack propagation rates and residual fracture strength.

If the structure is capable of experiencing failure of one or more primary members without suffering catastrophic failure, the structure is considered to be "*fail safe.*"

In effect, the inspection process, which is an essential element in this philosophy, examines the structure for evidence of damage. Repairs are made or damaged structure is reinforced to assure continued structural integrity. In this manner, the life of an aircraft may be extended repeatedly as long as the necessary inspections and repairs are economically justified.

For the design of a new structure, FOUR main parameters must be taken into account. First, a *material* with appropriate crack growth and fracture toughness performance must be selected. Second, the structural *configuration* and its influence on fatigue life or crack growth behaviour must be determined. Third, appropriate analyses must account for the cumulative effect of variable amplitude *loadings,* and stress levels must be chosen that provide long life. Finally, the thermal and chemical *environment* encountered in service must be considered.

The illustrative diagram from Hardrath[2], Figure 2, helps to achieve an Integrated Program of Research for the development of improved technology for structural integrity.

As indicated earlier, safe life analyses do not account for crack initiation, crack propagation, and fracture. Thus, the elongated "bricks" in the rear stack extend over these three phases of life. In practice, the empirical data from S-N diagram used in analyses are derived from tests of small specimens carried to complete failure. The four bricks in the stack represent the four major parameters that must be considered to solve a design problem under this philosophy.

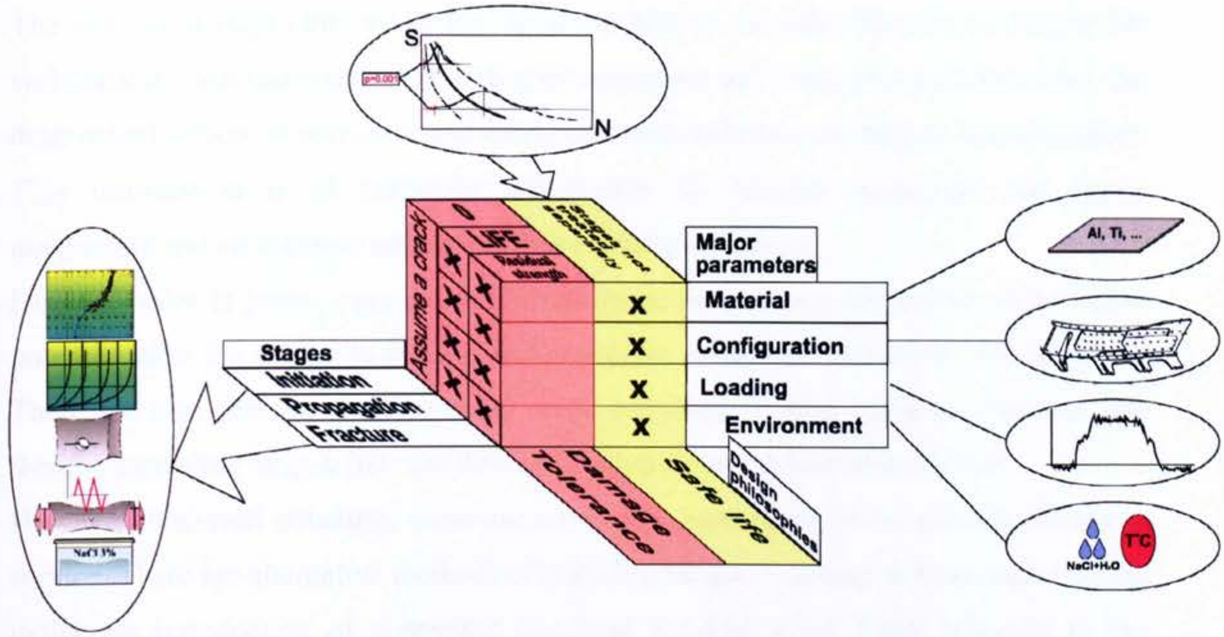

Figure 2 Unified Fatigue and Fracture

On the other hand, the damage tolerant philosophy, represented by the front stacks of bricks, acknowledges the existence of cracks, predicts their rate of growth, and identities the conditions that lead to fracture. Usually this philosophy is not concerned over how the crack was initiated. Thus, only one tall brick is shown, and it is labelled "Assume a crack." In practice, non-destructive inspection procedures are employed to determine whether cracks indeed exist but there may be cracks present below the detectable limit of the inspection equipment since the sensitivity is often limited for economic reasons. The same four major parameters: materials, configuration, loadings, and environment must be considered in turn to achieve a damage tolerant analysis and design.

Joints incorporating fasteners are a well established, reliable way of joining structural elements. The present work concerns the specific aspect of the fatigue performance of fastener holes where corrosion damage may occur. More specifically the fatigue performance of fastener hole cold expansion, the use of interference fit fasteners, the combination of the two processes and the effect of corrosion damage have been evaluated. All the specimens tested in this investigation were manufactured from 2024-T3 aluminium alloy plate.

Going back to design philosophies and basic knowledge on which they are established, from the foregoing research problem definition, the present work contributes mainly to damage tolerance philosophy. It implies research in fatigue performance, crack initiation and propagation in fastener holes subjected to cold expansion, the application of interference fit fasteners and the effects of corrosion damage.

The new knowledge obtained in the work can help to estimate the gain in fatigue life and crack growth rate associated with cold expansion and interference fit fasteners, the detrimental effects of corrosion and their combined influence on fatigue characteristics. This information is of particular importance for regular inspection and repair assignment and an accurate estimate of life extension obtained.

Fastener holes in joints, open holes (for drainage, inspections) are known to be major potential sites for cracks to initiate and propagate in aircraft structures (see Table 1). There are two obvious ways to delay crack initiation: reduce crack propagation rate thereby extending fatigue life: use different materials and reduce stress levels.

However in aircraft structures these are not viable, particularly if the aircraft already in service. There are alternative methods of reducing fatigue cracking at holes based on the deliberate introduction of controlled localized residual stress fields adjacent to the critical regions. Introducing an interference-fit fastener or cold working of fastener holes are widespread technologies in the aerospace industry which use this effect to improve the fatigue performance of structures.

It is frequently employed both at build and for subsequent repair schemes to enhance fatigue endurance.

The benefits of cold expansion are to increase the fatigue endurance of a component mainly due to a reduction in fatigue crack growth rates in the early stages of life (3). This reduction in growth rate arises because cracks have to grow through compressive residual stress fields created by the hole cold expansion process. The residual stresses are compressive in an annulus of material around the hole which extends for a few millimetres from the hole. This compressive residual stress region is balanced by a region of tensile residual stresses which extends for tens of millimetres away from the hole. Although the tensile residual stress region extends over a much greater area than the compressive region, the magnitude of these residual stresses is much smaller than the compressive stresses (4).

The use of an interference fit fastener will produce an improvement in the fatigue performance as well, but the mechanism of this system is different from pure cold expansion. Benefits in fatigue are attained by maintaining a tensile prestress around the hole. This reduces the effective stress amplitude without appreciably affecting the maximum stress. While tensile prestress is not beneficial, the reduced stress amplitude prolongs fatigue life.

The present work studies both technologies and considers their effect on the fatigue performance of fastener holes in 2024-T351 aluminium alloy separately and in combination.

The structure of the present work is given in Figure 3 3

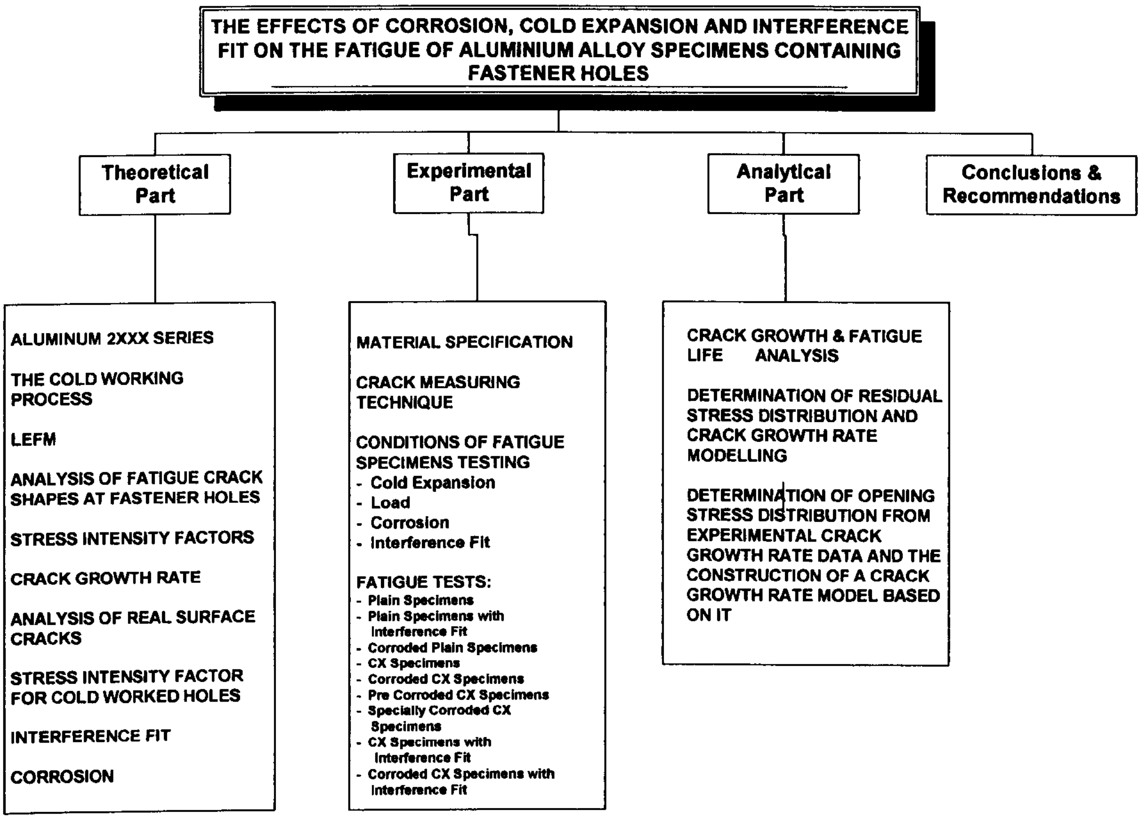

Figure 3 Structure of the Thesis

This consists of sections covering theory, experimental work, analysis, and conclusions. The theoretical section includes a short description of Al alloy 2024 and its' applicability in the aviation industry, a review of the cold expansion process and components associated with it (technology, residual stress, fatigue properties, etc.), the application of LEFM to this area of research.

The experimental section includes a description of material specifications, crack measurement methodology, of specimens testing conditions, test results and observations.

The analytical includes general analysis of the test results: crack growth rates and fatigue life, derivation residual stresses, opening stresses and crack growth rate modelling.

Finally, the section covering conclusions and recommendations summarises all analytical results and makes recommendations on the practical application of these results to obtain the best fatigue performance in real structures.

1 THEORETICAL SECTION

1.1 ALUMINIUM 2024

The discovery by a German metallurgist in 1911, that aluminium alloyed with copper could be made stronger than mild steel paved the way for aluminium framed and skinned aircraft. The use of these Duralumin alloys as they became known, enabled some of the aerodynamic forces to be carried by the stressed skin of the wings and fuselage. This resulted in very efficient airframes. Most of the aircraft in World War II were aluminium alloy stressed skin designs. Remarkably, the early aluminium alloys developed in the 1930s (2024) and 1940s (7075) are still used extensively today.
Al-Cu-Mg "Duralumin" (Al-3.5Cu-0.5Mg-0.5Mn) first widely used age hardening alloy (discovered accidentally in 1906 by Alfred Wilm). These alloys are normally roll clad with pure Al or Al-Zn to protect against corrosion. Alloy 2024 is perhaps the best known and most widely used aircraft alloy.
High strength aluminium alloys are used extensively in the wing structure and account for more than 75% of the total wing weight. Experience has shown that the alloys and tempers listed in the Table 2 offer adequate resistance to corrosion damage and fatigue cracking.

Table 2 Aluminium alloys used in Construction of Current Airbus Outer Wing Box Structure.

Component	Aluminium Alloy
Upper Skin	7150-T651
Upper Stringers	7150-T651
Lower Skin	2024-T351
Lower Stringers	2024-T351
Front Spar	7010-T7651
Rear Spar	7010-T7651
Ribs	7010-T7651

Figure 1.1.1 shows the design criteria in different fuselage areas for the A3XX if made of the conventional skin material 2024.

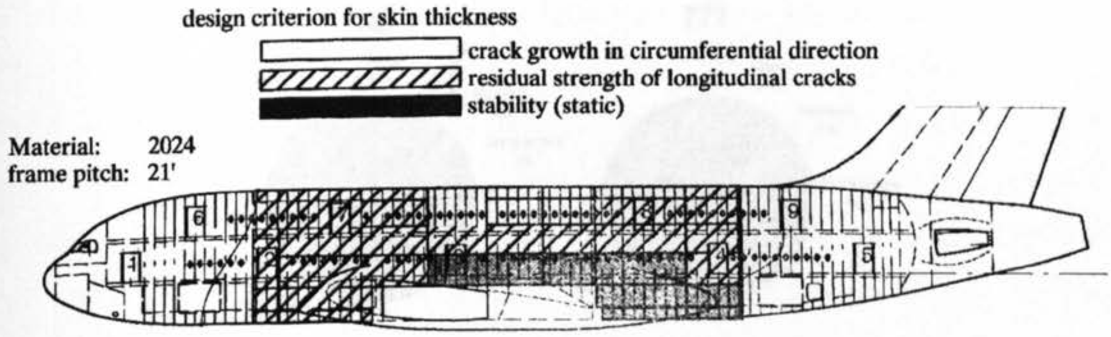

Figure 1.1.1Design criteria for A3XX fuselage sections

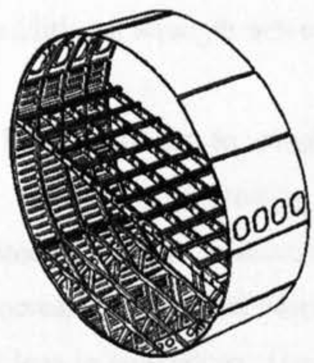

Figure 1.1.2 Stressed skin method of construction used in the fuselage of the Airbus A340

Figure 1.1.2 above shows the method of construction of the Airbus A340 fuselage comprising circumferential frames, longitudinal stringers and skins. All these components are fabricated from aluminium alloys. A new series of aluminium alloys have recently been developed by material scientists which contain the element lithium. These alloys are lighter and stiffer than existing alloys, and are now finding use on the latest aircraft designs.

Figure 1.1.3 below shows the actual proportion of structural materials used in the Boeing 747, which first flew in 1969, and the latest Boeing 777 which had its first flight on the 12th June 1994. Aluminium alloys constitute by far the biggest proportion of structural mass of most modern aircraft, with steels, titanium alloys and structural composites all accounting for approximately 10%.

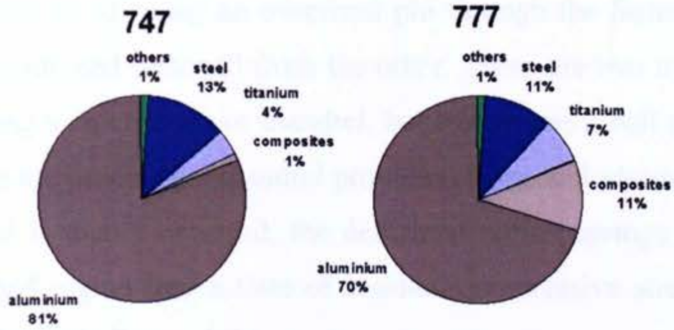

Figure 1.1.3 Structural materials mass distribution on the Boeing 747 and 777

The aluminium-copper alloys of the 2024 series are very strong and are therefore used for structural purposes, but the additional strength achieved is to the detriment of other properties.

These alloys require solution heat treatment to obtain optimum properties. In the solution heat-treated condition, mechanical properties are similar to, and sometimes exceed, those of low-carbon steel. In some instances, precipitation heat treatment (aging) is employed to further increase mechanical properties. This treatment increases yield strength, with an attendant loss in elongation. The effect on tensile strength is not as great.

1.2 THE COLD WORKING PROCESS

The term 'cold working' is applied to any process that results in plastic deformation at a temperature that does not affect the microstructural changes produced by the working.

Swage autofrettage (5), split sleeve cold expansion, solid sleeve cold expansion (6), interference fit fasteners (7), stress coin hole expansion method (8), roll peening (8), stress wave riveting (9), shot peening and roller burnishing (10) are some examples of cold-working processes.

Coldworking fastener holes is a mechanical method of strengthening metallic components by retarding crack growth around the hole. Cold expansion of fastener holes is an extensively used technology employed in both new build and in structural repairs to improve the fatigue performance of fastener holes.

The technique is based on developing a residual stress field surrounding the holes by the use of an oversized pin which is pulled through the hole, resulting in localised plastic deformation and the subsequent development of compressive residual stresses around the hole after the procedure. The new compressive stress field effectively decreases the stress concentration around these holes when the material is submitted to tensile cyclic loading, and therefore, the fatigue life and damage tolerance is enhanced.

The method consists of drawing an oversized pin through the fastener hole, which is inserted from one side and removed from the other. There are two main pin types, the most common using a tapered pin or mandrel, but sometimes a ball shaped pin is used instead [11]. During the process the mandrel provides elastic and plastic deformation, but when this mandrel is totally removed, the deformed region springs back, placing the plastically deformed region into a state of residual compressive stress. Typical stress distributions are shown in Figure 1.2.1.

Figure 1.2.1 Typical radial and tangential stress distribution in a hole subjected to cold expansion [12]

The peak tangential stress is usually, about equal to the compressive yield stress for the material. The compressive residual stress zone extends to a distance between one radius to one diameter from the edge of the hole. Extending beyond this point a tensile zone of lower magnitude is found [12]. The residual stresses arising from cold expansion in the radial direction are entirely compressive with a distribution as shown in the diagram. above.

From the use of this technique, the compressive residual stress field surrounding the hole substantially increases fatigue life, by approximately 3 to 10 times or more [12]. This success is due to the reduced applied stress ratio at the hole, leading to a lower stress intensity factor and an increase in crack growth life.

Fatigue and crack growth life are improved due to the consequent reduction in the effective tensile stresses at the hole periphery. If a crack develops at the hole and starts to propagate, the residual stresses reduce the effective stress intensity factor as illustrated in Figure 1.2.2[13] and hence reduce the crack growth rate.

Currently the most widely used method of cold expansion uses a pre-lubricated split sleeve between the mandrel and the hole. It is believed that, with the split sleeve method, there is less surface damage to the hole, because direct mandrel contact is avoided and more uniform and greater compressive stress is obtained which further increases fatigue life.

Figure 1.2.2 Schematic representation of the effect of cold-working on crack tip stress[13] in terms of Stress Intensity Factor.

1.2.1 SPLIT SLEEVE PROCESS

The cold expansion method most widely used in the aircraft industry is the split sleeve process developed by the Boeing Commercial Aeroplane Company in the early 70s and now marketed by Fatigue Technology Incorporated of Seattle [14].

The diagrams from Figure 1.2.3 to Figure 1.2.7, show the cold expansion procedure. The process development, whether using split sleeve or not, is always the same. In the sequence below, a split sleeve is utilised to expand a hole in a plate.

Figure 1.2.3 After selecting a mandrel to obtain the required interference, a pre-lubricated split sleeve is slipped onto the mandrel attached to the hydraulic puller unit [12].

Figure 1.2.4 The mandrel and sleeve are inserted through the hole [12].

Figure 1.2.5 When the puller unit is activated the mandrel slides down and the hole is expanded [12].

Figure 1.2.6 Finally, the sleeve is removed and discarded [12].

Figure 1.2.7 Now the hole is ready for reaming to obtain the final size [12].

On removal of the mandrel the elastically deformed material relaxes and exerts compressive tangential stresses on the plastically deformed region at the edge of the hole. The main difference between the split sleeve cold expansion method used in this research programme and solid sleeve cold expansion is that in the first method the split sleeve is removed then the hole is reamed before the fastener is fitted whereas in the second method the sleeve can be left in place when the fastener is fitted.

However it is important that whichever cold expansion process is used, the edge distance is sufficient to allow the plastic deformation to be constrained within material which has not exceeded the elastic limit.

If the compressive stresses are sufficiently large the compressive yield stress may be exceeded and reverse yielding may occur. This has the effect of reducing the net residual compressive stresses slightly.

Cassat [10] shows that cold expansion using a sleeve gives a bigger improvement in fatigue performance than that produced by shot peening and roller burnishing. Several investigators have found life improvements in split sleeve cold expanded specimens comparable to that found for solid sleeve cold expanded specimens [15].

1.2.2 LUBRICATION

This is a critical element in all cold expansion processes. Pre-lubrication prevents galling of the hole wall during the expansion process. Furthermore the mandrel slides along the inside of the sleeve which has a molybdenum-disulphide lubricant on its diameter (both surfaces). It has been shown [15] that improper sleeve lubrication may lead to axial sliding of the sleeve in the hole during cold expansion process.

1.2.3 DEGREE OF COLD EXPANSION

The degree of cold expansion ($E_{(FTI)}$) is usually expressed as percentage of the initial hole diameter. For the split-sleeve process the equation used is:

$$\frac{(D_2 - D_1)}{D_1} \times 100\,\% = E_{(FTI)} \qquad (1.2.1)$$

With D_1: initial hole diameter and D_2: mandrel diameter.

As shown, this is a relationship between the initial fastener hole diameter and the maximum mandrel diameter. However, the final hole diameter is not the same as the mandrel diameter because the plate springs back giving a final diameter in between the initial hole diameter and the mandrel diameter.

At the end of the process the final hole diameter D_3 will be given by:

$$D_3 = D_1 + (D_2 - D_1) \times RE = D_1\left(1 + E_{(FTI)} \times RE\right) \qquad (1.2.2)$$

RE is the retained expansion and is generally = 60% for aluminium alloys

The optimum percentage of interference required between mandrel and hole depends basically on the material to be expanded. For aluminium it is from 4% to 5% of mandrel interference, but for steels it is from 5% to 7% [12].

Figure 1.2.8 [16] depicts the typical relationship between the fatigue life for split sleeve cold expanded specimens and the applied expansion. Fatigue life improvement is not usually achieved unless the hole is expanded beyond the tensile yield strain of the material (typical yield strains of structural alloys correspond to expansions of 0.5 to 1% of the initial diameter). Further expansion results in significant fatigue life improvement until the onset of axial plastic displacement of the material. This is usually indicated by excessive surface upset surrounding both ends of the hole.

Figure 1.2.8 Effect of applied expansion [16].

Fatigue Technology Inc recommends that the hole expansion should be between 2% and 5% for most materials. 4% is recommended by FTI for aluminium alloy specimens with a hole size of 6.335mm as used in this investigation.

1.2.4 BENEFITS [illegible]

Coldworking offers many benefits to the aerospace industry. These benefits include:

- *Coldworking reduces rate of crack growth:* by retarding the crack growth rate, coldworking extends the life of a component. Research results from Finney[18], Ozeltin and Coyle [91] and Pell *et al.* [75], produced fatigue life enhancement factors from two to seven.
- *Coldworking reduces unscheduled maintenance:* by increasing the overall fatigue strength of components the probability of premature failure is significantly decreased.
- *Coldworking allows increased time between inspection intervals:* by decreasing the probability of premature failure, time between scheduled inspections can be increased.
- *Coldworking reduces maintenance costs:* the combination of increased fatigue life and fewer inspection intervals will reduce the overall maintenance costs.
- *Repair of original components:* the increased fatigue life will minimize fatigue problems between inspections. This increases the probability that original components can be repaired and reused. The need for redesigned components will be reduced.
- *Aircraft readiness is improved:* less downtime, due to less scheduled and unscheduled maintenance,

1.3 RESIDUAL STRESSES

1.3.1 DEFINITION

Residual stresses are the consequence of the plastic deformation of a body in relation to its free state. The residual stresses are present [19] in the body when no external load is applied.

The total residual stresses at any point in a body are the resultant of the superposition of three kind of residual stresses:

1. macro-stresses (first kind), homogeneous across many grains of the material, which are in equilibrium within the whole body;
2. micro-stresses (second kind), nearly homogeneous in microscopic areas (within a grain or part of grain in the material), they are in equilibrium across a number of grains;
3. inhomogeneous stresses (third kind) across submicroscopic areas which are in equilibrium across small parts of a grain.

The residual stresses obtained in a tube by cold expansion have been defined by Potter and Grant and are shown in Figure 1.3.1 [20]. Initially when the mandrel is in the hole, the hoop stress around the hole is tensile.

If ideal plastic behaviour is assumed as the hoop stress increases up to the yield stress it reaches a maximum value and a plastically deformed zone (elastic-plastic boundary ρ) forms around the hole. This elastic-plastic boundary was investigated by Ozdemir and is shown in Figure 1.3.2[21]. When the mandrel is removed the surrounding material which remains in the elastic range tries to return to its original dimensions thereby creating compressive stresses around the hole. Figure 1.3.1 shows that the hoop stress is most compressive at the edge of the hole.

It can be seen that secondary yielding occurs when the yield stress in compression is exceeded at the edge of the hole. The residual radial stress is zero at the edge and attains negative values between the hole and the outer surface of the tube.

***Figure 1.3.1** Hoop and radial stresses (a) with cold expanding mandrel inserted, (b) after removal of mandrel. R is the radius of the hole, x is the distance from the hole, σ is the residual stress and σ_y is the yield stress [20].exceeded at the edge of the hole. The residual radial stress is zero at the edge and attains negative values between the hole and the outer surface of the tube.*

Figure 1.3.2 Residual hoop and radial stresses evaluated for ideal –plastic material behaviour and Tresca yield criterion (open-end case) where the inner (hole) radius a= 5mm, the outer (cylinder) radius b = 20 mm and the elastic-plastic boundary = 10 mm (5mm away from the hole)[21]

1.3.2 DETERMINATION OF THE RESIDUAL STRESS DISTRIBUTION

Various techniques have been developed and used to determine the residual stress distribution; these could be divided into three groups: experimental, numerical and analytical approaches.

1.3.2.1 EXPERIMENTAL MEASUREMENT OF THE RESIDUAL STRESSES

The experimental techniques include the X-ray diffraction, neutron diffraction, Sachs' cutting method, photo-elastic and optical strain measurement. In general, accurate results can be achieved by using the experimental techniques as demonstrated by many published results [22, 23, 24, 25, 26, 27, 28, 29, 30, 31, 32, 33].

There are three main methods of characterising the residual stress field around cold worked holes [34]. First, there are X-ray [5, 35, 36, 37, 38, 39], or neutron diffraction [40, 41]) methods. They can be used non-destructively (as well as destructively) and involve the measurement of the elastic strain resulting from the presence of residual stresses.

The second method measures stresses by mechanically or chemically removing material, and recording the subsequent dimensional changes (reviewed in [42]).The most well known is Sach's boring technique [43].

Third, there are methods outlined by Hauk [44] which measure some stress dependent physical property, for example, ultrasonic sound velocity or magnetic properties Ogden [45], Lonsdale [46], strain gauge methods [10, 35, 47, 48, 49, 50], holography [51], laser interferometry [52, 53, 54] and Moiré interferometry.[52, 53, 54].

It should be pointed out that none of these methods measure residual stress directly but only measure the magnitude of physical quantities which depend on stress. In converting these physical quantities into stress inevitably some information is lost, often due to simplifying assumptions concerning the application on the method, the nature of the stress distribution and the material properties. In addition constraints on time, cost, and equipment limitations mean that compromises have to be made in developing measurement procedures.

<u>X-ray Diffraction method:</u>

This is a non-destructive method and consists of measuring components of strain directly from changes of lattice spacing in the crystal structure. As interatomic distances are proportional to stress they are considered as small gauge lengths.

From

$n\lambda = 2d \sin\theta$

where

2θ = angle between incident beam and reflected beam

d = interplanar spacing

λ = wavelength of neutrons

n = integer

By differentiating the equation, it can be seen that any change in lattice spacing corresponds to a change in the angle [21].

$$\Delta\theta = \tan\theta \frac{\Delta d}{d} \qquad \text{with} \qquad \varepsilon = \frac{\Delta d}{d}$$

Only residual stresses of the first and second kind can be calculated using this method. Because the X-ray wavelength results in very small penetration depth (less than 100 microns in most metals), only the near surface strains can be obtained. To study the changes in stresses in the thickness of a specimen layers of material may be removed and the strain data recorded. The X-ray method then becomes a destructive method.

Several researchers have used this method [55, 56, 57] to measure stresses in the surface of slices cut from autofrettage tubes [76, 58] and in the area around cold worked holes [35-39].

Neutron Diffraction method:

This method is also non-destructive and works like the X-ray method by measuring changes in interatomic distances. Neutron diffraction is the only technique where strain measurements can be taken within the section without material removal.
This technique is not widely available and is rather expensive compared to the X-ray method.

Sach's Boring technique:

Mesnager in 1919 [59] proposed a technique to identify the longitudinal, tangential and radial residual stresses in bars and tubes. Sachs modified this method in 1927. It consists of a destructive method which is limited to cylindrical bodies where only the radial residual stresses change and not those in the longitudinal and circumferential directions. The process consists of removing layers of material from the inner diameter of the cylinder and using strain gauges to measure the hoop and longitudinal strains.
Using the Sachs equation σ_Z (transverse), σ_Θ (hoop), σ_r (radial residual stress) are defined as follows:

$$\sigma_z(A) = E'\left\{(A_0 - A)\frac{\Delta}{dA} - \Delta\right\}$$

$$\sigma_r(A) = \frac{E'}{2}\left\{\frac{A_0}{A} - 1\right\}$$

$$\sigma_\theta(A) = E'\left\{(A_0 - A)\frac{d\Theta}{dA} - \frac{(A + A_0)}{2A}\Theta\right\}$$

A_0: original cross section

A: instantaneous hole area

Δ : transverse strain component in Sachs equation

Θ: hoop strain component in Sachs equation

E: Young's Modulus

ν: Poisson's ratio

E': $(E/1-\nu^2)$

However the measurements of the strains becomes difficult near the outer surface and here results can only be obtained by extrapolation. Buhler in 1952 [60] changed the position of the strain gauges to the inner surface of the hollow tube instead of on the outer surface and obtained data for the strains near the outer surface.

Later in 1991, Herman & Reid [40] used the Sachs cutting technique to determine the stress distribution around a cold worked hole, using a spark erosion technique.

1.3.2.2 NUMERICAL ANALYSIS OF RESIDUAL STRESS DISTRIBUTION

The numerical approach typically employs the finite element methods (FEM), which have been shown to be efficient for determining the residual stress distributions. The FE codes as ABACUS, ANSYS, PATRAN, NASTRAN and others are employed to evaluate the influence of plane stress and plane strain conditions.

To carry out FE simulation of the cold expansion process with or without split sleeve it is necessary to fulfil the following requirements:

- To specify geometry, dimensions of the parts and tools involving in the process and create their 2D or 3D models.
- To specify mechanical properties of materials from which the parts and tools are made. To describe the elastic behaviour Young's Modulus and Poisson's Ratio are required and to define the plastic behaviour Yield Strength, Ultimate Tensile Strength and maximum Elongation must be known..
- To describe the surfaces which will be in contact with each other and the contact behaviour.
- To specify all the boundary conditions (displacements and constraints) and loads applied to the model.
- To define the mesh of the different components which take part in the simulation.

Developing of computers and software mainly determine progress in FE analysis. Investigations during the last 10 years describe the simulation of the residual stress distributions especially for the mid-thickness range, i.e. neither plane-stress nor plane strain conditions [22, 23, 30, 61,62, 63, 64, 65]. An example of 2D FE simulation and the prediction of residual stress distribution is given in the work of M. Priest & others [30]. Figure 1.3.3 taken from [30] compares FE predictions with experimental X-ray data for a cold expanded hole in a specimen manufactured from Al 2024-T3 (the same material used here). They found that close to the hole edge at the exit face, the predicted tangential residual-stress distributions from FEA compared particularly well with the experimental X-ray measurements. However, the application of uniform displacement of the hole edge in the finite-element model does not allow differentiation between the entrance and exit faces. As a result, the finite-element model *overestimates* the magnitude of the residual stress at the entrance face. A more sophisticated finite-element analysis is therefore required in order to evaluate differences between stress distributions at the entrance and exit faces.

Figure 1.3.3 Comparison between X-ray measurements and integrated finite-element predictions [30]

More recent work presents 3D simulation models of the process and permits prediction of the 3D residual stress field [66, 67, 85]. The Figure 1.3.4 from work of Pavier & other[67] demonstrably illustrates the difference in residual stress distribution in the entrance side, mid-thickness and the exit side in comparison with 2D simulation.

Figure 1.3.4 Normalised residual stresses calculated using the 3D FEA of cold working: tangential residual stresses [66]

This work [66] demonstrates not only 3D finite element analysis but also the interaction and redistribution of the residual stress with applied load for a crack emanating from a cold worked fastener hole.

The finite element analysis is carried out with more sophisticated material models allowing isotropic and kinematic hardening, and the Bauschinger effect. Unfortunately, there are very few works on the subject with experimental proof of the validity of their analysis.

1.3.2.3 ANALYTICAL SOLUTIONS

Compared with numerical or experimental techniques, the closed-form solutions often provide a simpler and faster method to acquire residual stress distributions, because neither special equipment nor tedious calculation is needed in the analytical techniques. More importantly, relatively good results can be obtained, if the solution obtained is based on adequate assumptions and theory. With the development of the cold-expansion technology, a number of such models have been developed, such as those developed by Hsu and Forman [68], Rich and Impellizzeri [69], Chang [23], Ball [24, 70] and many others [71, 72, 73]. The accuracy of these published close-form models have been verified directly by either experimental measurements or numerical calculations or indirectly by fatigue life results.

Poolsuk and Shape [27] have re-evaluated the work of Mann and Jost [74] in plane stress conditions. They observed that some parameters such as yield criteria, reverse yielding behaviour and work hardening properties can affect the distribution prediction. They also defined the importance of the elastic-plastic boundary for the design and spacing of the hole location. For the prediction of residual stress in thick section metal specimens, Pell et al [75] have used the constraint condition where the approach to such calculations is similar to those needed in the autofrettage of a cylinder. Clark [76] has used these observations to predict fatigue crack growth from a cold expanded hole in a thick section aluminium alloy component.

Compared to the efforts in FEM or experimental measurement, these close-form models are simpler to use in assessing the beneficial effect of cold expansion. They can be very useful when combined with a computer program for fatigue crack growth life prediction, which is especially helpful at the component design stage.

While good agreement between fatigue test results and predicted lives was found by some researchers using the closed-form models [23, 24, 25, 61, 69, 70, 77], disagreements were also experienced by many others [26, 27, 28, 29, 30, 32, 33].

A short review of some analytical models was taken from Z.Wang & X.Zhang[78].

Four closed-form solutions are selected for this review, i.e. two plane-stress models, by Hsu and Forman (68) and Ball (70), and two plane-strain models, by Rich and Impellizzeri (69) and Chang (23).

The common issue among these solutions is how to model the reversed loading (or unloading) due to the mandrel removal. The notion that the yield limit of metals in reversed loading can be different from that in monotonic loading was first proposed by Bauschinger in 1886. For most engineering alloys, the reverse yield stress (σ_{ry}) is a fraction of the tensile yield stress (σ_y); this is the so-called Bauschinger or kinematic hardening effect. Assuming a linear hardening, this effect may be demonstrated for a one-dimensional problem (79). The yielding in tension will lower the reverse yield strength so that:

$$(\sigma-\alpha)=\pm\sigma_y$$

where α is the "kinematic shift" of the centre of the yield surface. As a result of this shift, with the initial yield limit σ_y being fixed, the reverse yield stress decreases and the uniaxial stress σ increases. In many studies, the shift of the yield surface centre is defined by:

$$d\alpha=\beta d\varepsilon^p \quad (0\le\beta\le1)$$

where β is a Bauschinger effect related parameter. This depends on the material type, stress state and the magnitude of applied plastic strain. β = 0 simulates isotropic hardening; β = 1 mimics kinematic hardening. For most engineering alloys, mixed hardening describes cyclic loading conditions better, therefore 0 < β < 1 for cyclic plasticity analysis.

Models based on plane-stress theory

The Hsu-Forman model (68) was developed by extending the Nadai theory (71) taking account of work hardening effects. The main assumptions were: (a) material behaviour followed the Ramberg-Osgood relationship; (b) yielding was governed by the Miscs-Hencky criterion; (c) elastic unloading for mandrel removal, hence no reverse yielding.

The Ball model (24, 70) extends the Hsu-Forman theory by including elastic-plastic unloading and, therefore, creating a reverse yielded zone. In the Hsu Forman model, Budiansky's solution (80) was only used for the loading step, but in Ball's model it was applied for both loading and unloading steps of the cold-working process to generalize the solution and to include any potential reverse yielding. Parameter β was introduced to account for the Bauschinger effect. Ball and Lowry evaluated their theory against some X-ray diffraction measurements for a 6.35-mm-thick 2124-T851 aluminium specimen (24), which showed good agreement. They verified the model further by comparing the predicted fatigue life with fatigue test results where good agreement was achieved.

Models based on plane-strain theory

The Rich-Impellizzeri model (69) is a modification of the elasto-plastic solution of Sachs (81) by including the elastic deformation of the mandrel. The model also assumed elastic unloading following the mandrel removal. The authors validated their theory against some test results for two alloys.

Chang's model was developed based on the elasto-plastic solution of a pressurized thick-walled cylinder of Sachs (81). It assumed perfectly plastic material, plane-strain condition under uniform pressure at the hole edge, and Mises-Hencky yield criterion. Residual stress distribution was computed for a 12.7-mm-thick 2024-T851 aluminium plate with a cold-worked hole and then used for predicting fatigue crack growth in the plate. Good correlation with test data was obtained.

Residual stress calculation

Residual stress distributions described by the four models given above were calculated for a simple dog-bone specimen with a cold-worked hole in the centre as shown in Figure 1.3.5. The specimen was made of 2024-T351 aluminium alloy having a width of 25 mm, thickness of 6 mm and hole diameter of 6.35 mm. The original Rich-Impellizzeri and Ball models were modified to account for the Bauschinger effect for this aluminium alloy. For the modified Rich-Impellizzeri model a reverse yield stress value equal to 60% of that in tension was assumed. For Hall's model, kinematic hardening (β = 1) was assumed for this alloy. The work hardening index n in the original Budiansky relation (80),, was assumed to be equal to 2.7 for the Hsu-Forman and Ball models. The differences in the theoretical predictions simply reflect the theoretical treatment of residual stresses adopted by different researchers.

Figure 1.3.5 also shows that the residual tangential stress distributions can be divided into three regions (A, B and C). Region A is at the vicinity of hole edge having compressive tangential stress and a reverse yield zone, region B is transitional between compression and tension with elasto-plastic stresses, and region C is the elastic region.

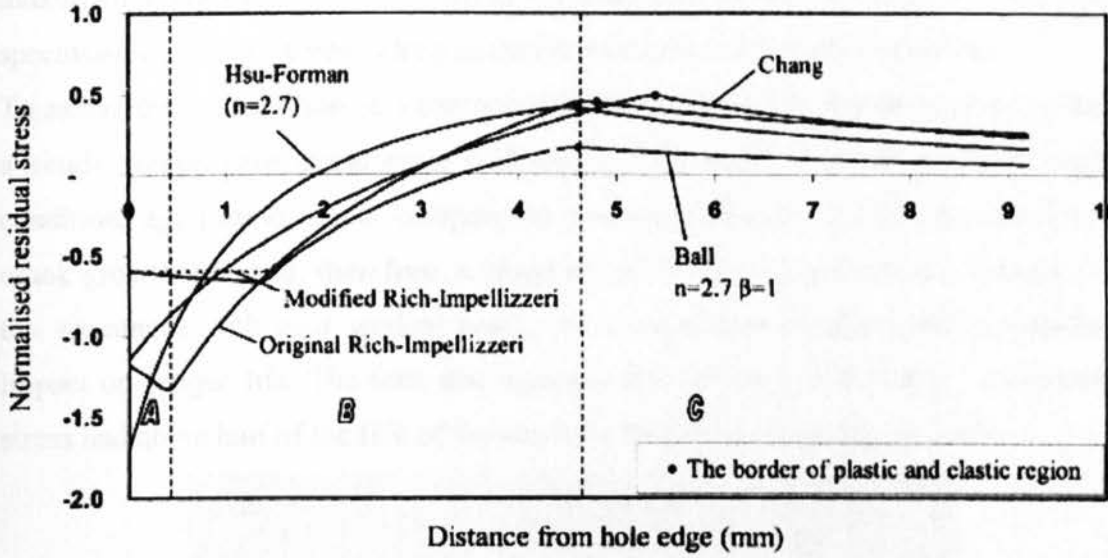

Figure 1.3.5 Residual stress distributions calculated by four different closed-form models.

1.4 FATIGUE BEHAVIOUR OF COLD EXPANDED HOLES

Many experimental results reveal that the cold expansion process, used in manufacture of aircraft structures significantly improves the fatigue life of the assemblies. The most common explanation of this is the reduction in the load cycle amplitude around the bore, which delays crack initiation. Hence the beneficial effect has been proved experimentally.

Philipps [82] tested open holes and holes with net fit and interference fit fasteners. He found a fatigue life improvement factor of 7.5 for a cold worked 2024-T851 aluminium alloy. Several other investigators have found fatigue life improvement factors resulting from cold expansion of between 5 and 10 [15, 82, 83]. Buch and Berkovits[84] obtained a fatigue life improvement factor of 12 for cold expanded lugs under manoeuvring loading in 7075-T6 and 5 for 2024-T3 lugs. Jongebbreu and de Konig [37] tested cold expanded 7075-T73 and 7079-T6 lugs with a commuter aircraft loading spectrum. They observed fatigue life improvement factors ranging up to more than 10.

Ball and Doerfler [85] conducted a series of constant amplitude fatigue crack growth tests of specimens from 2124-T851 (with and without cold working) in which the effects of a single compression overload and of fully reversed loading on cold work life improvement were investigated. Half of the specimens were cold worked to provide 4% expansion. Tests performed at a stress ratio of R= 0.1 (no compression) and a maximum stress of 25 ksi (175 MPa) revealed that the fatigue lives of cold worked specimens were 5 to 7 times as long as the life of the non-cold worked specimen.

To assess the contribution of a compressive overload, test specimens were subjected to a single compressive stress cycle (-25 ksi) (-175 MPa). For the non-cold worked condition, application of the compressive overload caused a slight acceleration in crack growth rate and, therefore, a slight reduction in crack growth life. However, for the specimens with cold worked holes, the compression overload had a significant impact on fatigue life. The tests that included the -25 ksi (-175 MPa). compressive stress had about half of the life of the two tests that did not (see Figure 1.4.1).

Figure 1.4.1 Constant amplitude fatigue crack growth results -effect of one compressive cycle on cold worked holes (R=0.1).[85]

Test results with non cold worked specimens are presented for comparison, and from these results it can be seen that while the compressive load applied to specimens significantly reduced the advantage of cold expansion, it did not completely eliminate it. The life improvement ratios dropped from 5 to 7 down to about 2.5.

The results of the four fully-reversed (R=-1.0) fatigue tests are presented in Figure 1.4.1 These tests had the same maximum stress as the tests at R=0.1 but with a much lower R, the resulting fatigue lives were much shorter. The existence of the compression loading reduced the benefit of cold expansion. The fatigue lives of the cold worked specimens were approximately 2 times as long as the lives of the non-cold worked specimens.

Grandt and Potter [20] used Philipps[82], Crews[86] and their own results to compare the experimental and theoretical values for optimum interference level as a function of hole size.

However, Chandawanich [15] also suggested the existence of an optimum degree of cold expansion. He observed that the fatigue life does not increase continuously with an increasing degree of cold expansion [87]. 4% expansion has been reported [88] to result in the maximum fatigue endurance in aluminium alloys.

For 7075-T6 specimens J. Schijve and F.A. Jacobs [8] also observed an increase in the fatigue life and the optimum hole expansion was found to be between 4% to 6%. She Gong-Fan et al [89] found that the fatigue life increased by a factor of between 2.75 and 5.1 for 7075-T6 specimens expanded by 3.6%. This optimum degree of cold work is related to the yield stress of the material (see below) since the maximum compressive residual stress is limited by the yield strength.

1.4.1 FACTORS AFFECTING THE FATIGUE BEHAVIOUR OF COLD EXPANDED SPECIMENS

Yield stress

Jongebreur and de Konig [37] showed that lower yield stress gave lower compression hoop stresses at the edge of the hole. Shijve & al [8] showed in Figure 1.4.2, assuming that the maximum compressive stress at the edge of the hole was equal to the yield stress, that higher residual stresses can be generated in higher strength material. The figure also shows that the superposition of compressive residual stresses and tensile residual stresses gives a total stress distribution which is compressive at the edge of the hole for higher yield stress values.

Effect of hole geometry:

According to Philipps [82], Mann et al [90] fatigue life is not affected by the edge margin when it exceeds 1.75 times the hole diameter or by hole spacing when it is at least equal to three times the hole diameter. Jongebreur and de Konig [37] also found that the development of the compressive tangential stress area was affected by the distance between the hole and the edge such that smaller edge hole distances produces smaller compressive stress areas.

Effect of the split sleeve:

The hole deformation is non-uniform during the cold expansion process due to the presence of the split in the sleeve, which has a tendency to open up when the mandrel passes through. Ozelton and Coyle [91] have defined this non-uniformity of plastic deformation as the "pip" (Figure 1.4.3).

Figure 1.4.2 Qualitative pictures of residual stresses after cold work and stress due to external load[8].

Figure 1.4.3 Hole configuration after split sleeve cold working [91].

They observed that primary shear cracks may appear at the pip location. In most cases, a final ream is carried out to remove the majority of cracks. It has been observed [92] that the position of the split in the sleeve played an important part in the residual stress distribution and thus in the fatigue performance. Figure 1.4.4. [92] shows the hoop stresses versus the distance from the edge of the hole from X-ray measurements on the outlet face and Sachs measurements at mid section. It can be seen that the more compressive areas are at the split sleeve position for the outlet face and at 90° from the "pip" at mid thickness. The areas with the lowest compressive residual stresses are at 180 ° for the outlet side and for the mid section. It is therefore important that this region does not coincide with the position of crack initiation.

Figure 1.4.4 Variation of residual stress distributions with angular location [92].

Effect of material thickness

Sharpe [55] noted that the fatigue life of the specimen can be reduced when large amounts of coldworking damage the hole.

R Cook [22, 92] found that the fatigue performance of a thick aluminium alloy specimen was higher than that for thin specimens due to the compressive residual hoop stresses being higher in the centre of the thick specimens than near the specimen surface.

Effect of reaming:

R.Cook [92] observed that reaming of holes after cold expansion reduces the fatigue endurances (for 2% expansion) since it leads to residual tensile stresses at the edge of the hole. These stresses reduced the residual hoop stress value induced by cold expansion [92]. He noted that this effect became less marked with increasing expansion level (4% or 6 % expansion).

Cold working of precracked holes:

The beneficial effect of cold working of holes containing pre-existing cracks has been noted by Petrak et al [9] and Jongebreu et al [37]. Shijve et al [8] concluded that completely removing small cracks prior to cold expansion will give a significant improvement in fatigue life.After repairing cracked holes (re-drilling, reaming and cold-working), Köbler [93] found that for a stress amplitude equivalent to 10 % of the maximum yield stress, the crack propagation life was increased by up to 6 times. On the other hand, Philipps [82] noted that the fatigue performance for precracked holes was similar to that of uncracked specimens. Pell et al [94] did not notice any difference in fatigue life for uncracked and cracked holes (to a crack length of 0.75 mm) in thick section material.

Effect of temperature

There are instances where components are used at elevated temperatures. For example during supersonic flight the speed of Concorde reaches 2.05 Mach and temperatures arising from aerodynamic heating are anticipated to be in the range 100-130°C. For aluminium alloys creep and relaxation mechanisms become active at this temperature. Furthermore, the proposed supersonic transport aircraft, currently in a development stage, will be required to fly at a speed as high as Mach 2.4, thus giving rise to temperatures of 160°C and higher [95]. The fatigue life improvement of cold expanded fastener holes is attributed to the presence of compressive residual stresses induced through cold expansion. Exposure to elevated temperature can give rise to residual stress relaxation [96] and could therefore significantly affect the fatigue life. Nevertheless, depending on the applied temperature and loading conditions the beneficial effects from cold expansion can still be retained [97]. It is important to examine whether fatigue life improvement from cold expansion is still retained at elevated temperatures.

In paper [98] results from residual stress measurements and fatigue crack growth tests are reported and presented below. All measurements and tests were carried out on aluminium alloy (Al 2650), an alloy developed for advanced supersonic transport (AST) applications. Residual stress measurements were made on specimens containing holes after cold expansion and after exposure to various temperatures and loading conditions. A series of fatigue crack growth tests were carried out using plates containing plain holes and cold expanded holes in Al 2650.

Results revealed that residual stress relaxation occurred as a result of exposure at 150°C. The magnitude of relaxation was shown to be dependent on the level and the sign of externally applied load. Fatigue crack growth tests have been carried out at 20^0C and 150°C for both cold expanded and non-cold expanded conditions. Fatigue crack growth rates in specimens containing cold expanded fastener holes were affected significantly by elevated temperature exposure. Depending on the exposure time and loading conditions the fatigue life improvement was found to be between one and greater than 10 for tests at 20°C.

The measurements for the test conditions are shown in Figure 1.4.5. Only hoop residual stresses for θ =90° are shown.

This angular position corresponds to the position for crack growth in fatigue loading and hoop stresses are the most relevant for fatigue crack growth. Results demonstrate that indeed residual stress relaxation occurred close to the hole edge. The maximum compressive residual hoop stress relaxed by about 80 MPa. In the case of exposure to high temperature even greater relaxation occurred. The most detrimental case was the application of compressive loading at 150°C. This is not unexpected since externally applied compressive stresses are superimposed on compressive residual stresses that arise from cold expansion.

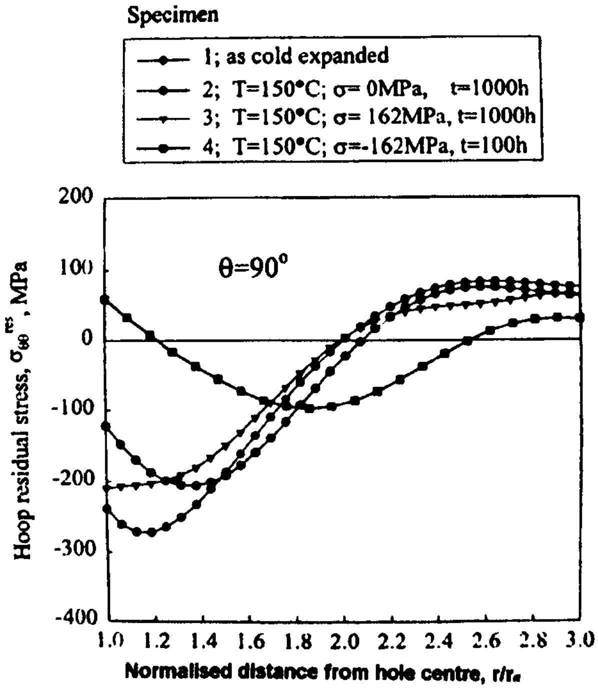

Figure 1.4.5 Hoop residual stress distribution for various loading and temperature conditions

1.4.2 CRACK INITIATION AND PROPAGATION IN COLD EXPANDED SPECIMENS

For non cold worked specimens, Chandawanich (54) observed that cracks initiate on one side of the hole at 90° from the tensile loading axis. He also noted that additional cracks were initiated on the other side of the hole. At initiation these two cracks did not necessary form throughout the full thickness of the material. Su and al (39) observed that 90% of the cracks were found at the bore and were semi-elliptical in form. Forsyth and Powell (74) also noted that crack growth was faster along the bore of a hole than along the radial direction.

For a specimen with a coldworked hole, fatigue cracks initiate almost simultaneously on diametrically opposite sides of the hole (15). The cracks seemed to initiate more frequently from the corner of the hole (39, 99) and at the inlet side (82, 100) of the split sleeve expanded holes. Cracking on the mandrel exit side was less common (90) . Cracks starting at the edge of the hole from the inlet side were found to propagate through the thickness of the specimen before growing along the surface to failure (100).

R.Cook (22) observed that cracks initiate with equal probability on the mandrel inlet face and outlet face. However like Pell et al (75) and Clark (76) he found that cracks grow faster on the inlet side than on the outlet side. This is probably due to the residual compressive hoop stresses being smaller at the mandrel entrance side [15, 37]. As crack initiation is induced by cyclic shear stress, Schijve and al [8] underlined the effect of the compressive residual stresses on the retardation of crack growth.

Finally R. Cook also found that fatigue life improvements due to cold expansion are mainly due to an increase in the duration of the crack propagation phase. Colon and Reids [101] also proved by theoretical analysis that cold expansion improves the fatigue life by retarding the crack growth. In comparison to non cold expanded specimens, the crack growth rates of cold expanded specimens are lower and their fatigue lives are longer [102].

The influence of the stress ratio on crack propagation in cold expanded specimens has been investigated by Torr [102]. He found that a change from a positive stress ratio to a negative stress ratio reduced the rate of crack propagation. The effect of applied stress has been demonstrated by Petrak and Stewart [9]. They found that low stresses retard fatigue cracks more than higher loads.

1.4.3 EXPERIMENTAL AND PROMISING COLD EXPANSION TECHNOLOGIES FOR IMPROVING THE FATIGUE PERFORMANCE OF HOLES

The effects of concurrent cold-expansion and ring-indentation on the growth of fatigue cracks emanating from circular holes

This work [103] describes a more efficient method for obtaining fatigue life enhancement of a structural member with fastener holes. Residual stresses were induced onto premachined holes using a ring-indentation process near the fastener hole combined with cold-expansion.

The specimens made from 6061-T6 aluminium alloy with drilled and reamed holes were cold-expanded with a tailor-made mandrel. The hole surface was protected from excess pressure imparted by the mandrel by the use of split sleeves. Finally the process of plastic indentation was performed. Ring punches with a thickness of 0.5 mm were indented around holes. Three types of ring punch, with average diameters of 9.7 (specimens A), 12.7(specimens B) and 16.7 (specimens C) mm, were used as illustrated in Figure 1.4.6. The indentations were located in the region of the elastic-plastic boundary around cold-expanded hole. Three different indentation pressures, 980, 1080 and 1180 MPa were arbitrary chosen and applied.

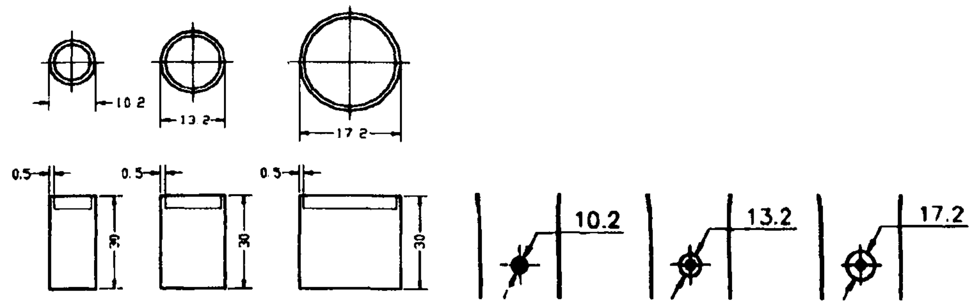

Figure 1.4.6 Circular rings and corresponding indentations on the specimens

The Figure 1.4.7 (a) shows the residual stress distribution around a hole resulting from a combination of cold-expansion and ring-indentation. The indentation pressure for the three specimens was 1180 MPa. It can be observed that a complex residual hoop stress field are introduced around a hole by ring-indentation after hole cold-expansion. The combined process provided a significant increase in the compressive residual stresses in the region immediately adjacent to the surface of the hole compared with that from cold-expanded hole alone. The optimum position of ring-indentation was produced by the indentation located in the region of the elastic-plastic boundary around the cold-expanded hole (type B), giving the biggest increase of compressive residual stress at the hole boundary. On the other hand, when the indentation is placed very near to the hole or far away from the hole, its effect becomes weak.

Figure 1.4.7 (b). shows the effects of different degrees of indentation pressure on the residual stress field. The indentation was located in the region of elastic-plastic boundary around the cold-expanded hole using the B-circular ring. It can be seen that the maximum hoop stresses and residual stresses increase as the relative indentation pressure increases, but when a 980 MPa indentation pressure is applied its influence becomes weak.

The growth of the radial cracks from the specimen holes is shown in Figure 1.4.8 (a). It was found from the figure that the lowest pressure (980 MPa) creates little difference in the fatigue data over cold-expansion, but when the indentation pressure is increased, this is reflected in crack growth. However, if a comparison is made between (CX, type B, 1080MPa) and (CX, type B, 1180MPa) specimens, the total fatigue life of the (CX, type B, 1180MPa) specimen is longer. Consequently it can be clearly discerned that the retardation of crack is more clearly presented as the relative indentation pressure increases. This phenomenon is related to the distribution of compressive residual stress around a hole in Figure 1.4.7 (b) and crack growth is further retarded with increasing compressive residual stress.

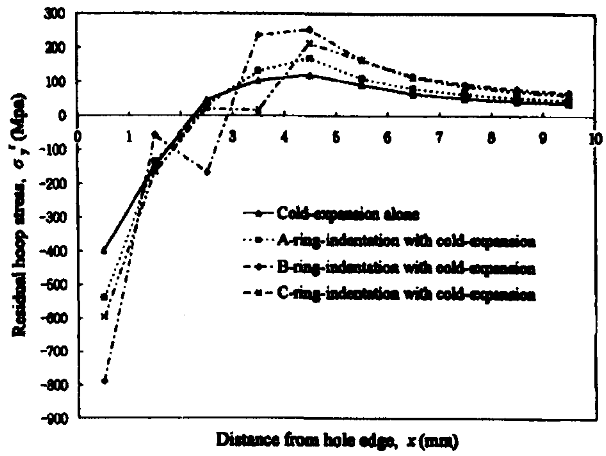

(a)

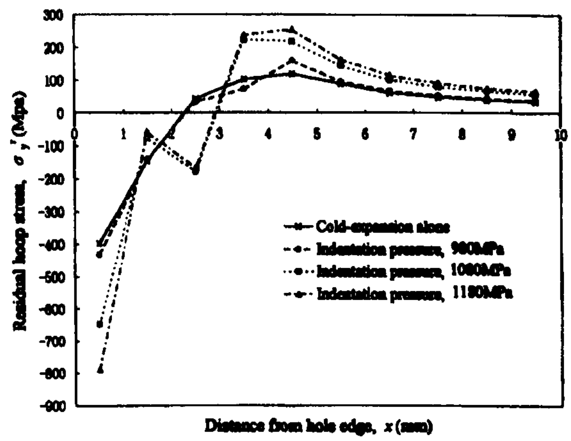

(b)

Figure 1.4.7 Effect of punch location on the distribution of residual hoop stresses – (a); Effect of indentation pressure on the distribution of residual hoop stresses - (b)

The fatigue crack growth rate vs crack length for non-worked, cold-expanded and combination-worked specimens is shown in Figure 1.4.8 (b). Three specimens have about same crack growth rate at a crack length of 3 mm. At longer crack lengths, the growth rate of cold-expanded specimens is higher than that for non-worked specimen, while at smaller crack lengths a lower growth rate is obtained from combination-worked specimens. In particular, the retardation of growth rate is more clearly presented when the crack had grown into the indentation area. A possible explanation of this phenomenon in crack growth rate is the distribution of compressive residual stress inside the indentation area. The boundary between the residual compressive and tensile stresses occurs at about 3 mm from the hole edge, as shown in Figure 1.4.7 (a). On the other hand, when the crack passes through the indentation area the growth rate increased rapidly.

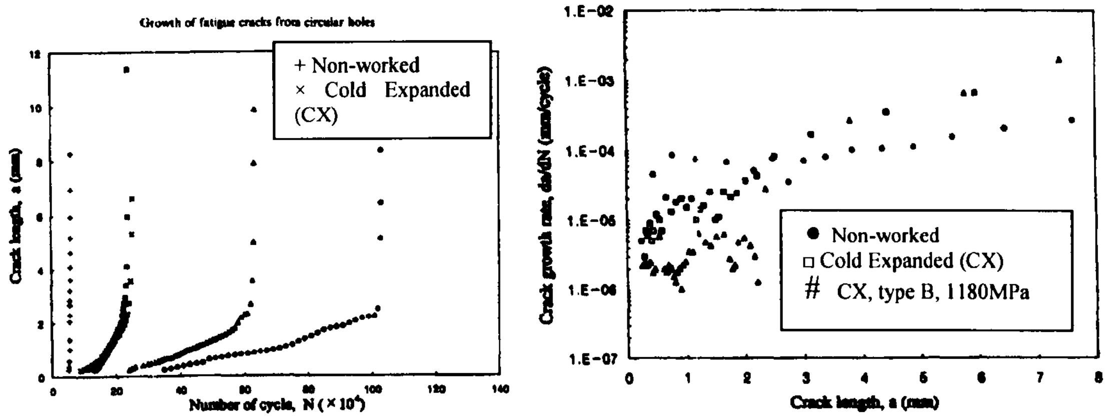

(a) (b)

Figure 1.4.8 Crack growth curves –(a); Fatigue crack growth rates - (b)

Thus, it has been demonstrated that the adoption of a combined process can provide a significant improvement in fatigue life for a specific fastener configuration. The fatigue crack retardations are observed after the application of the method, and the retardation effect is, indeed, far greater than that obtained with cold-expansion alone.

Cold expansion with tapered pin and mating split sleeve with taped bore

Authors of the work [104] reports of new cold expansion method with tapered pin and mating split sleeve with tapered bore.

Using a tapered pin and inserting it from one side of the hole and removing from the other side results in uneven (and thus poor) residual stress distribution through the plate thickness at the hole surface. This is found to occur whether or not a parallel-walled split sleeve (i.e., one having a constant wall thickness) is used. It is found that using a tapered pin creates less compressive tangential residual stress locally at the pin entrance face compared to the mid-plane and exit face of the plate at hole edge. The lower the compressive residual stress created at the entrance face it is more vulnerable to early crack initiation and propagation in that region when the holed plate is subjected to cyclic loading.

To avoid a non-uniform tangential residual stress distribution, resulting from using a ball or tapered pin (either with or without parallel sleeve), a new method of cold expansion is proposed which uses a tapered pin with a mating split sleeve having a tapered bore (Figure 1.4.9). With this method a tapered pin is pushed by a predetermined amount into a mating split sleeve (which is initially located in the hole) to achieve a desired amount of radial expansion and then withdrawn. The tapered pin and sleeve bore angle that was used had a total angle of just under 4° and was chosen so that a standard tapered reamer could be used.

Figure 1.4.9 Cold expanding a hole using a tapered pin with a mating tapered split sleeve. (104)

Having a tapered pin with a mating taper bored sleeve requires a greater pushing force compared to using a ball or tapered pin directly, or even using a sleeve with a parallel wall thickness, as radial pressure is applied across the full depth of the hole rather than locally. However, this force is necessary if the hole is to expand and spring back uniformly through the complete plate thickness and result in a much more even distribution of compressive tangential residual stress.

This reasoning has been supported by the results of a theoretical study using a multicomponent, three dimensional, finite element model with elastic/plastic non-linear material simulation (The tangential residual stress distribution in the presented novel method is much more uniformly distributed, as shown in Figure 1.4.10 ., whereas in the parallel sleeved method the tangential residual stress at the entrance face is less compressive than at other planes (as shown in Figure 1.4.11). In the specimens that were cold expanded by a tapered pin with parallel split sleeve, all fatigue cracks started from the hole edge at (or near) the entrance face. However, with the specimens treated using the newly proposed cold expansion method, cracks started at random locations—at the hole edge of the entrance and exit faces or even far from the hole edge.

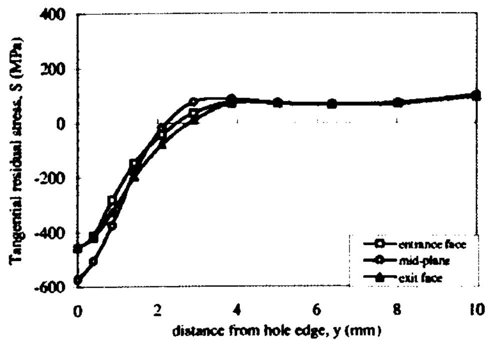

Figure 1.4.10 FE predicted tangential residual stress distribution for three planes at the smallest cross section

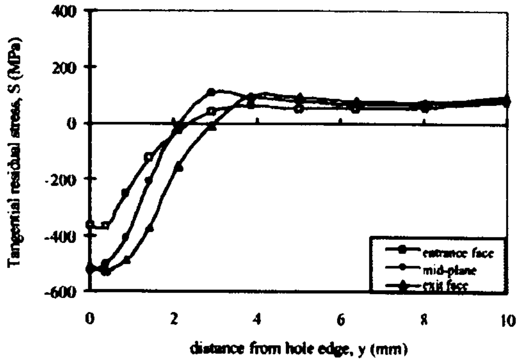

Figure 1.4.11 FE predicted tangential residual stress distributions around a cold expanded hole using a tapered pin with a parallel split sleeve

This shows that the vulnerable region around hole edge was strengthened due to the compressive tangential residual stress formed by cold expansion treatment and thus cracks tried to initiate from micro-structurally weak regions away from the hole location.

1.5 ELEMENTS OF LINEAR ELASTIC FRACTURE MECHANICS (LEFM)

It necessary to know some elements of linear fracture mechanics to be able to predict the crack growth and crack growth rate through the area subjected to cold expansion. Stress Intensity Factor is one of the most important parameter for the prediction and the basics of LEFM given below lead up to its explanation.

Most of the material for this section has been compiled from refs[105, 106, 107]

1.5.1 STRESS ANALYSIS OF CRACKS

The fracture of flawed components may be analyzed by a stress analysis based on concepts of elastic theory. Using modifications of analytical methods described by Westergaard [108], Irwin [109] published solutions for crack-tip stress distributions associated with the three major modes of loading shown in Figure 1.5.1. Note that these modes involve different crack surface displacements.

Mode I. Opening or tensile mode, where the crack surfaces move directly apart.

Mode II. Sliding or in-plane shear mode, where the crack surfaces slide over one another in a direction perpendicular to the leading edge of the crack.

Mode III. Tearing or antiplane shear mode, where the crack surfaces move relative to one another and parallel to the leading edge of the crack.

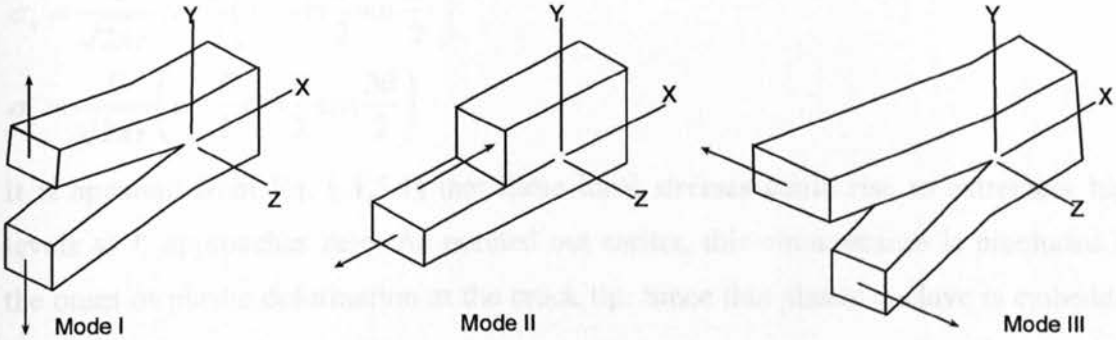

Figure 1.5.1 Basic modes of loading involving different crack surface displacements.

Mode I loading is encountered in the overwhelming majority of actual engineering situations involving cracked components. Consequently, considerable attention has been given to both analytical and experimental methods designed to quantify Mode I stress-crack-length relations. Mode II is found less frequently and is of little engineering importance. One example of mixed Mode 1-11 loading involves axial loading (in the Y direction) of a crack inclined as a result of rotation about the Z axis Figure 1.5.3
Even in this instance, analytical methods [110] show the Mode I contribution to dominates the crack-tip stress field when $\beta > 60^{\circ}$ can this be lowered. Mode III may be regarded as a pure shear problem such as that involving a notched round bar in torsion.
For the notation shown in
Figure 1.5.3, ***the crack-tip stresses are found to be***

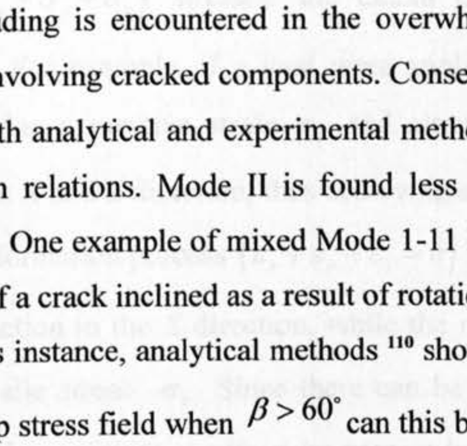

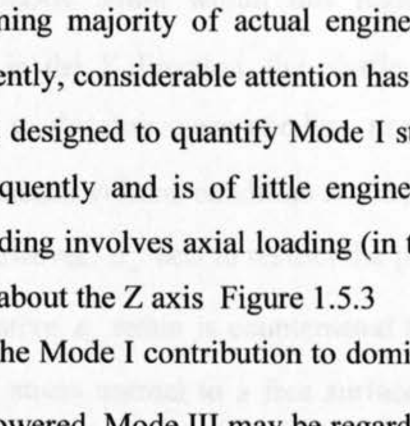

Figure 1.5.2 Crack inclined β degrees about z axis. Mode I dominates when

$\beta > 60^{\circ}$

Figure 1.5.3 Distribution of stresses in vicinity of crack tip

$$\sigma_y = \frac{K}{\sqrt{2\pi r}} \cos\frac{\theta}{2}\left(1 + \sin\frac{\theta}{2}\sin\frac{3\theta}{2}\right) \qquad (1.5.1)$$
$$\sigma_x = \frac{K}{\sqrt{2\pi r}} \cos\frac{\theta}{2}\left(1 - \sin\frac{\theta}{2}\sin\frac{3\theta}{2}\right)$$
$$\sigma_z = \frac{K}{\sqrt{2\pi r}} \left(\sin\frac{\theta}{2}\cos\frac{\theta}{2}\cos\frac{3\theta}{2}\right)$$

It is apparent from Eq. (1.5.1) that these local stresses could rise to extremely high levels as r approaches zero. As pointed out earlier, this circumstance is precluded by the onset of plastic deformation at the crack tip. Since this plastic enclave is embedded within a large elastic region of material and is acted upon by either biaxial $(\sigma_x + \sigma_y)$ or triaxial $(\sigma_x + \sigma_y + \sigma_z)$ stresses, the extent of plastic strain within this region is suppressed. For example, if a load were applied in the *Y* direction, the plastic zone would develop a positive strain ε_y and attempt to develop corresponding negative strains in the *X* and *Z* direction, thus achieving a constant volume condition required for a plastic deformation process $(\varepsilon_x + \varepsilon_y + \varepsilon_z = 0)$. However, σ_x acts to restrict the plastic zone contraction in the *X* direction, while the negative ε_z strain is counteracted by an induced tensile stress σ_z. Since there can be no stress normal to a free surface, the through-thickness stress σ_z must be zero at both surfaces but may attain a relatively large value at the mid-thickness plane. At one extreme, the case for a thin plate where σ_z cannot increase appreciably in the thickness direction, a condition of *plane stress* dominates, so

$$\sigma_z \approx 0 \qquad (1.5.2)$$

In thick sections, however, a σ_z stress is developed, which creates a condition of triaxial tensile stresses acting at the crack tip and severely restricts straining in the *z* direction. This condition of *plane strain* can be shown to develop a through-thickness stress

$$\sigma_z \approx \nu(\sigma_x + \sigma_y) \qquad (1.5.3)$$

The distribution of σ_z stress through the plate thickness is sketched in Fig. 8.6 for conditions of plane stress and plane strain.

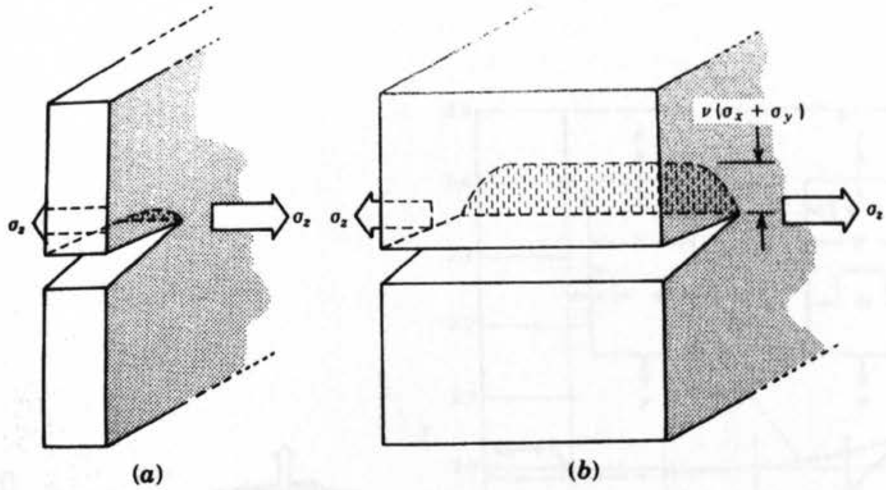

Figure 1.5.4 Through-thickness stress σ_z in (a) thin sheets under plane-stress state and (b) thick plates under plane-strain conditions.

An important feature of Eq. (1.5.1) is the fact that the stress distribution around any crack in a structure is similar and depends only on the parameters r and θ. The difference between one cracked component and another lies in the magnitude of the stress field parameter *K,* defined as the ***stress-intensity factor***. In essence, *K* serves as a scale factor to define the magnitude of the crack-tip stress field. From Irwin's paper we see that

$$K = f(\sigma, a) \tag{1.5.4}$$

where the functionality depends on the configuration of the cracked component and the manner in which the loads are applied. Many functions have been determined for various specimen configurations and are available from the fracture mechanics literature (110, 111, 112, 113). Solutions for plate with crack are shown in Fig. 8.7 for both commonly encountered cracked component configurations and standard laboratory test sample shapes, where the function is defined by *Y(a/W).*

Figure 1.5.5 Stress Intensity Factor solutions for plate with crack [114]

Consistent with Eq. (1.5.1), the stress-intensity factor is most often found to be a function of stress and crack length. The solution for the centre-cracked panel, however, deserves further comment here. Accurate stress-intensity-factor solutions in polynomial form for this configuration were reported by several investigators with the results shown graphically in Figure 1.5.5 (c) More recently, Feddersen [115] noted that these polynomial expressions could be described with equal precision but much more conveniently by a secant expression with the form

$$K = \sigma\sqrt{\pi a} \cdot \sqrt{\sec \pi a / W} \qquad (1.5.5)$$

Crack Emanating from a Round Hole

These configurations (Figure 1.5.6) is commonly found in engineering practice (especially in aircraft components, which contain many rivet holes) since cracks often emanate from regions of high stress concentration.

These cases are the most relevant for crack configurations observed in present test and will be considered later in details in Section 1.7 ***Stress Intensity Factors***

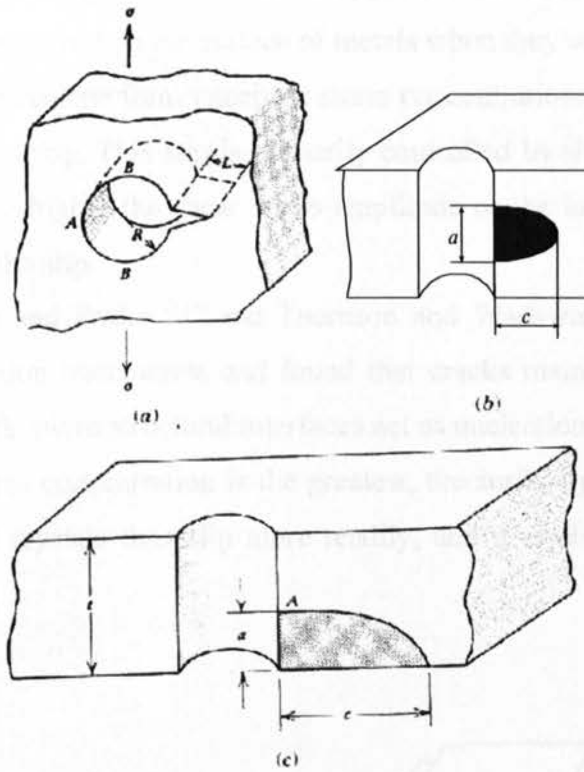

Figure 1.5.6 Complex crack configurations, (a) Crack emanating from hole; (b) semielliptical crack at hole; (c) quarterelliptical corner crack emanating from through-thickness hole.

1.5.2 CRACK INITIATION

Metals are crystalline in nature, which means atoms are arranged in an ordered manner. Most structural metals are polycrystalline and thus consist of a large number of individual ordered crystals or grains. Each grain has its own particular mechanical properties, ordering direction, and directional properties. Some grains are oriented such that planes of easy slip or glide are in the direction of the maximum applied shear stress. Slip occurs in ductile metals within individual grains by dislocations moving along crystallographic planes. This creates an appearance of one or more planes within a grain sliding relative to each other. Slip occurs under both monotonic and cyclic loading.

Figure 1.5.7 (*a*) shows an edge view of coarse slip normally associated with monotonic and high stress amplitude cyclic loading. Under lower stress amplitude cyclic loading fine slip occurs as shown in Figure 1.5.7(*b*). Coarse slip can be considered an avalanche of fine movements. Slip lines shown in Figure 1.5.7 appear as parallel lines or bands within a grain when viewed perpendicular to the free surface. Both fine and coarse slip are studied with prepolished, etched specimens using optical and electron microscopy techniques.

Forsyth [116], using electron microscopy, showed that both slip band intrusions and extrusions occurred on the surface of metals when they were subjected to cyclic loading. Slip band intrusions form excellent stress concentrations, which can be the location for cracks to develop. This slip is primarily controlled by shear stresses rather than normal stresses. The higher the shear stress amplitude or the larger the number of repetitions, the greater the slip.

Plumbridge and Ryder [117] and Thomson and Wadsworth [118] have examined fatigue crack initiation phenomena and found that cracks mainly initiate at the metal surface (unless weak micro structural interfaces act as nucleation sites). It is at the metal surface that the stress concentration is the greatest, the surface grains are less constrained than the interior crystals thus slip more readily, and it is also subject to the effects of the atmosphere.

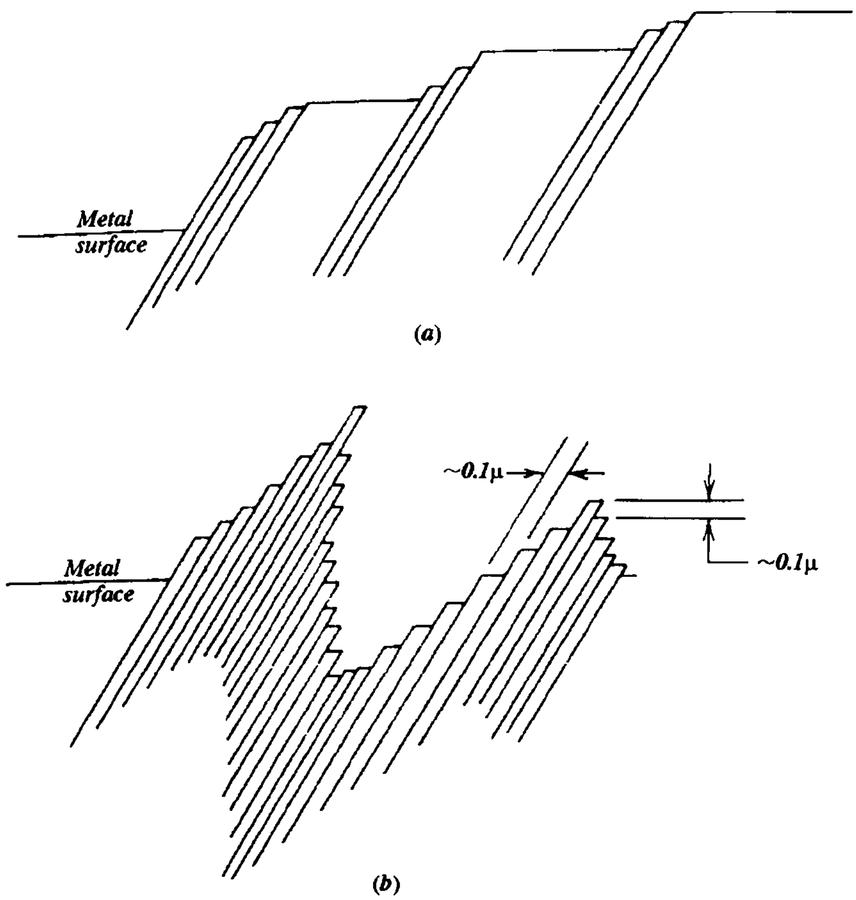

Figure 1.5.7 Slip in ductile metals due to external loads. (a) Static (steady stress (b) Cyclic stress.

Fatigue cracks initiate in local slip bands and initially tend to grow in a plane of maximum shear stress range. This growth is quite small, usually of the order of several grains. As cycling continues, the fatigue cracks tend to coalesce and grow along planes of maximum tensile stress range. The two stages of fatigue crack growth are called stage I and stage II [116].

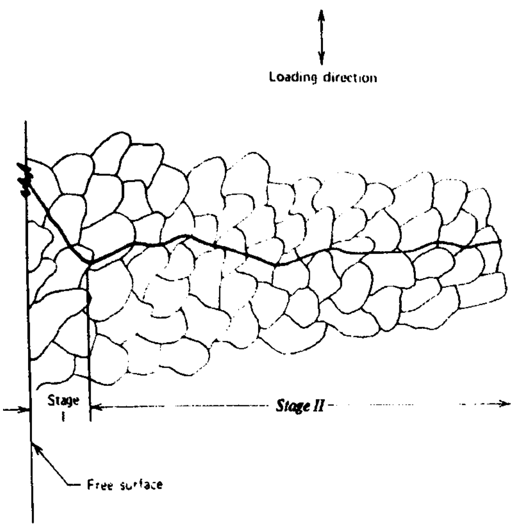

Figure 1.5.8 Schematic illustration of the deformation at a fatigue crack tip during one loading cycle [120].

Figure 1.5.9 Schematic of stages I and II transcrystalline microscopic fatigue crack growth

Fatigue crack growth is shown schematically as a microscopic edge view in Figure 1.5.9, where a fatigue crack initiates at the surface and grows across several grains controlled primarily by shear stresses, and then grows in a zigzag manner essentially perpendicular to, and controlled primarily by, the maximum tensile stress range. Most fatigue cracks grow across grain boundaries (transcrystalline) as shown; however, they may also grow along grain boundaries (intercrystalline) but to a much lesser extent. Slip line progression, similar to that in Figure 1.5.9, precedes the fatigue crack tip vicinity as the crack grows across the material.

Figure 1.5.8 [119] shows the deformation at a fatigue crack tip during one loading cycle.

It may be assumed that crack nucleation can start from the first load cycle, the crack can propagate at each successive load cycle and as seen previously a microcrack may initiate from the slip band. Ashby and Jones [120] have shown that for a typical engineering material containing defects, the crack will advance and link with the defect, increasing the rate of crack growth.

The fatigue mechanism in high strength or brittle metals may not contain slip band formations. Microcracks are often formed directly at discontinuities, such as inclusions or voids, and then grow along planes of maximum tensile stresses.

Fatigue crack growth is shown schematically as a microscopic edge view in Figure 1.5.9, where a fatigue crack initiates at the surface and grows across several grains controlled primarily by shear stresses, and then grows in a zigzag manner essentially perpendicular to, and controlled primarily by, the maximum tensile stress range. Most fatigue cracks grow across grain boundaries (transcrystalline) as shown; however, they may also grow along grain boundaries (intercrystalline) but to a much lesser extent.

The mechanism of fatigue described above is summarized schematically in Figure 1.5.10[121].

Figure 1.5.10 Schematic representation of the fatigue process[121]

Slip occurs first, followed by fine cracks that can be seen only at high magnification. These cracks continue to grow under cyclic loading and eventually become visible to the unaided eye. The cracks tend to combine such that just a few major cracks grow.

These cracks (or crack) reach a critical size and sudden fracture occurs. The higher the stress magnitude, the sooner all processes occur.

1.5.3 CRACK PROPAGATION AND CRACK GROWTH RATE

Typical constant amplitude crack propagation data are shown in Figure 1.5.11. The crack length, *a,* is plotted versus the corresponding number of cycles, *N,* at which the crack was measured. As shown, most of the life of the component is spent while the crack length is relatively small. In addition, the crack growth rate increases with increased applied stress.

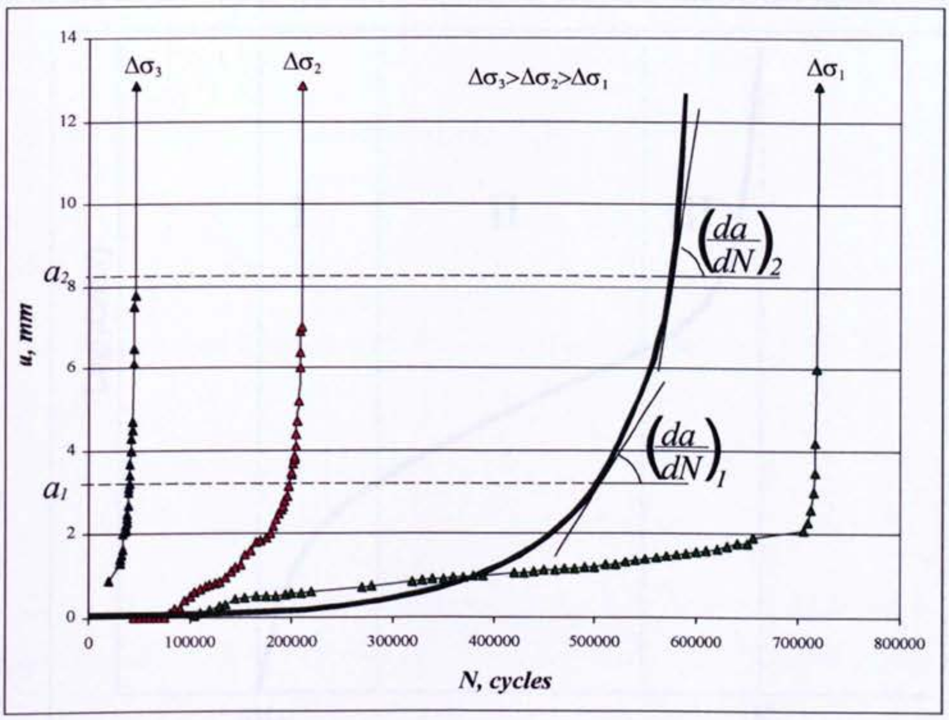

Figure 1.5.11 Constant amplitude crack growth data taken from present work

Starting with crack initiation, cyclic loads are applied and the resulting change in crack length is monitored and recorded as a function of the number of load cycles. Many monitoring techniques have been employed, such as the use of a calibrated travelling microscope, eddy current techniques, electropotential measurements, compliance measurements, and acoustic emission detectors. The fatigue crack growth rate is determined from such a curve either by graphical procedures or by computation. From these methods, the crack growth rates resulting from a given cyclic load are $\left({da}/{dN}\right)_1$ and $\left({da}/{dN}\right)_2$ when the crack is of lengths a_1, and a_2, respectively. It is important to note that the crack growth rate most often increases with increasing crack length. It is most significant that the crack becomes longer at an increasingly rapid rate, thereby shortening component life at an alarming rate. An important corollary of this fact is that most of the loading cycles involved in the total life of an engineering component are consumed during the early stages of crack extension when the crack is small and, perhaps, undetected.

Values of $\log(da/dN)$ can be plotted versus $\log(\Delta K)$, for a given crack length, using the equation

$$\Delta K = K_{\max} - K_{\min} = \Delta\sigma\sqrt{\pi a} f(g) \qquad (1.5.6)$$

where $\Delta\sigma$ is the remote stress applied to the component.

A plot of log *da/dN* versus log *AK*, a sigmoidal curve, is shown in Figure 1.5.12.

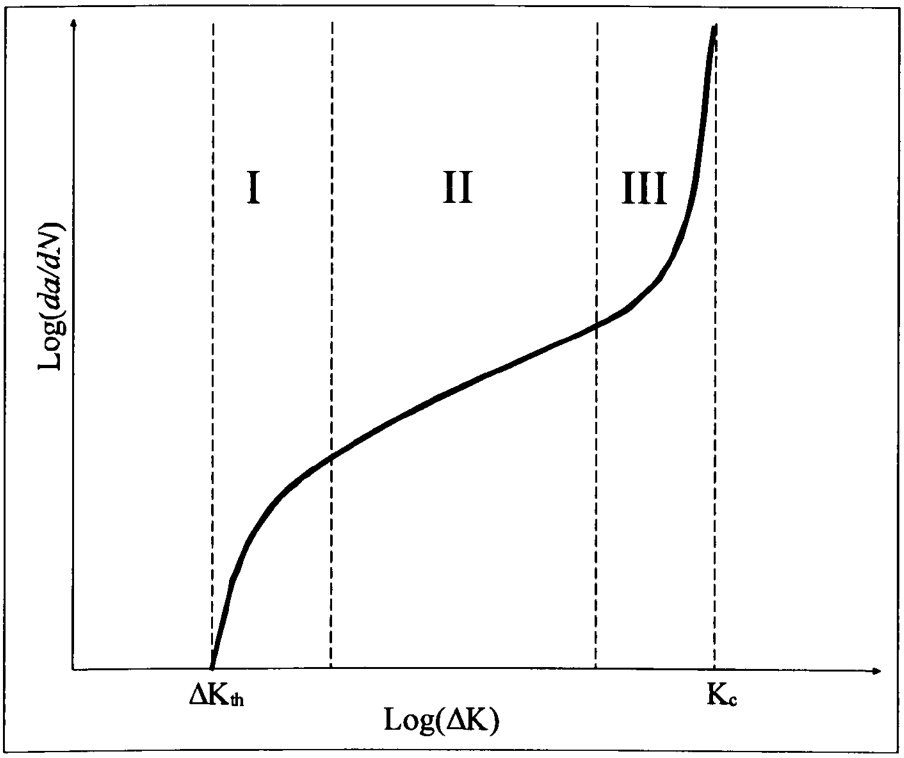

Figure 1.5.12 Three regions of crack growth rate curve

This curve may be divided into three regions. At low stress intensities, Region I, cracking behaviour is associated with threshold, ΔK_{th}, effects. In the mid-region, Region II, the curve is essentially linear. Many structures operate in this region. Finally, in Region III, at high ΔK values, crack growth rates are extremely high and little fatigue life is involved. These three regions are discussed in detail in the following sections.

Region II

Most of the current applications of LEFM concepts to describe crack growth behaviour are associated with Region II. In this region the slope of the $\log(da/dN)$ versus

$\log(\Delta K)$ curve is approximately linear and lies roughly between 10^{-6} and 10^{-3} in./cycle. Many curve fits to this region have been suggested. The Paris [122] equation, which was proposed in the early 1960s, is the most widely accepted. In this equation

$$\frac{da}{dN} = C(\Delta K)^m \qquad (1.5.7)$$

where C and m are material constants and ΔK is the stress intensity range $K_{\max} - K_{\min}$. The material constants, C and m, can be found in the literature and in data books. Values of the exponent, m, are usually between 3 and 4.

The crack growth life, in terms of cycles to failure, may be calculated using Eq. (1.5.7). The relation may be generally described by

$$\frac{da}{dN} = f(K)$$

Thus, cycles to failure, N_f, may be calculated as

$$N_f = \int_{a_i}^{a_f} \frac{da}{f(K)} \qquad (1.5.8)$$

where a_i, is the initial crack length and a_f is the final (critical) crack length. Using the Paris formulation,

$$N_f = \int_{a_i}^{a_f} \frac{da}{C(\Delta K)^m} \qquad (1.5.9)$$

Because ΔK is a function of the crack length and a correction factor that is dependent on crack length [see Eq. (1.5.6)], the integration above must often be solved numerically. As a first approximation, the correction factor, $f(g)$, can be calculated at the initial crack length and Eq. **(1.5.9)** can be evaluated in closed form.

As an example of a closed form integration, fatigue life calculations for a small edge-crack in a large plate (see Figure 1.5.5) are performed below . In this case the correction factor, $f(g)$, does not vary with crack length. The stress intensity factor range is

$$\Delta K = 1.12\sigma\sqrt{\pi a} \qquad (1.5.10)$$

Substituting into the Paris equation yields

$$\frac{da}{dN} = C\left(1.12\Delta\sigma\sqrt{\pi a}\right)^m \qquad (1.5.11)$$

Separating variables and integrating (for $m \neq 2$) gives

$$N_f = \int_{a_i}^{a_f} \frac{da}{C\left(1.12\Delta\sigma\sqrt{\pi a}\right)^m} = \frac{2}{(m-2)C\left(1.12\Delta\sigma\sqrt{\pi}\right)^m}\left(\frac{1}{a_i^{(m-2)/2}} - \frac{1}{a_f^{(m-2)/2}}\right) \quad (1.5.12)$$

Before this equation may be solved, the final crack size, af a_f must be evaluated. This may be done as follows:

$$\Delta K = \Delta\sigma\sqrt{\pi a} f(g)$$

$$a_f = \frac{1}{\pi}\left[\frac{K_c}{\sigma f(g)}\right]^2 = \frac{1}{\pi}\left[\frac{K_c}{1.12\sigma_{\max}}\right]^2 \quad (1.5.13)$$

For more complicated formulations of ΔK, where the correction factor varies with the crack length, a, iterative procedures may be required to solve for a_f in Eq. (1.5.13)

It is important to note that the fatigue-life estimation is strongly dependent on a_i and generally not sensitive to a_f (when $a_i << a_f$). Large changes in a_f result in small changes of N_f, as shown schematically in Figure 1.5.13.

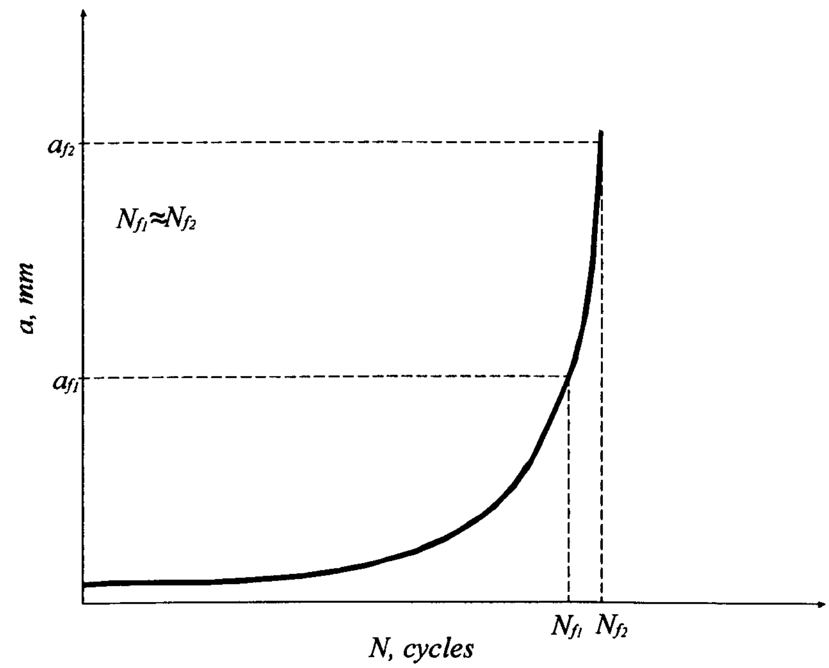

Figure 1.5.13 Effect of final crack size on life

Region I

Region I of the sigmoidal crack growth rate curve is associated with threshold effects. Below the value of the threshold stress intensity factor, K_{th}, fatigue crack growth does not occur or occurs at a rate too slow to measure. (The smallest measured rates are larger than approximately 2.5 10^{-7} mm/cycle. This corresponds to the spacing between atoms in most metals.)

The fatigue threshold for aluminium alloys is usually between 1.7 and 6 MPa$\sqrt{m}$. The fatigue threshold is dependent on the stress ratio, $R, R = \sigma_{max}/\sigma_{min}$ as well.

The threshold value may be of use when a part is subjected to low stress levels and a very large number of cycles. A good example of this would be power trains that operate at very high speeds.

Region III

In Region III, rapid, unstable crack growth occurs. In many practical engineering situations this region may be ignored because it does not significantly affect the total crack propagation life.

The point of transition from Region II to Region III behaviour is dependent on the yield strength of the material, stress intensity factor, and stress ratio. Forman's equation [123] was developed to model Region III behaviour, although it is more often used to model mean stress effects. This equation,

$$\frac{da}{dN} = \frac{C(\Delta K)^m}{(1-R)K_c - \Delta K} \qquad (1.5.14)$$

predicts the sharp upturn in the $\frac{da}{dN}$ versus ΔK curve as fracture toughness is approached.

Region III is of most interest when the crack propagation life is on the order of 10^3 cycles or less. At high stress intensities, though, the effects of plasticity start to influence the crack growth rate because the plastic zone size becomes large compared to the dimensions of the crack. In this case, the problem should be analyzed by some elastic-plastic fracture approach such as the J-integral or the crack-tip opening displacement (COD) methods.

1.5.4 CYCLIC STRESS CONTROLLED FATIGUE

Most of material of this section was derived from book of R.W. Hertzberg, Deformation and Fracture Mechanics of Engineering Materials [105]

Many engineering components must withstand numerous load or stress reversals during their service lives. Examples of this type of loading include alternating stresses associated with a rotating shaft, pressurizing and depressurizing cycles in an aircraft fuselage at takeoff and landing, and load fluctuations affecting the wings during flight. Depending on a number of factors, these load excursions may be introduced either between fixed strain or fixed stress limits; hence, the fatigue process in a given situation may be governed by a strain- or stress-controlled condition.

One of the earliest investigations of stress-controlled cyclic loading effects on fatigue life was conducted by Wöhler [124], who studied railroad wheel axles that were plagued by an annoying series of failures. Several important facts emerged from this investigation, as may be seen in the plot of stress versus the number of cycles to failure (a so-called *S-N* diagram) given in Figure 1.5.14. First, the cyclic life of an axle increased with decreasing stress level and below a certain stress level, it seemed to possess infinite life—fatigue failure did not occur (at least not before 10^6 cycles). Second, the fatigue life was reduced drastically by the presence of a notch. These observations have led many current investigators to view fatigue as a three-stage process involving initiation, propagation, and final failure stages (Figure 1.5.15).

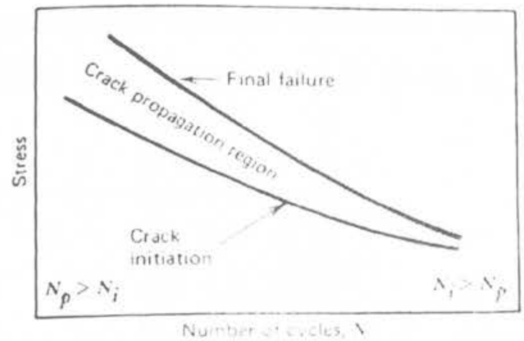

Figure 1.5.14 Wohler's S-N curves for Krupp axle steel *(125)*

Figure 1.5.15 Fatigue life depends on relative extent of initiation and propagation stages.

When design defects or metallurgical flaws are present, the initiation stage is shortened drastically or completely eliminated, resulting in a reduction in potential cyclic life. For many years, laboratory tests have been conducted in bending (rotating or reversed flexure), torsion, pulsating tension, or tension-compression axial loading. Such tests have been conducted under conditions of constant load or moment.

Standard definitions regarding key load or stress variables are shown in Figure 1.5.16 and defined by

$$\Delta\sigma = \sigma_{\max} - \sigma_{\min}, \sigma_a = \frac{\sigma_{\max} - \sigma_{\min}}{2}, \sigma_m = \frac{\sigma_{\max} + \sigma_{\min}}{2}, R = \frac{\sigma_{\min}}{\sigma_{\max}}$$

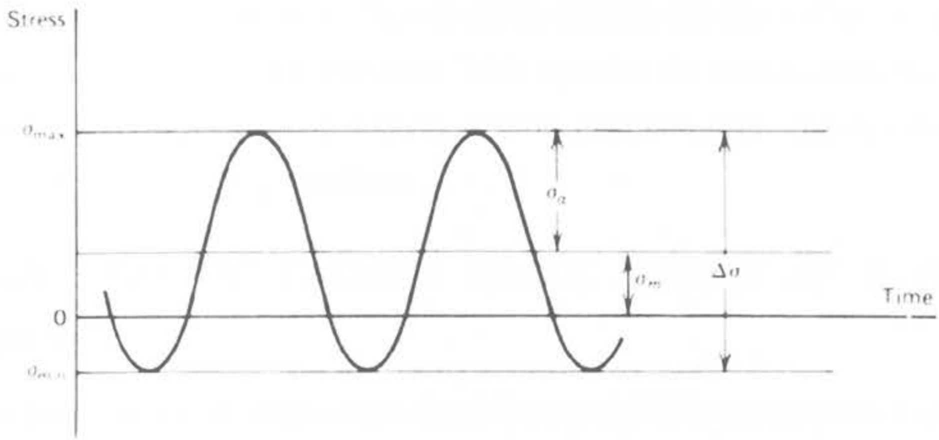

Figure 1.5.16 Nomenclature to describe test parameters involved in cyclic stress testing.

Most often, S-N diagrams similar to that shown in Figure 1.5.14 are plotted, with the stress amplitude given as half the total stress range. Another example of constant load amplitude fatigue data for 7075-T6 aluminium alloy notched specimens is shown in Figure 1.5.17.

Figure 1.5.17 Constant load amplitude fatigue data for 7075-T6 aluminium alloy notched specimens (0.25-mm root radius)[126]

Note the considerable amount of scatter in fatigue life found among the 10 specimens tested at each stress level. The smaller scatter at high stress levels is believed to result from a much shorter initiation period prior to crack propagation. The existence of scatter in fatigue test results is common and deserving of considerable attention, since engineering design decisions must be based on recognition of the statistical character of the fatigue process. The origins of test scatter are manifold. They include variations in testing environment, preparation of the specimen surface, alignment of the test machine, and a number of metallurgical variables. With regard to the testing apparatus, the least amount of scatter is produced by rotating bending machines, since misalignment is less critical than in axial loading machines.

1.6 ANALYSIS OF FATIGUE CRACK SHAPES AT FASTENER HOLES

Fatigue cracks in aircraft commonly initiate from stress concentrations such as fastener holes in mechanically fastened joints. There are a number of ways how fatigue cracks may propagate from the hole through the material. The crack front shape depends on many factors. The main factors are: the geometry of the hole and aircraft detail, loading conditions, the properties of the material, the presence of residual stresses and so on. In the present work the most common and simple example of aircraft structure was taken – a plate of 5mm thickness containing a central hole and subjected to tensile loading. In addition the specimens were subjected to various forms of treatment (cold expansion and interference fit) and simulation of real conditions of operation (cyclic tensile loading and corrosion). All of these factors definitely influenced the crack front shape and its propagation. Many publications are available which provide information about the types of crack which initiate and grow from a hole. Despite the many possibilities of crack propagation, normally, in cases like ours one has to deal with three types of cracks: though thickness cracks, corner cracks, and semielliptical cracks. The cracks may be asymmetrical and may change their shape during the propagation. All of these types are of course a simplification of the real situation. For instance, G. Clark 127 , described a photo of a crack with complicated crack front shape as shown below in Pell's paper :

Figure 1.6.1 Fracture surface of specimen tested by Pell et. al.[128] ; the specimen contains a cold expanded hole. The crack is longer at the entry side of the specimen, and displays pronounced asymmetry.

Numerical simulation techniques are employed for the detailed investigation into cases like this as these predictive methods are not confined by shape constraints(129, 130, 131).
Most of the engineering methods dealing with the fatigue growth calculation for part-through planar cracks reduce the problem from one with an infinite number of degrees of freedom to one with two degrees of freedom. This reduction is usually achieved by assuming the front of propagating cracks during the fatigue process has a simplified shape. The experimental fatigue growth laws, which relate the range of stress intensity factor to the crack growth rate and are usually obtained from standard small specimens, are then applied independently to two characteristic points of the assumed crack shape. Such predictive procedures involve two considerations. First, the shape of propagating cracks during fatigue growth needs to be properly assumed from a large amount of experiments focusing on the study of crack shape development. Second, a wide range of stress intensity factor (SIF) solutions of good accuracy should be obtained by either numerical or experimental means. During the investigations carried out by several researchers [132, 133, 134, 135] for fatigue growth studies of corner cracks emanating from holes, the shape assumption method has been used. Most of the investigators assumed that the front of growing cracks is of the quarterelliptical shape. Detailed investigation into crack front shapes of corner cracks was conducted by A.F. Grandt and D.E. Macha[136]. They presented detailed data which describe fatigue growth, including shape changes, of corner cracks at holes. Their investigation was based on a series of fatigue tests, conducted by Snow [137], with transparent specimens. In their concluding remarks they reported: "...prior to penetration through the rear surface, the flaw growth is slightly faster along the bore of the hole and maintains a shape which is modelled fairly well by a quarter ellipse. After penetration, the crack grows rapidly along the rear surface in an apparent attempt to reach a symmetric through-thickness configuration." They made a comparison between assumed part-elliptical and natural fatigue crack shapes for corner and through-cracked holes, Figure 1.6.2. It follows from the figure that elliptical function are very compatible with the shape of a natural corner crack and can be used for predicting the size of a bore crack from knowledge of the size of surface crack .

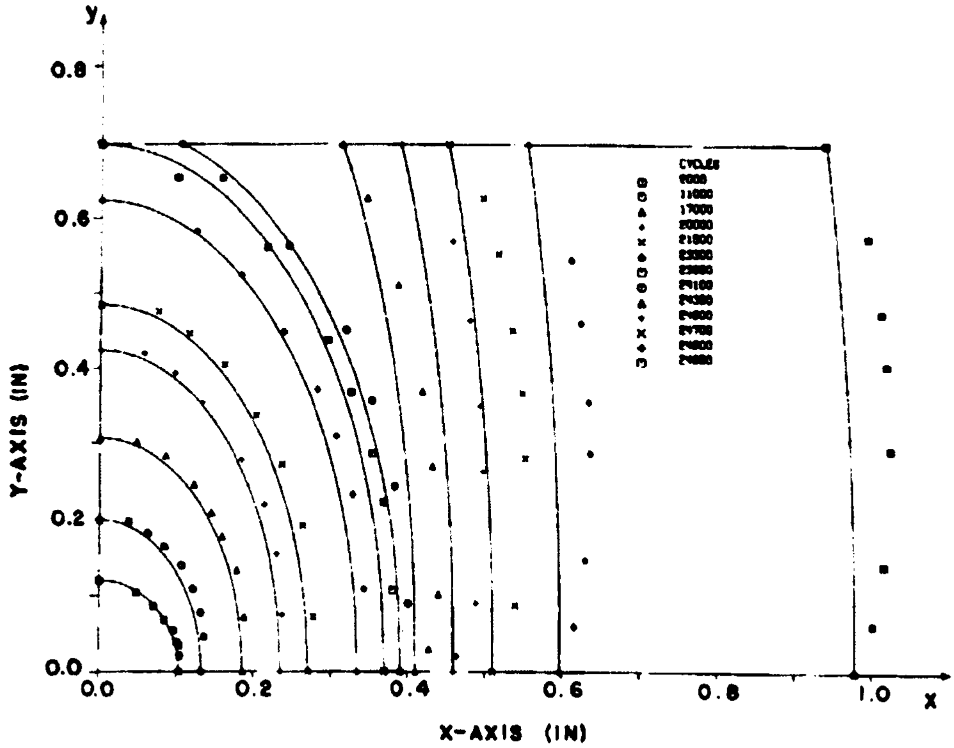

Figure 1.6.2 Comparison of part-elliptical and natural fatigue crack shapes for corner and through-cracked holes

In some cases the shape of the crack front may conform adequately to a geometrical shape for which a solution exists, *e.g.* a quarter-elliptical corner flaw, however, in many cases the crack fronts may be irregular and not conform to standard solutions.

Authors of the next source [138] reported an analysis of the results of residual static strength tests of loaded pin-lug specimens containing fatigue cracks, using linear elastic fracture mechanics. In the group of 34 specimens concerned there was a wide variation of cracked area, crack asymmetry, and crack front shape (see Figure 1.6.3 a -Failure section of specimens showing cracked area and failing load, b – Methods of defining crack length(see Figure 1.6.3 a).

Two situations were envisaged. In one it was postulated that only one face of the lug could be observed and that the engineer would assume through-cracks of the lengths so observed. In the other case, both faces of the lug could be observed. In this latter event the engineer could either base his analysis on the average of the two observed surface crack lengths (one such pair of measurements on each side of the pin hole) or he could take the longest crack length on each side of the pin, irrespective of the face on which the crack was evident. Summarising, calculations of K were based on five differing concepts of the significant crack length parameter. Using the concepts listed below, a "crack length" measurement was obtained for the cracking on each side of the hole, to provide values of a_1, and a_2 for use in the calculation of

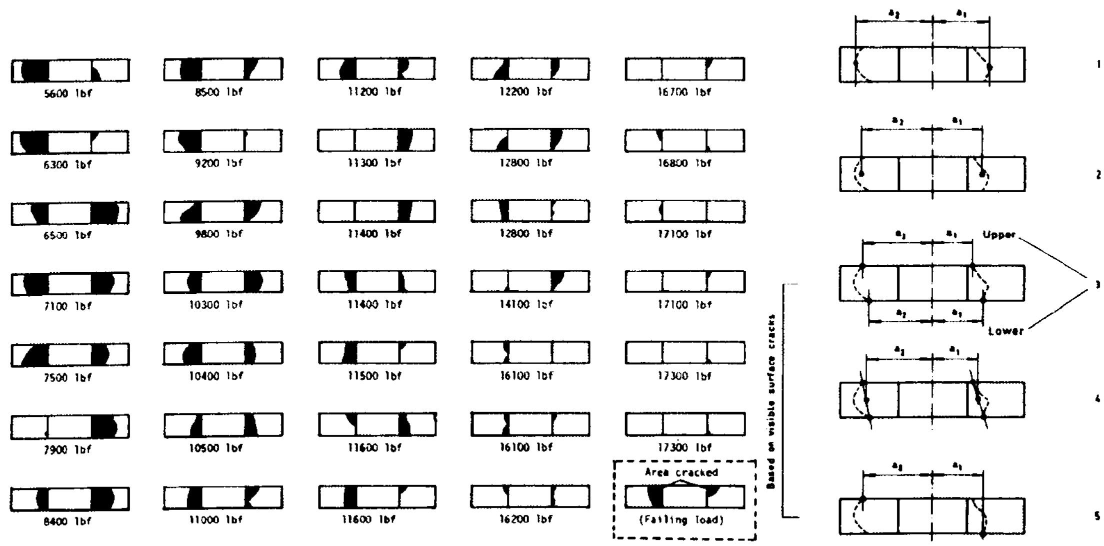

a *b*

Figure 1.6.3 a -Failure section of specimens showing cracked area and failing load, b – Methods of defining crack length This picture is distorted

the stress intensity factor. The crack length concepts are illustrated in Figure 1.6.3 b. The analysis was performed on the basis of five different assumptions regarding the definition of crack length with a curved or irregular crack front. The definitions of length included maximum distance from the pin centre-line to any point on the crack front, average distance from the centre-line to the crack front and average length of the cracks observable on the flat surfaces of the lug measured from the pin centre-line (considered separately on each side of the hole).

The results of the analysis showed that the above methods of definition of crack length generally resulted in comparatively small differences in predicted values of crack tip stress intensity factor. However, the predicted values of K at failure did not agree well with measured values of K_c for the material concerned. The errors were generally such that a conservative (safe) estimate of residual strength would be made in engineering prediction except at very short crack lengths.

1.7 STRESS INTENSITY FACTORS

To predict crack-propagation life and fracture strength, accurate stress intensity factor solutions are needed for these crack configurations. But, because of the complexities of these problems as outlined above, exact solutions are not available. Instead, investigators use approximate analytical methods, or engineering estimates, to obtain the stress intensity factors.

Through thickness cracks with a straight crack-front, quarter elliptical corner cracks at a hole and semielliptical cracks at a hole were the most relevant types of crack shapes in the case of the experimental work carried out here..

The through thickness crack is one of the best known and widely used cases of crack propagation and the SIF solutions represented in many papers are approximations of the Bowie (162) solution (for examples see Section 1.7.1)

A brief survey of solutions for corner cracks at a hole presented below was taken from work of X.B. Lin, R.A. Smith (158).

Many efforts (139-157) have been made during the past two decades to evaluate the stress intensity factor for corner cracks emanating from fastener holes. Table 3 briefly summarizes in chronological order, the main features of most of the studies relating to this problem.

Table 3 Summary review of SIF for corner cracks at fastener holes

Reference	Crack geometry	Load	Method	Main results
McGrwan and Smith (139)	Single 1/4-elliptical crack	Tension	Photoelasticity + numerical analysis	K_A, K_C
Shah (140)	Single and double 1/4-elliptical cracks	Several loads	Approximate analytical method	K along crack front
Smith el al. (141)	Single 1/4-elliptical crack		Photoelasticity	$K_A.K_C$
Kullgren et al. (142)	Single 1/4-elliptical crack	Remote tension	FE alternating method	K along crack front
Kullgren and Smith (143)	Single and double 1/4-elliplical cracks	Several tension loads	FE alternating method	K along crack front
Raju and Newman (144)	Double 1/4-elliptical cracks	Remote tension and bending	Finite element method	K along crack front (nine points)
Rudd et al. (145)	Double 1/4-clliptical cracks	Remote tension	Approximate analytical method	K: equation
Grandt and Kullgren (146)	Single 1/4-elliptical crack	Crack face pressure	FE alternating method	K along crack front
Grandt and Kullgren (147)	Single 1/4-elliptical crack	Crack face pressure	FE alternating method	K along crack front
Heath and Grandt	Single 1/4-	Remote tension	FE alternating	K along crack

[148]	elliptical crack		method	front (seven points)
Schijve[149]	Single actual shape =;single 1/4-elliptical crack	Remote tension	Fatigue tests	K along crack front
Atluri and Nishioka[150]	Single 1/4-elliptical crack	Pin-load	FE alternating method	K_A, K_C
Newman and Raju [151]	Single and double 1/4-elliptical cracks	Remote tension and bending	Fitting to results of Raju and Newman ([144])	Equation for K along crack front (any point)
Berkovits and Prinz[152]	Single parabolic crack	Not specific	Slice synthesis method	KA,KC
Perez et al.[153]	Single 1/4-elliptical crack	Crack face pressure	Weight function	K_A, K_C
Shin[154][155]	Single and double actual shape l/4-elliptical cracks	Remote tension	Fatigue tests	K along crack front
Vainshtok and Varfolomeyev[156]	Single 1/4-elliptical crack	Not specific	Weight function	K along crack front
Guo[157]	Single 1/4-elliptical crack	Biaxial and pin-load	Approximate analysis	K equation along crack front

A variety of methods have been used to estimate the SIF values, such as approximate analytical analysis, finite element (FE), weight function, photoelasticity, and fatigue tests. Corner cracks were mostly assumed to have a quarter-elliptical crack front in numerical investigations, because the propagating cracks actually observed in experiments approximate to a quarter-elliptical shape. However, a different crack front shape, a parabolic shape, was also analyzed by Berkovits and Prinz [152] who thought that the parabolic profile might be a better approximation than the quarter-ellipse, according to the results observed in their fatigue tests. Single or two symmetric corner crack configurations with different limited geometry parameters, i.e. depth ratio $\left(a/t\right)$, aspect ratio $\left(a/c\right)$ and radius ratio $\left(r/t\right)$, as shown in Figure 1.7.7, were analyzed usually according to the needs of the investigators. Approximate equations relating the SIF of the single crack to that of the double crack configuration were also proposed by Shah [140] and Schijve [149], by which the application of these limited results can be widened. The loads applied to the crack geometry, as shown in Table 3, varied from remote tension and bending to more complex crack face pressures, with different gradients along the plate surface or along both the plate and hole surfaces; the latter can allow the SIF to be evaluated readily for complex loads, like residual stresses.

The SIF solutions were usually given by investigators at least at both end points of the crack front, as seen in Table 3. More SIF values were also reported by many investigators at several interior points of the crack front. However, it should be noted that K_A and K_C [(153)] in Table 3 actually denote the average stress intensity factors associated with the hole and plate surface directions, respectively. The SIF results were mostly presented in figure or table formats. For convenience, Newman and Raju [(151)] fitted equations to the SIF results obtained mainly by their finite element analyses on a series of double crack configurations [(144)]. These equations are similar to those they reported for surface cracks in plates, and can be used to calculate the SIF value at any position along the crack front for a single crack or for two symmetric quarter-elliptical corner cracks located at circular hole edges, provided that the crack geometry calculated is within its specific range.

Lin and Smith employed in their paper [(158)] both a "quarter-point displacement" and J-integral methods to evaluate the SIFs for two symmetric quarter-elliptical corner cracks at the root of fastener holes in finite thickness plates under remote tension. These two methods employ different principles, although they are both constructed on the basis of linear elastic fracture mechanics (LEFM).

Newman and Raju [159] used three dimensional finite element analyses to calculate the Mode I stress intensity factor variation along the crack front for a quarter-elliptical corner and semi-elliptical surface cracks at a hole subjected to remote tensile loading. These solutions were used in the present work for SIF calculation (see Sections 1.7.2, 1.7.3)

The SIF solutions for relevant crack types are given in the sections below.

1.7.1 THROUGH CRACKS

For straight fronted cracks from a hole penetrating through the specimen thickness (Figure 1.7.1). the following two equations were used to obtain the mode I stress intensity factor K_I

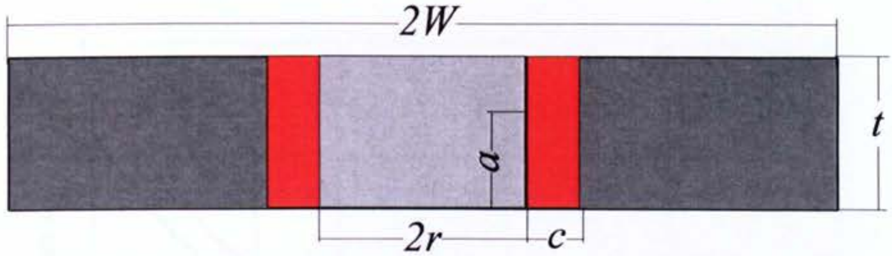

Figure 1.7.1 Straight fronted crack

- <u>Grandt's equation</u> [160]

$$K_1 = \sigma\sqrt{\pi c}\left[\frac{F_1}{F_2 + c/r} + F_3\right]\sqrt{\sec\left(\frac{\pi c}{2W}\right)} \qquad (1.7.1)$$

where the values $F_1 = 0.6865; F_2 = 0.2772; F_1 = 0.9439$ are applicable where c/r is less than 10.

- <u>Newman's equation</u> [161] (an equation fitted to Bowie's numerical results[162]),

$$K_1 = \sigma\sqrt{\pi c}F(\lambda)\sqrt{\sec\left(\frac{\pi c}{2W}\right)} \qquad (1.7.2)$$

Newman's calibration factors for an asymmetric crack are

$$F_{\rightarrow}(\lambda) = 0.707 - 0.18\lambda + 6.55\lambda^2 - 10.54\lambda^3 + 6.85\lambda^4 \qquad (1.7.3)$$

And for a symmetric crack

$$F_{\leftrightarrow}(\lambda) = 1 - 0.15\lambda + 3.46\lambda^2 - 4.17\lambda^3 + 3.58\lambda^4 \qquad (1.7.4)$$

where

$$\lambda = \frac{r}{r + c};$$

Both solutions contain a correction function for width of the specimen $\sqrt{\sec\left(\frac{\pi c}{2W}\right)}$. The Figure 1.7.2 and Figure 1.7.3 present both of the suggested solutions. It is clear that they have fairly small disagreement and both can be used for further data processing. Newman's solution was selected since it agrees within $\pm 2\%$ of the numerical values given by Bowie, whereas Grandt's is within $\pm 3\%$.

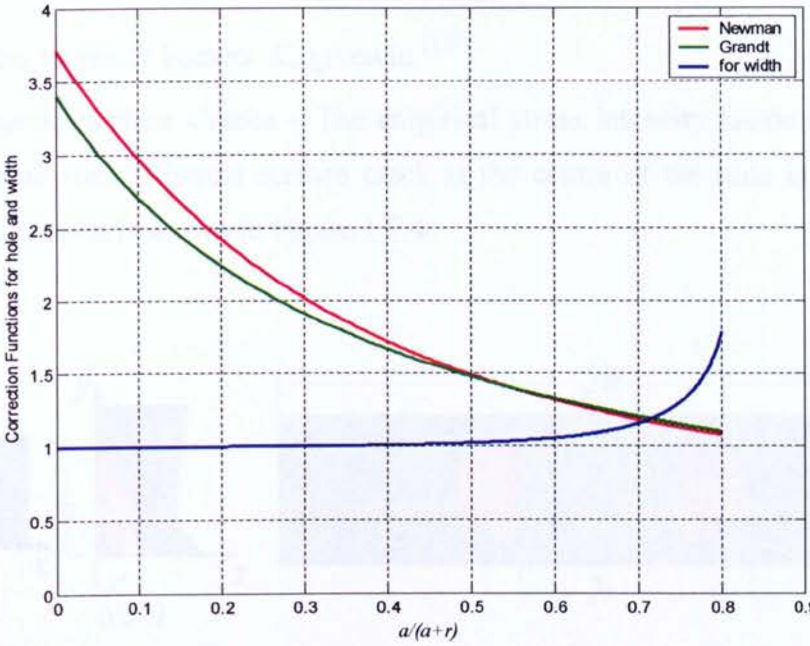

Figure 1.7.2 Correction functions for hole and width in case of for a through crack

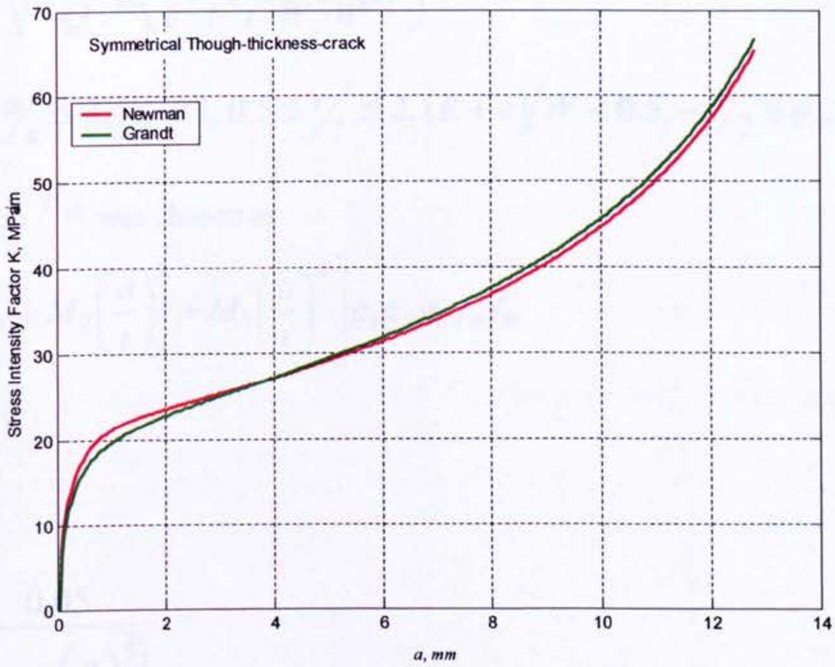

Figure 1.7.3 SIF according to Newman (1.7.2) and Grandt (1.7.1)solutions for a Through Crack versus crack length

1.7.2 SEMIELLIPTICAL CRACK AT A HOLE

Mode I Stress Intensity Factors K_1 given in [(159)]

Two-Symmetric Surface Cracks – The empirical stress intensity factor equation for a two-symmetric semi-elliptical surface crack at the centre of the hole in a finite plate subjected to tension is shown in Figure 1.7.4.

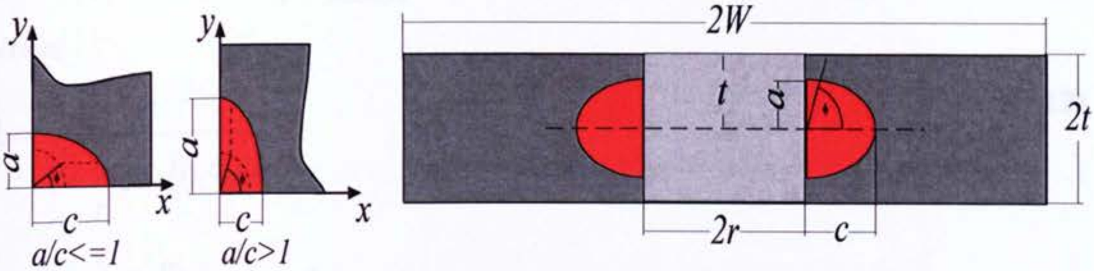

Figure 1.7.4 Semi-elliptical Surface Crack at hole

$$K_1 = \sigma\sqrt{\pi\frac{a}{Q}}F_{sh}\left(\frac{a}{c},\frac{a}{t},\frac{r}{t},\frac{r}{W},\frac{c}{W},\phi\right) \qquad (1.7.5)$$

for $0.2 \le a/c \le 2, a/t < 1, 0.5 \le r/t \le 2, (R+c)/W < 0.5, -\pi/2 \le \phi \le \pi/2$.

The function F_{sh} was chosen as

$$F_{sh} = \left[M_1 + M_2\left(\frac{a}{t}\right)^2 + M_3\left(\frac{a}{t}\right)^4\right]g_1 g_2 g_3 f_\phi f_W \qquad (1.7.6)$$

For $a/c \le 1$

$$M_1 = 1. \qquad (1.7.7)$$

$$M_2 = \frac{0.05}{0.11 + \left(\frac{a}{c}\right)^{3/2}} \qquad (1.7.8)$$

$$M_3 = \frac{0.29}{0.23 + \left(\frac{a}{c}\right)^{3/2}} \qquad (1.7.9)$$

$$g_1 = 1 - \frac{\left(\frac{a}{t}\right)^4}{1. + 4\left(\frac{a}{c}\right)} \cos\phi \tag{1.7.10}$$

$$g_2 = \frac{1 + 0.358\lambda + 1.425\lambda^2 - 1.578\lambda^3 + 2.156\lambda^4}{1 + 0.08\lambda^2} \tag{1.7.11}$$

Where

$$\lambda = \frac{1}{1 + \frac{c}{r}\cos(0.9\phi)} \tag{1.7.12}$$

The function g_3 is given by

$$g_3 = 1 + 0.1(1 - \cos\phi)^2 \left(1 - \frac{a}{t}\right)^{10} \tag{1.7.13}$$

The function f_ϕ and f_w are given by

$$f_\phi = \left[\left(\frac{a}{c}\right)^2 \cos^2\phi + \sin^2\phi\right]^{1/4} \tag{1.7.14}$$

$$f_w = \left[\sec\left(\frac{\pi r}{2W}\right) \sec\left(\frac{\pi(2r + nc)}{4(W - c) + 2nc}\sqrt{\frac{a}{t}}\right)\right]^{1/2} \tag{1.7.15}$$

where n=1 is for a single crack, n=2 is for two-symmetrical cracks, and the hole is located in the centre of the plate

For $a/c > 1$

$$M_1 = \sqrt{\frac{c}{a}} \tag{1.7.16}$$

The functions M_2, M_3, and f_w are given by (1.7.8)-(1.7.9) and (1.7.15)

$$f_\phi = \left[\left(\frac{c}{a}\right)^2 \sin^2\phi + \cos^2\phi\right]^{1/4} \tag{1.7.17}$$

$$f_W = \left[\sec\left(\frac{\pi r}{2W}\right) \sec\left(\frac{\pi(2r + nc)}{4(W - c) + 2nc} \sqrt{\frac{a}{t}} \right) \right]^{1/2} \quad (1.7.18)$$

Effects of plate thickness and crack shape.

Figure 1.7.5 - Figure 1.7.6 show the distribution of boundary-correction factors, F_{sh}, and stress intensity factor K_1 along the crack front for two symmetric semi-elliptical cracks at a hole. The effects of crack size $\left(a/t\right)$ on the distribution of boundary-correction factor, F_{sh}, and accordingly stress intensity factor K_1 along the crack front for different crack shapes characterised by $\left(a/c\right)$ are shown in Figure 1.7.5. It is shown that the F_{sh} and K_1 maximal values are reached at a parametric angle equal $\phi = \pi/2$ (90°) regardless of the relations $\left(a/t\right)$, characterised crack size and $\left(a/c\right)$ characterised crack shape.

The effects of crack shape $\left(a/c\right)$ at different crack sizes on the distribution of boundary-correction factors are shown in Figure 1.7.6. Here we can also see that the F_{sh} and K_1 maximal values are reached at $\phi \approx 90°$.

Therefore we can make $\phi \approx 90°$ for our further K_1 calculation

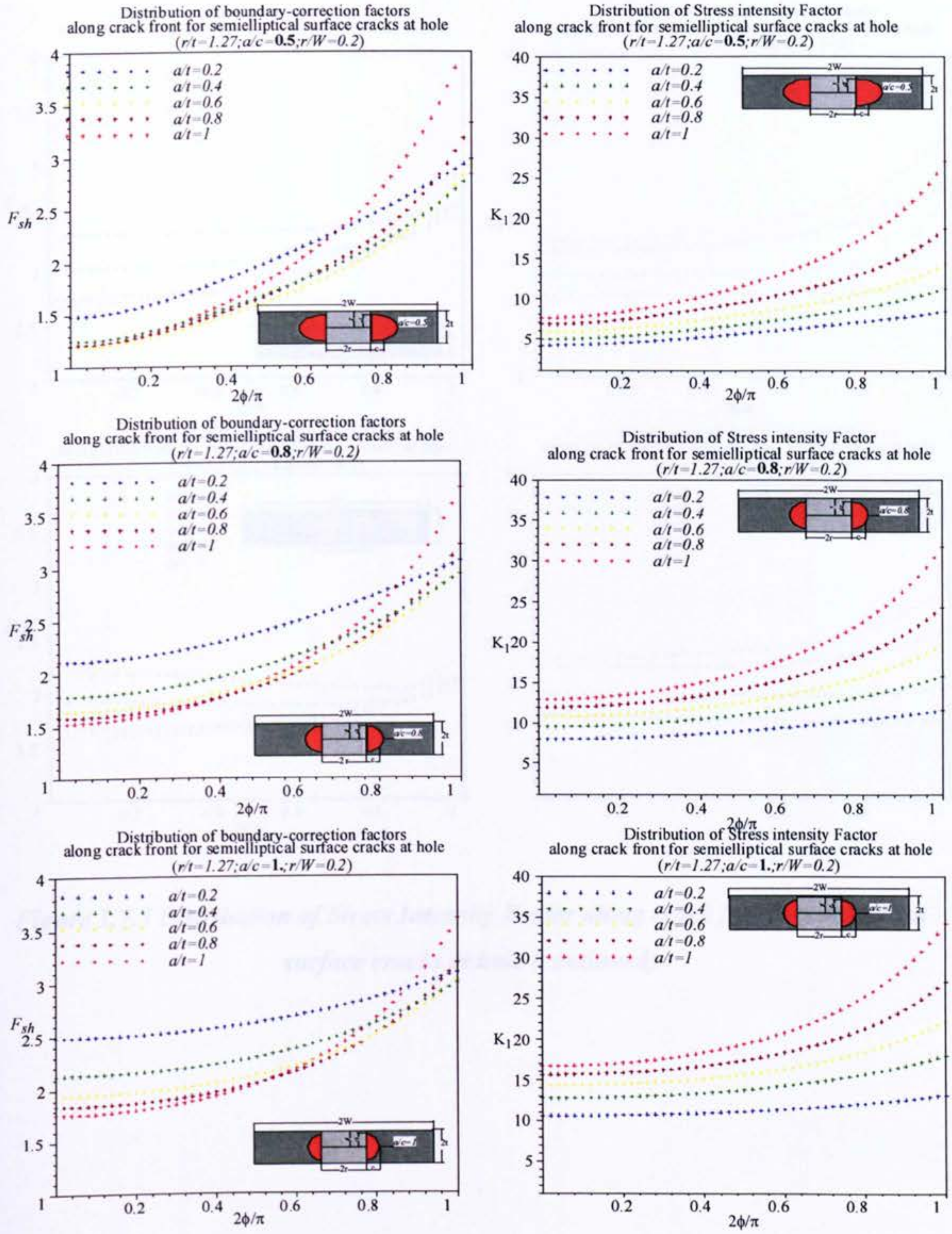

Figure 1.7.5 Distribution of Stress Intensity Factor along crack front semielliptical surface cracks at hole

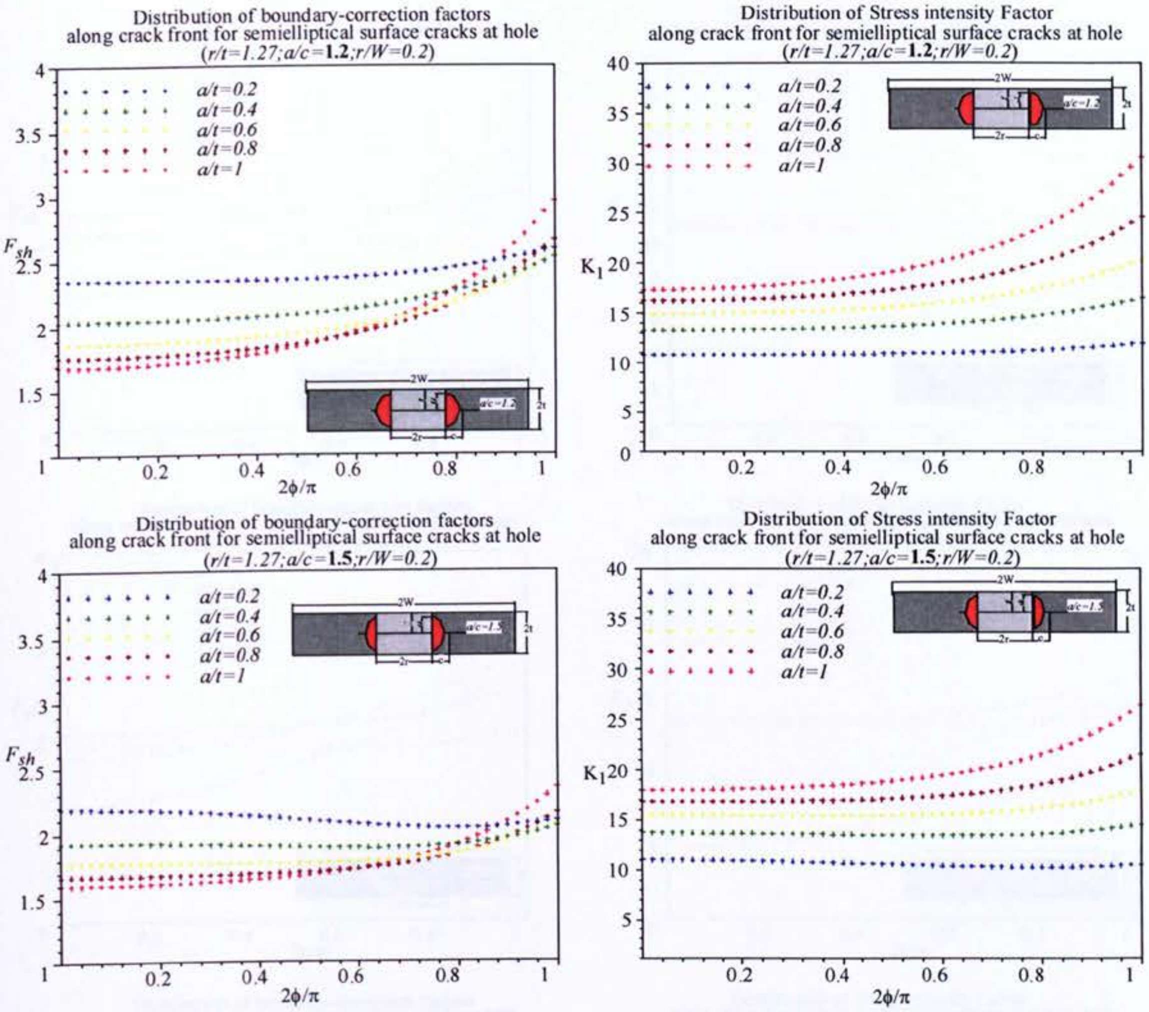

Figure 1.7.5 Distribution of Stress Intensity Factor along crack front semielliptical surface cracks at hole (continued)

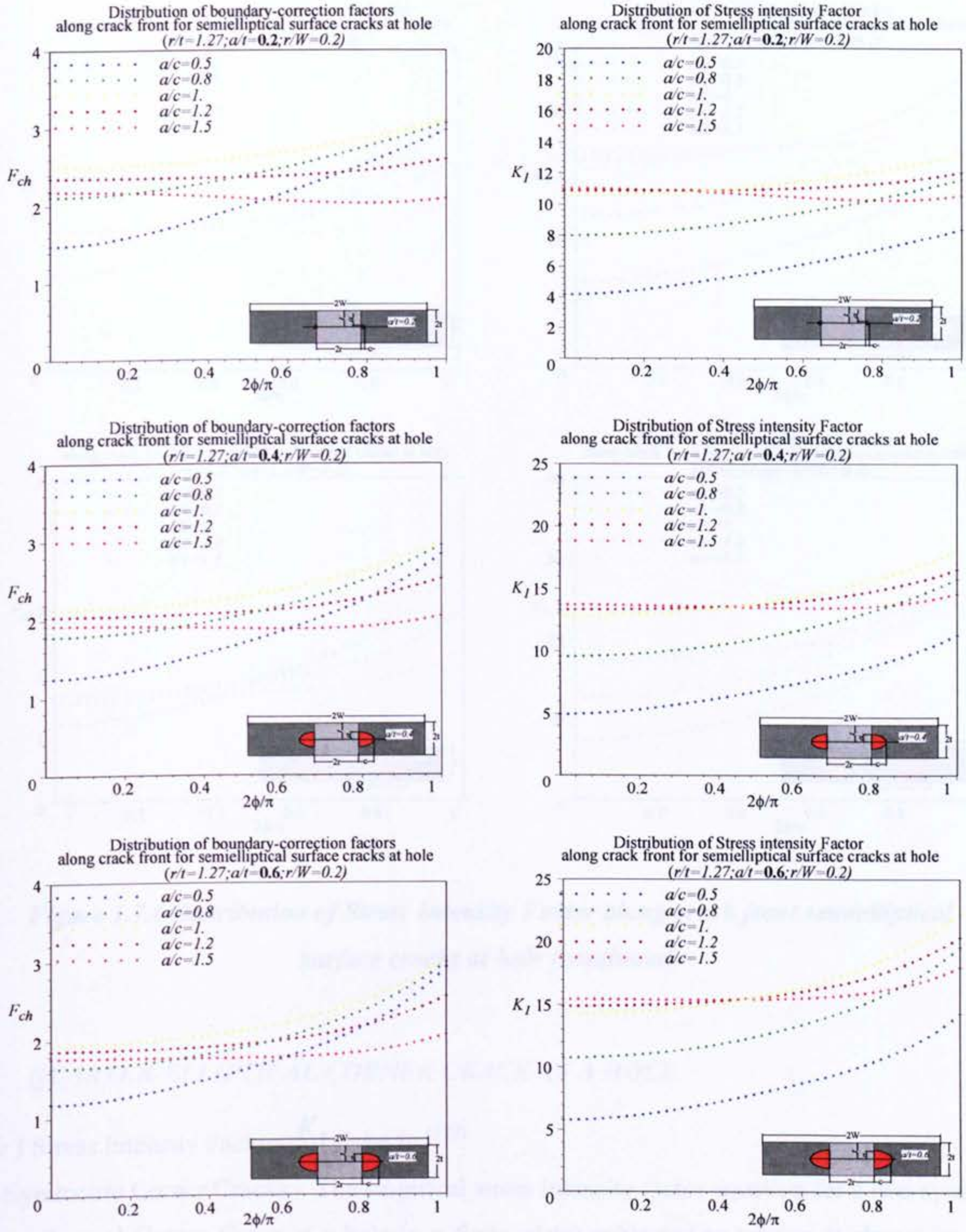

Figure 1.7.6 Distribution of Stress Intensity Factor along crack front semielliptical surface cracks at hole

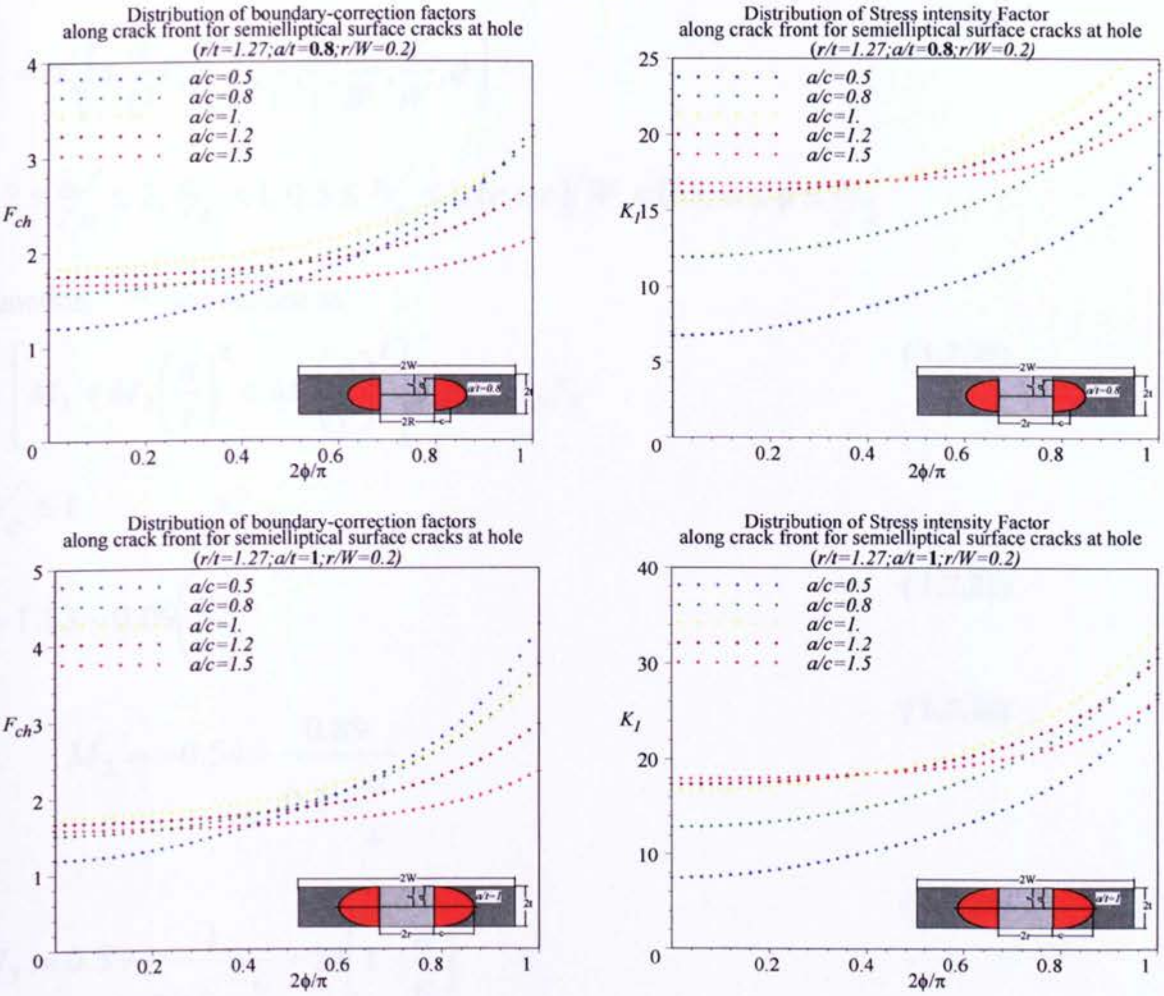

Figure 1.7.6 Distribution of Stress Intensity Factor along crack front semielliptical surface cracks at hole (continued)

1.7.3 QUARTER-ELLIPTICAL CORNER CRACK AT A HOLE

Mode I Stress Intensity Factors K_1 given in [159]

Two-Symmetric Corner Cracks – The empirical stress intensity factor equation for a two-symmetric Quarterelliptical Corner Crack at a hole in a finite plate) subjected to tension is shown in Figure 1.7.7.

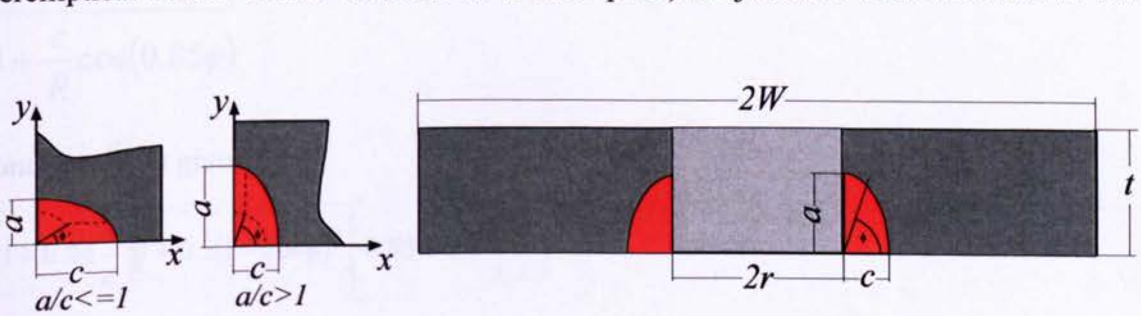

Figure 1.7.7 Corner Crack at a hole and coordinate system used to determine parametric angle

$$K_1 = \sigma\sqrt{\pi\frac{a}{Q}}F_{ch}\left(\frac{a}{c},\frac{a}{t},\frac{r}{t},\frac{r}{W},\frac{c}{W},\phi\right) \tag{1.7.19}$$

for $0.2 \le a/c \le 2,\ a/t < 1,\ 0.5 \le r/t \le 1,\ (r+c)/W < 0.5,\ 0 \le \phi \le \pi/2$.

The function F_{ch} was chosen as

$$F_{ch} = \left[M_1 + M_2\left(\frac{a}{t}\right)^2 + M_3\left(\frac{a}{t}\right)^4\right]g_1 g_2 g_3 f_\phi f_W \tag{1.7.20}$$

For $a/c \le 1$

$$M_1 = 1.13 - 0.09\left(\frac{a}{c}\right) \tag{1.7.21}$$

$$M_2 = -0.54 + \frac{0.89}{0.2 + \frac{a}{c}} \tag{1.7.22}$$

$$M_3 = 0.5 - \frac{1}{0.65 + \frac{a}{c}} + 14\left(1 - \frac{a}{c}\right)^{24} \tag{1.7.23}$$

$$g_1 = 1 + \left[0.1 + 0.35\left(\frac{c}{a}\right)\left(\frac{a}{t}\right)^2\right](1 - \sin\phi)^2 \tag{1.7.24}$$

$$g_2 = \frac{1 + 0.358\lambda + 1.425\lambda^2 - 1.578\lambda^3 + 2.156\lambda^4}{1 + 0.13\lambda^2} \tag{1.7.25}$$

where

$$\lambda = \frac{1}{1 + \frac{c}{R}\cos(0.85\phi)} \tag{1.7.26}$$

The function g_3 is given by

$$g_3 = \left(1 + 0.04\frac{a}{c}\right)\left[1 + 0.1(1 - \cos\phi)^2\right]\left[0.85 + 0.15\left(\frac{a}{t}\right)^{1/4}\right] \tag{1.7.27}$$

The function f_ϕ and f_w are given by

$$f_\phi = \left[\left(\frac{a}{c}\right)^2 \cos^2\phi + \sin^2\phi\right]^{1/4} \tag{1.7.28}$$

$$f_W = \left[\sec\left(\frac{\pi r}{2W}\right)\sec\left(\frac{\pi(2r+nc)}{4(W-c)+2nc}\sqrt{\frac{a}{t}}\right)\right]^{1/2} \tag{1.7.29}$$

For $a/c > 1$

$$M_1 = \sqrt{\frac{c}{a}}\left(1 + 0.04\frac{c}{a}\right) \tag{1.7.30}$$

$$M_2 = 0.2\left(\frac{c}{a}\right)^4 \tag{1.7.31}$$

$$M_3 = -0.11\left(\frac{c}{a}\right)^4 \tag{1.7.32}$$

$$g_1 = 1 + \left[0.1 + 0.35\left(\frac{c}{a}\right)\left(\frac{a}{t}\right)^2\right](1-\sin\phi)^2 \tag{1.7.33}$$

$$g_2 = \frac{1 + 0.358\lambda + 1.425\lambda^2 - 1.578\lambda^3 + 2.156\lambda^4}{1 + 0.13\lambda^2} \tag{1.7.34}$$

$$\lambda = \frac{1}{1 + \frac{c}{r}\cos(0.85\phi)} \tag{1.7.35}$$

$$g_3 = \left(1.13 - 0.09\frac{c}{a}\right)\left[1 + 0.1(1-\cos\phi)^2\right]\left[0.85 + 0.15\left(\frac{a}{t}\right)^{1/4}\right] \tag{1.7.36}$$

$$f_\phi = \left[\left(\frac{c}{a}\right)^2 \sin^2\phi + \cos^2\phi\right]^{1/4} \tag{1.7.37}$$

$$f_W = \left[\sec\left(\frac{\pi r}{2W}\right)\sec\left(\frac{\pi(2r+nc)}{4(W-c)+2nc}\sqrt{\frac{a}{t}}\right)\right]^{1/2} \tag{1.7.38}$$

Effects of plate thickness and Crack Shape - Figure 1.7.8- Figure 1.7.9 show the distribution of boundary-correction factors, F_{ch}, and stress intensity factor K_1 along the crack front for two symmetric quarterelliptical corner cracks at a hole. The effects of crack size $\left(a/t\right)$ on the distribution of boundary-correction factor, F_{ch}, and accordingly stress intensity factor K_1 along the crack front at different crack shapes characterised by $\left(a/c\right)$ are shown in Figure 1.7.8.

It is shown that the F_{ch} and K_1 maximal values are reached at a parametric angle equal $\phi = \pi/2$ (90°) regardless of the relations $\left(a/t\right)$ characterised crack size and $\left(a/c\right)$ characterised crack shape.

The effects of crack shape $\left(a/c\right)$ at different crack sizes on the distribution of boundary-correction factors are shown in Figure 1.7.9. Here we can again see that the F_{ch} and K_1 maximum values are reached at ϕ=90°.

Therefore we can assume ϕ = 90° for further K_1 calculations.

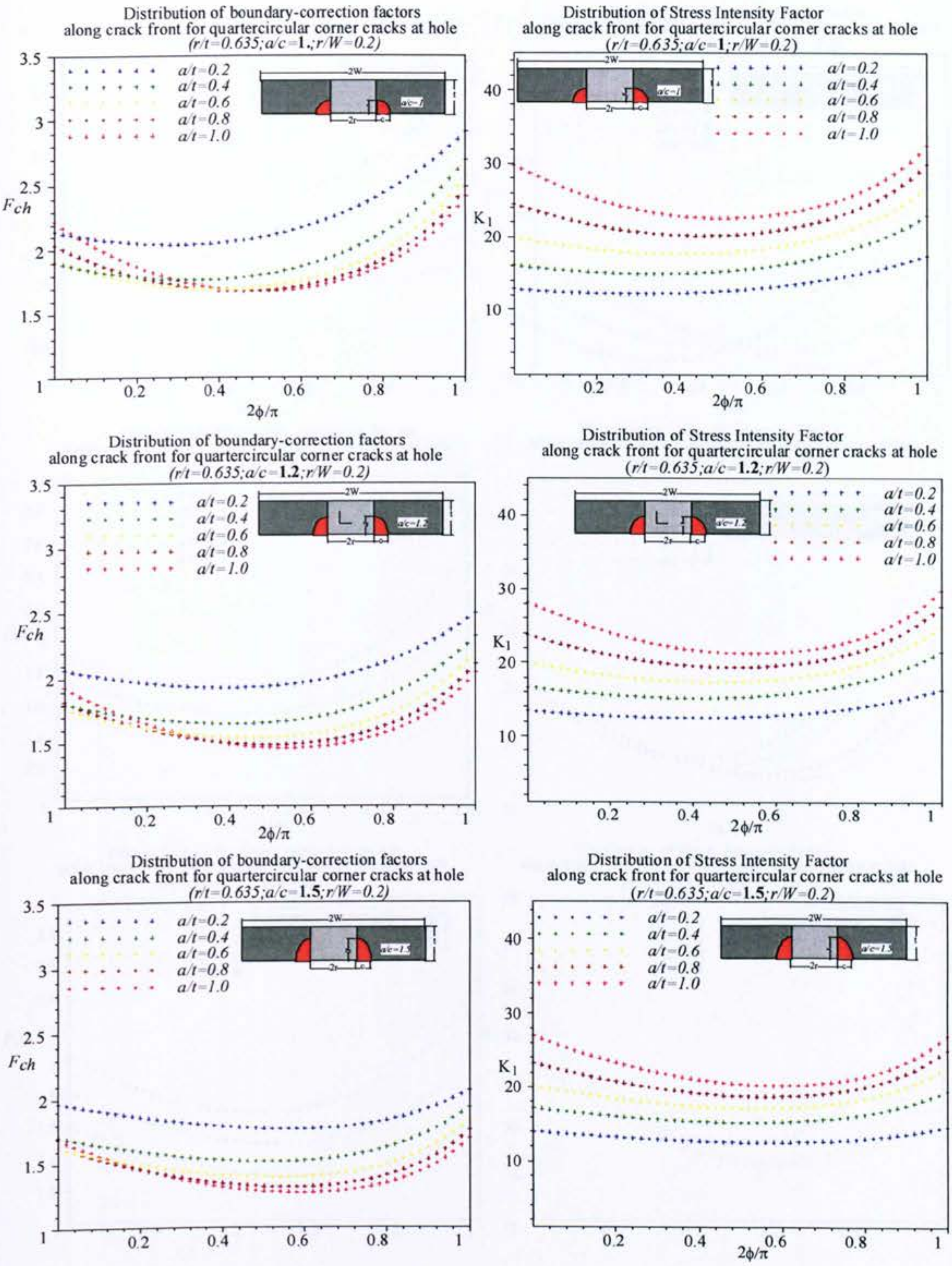

Figure 1.7.8 Distribution of Stress Intensity Factor along crack front quartercircular corner cracks at hole

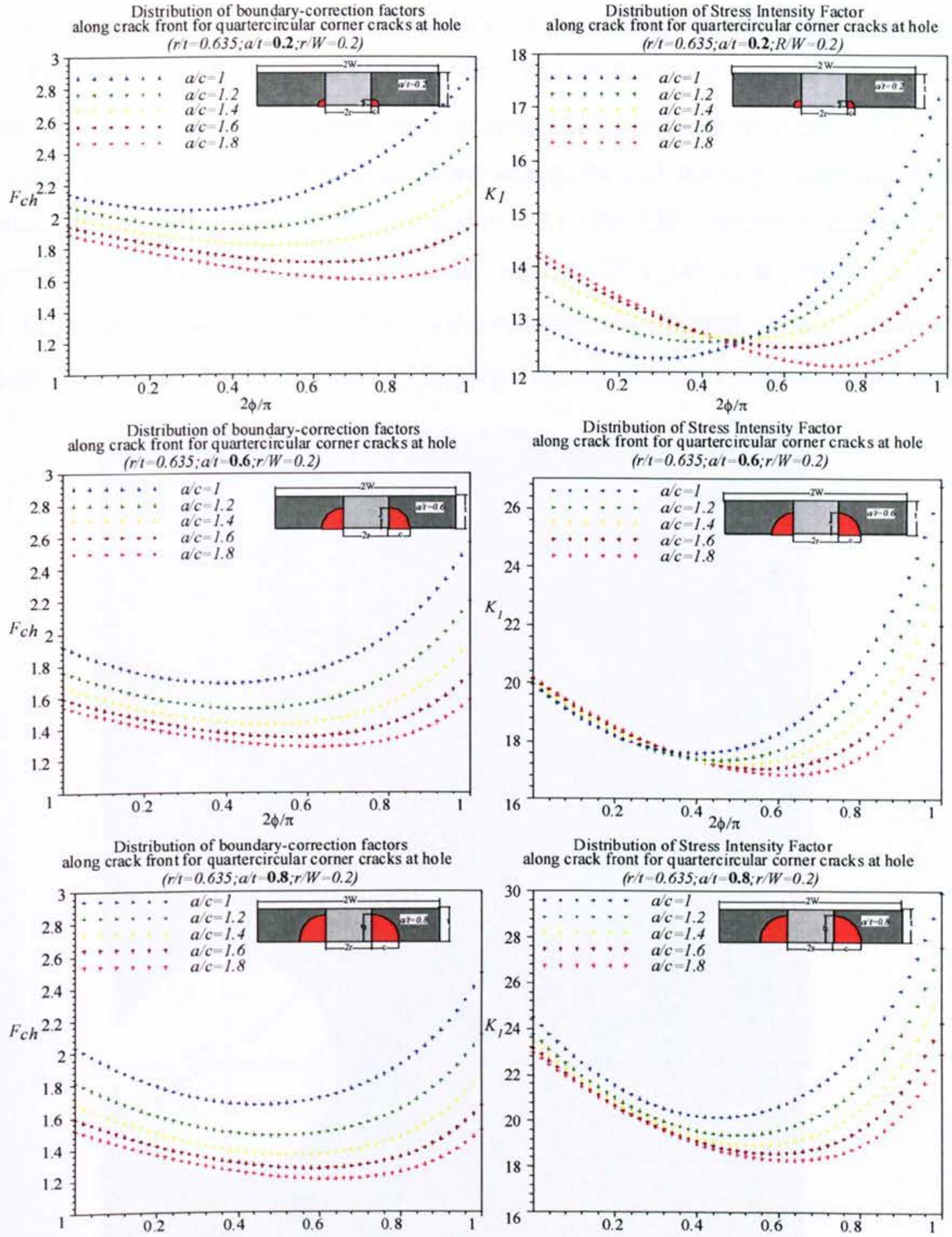

Figure 1.7.9 Distribution of Stress Intensity Factor along crack front quartercircular corner cracks at hole

1.7.4 COMBINED APPLIED SIF ACCORDING TO NEWMAN'S SOLUTION FOR A SEMI-ELLIPTICAL CRACK AT A HOLE AND A SUBSEQUENT THOUGH CRACK

The SIF for a semi-elliptical surface crack at hole was considered in chapter 1.7.2. The SIF distribution along a semi-elliptical crack front was given and the angle corresponding to the maximum SIF was determined (≈90°). In Figure 1.7.10 the SIF function is shown for a semi-elliptical crack corresponding to the parametric angle $\phi \approx 90°$ at which the SIF for semielliptical crack K_1 reaches a maximum. Then, the crack transforms into a through crack in a very short time and from that point the SIF is characterised by propagation of this crack front configuration.

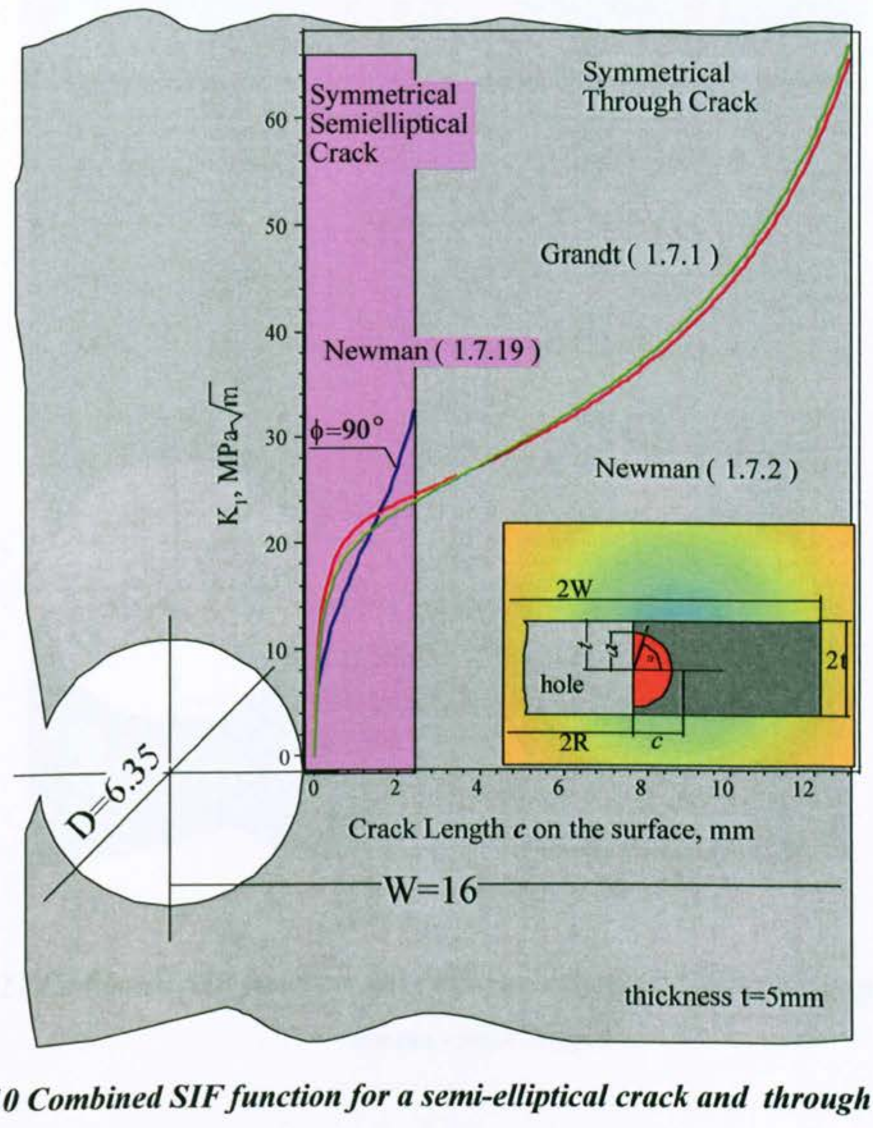

Figure 1.7.10 Combined SIF function for a semi-elliptical crack and through crack versus crack length

1.7.5 SIF ACCORDING TO NEWMAN'S SOLUTION FOR A QUARTER-ELLIPTICAL CORNER CRACK AT A HOLE AND SUBSEQUENT THOUGH CRACK

In this case, we have almost the same problem as above. The SIF function for a quarter-elliptical corner crack reaches a maximum when the parametric angle $\phi \approx 90°$. At this point the SIF function according to Newman's or Grandt's solutions model the process more accurately.

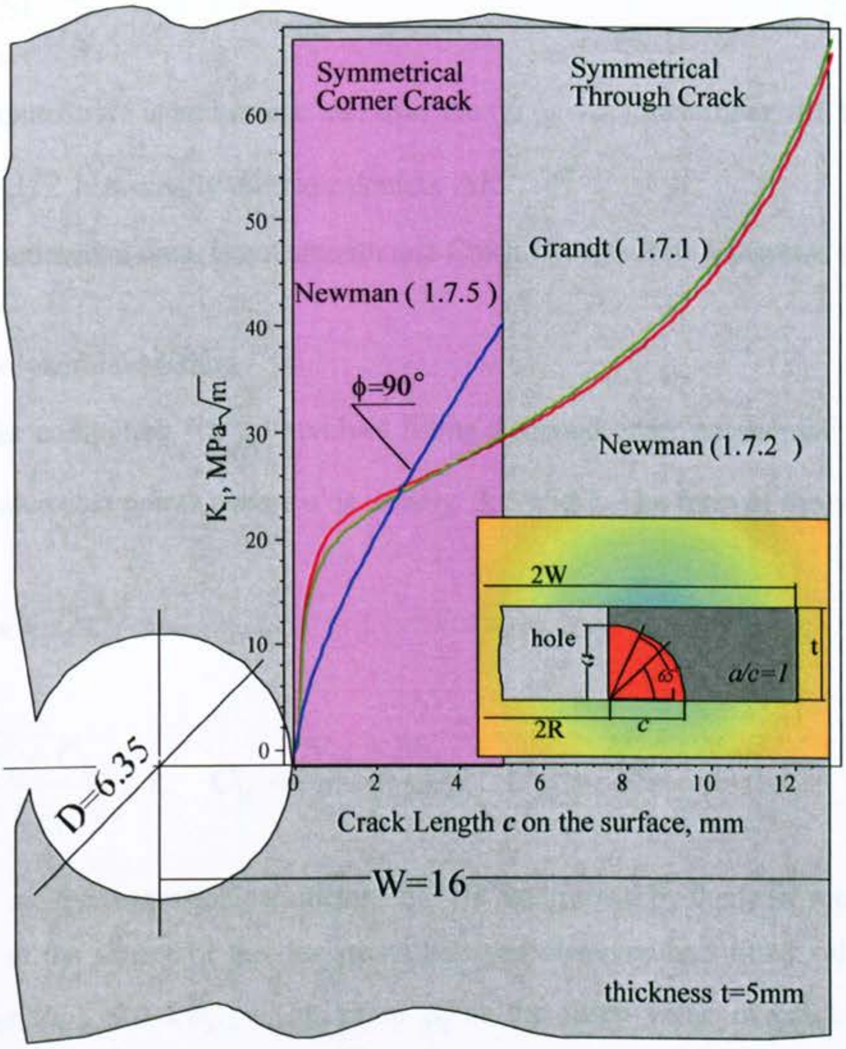

Figure 1.7.11 Combined SIF function for a quarter-elliptical corner crack and a through crack versus crack length

1.7.6 METHODS FOR COMPUTING CRACK GROWTH RATE

The tables containing crack length values a_i and the corresponding number of load cycles N_i are used as initial data for crack growth rate determination.

Secant method

The secant or point-to-point technique for computing the crack growth rate simply involves calculating the slope of the straight line connecting two adjacent data points on the a versus N curve. It is more formally expressed as follows:

$$\left(\frac{da}{dN}\right)_{\bar{a}} = \frac{a_{i+1} - a_i}{N_{i+1} - N_i}$$

Since the computed rate is an average rate over the $(a_{i+1} - a_i)$ increment, the average crack length, $\bar{a} = \left(a_{i+1} - a_i\right)/2$ is normally used to calculate ΔK

Herein the experimental data is not smooth and Crack Growth Rate Diagrams feature a high degree of scatter.

Incremental Polynomial Method

The method for computing da/dN involves fitting a second order polynomial (parabola) to sets of (2n+1) successive data points, where n is usually 3, 5 and 7. The form of the equation for best fit is as follows:

$$a_i = z_0 + z_1 x + z_2 x^2,$$

where

$$-1 \le x_i = \frac{N_i - C_{1i}}{C_{2i}} \le 1; \quad C_{1i} = \frac{N_{ip} + N_{i1}}{2}; \quad C_{2i} = \frac{N_{ip} - N_{i1}}{2};$$

and z_0, z_1, z_2 are the regression parameters that are determined by the least squares method (that is, minimization of the square of the deviations between observed and fitted values of crack length) over the range $a_{i-n} \le a \le a_{i+n}$. The value a_i is the fitted value of crack length at N_i. The parameters C_1, C_2 are used to scale the input data, thus avoiding difficulties in determining the regression parameters. The rate of crack growth at N_i is obtained from the derivative of the above parabola, which is given by the following expression:

$$\left(\frac{da}{dN}\right)_{\bar{a}} = \frac{z_1}{C_2} + 2z_2 \frac{\left(N_i - C_1\right)}{C_2^2}$$

The value of ΔK associated with this da/dN value is computed using the crack length, $\bar{a}_i$, corresponding to N_i.

The Figure 1.7.12 shows a comparison of Secant and Polynomial methods of crack growth rate estimation. It can be seen that Secant method gives the largest scatter in experimental points while a

7-points Polynomial smoothes out scatter and clearly indicates the main trends of crack growth rate changes. The 7-points Polynomial method will be used for computing crack growth rate in Section 2.4.

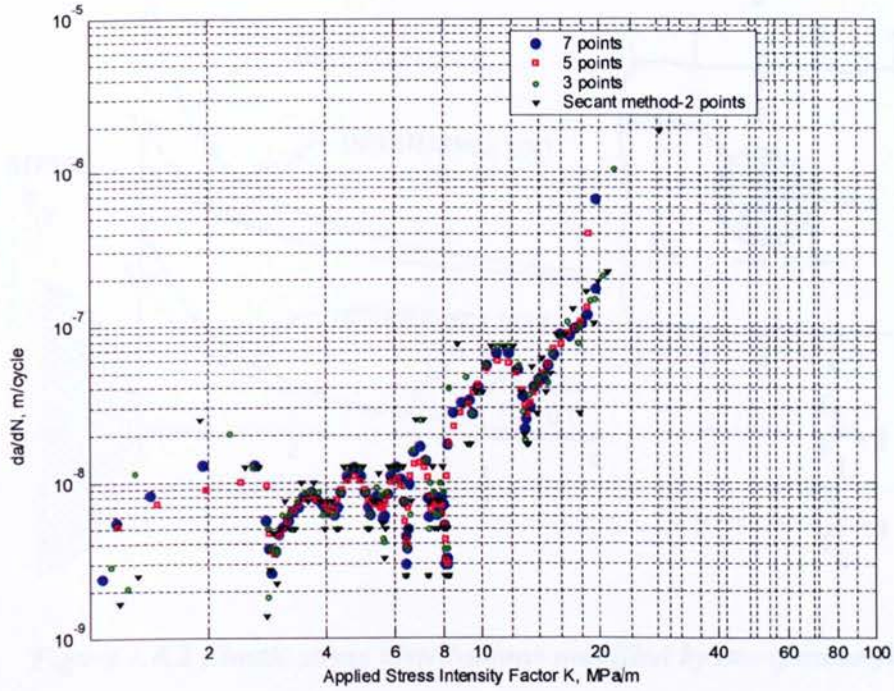

Figure 1.7.12 Comparison of Secant and Polynomial methods of crack growth rate estimation

1.8 INTERFERENCE FIT

Herman's article [163] relating to the 3D stress distribution around cold expanded holes in aluminium alloys was used for this analysis.

His representation of "Stress at full mandrel engagement" was considered as if it was equivalent to the stress distribution caused by an oversized fastener used for interference fit although in fact the magnitude of expansion is about 3-4 times larger. The diagram (b) shows tangential tension stress

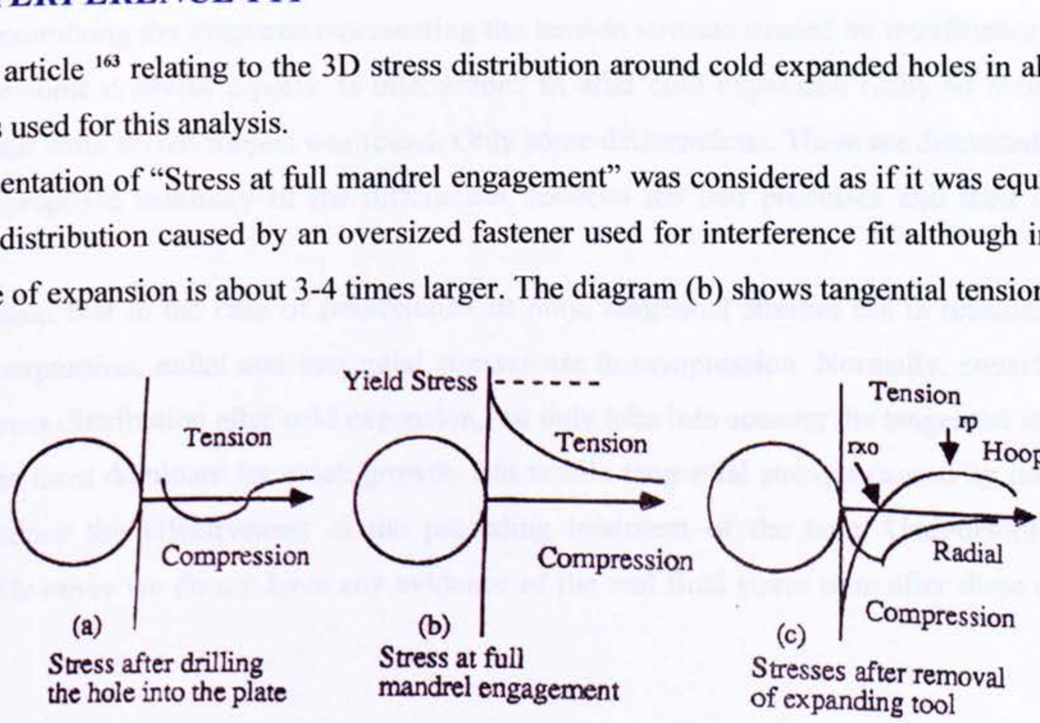

Figure 1.8.1 Events of cold expansion of fattener hole; (a) after drilling the hole into the plate, (b) during the expansions and (c) after removal of expanding tool

An article by Hardrath [164] gives a similar picture of stress distribution for a bolt inserted into a hole with interference fit. The stress notification σ_{yy} is used hence, it probably means tangential stress.

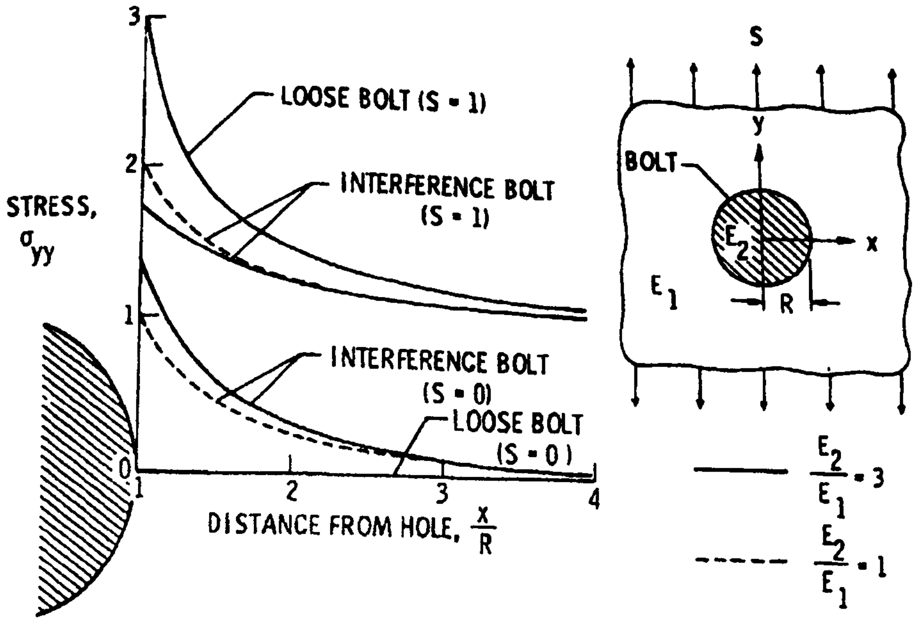

Figure 1.8.2 Elastic stress distributions modified by interfenece-fit bolt

It is well known that the combination of cold expansion & interference fit gives a larger improvement in fatigue life than either one of them undertaken separately although some authors disagree with this..

However examining the diagrams representing the tension stresses caused by interference fit, there seem to be some doubtful aspects. Is interference fit after cold expansion really so harmless. No experimental work on the subject was found. Only some deliberations. These are discussed below.

This is a proposed summary of the differences between the two processes and their combined effects..

It can be seen that in the case of interference fit only, tangential stresses are in tension, whereas after cold expansion, radial and tangential stresses are in compression. Normally, considering the residual stress distribution after cold expansion, we only take into account the tangential stresses, as they are the most dominant for crack growth. But tensile tangential stresses caused by interference fit may reduce the effectiveness of the preceding treatment of the hole. Undoubtedly, this is arguable. However we do not have any evidence of the real final stress state after these combined processes.

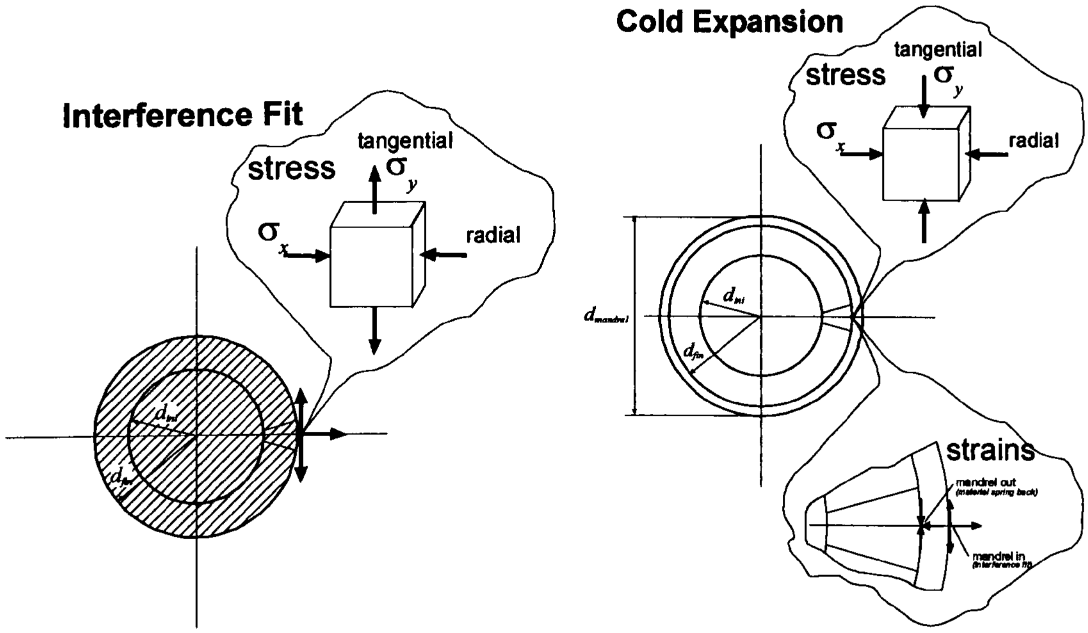

Figure 1.8.3 Stress station on the side of of hole after interference fit and after cold expansion

1.8.1 SOME PUBLISHED POINTS OF VIEW ON THE SUBJECT

Grandt, A.F Jr, Potter,R.M (1979), *An Analysis of Residual Stresses and Displacements due to Radial Expansion of Fastener Holes*, Air Force Materials Laboratory, Wright-Patterson Air Force Base, Ohio, Technical Report AFML-TR-79-4048. [20]

The residual stresses obtained in a tube by cold expansion have been defined by Potter and Grant and are shown in Figure 1.3.1. Initially when the mandrel is in the hole, the hoop stress around the hole is tensile.

These diagrams show different levels of mandrel interference. In the case of bolt interference fit it consists of 1-1.5% (in our case 1.37%!), i.e. much lower than from cold expansion (3-5%). It can be seen from the figure above that the plastic/elastic boundary (the top ridge in the curves), corresponding to a small level of interference, is close to the hole edge. This means that for interference fit the material around the hole is mainly in the plastic zone.

Figure 1.8.4 Hoop and radial stresses (a) with cold expanding mandrel inserted, (b) after removal of mandrel. R is the radius of the hole, x is the distance from the hole, σ is the residual stress and σ_y is the yield stress [(20)].exceeded at the edge of the hole. The residual radial stress is zero at the edge and attains negative values between the hole and the outer surface of the tube.

C R Smith, Experimental Mechanics 5(8) 19A, 1965 [165]

A suitable analogy to the stress cycle at a point of concentration is the case where a large deformation can be observed at the point representing the stress at the concentration. Such is the example in Figure 1.8.5, where the cyclic stress at the concentration is represented by the stretch of *a rubber like cement joining two sections of a wooden board (Figure 1.8.5A). The hole through the centre accommodates a wooden dowel that is scarfed diagonally to allow wedging the two board sections apart as shown in Figure 1.8.5B.*

Tensile loads applied to both ends of the board cause the cement to stretch so that, for repeated loading, the stress cycle at the concentration can be represented by the sine wave in Figure 1.8.5A. Wedging the joint apart to a position equivalent to one half the amplitude of Figure 1.8.5A would not effect maximum deformation; however, the minimum stress is one-half of the maximum stress: the stress ratio, R, equals 0.5 with R the ratio of the minimum stress divided by the maximum stress. Changing the stress ratio from R = 0 (as represented in Figure 1.8.5A) to R +0.5 can increase the fatigue life of an aluminum-alloy structure from 5 to more than 100 times, depending upon the magnitude of loading.

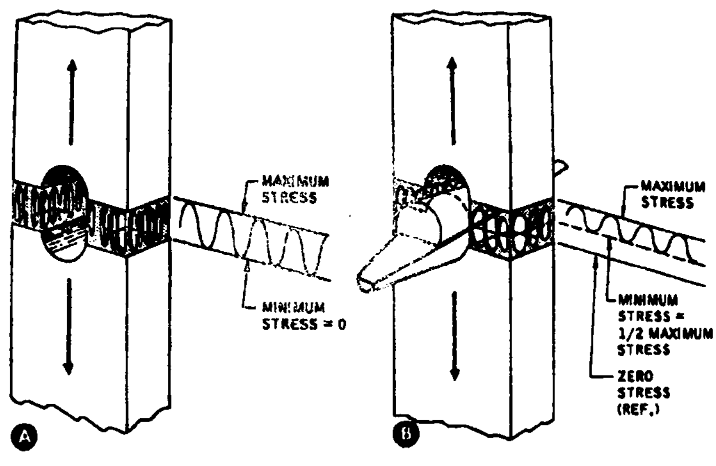

Figure 1.8.5 Model illustrating behaviour of an interference fastener

Benefits in fatigue are due specifically to the interference between the tapered bolt and the hole, maintaining tension prestress around the periphery of the hole. This reduces stress amplitude without appreciably affecting the maximum stress. While tension prestress is not beneficial, it reduces stress amplitude for a prolonged fatigue life.

1.8.2 ANALYSIS OF LOCAL STRESSES IN SPECIMENS AFTER COLD EXPANSION AND INTERFERENCE FIT

Some thoughts about the contribution of interference fit and cold expansion to fatigue resistance are presented below. . Oversize fasteners, such as taper locks (trade name) improve life to crack initiation and decrease the rate of growth of small cracks. In cold work, the oversized pin is removed, allowing the material beyond the plastically deformed region to elastically recover which induces residual compressive stresses to a depth of 3-4mm below the surface of the edge of the hole. In the case of interference fit the oversized fastener is left in, causing induced tensile stresses.

An analysis of the interaction of applied stress with the stresses induced in a fastener hole caused by different degrees of interference fit, cold expansion, and the combination of the two procedures is given below. These considerations will be conducted with aid of $\sigma_l(\sigma_a)$ diagram (relation of local stress to applied) according to Broek's [166] method of local stress assessment after cold work or interference fit treatment. Only one location is considered – the lateral edge of the hole along the transverse centreline which is the most probable point for crack initiation. Only tangential stresses are considered here.

Case I: Plate with a hole without interference fit

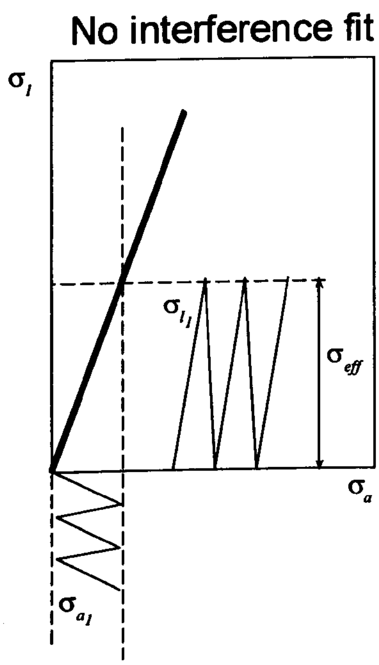

Figure 1.8.6 Plate with a hole without interference fit

It is known that stress concentration factor for a hole $k = {}^{\sigma_l}\!/_{\sigma_a} = 3$. Subjecting the plate to applied stress with $\sigma_{\min} = 0$, the local stress σ_l at the indicated point will be 3 times σ_a and the σ_{eff} range will be between 0 and $\sigma_{l_1} = 3\sigma_a$.

The bold straight line represents the stress concentration factor for a hole which is a transfer function from applied to local stress.

Broek's simplified method of local stress analysis.

In order to simplify the explanation, consider a rectangular hole, as in Figure .

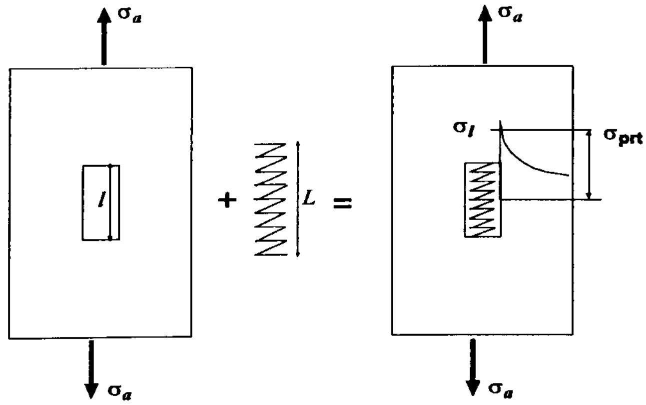

Figure 1.8.7 Representation of simlified model for local stress analysis

If the applied stress varies between 0 and σ_a then the local stress cycles between 0 and σ_l (stress concentration factor $k = \sigma_l / \sigma_a$). Now put an oversize spring L in the hole l.

As the spring is too large (interference), there will be a pre-tension,stress σ_{prt} at the edge of the hole. Assuming elastic behaviour it can be established how the local stress will vary during cycling of the applied stress. If the plate is stretched, the hole will stretch. Eventually the size of the hole will be $l + \Delta l = L$. Then the spring will be loose and it can be taken out. From then on the behaviour will be as that of an open hole.

Some cases of local stress changes through cold expansion and interference fit will be considered bearing Broek's assumption in mind.

Case II: Plate with a hole with low level of interference fit

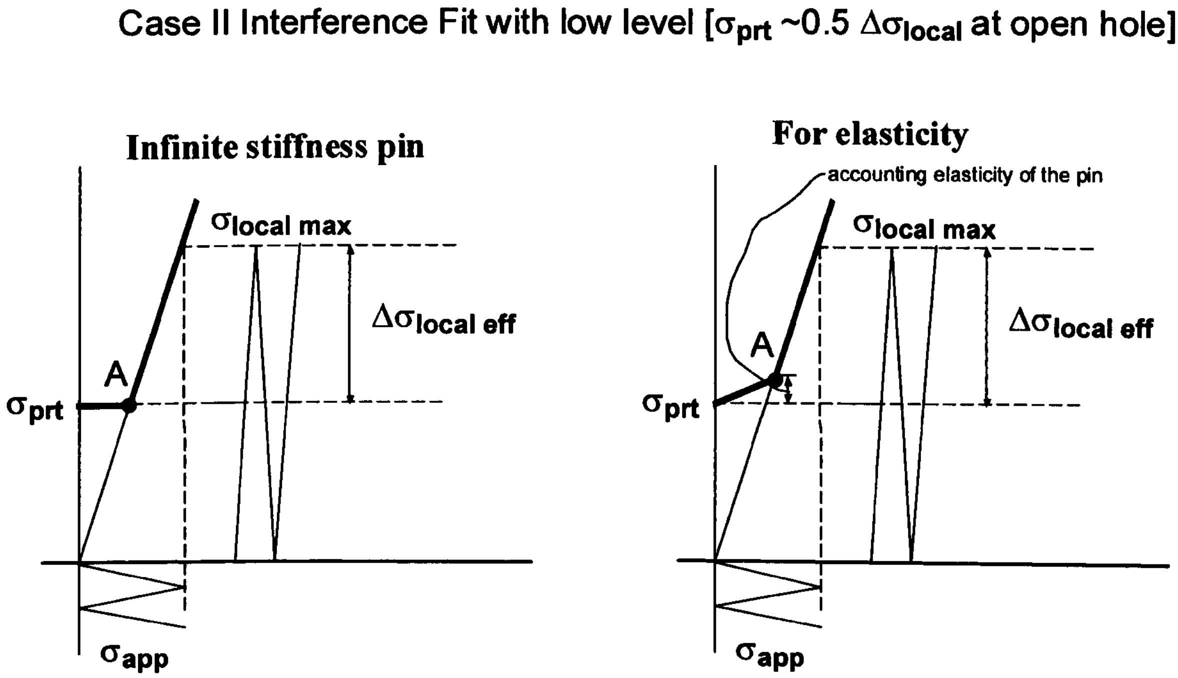

Figure 1.8.8 Plate with a hole with low level of interference fit

Here are presented 2 cases: one for an infinite stiffness pin and the second with allowance for pin elasticity.

According to Broek's method, the pin can be represented by an elastic spring. In the case of an elastic pin, point A is the point at which the hole is stretched to the state when the pin can be taken out. i.e. σ_{prt} level and some degree of elastic stresses, due to elastic pin deformation, will be overcome. The point A is the point when the behaviour of the hole will be as that of an open hole.

Interference fit creates a pretension stress σ_{prt} field around the hole (in the tangential direction!!!).

Suppose $\sigma_{prt} = \frac{1}{2}\sigma_l$. The applied stress cycle remains the same, hence, the max level of local stress remains the same as in the previous case. On the other hand, the pretension stress σ_{prt}, caused by a pin with interference fit, does not allow the local stress to drop down as low as the σ_{prt} level. It cuts off the lower part of the local stress cycle and the $\Delta\sigma_{localeff}$ range in this case will be between σ_{prt} and maximum local stress. The gain is obvious –a reduction of *R*.

As observed in the diagrams, the bold line representing the effective stress increases in slope through σ_{prt} to point A to the $\sigma_{local\max}$ point. According to Broek, "*Whether the line σ_{prt} - A is straight or curved does not matter for the explanation*"

Case III: Plate with a hole with a high level of interference fit

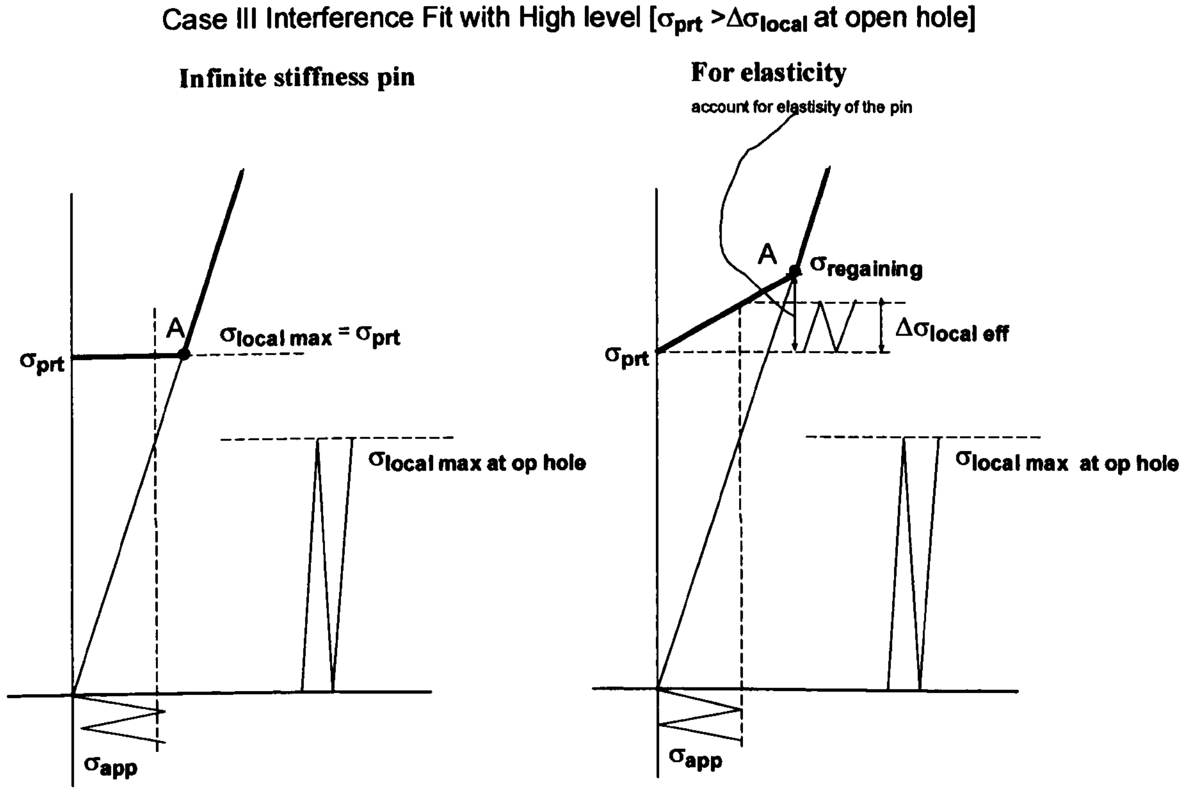

Figure 1.8.9 Plate with a hole with a high level of interference fit

The situation is the same as previously, but the pretension stress σ_{prt} is more than the maximum local stress caused by the applied stress.

Following the same logic as above, increasing the degree of interference fit increases the static σ_{prt} level until exceeds the maximum local stress.

In the case of the infinitely stiff pin, under the applied load indicated, the local stress level will be constant and equal to σ_{prt}. There will be no changes in stress. In the case of an elastically deformable pin, the stress changes will only occur due to the elasticity of the pin. and the surrounding material.

The bold line through r σ_{prt} to point A then to point $\sigma_{regaining}$ represents the effective stress factor and shows the level of the maximum local stresses and their range. The point A at which stress is equal to $\sigma_{regaining}$ is so called regaining point where the effective stress regains the value of an open hole.

Case IV: Plate with cold expanded hole

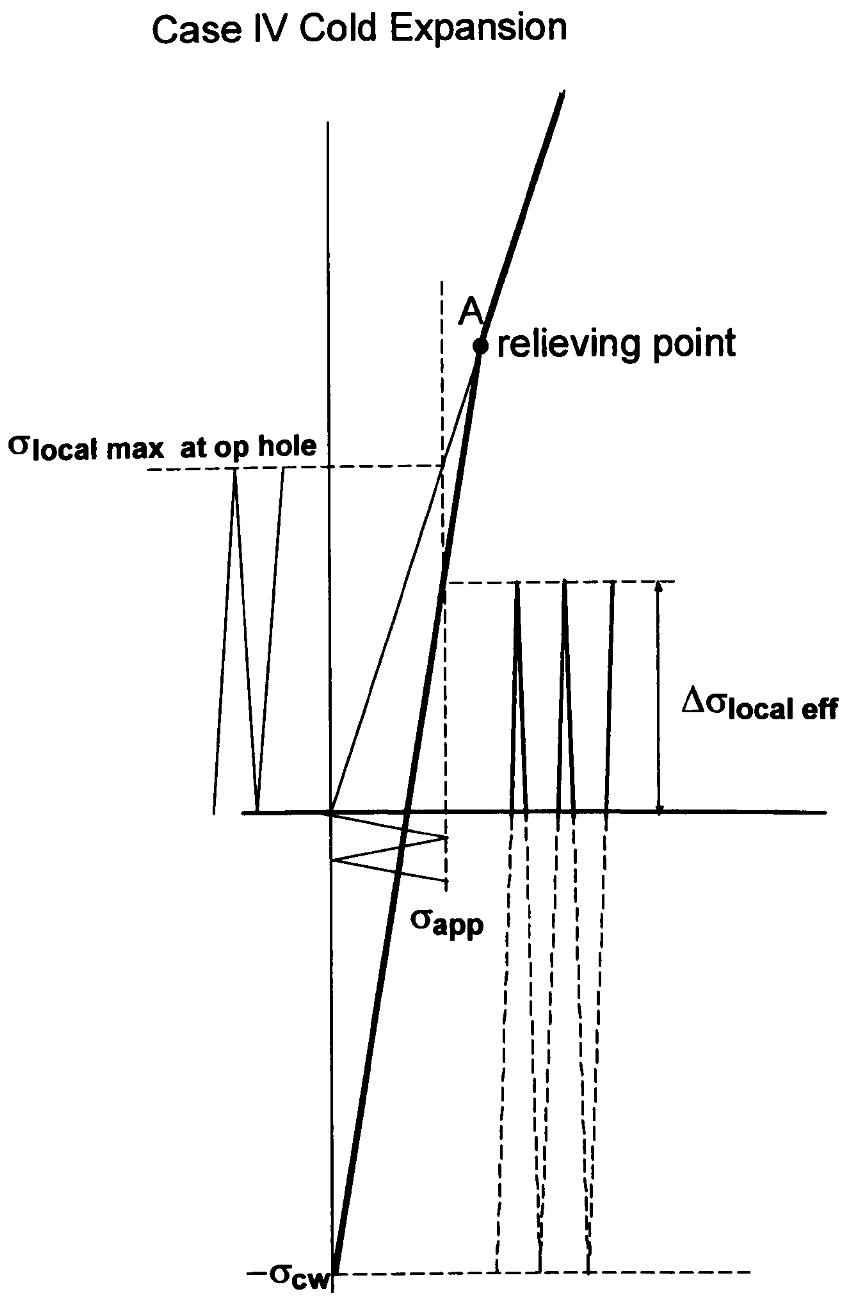

Figure 1.8.10 Plate with cold expanded hole

As the initial stress before an external load is applied is compressive σ_{cw}, the effective part of the applied cyclic stress will only be the tensile part above zero.

It can be seen how the effective stress changes from σ_{cw} to A (the relieving point). According to the function, the gain is obtained through the reduction of the maximum level of local stresses.

Case V: Plate with cold expanded hole and interference fit pin

This case is the most controversial and will be given exactly from Broek's text

It is sometimes argued that the combination of cold work and interference gives an even larger improvement. However, a simple assessment of the situation shows that in general this cannot be so, as shown in Figure 9.28.

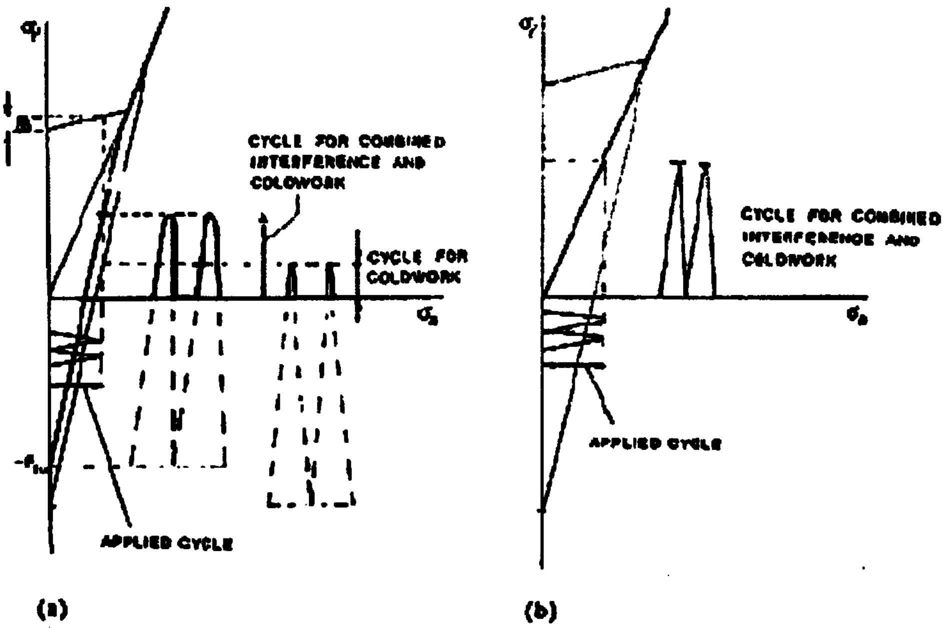

Figure 1.8.11 Combination of cold work and interference. (a) Net positive effect; (b) Cancelling of effects

The local stress range is effectively larger. Indeed if $\sigma_{prt} = F_{ty}$ the two effects cancel completely (Figure 9.28b). Hence, the combination is worse than either interference or cold work alone. Claims that combinations are better are fortuitous. for which there can be two reasons (Figure 9.28):

(a). The range from zero in cold work is somewhat larger than with the combination ($R = 0$), but the difference may be small in certain cases. If the interference reduces fretting (which it will) the combination may give longer life.

(b). Figures 9.28 are not entirely true to nature because they are for elastic behaviour but plastic deformation occurs locally.

Yet, it is fortuitous if the combination is better in a certain test. Whether it is or not depends upon spectrum (plastic deformation at high loads), the material and the hardness of the interference pin or bushing (fretting). It will be easy to show cases where the opposite is true. The foregoing explanations, showing that the effects are due to opposite causes bears this out. Claims that cold work and interference are basically the same, clearly are unfounded.

Arguments for benefit of combinations of cold work and interference fit

Broek's simplified way of representing the effects of cold expansion or interference fit on the local stresses at the side of the hole under applied load is convenient and simple to understand. In each case it indicates why fatigue life can be extended employing the technologies separately. However in the case of a combination of the two treatments Broek's analysis suggests an effect which contradicts the experimental results.

Broek suggests the main advantage from the combined treatments may arise from the reduction in fretting damage at the hole. However if this were true it doesn't explain why the fatigue performance for a plate containing a fastener hole is still improved by an interference fit fastener in tests where the fastener is not subjected to load.

There are number of reasons which could explain this inconsistency.

Broek's method accounts for the only one particular point –the side wall of the hole.

This analyzes the combined effects of residual stresses from cold expansion, plus the induced, interference fit, stresses using linear superposition. However, the real picture requires a non linear estimation.

The situation may be envisaged as follows:

The largest improvement in fatigue performance for aluminium alloys is achieved with a degree of cold expansion between 4-5%, while interference fit fasteners typically achieve an optimum fatigue performance at 1.5%. interference. This means that the compressive residual stresses from cold expansion will be significantly larger in absolute terms than the counteracting pretension stresses from interference fit. Moreover, the depth of the induced compressive stress zone due to cold expansion is greater than the depth of the tensile strain zone from interference fit. Hence this tensile stress zone from interference fit is surrounded by the zone of compressive residual stresses remaining from cold expansion.

In addition, under applied load the hole will stretched in the longitudinal direction and contract in the lateral direction. Owing to this deformation of the hole, an interference fit pin will offer resistance and cause additional compressive stresses in the transverse middle section which lead to further complex stress redistribution. Unfortunately, no publications accounting for the mutual effects of cold expansion and interference fit on stress redistribution were found. On the other hand, there are many papers confirming the beneficial effects of the combined treatments on fatigue life and crack growth rate and the work carried out at Kingston University shows clearly that the combined treatment offers a large improvement in fatigue performance.

1.9 CORROSION

Corrosion is the gradual physicochemical destruction of materials by the action of the environment (most frequently liquid or gaseous). The loss is irrecoverable.

A characteristic of metallic corrosion is the change of the metal to an oxidised state due to a heterogeneous chemical or electrochemical surface reaction. At normal ambient temperatures an electrochemical process will take place by anodic dissolution. For example, in moist air where a thin film of water may form on the metal, an electrochemical process can take place, the thin film acting as connecting the electrolyte is required. Metals first dissolve as ions and solid products may or may not form by subsequent reactions.

At room temperature, the nature of any oxidising reactants is very important in the progress of electrochemical corrosion. A number of methods are available for the prevention of corrosion in metals. These include cathodic and anodic protection, surface coatings and the selection of alternative alloys with higher corrosion resistance [(167)].

1.9.1 CORROSION RESISTANCE

Aluminium and its alloys are known to have good resistance to corrosion. When aluminium is in contact with the oxygen, a dense impervious film of aluminium oxide (Al_2O_3) forms on the surface of the metal and protects it from further oxidation.

The corrosion resistance of the aluminium alloy depends on the existence and stability of this film.

The principal factors governing the corrosion resistance of the aluminium and its alloys are described below.

1.9.2 ELECTRODE POTENTIAL OF ALUMINIUM OR ITS ALLOYS IN COMPARISON WITH OTHER METAL ALLOYS

In reference [168], a table of dissolution potentials of metals and alloys in relation to a decinormal calomel electrode in a solution of 53g/litre NaCl + 3g/litre H_2O_2, shows that apart from Magnesium and Zinc, the common metals are cathodic to aluminium, hence aluminium could corrode in heterogeneous combinations. This can only predict the risk of galvanic corrosion and cannot forecast the actual corrosion susceptibility which may depend on other factors.

1.9.3 THE EFFECT OF HEAT TREATMENT

Aluminium alloys are used both in the cast and wrought conditions. Their mechanical properties can be improved by precipitation hardening. These treatments govern not only the distribution and the importance of the alloy constituents, but also the level of the residual stresses in the component which are very important for corrosion resistance. The development of T7 two stage tempering treatments to avoid intergranular corrosion and improve resistance to stress corrosion cracking of Al-Zn-Mg-Cu alloys is a good example.

1.9.4 THE EFFECT OF PH

For pH values from 4.5 to 8.5, the alumina film is stable in water (Pourbaix diagram [169]). Hence the corrosion resistance of aluminium is higher at pH values between 4 and 9. At these pH values the aluminium forms an oxide or hydroxide layer.

In more acid or basic environments the alumina film is unstable and can dissolve in as Al^{3+} and AlO^{2-} respectively.

Three zones can be defined:

- the corrosion domain: the metal is subjected to corrosion; no electrochemical equilibrium state can be reached;
- the passivity domain: the metal and the electrolyte will form from their respective elements a layer, so-called passive layer, which will protect the metal against the medium aggression;
- the immune domain: the metal is not subjected to any aggression from the medium.

The Pourbaix diagram supposes that the metal is pure aluminium and that the solution it is immersed in only contains ions of this metal. However, any modification of either the metal or the solution can affect the diagram and hence the corrosion characteristics.

1.9.5 TYPES OF CORROSION

1.9.5.1 ATMOSPHERIC CORROSION

Most of the aluminium alloys have a good resistance to atmospheric corrosion. This may vary from one geographic location to another depending on weather factors (precipitation, temperature changes) and environment (urban and industrial pollutants and proximity to water). Three types of atmospheric corrosion can be distinguished:

- Dry atmospheric corrosion: in the complete absence of a film of moisture on the metal surface,

- Moist atmospheric corrosion: in a relative humidity of less than 100%, which proceeds under an extremely thin, invisible film of electrolyte formed on the surface by capillary action, adsorption or chemical condensation. A typical example of moist atmospheric corrosion is the rusting of iron in the absence of direct contact with water,
- Wet atmospheric corrosion: in a relative humidity of 100% and direct moisture contact (droplets of condensed moisture/ presence of film of moisture on the surface visible to the naked eye).

It is extremely difficult in practice to differentiate between these three types of atmospheric corrosion and gradual transition from one to another is possible. Wet atmospheric corrosion is similar to the complete immersion of the metal in an electrolyte and is caused by local microcells. The surface condition has been shown to influence the critical humidity. Critical humidity is the level at which a drastic increase in the rate of atmospheric corrosion takes place (moist atmospheric corrosion) (167). Vernon found that this critical humidity is determined by the formation of a continuous, condensed film of moisture resulting from hydration of salts, corrosion products or other films that might be present on the surface or from capillary condensation. Critical humidities observed were lower than 100%, leading to a transition from a purely chemical mechanism of corrosion to a much more intensive electrochemical mechanism. Dry atmospheric corrosion produces the deterioration of the metal by chemical mechanisms involving the reaction of gaseous agents.

1.9.5.2 ATMOSPHERIC CORROSION IN HIGH PURITY WATER:

The rapid formation of a protective film on the surface of aluminium alloys rapidly inhibits any further reaction occurring with water. The amount of metal dissolved by the water is negligible.

1.9.5.3 ATMOSPHERIC CORROSION IN NATURAL WATER:

Several factors control the corrosive effects of natural water on aluminium such as:

- water temperature,
- pH conductivity,
- corrosion potentials and pitting potentials of the specific alloys,
- presence /absence of heavy metals,

1.9.5.4 ATMOSPHERIC CORROSION IN SEAWATER:

3xxx, 5xxx and 6xxx alloys are more resistant to seawater than the 2xxx and 7xxx series aluminium alloys containing copper.

It has been found (170) that the corrosion rate is increased by decreasing temperature, pH and flow velocity and by increased dissolved oxygen. It is caused by the combination of low pH and low temperature.

1.9.5.5 EFFECT OF EXPOSURE TIME:

The corrosion rate of aluminium decreases with time to a relatively low steady rate. This deceleration of corrosion occurs regardless of alloy composition, type of environment or the parameter by which the corrosion is measured. However, loss in tensile strength, which is influenced somewhat by pit acuity and distribution but is basically a result of loss of effective cross-section, decelerates more gradually than depth of attack. The decrease in rate of penetration of corrosion is dramatic. In general, rate of attack at discrete locations which is initially about 0.1 mm/year, decreases to much lower and nearly constant rates within a period of months to 2 years.

1.9.5.6 GALVANIC CORROSION

When two metals are electrically connected together, the more anodic metal is reduced. This type of corrosion is important for aluminium as among the most common metals only Magnesium and Zinc are more anodic and ensure its protection.

In very conductive environments such as seawater, aluminium should be isolated from other metals. In less conductive environments (urban atmosphere), stainless steel may be safely used with aluminium rather than the more dangerous combinations of aluminium with graphite, mild steel or copper alloys.

1.9.5.7 INTERGRANULAR CORROSION

This type of corrosion is due to the selective attack of grain boundaries by corrosive media. It is caused by the potential difference between the grain boundary region and the adjacent grains. The study of this kind of corrosion is very complex and it seems that the mechanisms vary with different alloys systems. In the copper bearing 7xxx series alloys, it appears to be due to copper depleted bands along the grain boundaries. Because intergranular corrosion is involved in SCC of aluminium alloys, it is often presumed to be more deleterious than pitting general corrosion.

For Al-Cu alloys, good corrosion resistance to intergranular corrosion can be obtained by rapid quenching of the solid solution formed during solution heat treatment. When it is not possible (for thick sections), an increase in the corrosion resistance can be obtained by two stage tempering treatments (T7) [171].

1.9.5.8 STRESS CORROSION CRACKING

Stress corrosion cracking is a problem in some aluminium alloys and is characterised by the formation and propagation of intergranular cracks under the simultaneous action of corrosion and a relatively high static stress [172].

This phenomenon is of particular concern in the aircraft industry.

The 1xxx, 3xxx, 4xxx, 5xxx (with 3% or less Mg) and 6xxx series alloys are not susceptible to stress corrosion cracking (SCC)[173].

The phenomena of SCC is mainly a concern for the high strength aluminium alloys of the 2xxx and 7xxx series. The susceptibility to SCC can be minimised or annihilated by the use of different heat-treatments and quenching procedures [174].

In many cases, susceptibility to SCC of an aluminium alloy cannot be predicted reliability by examining its microstructure. The effect of stress is important as the development of SCC depends on both duration and magnitude of the tensile stress at the surface.

1.9.5.9 EFFECT OF ENVIRONMENT

Research indicates that water or water vapour is the key environmental factor required to produce SCC in aluminium alloys. Halide ions have the greatest effects in accelerating attack. Chloride is the most important ion as it is a natural constituent of marine environment and is present in other environments as a contaminant [175].

1.9.5.10 EXFOLIATION CORROSION

This type of corrosion occurs in some high strength aluminium alloys. The corrosion products generated during this process cause the build up of internal stresses which cause the metal surface to peel or blister with severe cases suffering large metal loss arising from burst blisters. Exfoliation corrosion is most predominant in alloys that are susceptible to intergranular corrosion (Al-Cu, Al-Zn-Mg-Cu alloys) but it can occur in alloys that are normally resistant to this type of attack.

A number of investigators have found exfoliation to have an effect on the fatigue life of aircraft components. Berman [176] proposed that fatigue could initiate from exfoliation corrosion. Shaffer and al [177] observed that severely exfoliated 7075-T6 wing spar caps suffered a reduction in fatigue life between 40-60% compared to the uncorroded components and concluded that the existence of exfoliation, but not necessarily the amount, was a determining factor in fatigue life.

1.9.5.11 PITTING CORROSION

As in all metals where corrosion resistance is linked to the presence of an oxide layer, aluminium is sensitive to pitting corrosion. It appears as little crevices while the rest of the surface remains unbroken. This implies specific interactions between some anions of the electrolyte and the film.

Generally, the passive films are less stable as the concentration is higher. The reactive anions are the halides and also ions such as SO^{2-}, NO^{3-}, CrO_4^{2-} and ClO_4^-.

The number and shape of the pits vary according to the experimental conditions.

Two kinds of pits can be found:

- deep pits: these propagate in the crystallographic directions and have a very disastrous influence on the mechanical behaviour [178]. The circumference of the pit is the cathode, the hole being the anode
- hemispherical pits: This type of pit is less dangerous in terms of the effect on mechanical properties. They are observed on metals polarised cathodically.

R.T. Foley found that in practise, pits are very seldom hemispherical or even of regular geometry [179].

It has been recognised [180, 181] that pitting corrosion is generally caused by the local destruction of the passivating oxide film under chemical conditions that activate certain anodic sites, but also maintain the corrosion potential above a certain critical value [182, 183, 184]. This local destruction is the result of either a local dissolution of the film [185] or an attack in the surface oxide film [186, 187, and 188] where impurity centres, weak spots are present.

Processes involved in localised corrosion

Five successive steps are involved in localised corrosion:

1) Local adsorption of ions on the surface of the oxide film.

The adsorption of anions that would promote pitting corrosion on the oxide-covered aluminium surface is a competitive process. That is, chloride or another aggressive ion is absorbed completely with hydroxyl ions or water molecules, that would, if absorbed tend to promote passivity [179]. Berzins et al [189] and Videm [190] both concluded in their work that chlorides are adsorbed at sites that subsequently form pits. Hübner and Wranglén indicated in their results that there is a certain preference for pits to initiate at the grain boundaries but pits may also form within the grain. Other studies [191,-192] concluded that aggressive sulphate and chromate ions are also absorbed. Those studies have adequately demonstrated the adsorption of anions on oxide-coated aluminium. Furthermore, from a consideration of the known heterogeneity of metal surfaces, it may be assumed that this adsorption will be not uniform. In this case it is suggested that specimens of aluminium and its alloys oxidised in air or by an anodising process, could contain flaws in the film at which pits maybe initiated [193].

2) Penetration of the electrolyte through flaws existing in the film [193].

These flaws may be :

- "Residual Flaws" caused by copper rich or iron rich segregates interfering with oxide growth in their vicinity [194]. W.K Johnson [195] found that a pit forms due to electrochemical action produced by the presence of natural defects in the metal surface such as mechanical flaws or breaks in the oxide film and particles of Al_3Fe (or other cathodic constituents. This was observed in electrolyte (e.g. natural water) containing oxygen and cations such as chlorides, bicarbonates and sulphates.

The result of Hübner and Wanglin's work [196] and others [190, 197-, 198] showed that pits may initiate in the grain but that there is a certain preference for initiation at the grain boundaries. This can be explained by the fact that Al_3Fe precipitates due to the segregation of iron [199]. This will cause thinning of the oxide film or defect formation in this film, which by adsorption of chloride ions will lead to latent anodic points. Hübner [196] also found that as the Al_3Fe particles have a more positive electrode potential than the solid solution, they act as good cathodic sites. They concluded that the transformation of an anodic area into a pit seems to be governed by the availability of such local cathodes.

- "Mechanical Flaws": these may be produced by relief of stresses in the film due to oxide formation over mechanical surface defects such as scratches and voids associated with vacancy coalescence [200]. During the formation of thin oxide films in contact with air, mechanical flaws are formed. Anodising or immersion in chromate solution appears to reduce this problem.

There is however, no real distinction between mechanical and residual flaws. Iron rich segregates (Al_3Fe) found in Al-Fe alloys, permit the formation of an oxide film above them. Nevertheless, they cause cracking of the film at their peripheries, thus effectively producing mechanical or mechano-residual flaws [193].

3) Chemical reaction of the adsorbed anion.

The adsorbed anion reacts with the aluminium ion in the aluminium oxide lattice or the precipitated aluminium hydroxide. These chemical reactions are extremely complicated, however there appear to be a well–characterised aluminium-anion reaction products [201, 202, 203]. The first of these are aluminium complex ions, such as $AlCl^{++}$ and $AlCl^-_4$ and transitory compounds such as $Al(OH)Cl_2$ and $Al(OH)_2Cl$. The second are stable, covalent compounds such as those formed with SO^-_4, for example, the basic aluminium sulphate [204]. The chemical reaction between aluminium and chloride ions shows that the low energy compounds, Al_2O_3 and $Al(OH)_3$ react with the CL ion to pass through stages represented by $Al(OH)_2Cl$ and $Al(OH)_2Cl_2$ and then through transitory complexes such as $AlCl^{++}$ and $Al(OH)^{++}$ [205].

4) Thinning of the oxide film by dissolution.

Studies offer independent evidence that even in the absence of other effects (mechanical, etc.), the oxide film on aluminium would be expected to be thinned upon exposure to aqueous solution [206, 207] . Wood et al have presented a strong case for the significant involvement of flaws in the oxide film [193]. They showed that the direct linkage of flaws to pit initiation is also reasonable, particularly because such sites would be the preferred sites for adsorption, and once adsorption occurs the development of an active centre should be the next logical step. The active centre is then the site for accelerated film thinning.

Pryor and al found that the adsorption of anions at the oxide-electrolyte supposedly produces a high electrical field that draws the aluminium ions through the film.

5) Direct attack of the exposed metal.

Once the film is sufficiently thinned, the high degree of reactivity of metallic aluminium ensures rapid attack and pit propagation. Because the film is thinned locally, the attack on the metal will also be concentrated in the geometrical sense. A number of reactions or physical processes are involved at any given time (see Hübner and Wanglin's work [196]). The direct attack of the exposed metal differs in a basic manner from the pit initiation reaction. This latter is concerned with the interaction, chemically or physically, of the oxide film with the solution environment. The growth of the pit involves the interaction of aluminium metal directly with an environment that is changing as the reaction proceeds. Upon recognising this different behaviour, the usefulness of disclosing a single phenomenon for correlating the entire four-step pitting process becomes evident. The electrochemical mechanism of pit growth in aluminium is explained below and in Hübner and Wanglin's work [196].

Growth of Corrosion Pits

Inside the pit, several phenomena can occur which may prevent repassivation. There is a limited supply of oxygen [208, 209]. The pH is low due to hydrolysis of metal ions [193, 208]. The chloride ions migrate into the pit with the current generated by the pit corrosion cell [193, 210] and a concentrated salt solution is formed is formed of high electrical conductivity [211].

At the pit mouth, a porous hydroxide diaphragm will form which inhibits mixing. Near the pit mouth a reduction in oxygen (O_2) will occur, limiting the supply of Oxygen inside the pit [116]. This reduction is accompanied by a dissolution of the metal which will create an excess of positive charge (Al^{3+}) at the pit base and migration of the chloride ions occurs to offset the imbalance. This will lead to an increase in metal chloride concentration in the pit. These salts being subjected to hydrolysis, the hydrogen ion concentration will increase, lowering the pH inside the pit and promote an increase dissolution rates. These phenomena will prevent repassivation.

Outside the pit, general attack will be prevented by the presence of corrosion current which provides cathodic protection. The deposition of more noble metals, particularly Copper [209, 212], increases the effectiveness of cathodic sites [213, 214, 215]. These metals will facilitate the maintenance of an electrode potential more noble than the critical pitting or break through potential.

Termination of pitting corrosion Convection currents bringing about intermingling of the anodic and cathodic products of reactions can produce precipitation of a protective film over the active anodes thus stifling the corrosion [216].

Figure 1.9.1 Electrochemical mechanism of pit growth on aluminium [196].

2 EXPERIMENTAL PART

2.1 *MATERIAL SPECIFICATION*

The 2024-T351 aluminium alloy was provided by QinetiQ. The alloy was supplied in the T351 condition as rolled plates with a nominal thickness of 20 mm.

The T351 treatment involves the following procedure:

Solution heat treated at 495±5°C,

Cold water quenched,

Stretched to a permanent extension of between 1.5% and 2.5% :

followed by ageing at room temperature for a period not less than 48 h.

The major alloy constituents were nominally 4.4% Cu, 1.5% Mg and 0.6% Mn. Detailed chemical composition is given in

Table 4 Chemical composition (in wt %)

aluminium alloy	Si	Ft-	Cu	Mn	Mg	Cr	Zn	Ti	Ni	Zr	Li
2024	.10	.18	4.35	.67	1.36	0.02	.07	.03	-	.01	-

The basic mechanical properties for the alloy are given in Table 5.

Table 5 Mechanical properties of Al 2024

	Elastic modulus, E (GPa)	0.1% Proof Stress(MPa)
Longitudinal orientation	72	365
Transverse orientation	72	295

The longitudinal direction is parallel to the rolling direction, and no through thickness properties were available.

2.2 *SPECIMENS AND TEST EQUIPMENT.*

2.2.1 *SPECIMENS MANUFACTURING*

Flat plate specimens were manufactured from the material supplied so that the major axis of each specimen was orientated along the rolling direction of the material. The specimen configuration used for the experiments is similar to the design suggested in the ASTM standard E647[217].

The specimens were rectangular, 180 mm x 32 mm x 6.35 mm, containing a central drilled hole Figure 2.2.1. The diameter of the drilled and reamed hole was 6.35 mm in case of plain specimens and 6.235 mm after final reaming of CW specimens.

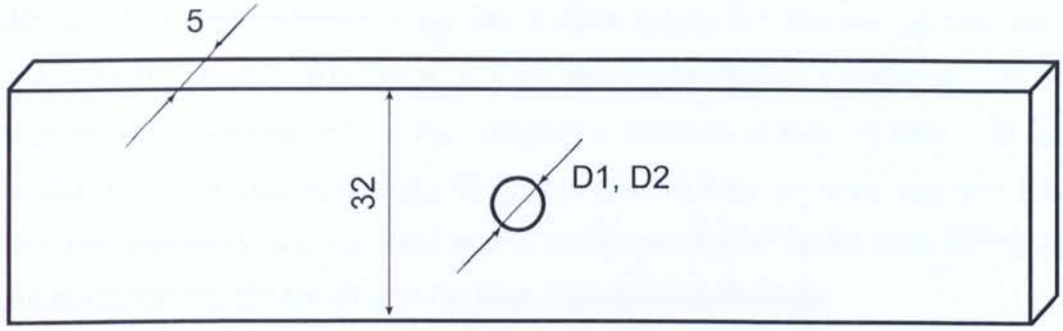

Figure 2.2.1 Dimensions of the specimen

2.2.2 TEST EQUIPMENT

All fatigue tests were carried out on 300 kN and 100kN Mayes (***Figure 2.2.2***) universal testing machines (servo-hydraulic testing machines).

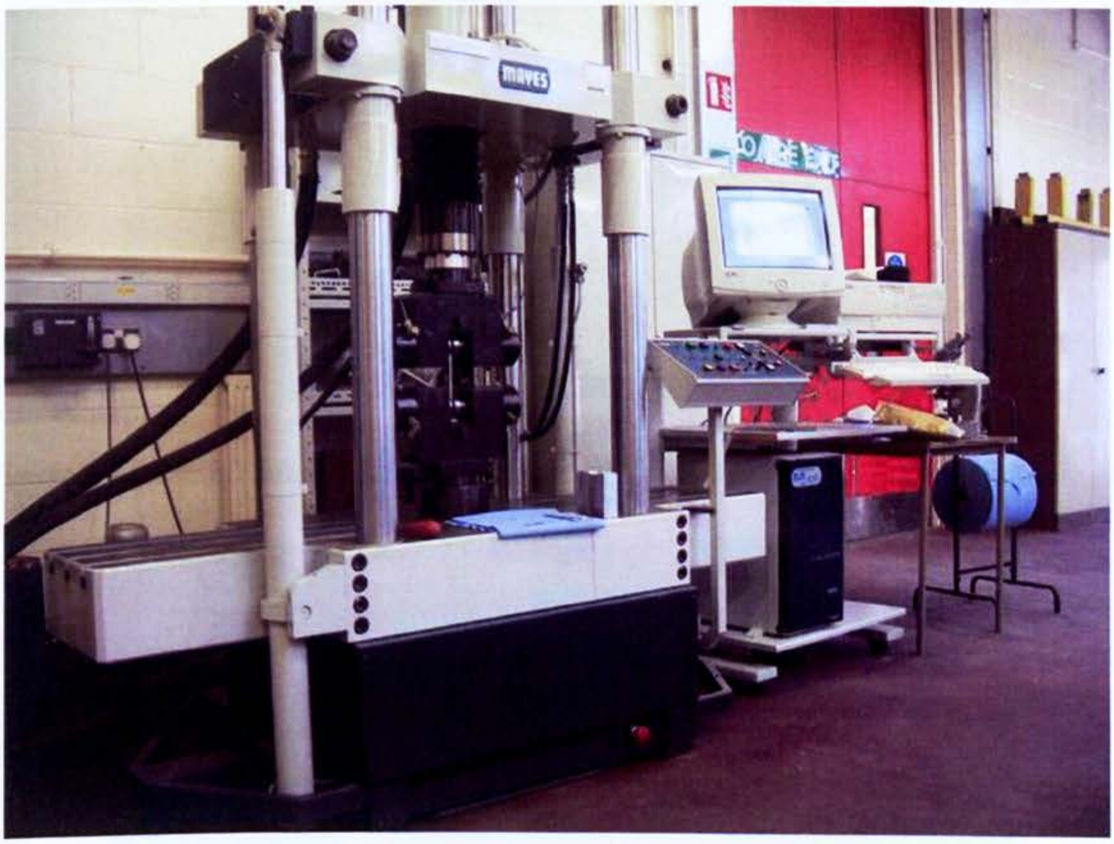

Figure 2.2.2 Mayes universal 100kN testing machine

The 300kN machine was supplied with mechanical friction grips to take a minimum specimen thickness of 10 mm. For tests using this machine aluminium alloy pads were bonded to both ends of the specimens with epoxy resin to avoid premature failure from the grip region. The pad dimensions were 60mm long × 40mm wide × 4.92 mm thick.

The 100kN machine had hydraulic grips (see Figure 2.2.3) and did not require any specimen modifications. To fix a specimen in the grips, a special central alignment attachment was made.

Both machines were supplied with a PC compatible Rubicon control system with an interface running under Windows (see Figure 2.2.4). The control system set max and min levels of the applied load and frequency, and recorded and/or set the number of cycles until failure or standby.. The machines maintained the preset standby load required automatically.

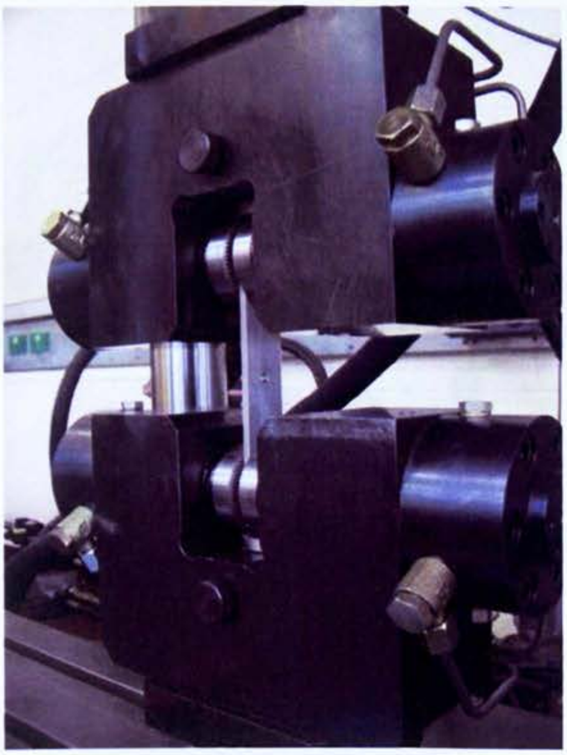

Figure 2.2.3 100 kN Mayes test machine with a specimen mounted in the hydraulic grips

Figure 2.2.4 The Rubicon Control System Block and its interface

2.2.3 CRACK MEASURING TECHNIQUE

Crack lengths were measured through the use of acetate replicas, which were examined under an optical microscope Figure 2.2.5

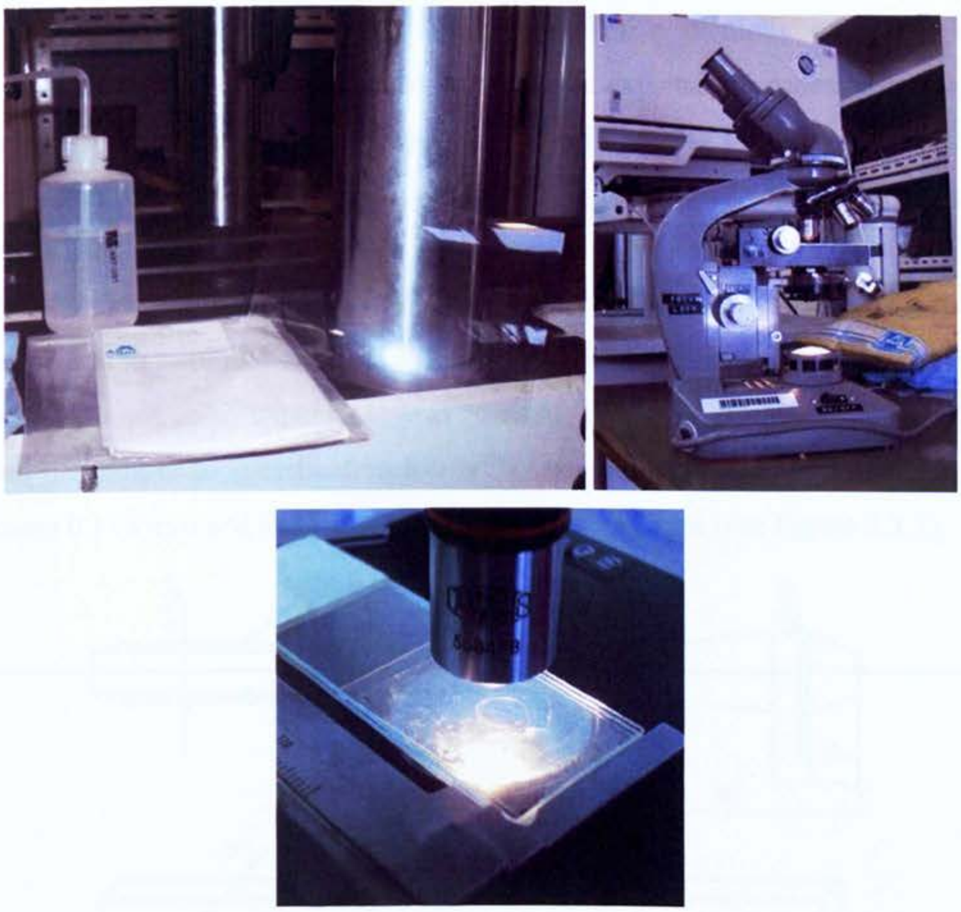

Figure 2.2.5 Acetate replica sheets and optical microscope and crack measurement

The procedure consisted of periodically stopping the fatigue testing at the end of a loading block, applying a static standby load equal to approximately 80% of the peak load (to increase the visibility of the crack tip), and applying a cellulose acetate strip softened with acetone to the surface of the specimen. Cellulose acetate replicas on the plate surfaces covered an area 15mm above and below the centre-line of the hole across the whole width of the specimen. The replicas were then examined under an optical microscope. The crack lengths were measured on both sides of the specimen. The crack length data obtained is considered accurate to within 10 μm.

Measurements of the growing fatigue crack have been recorded for crack sizes of ~ 0.05mm until final fracture. For all specimens, cracks propagating on both "inlet" and "outlet" faces were measured.

2.3 *THE MANUFACTURE OF FATIGUE SPECIMENS FOR TESTING*

2.3.1 *COLD EXPANSION*

Specimens were manufactured with plain holes drilled to a diameter of 4 mm and then after preliminary drilling and reaming subjected to the cold expansion process after which the final diameter was about 6.235 mm. The cold expansion process involved in this research used a standard technique employed extensively in the aircraft industry. The process consisted of pulled a tapered mandrel through the predrilled hole. For each hole, a hardened stainless steel split sleeve was inserted into the hole. The sleeve was used to prevent the direct contact between the hole and the sliding mandrel, and to minimise material flow in the thickness direction

Hole preparation and cold expansion was carried out at QinetiQ using FTI tooling and recommended procedures to specification 8-0-N[218]. The mandrel major diameter was 5.66 mm, the sleeve thickness 0.176 mm and the initial hole diameter 5.742 mm (see Figure 2.3.1).

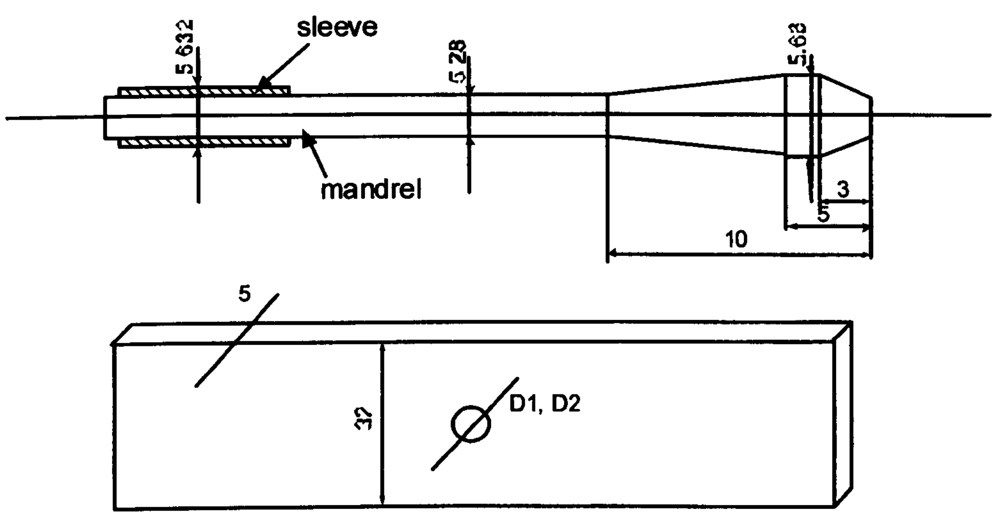

Figure 2.3.1 Dimensions and shape of the mandrel, split sleeve and holes in the specimen

The degree of cold expansion is given by

$$\frac{(D_2 - D_1)}{D_1} \times 100\,\% = E_{(FTI)} \qquad \textbf{(2.3.1)}$$

With D_1: initial hole diameter and D_2: mandrel diameter.

From equation (2.3.1), the degree of cold expansion was found to be 4.49 %. The diameter contracts after mandrel removal but retains about 71% of the expansion.

At the end of the process the final hole diameter D_3 will be given by:

$$D_3 = D_1 + (D_2 - D_1) \times RE = D_1\left(1 + E_{(FTI)} \times RE\right) \qquad \textbf{(2.3.2)}$$

RE is the retained expansion and is generally = 60% for aluminium alloys

At the end of the process the final hole diameter was 5.934 mm i.e. very close to that given by equation (2.3.2). The final reaming increased the hole size to 6.235 mm. The hole is reamed after cold expansion (post -reamed) to ensure that it is circular before a fastener is installed. This also removes the pip of material formed during cold expansion by the gap in the split sleeve.

For all the specimens the split mandrel was positioned so that the gap in the sleeve was at 0 degrees to the proposed loading direction.

The diameters corresponding to each phase of hole manufacture and the percentage of cold expansion are given in Table 6

Table 6 Typical parameters for fastener hole manufacture

Start ream diameter (mm)	Cold Expansion diameter (mm)	final ream diameter (mm)	Degree of CX, %	Retained expansion,% ()	Estimated final hole diameter ()	Error of estimation, %
5.742	5.932	6.232	4.491	70.370	5.923	0.160
5.742	5.934	6.232	4.491	71.111	5.923	0.194
5.748	5.936	6.238	4.391	71.212	5.925	0.191
5.746	5.932	6.236	4.424	69.925	5.924	0.136
5.739	5.934	6.235	4.540	71.429	5.921	0.212
5.741	5.933	6.234	4.507	70.849	5.922	0.183
5.741	5.938	6.237	4.507	72.694	5.922	0.267
5.741	5.933	6.238	4.507	70.849	5.922	0.183
5.741	5.938	6.24	4.507	72.694	5.922	0.267
5.739	5.932	6.237	4.540	70.696	5.921	0.178
5.74	5.933	6.234	4.524	70.956	5.922	0.189
5.74	5.938	6.235	4.524	72.794	5.922	0.273
5.743	5.933	6.235	4.474	70.632	5.923	0.171
5.742	5.934	6.232	4.491	71.111	5.923	0.194
5.74	5.935	6.233	4.524	71.691	5.922	0.223
5.742	5.932	6.233	4.491	70.370	5.923	0.160
5.743	5.935	6.238	4.474	71.375	5.923	0.204
5.745	5.933	6.236	4.441	70.412	5.924	0.158
5.748	5.932	6.238	4.391	69.697	5.925	0.123
5.744	5.933	6.238	4.457	70.522	5.923	0.165
5.741	5.935	6.233	4.507	71.587	5.922	0.217
5.74	5.938	6.234	4.524	72.794	5.922	0.273
Average values						
5.742	5.934	6.235	4.487	71.171	5.923	0.196

2.3.2 *FATIGUE LOADING*

Fatigue tests were carried out under constant amplitude sinusoidal loading at a stress ratio of R=0.1 and a frequency of 10 Hz. 10 Hz is a frequency typically used for fatigue tests. All specimens were tested in normal atmospheric conditions. Maximum net stress values of 175, 200, 210 MPa were used in the initial investigation and a stress level of 210 MPa was chosen as basic stress to compare fatigue test results.

The stress values were converted from MPa to load units kN for the inputs required in the testing machine control programme i.e. F_{max}, F_{min}, F_{SB} (SB-Standby Load).

$$F_{max} = \sigma_{max} S_{net} = \sigma_{max} (W - D)t; F_{min} = RF_{max}; F_{SB} = 0.8F_{max} \quad \textbf{(2.3.3)}$$

here W - width ; D - hole diameter ; t - specimen thickness; S_{net}=0.000128 m^2 - cross-section net area; R stress ratio;

Table 7 Stress and Load parameters

$\sigma_{\max net}$, MPa	F_{max}, kN	F_{min}, kN	F_{SB}, kN	$\sigma_{\max remote (gross)}$, MPa
200	25.65	2.565	20.52	160.3125
210	26.9325	2.69325	21.546	168.3281

2.3.3 CORROSION

27 specimens were subjected to artificial corrosion in saline solution of 3.5%NaCl.

The solution was prepared using distilled water in which 3.5 ± 0.1 part by weight of NaCl in 96.5 parts of water. An industrial salt containing a minimum of 99.5 % NaCl, assay (dry basis) was used for all the test solutions. The specimens were completely immersed in the vertical position in glass jars. After exposure, specimens were rinsed with distilled water then cleaned with acetone to stop the corrosion process as the accumulated salt and corrosion products are hygroscopic.

2.3.4 INTERFERENCE FIT FASTENERS

10 cold expanded (CX) specimens were manufactured with a tapered titanium interference fit bolt inserted in the hole. The maximum diameter of the bolt body was 6.32 mm and the diameter of CX fastener hole was 6.235. Thus, from (2.3.1) the interference fit was 1.3%.

After insertion of the fastener, the head and tail were cut off and discarded. Both fastener surfaces were polished back to the level of the specimen surface to enable accurate acetate replicas to be taken.

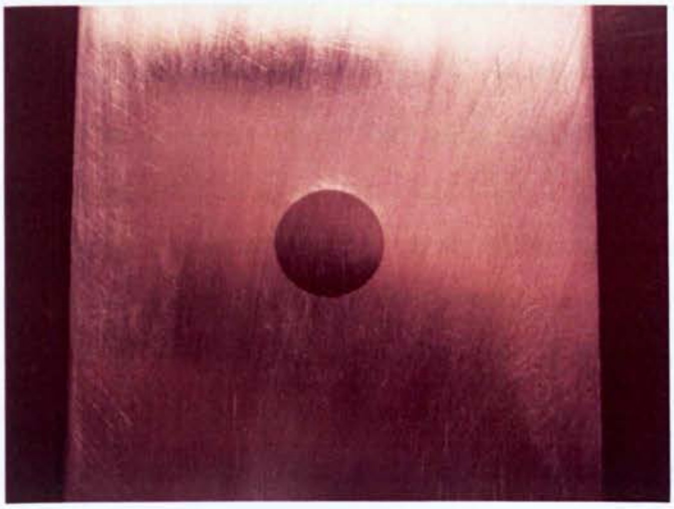

Figure 2.3.2 Specimen with an interference fit fastener

2.4 FATIGUE TESTS

2.4.1 PLAIN SPECIMENS

2.4.1.1 CRACK GROWTH ANALYSIS. PLAIN SPECIMENS

7 plain specimens were tested in total. 4 at a net load of 200 MPa (gross (total cross section area including hole) stress 160.3MPa) and 3 at a net stress of 210 MPa (gross 168.3 MPa). Crack growth diagrams are given in the Figure 2.4.1

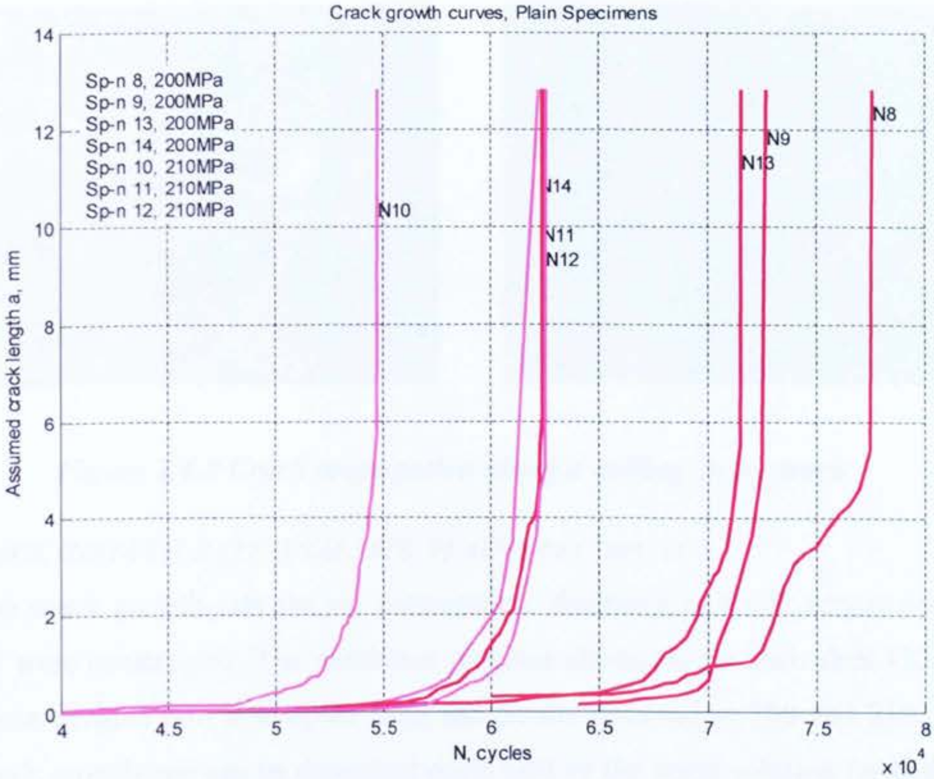

Figure 2.4.1 Crack growth curves. Plain specimens.

It is clear that fatigue lives of the specimens №10, 11, 12 tested under σ_{net}=210MPa are shorter than the specimens tested at stress levels under 200 MPa. Quantitative data on total life, crack initiation life, and crack propagation life, as well as observations of the surface crack form, crack symmetry and pictures of the fracture surfaces are given in of the Appendix

Acetate sheet replica analysis observed during the experiment reveals interesting features of the crack propagation. From the beginning of crack detection until final fracture, the crack propagated along milling cutter tracks which are shown very precisely and distinctly on the replica (see Figure 2.4.2). Thus, we can conclude that milling cutter tracks are rather influential concentrators and are important factors for crack propagation, at least for the surface cracks.

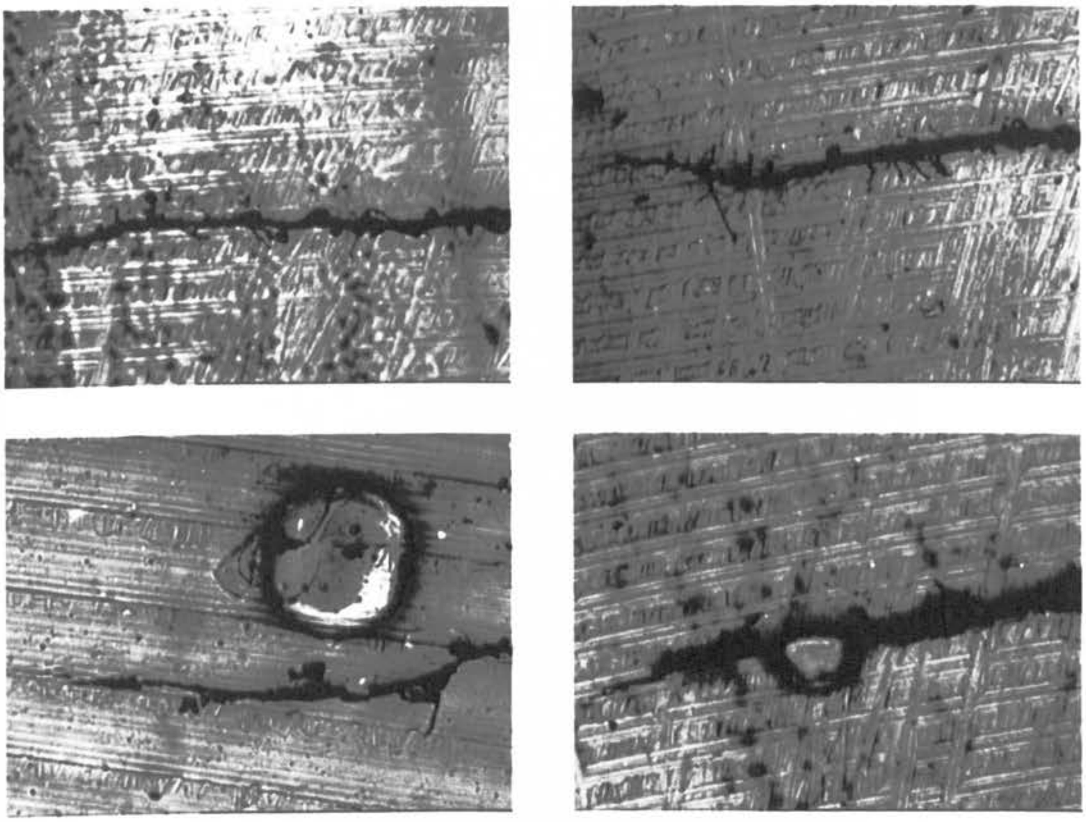

Figure 2.4.2 Crack propagation along a milling cutter track

2.4.1.2 CRACK GROWTH RATE ANALYSIS. PLAIN SPECIMENS

To assess the crack growth rate during propagation, diagrams of CGR versus crack length (see Figure 2.4.3) were constructed. The combined diagram shows all the individual CGR diagrams for every specimen divided into 2 samples from the results obtained at 200 and 210 MPa. It can be noted that crack growth rate can be described quite well by the linear solution for both samples.

The same observation applies for the CGR versus applied SIF diagram (see Figure 2.4.4). The CGR results are given on the same basis for 200MPa and 210MPa. Furthermore, different types of cracks (corner and through) were processed with suitable SIF solutions

and this is shown in the figure.

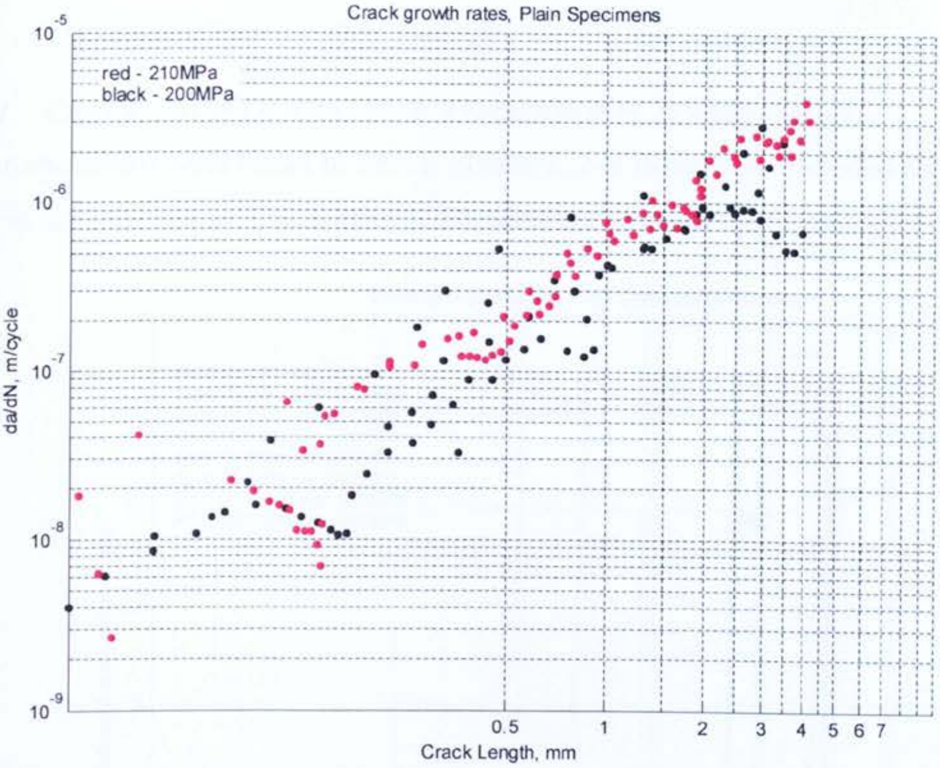

Figure 2.4.3 Crack growth rate versus crack length

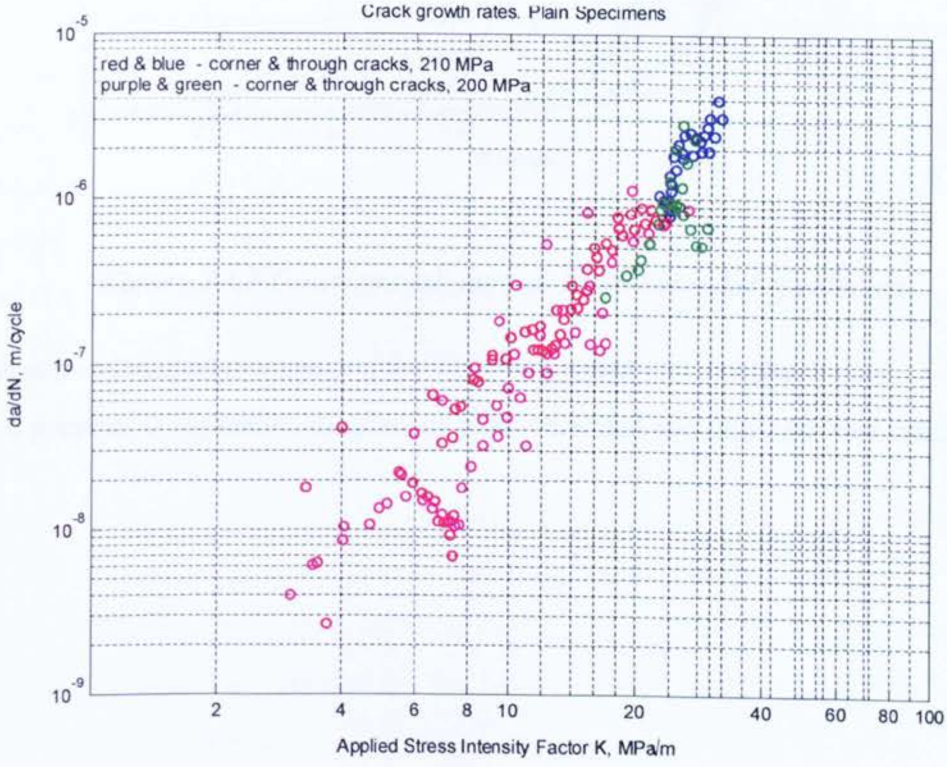

Figure 2.4.4 Crack growth rate versus applied SIF

2.4.2 CORRODED PLAIN SPECIMENS

2.4.2.1 CRACK GROWTH ANALYSIS. CORRODED PLAIN SPESIMENS

8 plain specimens were tested in total at 200MPa. 2 of these were corroded for 24 hours, 2 for 72 hr, 2 for 96 hr, 2 for 168 hr. Crack growth diagrams are given in the Figure 2.4.5.

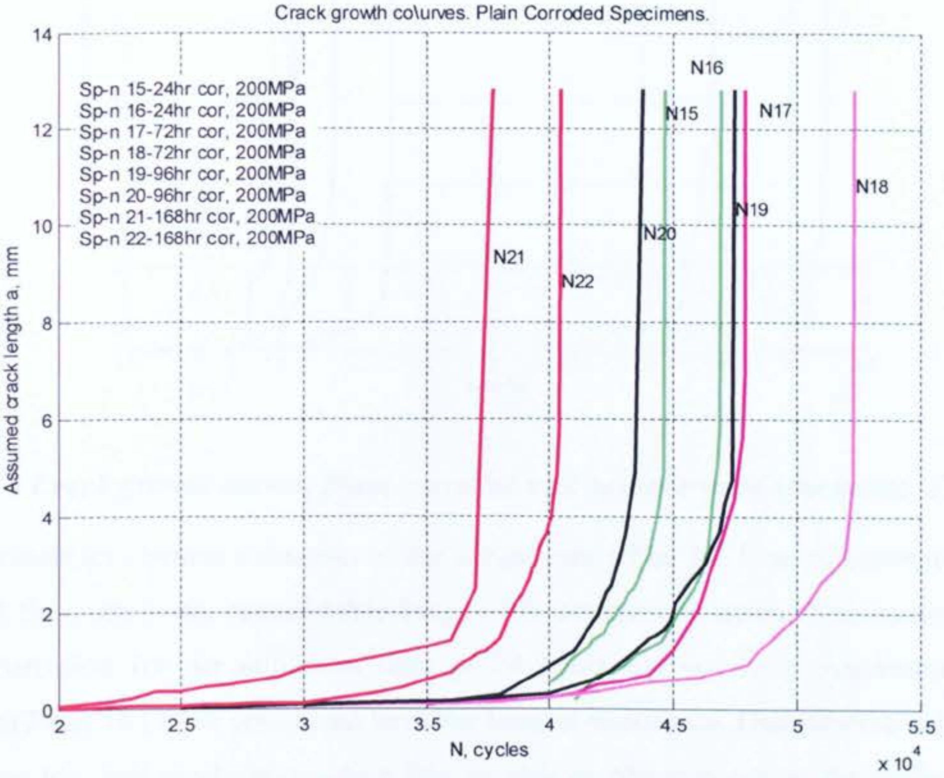

Figure 2.4.5 Crack growth curves. Plain corroded specimens.

4 specimens were subjected to corrosion for 72 hr and tested at 210 MPa.

Figure 2.4.6 presents comparative diagram of plain corroded and non-corroded specimens.

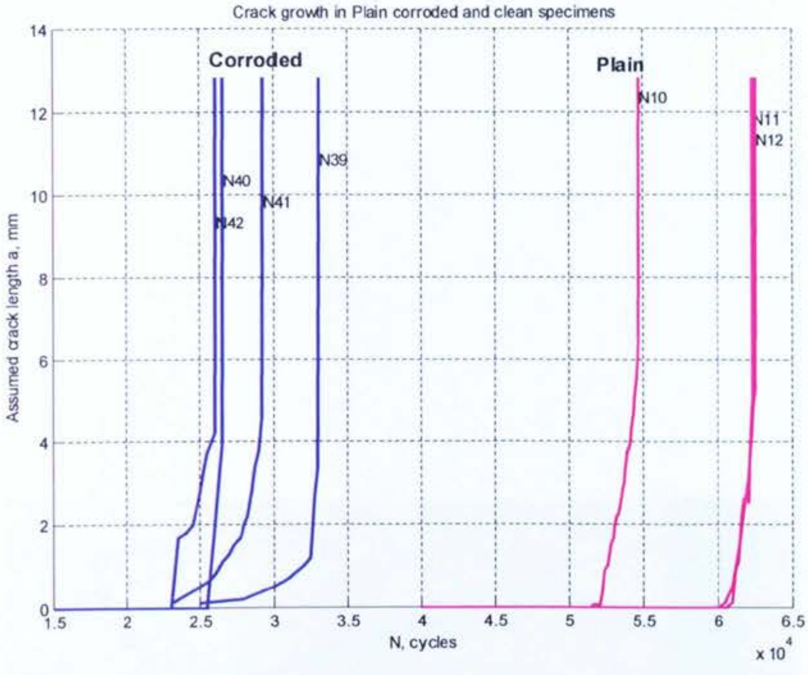

Figure 2.4.6 Crack growth curves. Plain corroded and non-corroded specimens. 210MPa

The figure reveals an obvious reduction in the fatigue life when the time of corrosion exposure is increased. At the same time, considerable fatigue life scatter was noted. Specimens №15 and 16 exposed to corrosion for the minimum time of 24 hours did not have maximum life whereas specimens №17 and 18 (72 hr corrosion) have the longest endurance. Quantitative data on total life, crack initiation life, and crack propagation life, as well as observations of the surface crack form, crack symmetry and fracture surfaces are given in in Appendix.

It has been noted that the cracks propagated along the milling cutter tracks as well and that corrosion pits did not affect the crack path. It can be assumed therefore that milling cutter tracks are more significant stress concentrators than the corrosion pits formed on the surface of the specimens after immersion in 3.5%NaCl solution

Initiation of several micro cracks on opposite hole edges and the subsequent dominance of one of them was observed in this case (see ***Figure 2.4.7***, ***Figure 2.4.8***, ***Figure 2.4.9***).

It was observed that the cracks had initiated on the hole edges, spread as corner cracks then gradually changed into through cracks. All the cracks initiated on the edges left by the reamer on the outlet sides of the specimens.

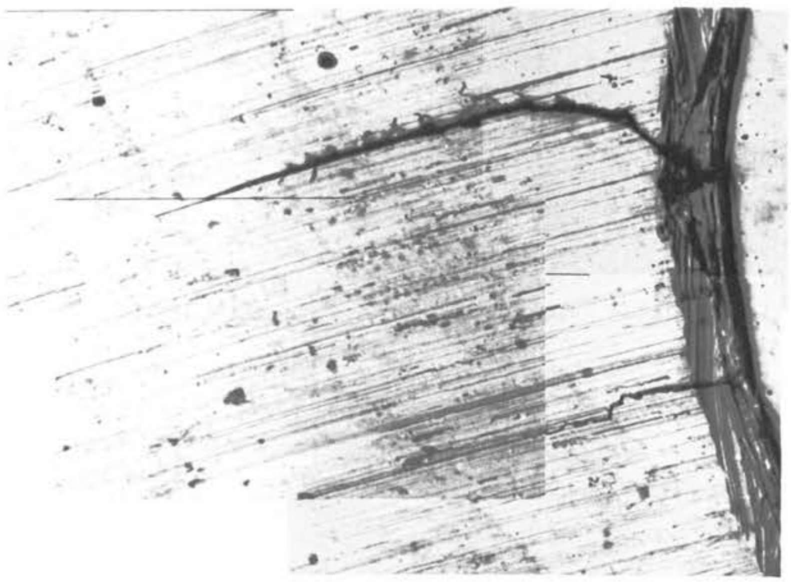

Figure 2.4.7 Initiatiation of several micro cracks on the hole edge

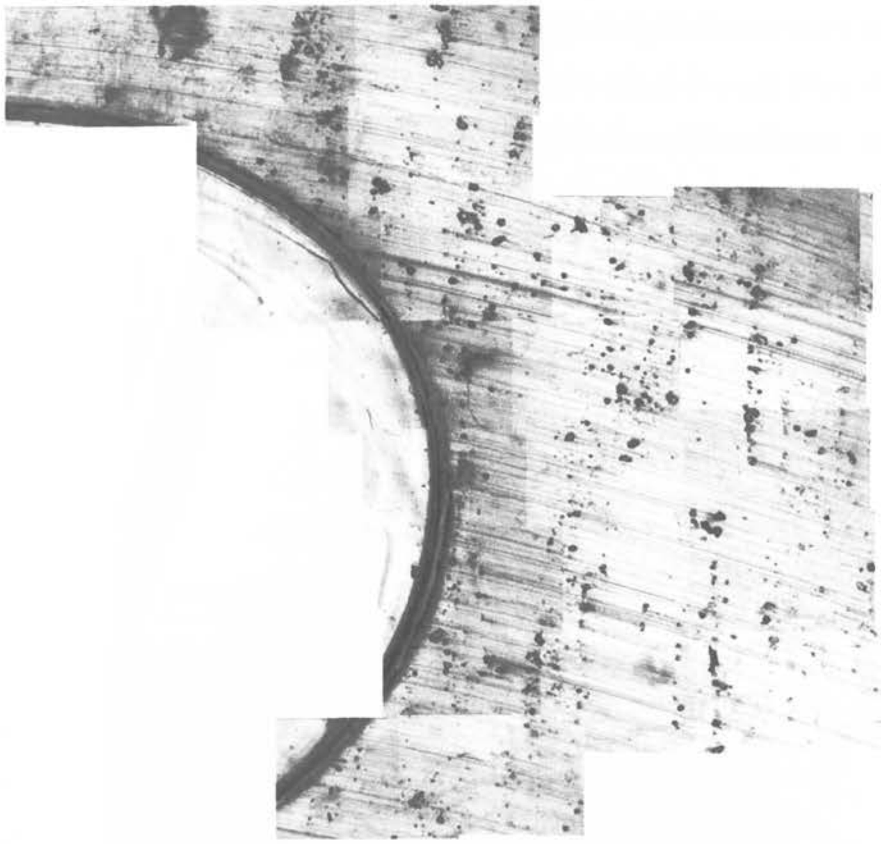

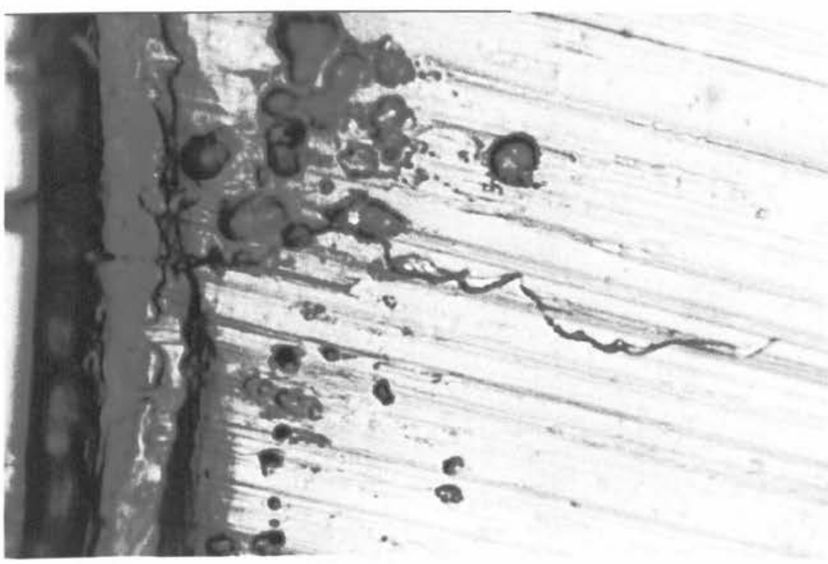

Figure 2.4.8 Corrosion pit distribution and crack propagation across surface of the specimen with milling cutter tracks.

In one case only (corrosion 168 hr, σ =200MPa) fatigue crack initiatiation from corrosion pits was observed. The crack initiated from a group of corrosion pits located away from the hole edge. As shown in ***Figure 2.4.9*** the crack reached the edge of the hole and then began to propagate away from the hole

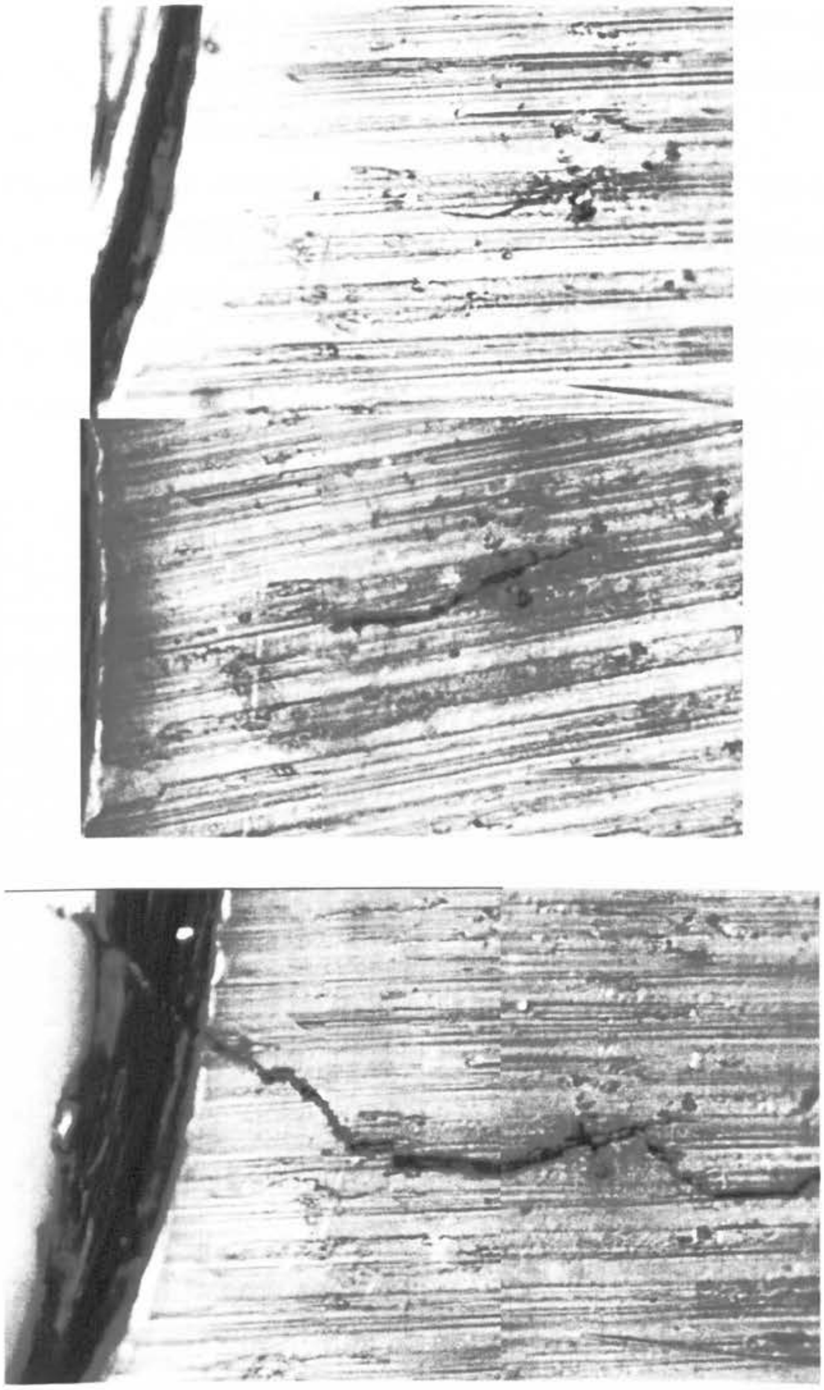

Figure 2.4.9 Fatigue crack initiation and propagation from corrosion pits

2.4.2.2 CRACK GROWTH RATE ANALYSIS. CORRODED PLAIN SPECIMENS

To assess the crack growth rate during propagation a diagram of crack growth rate versus crack length (see ***Figure 2.4.10***) was constructed. The combined diagram shows all the individual CGR diagrams for every specimen divided into 4 samples according to results obtained for 24, 72, 96 and 168 hours corrosion exposure specimens. It can be noted that the experimental data points of these four samples obey one law as shown by the non-corroded plain specimens tested previously. Crack growth rate can be described by a linear solution quite well for all samples.

The same observation can be made in the case of the crack growth rate versus applied SIF diagram (see ***Figure 2.4.11***). The crack growth rate results in this case are grouped together as there were no significant differences between individual diagrams.

Figure 2.4.12, ***Figure 2.4.13*** show crack growth rate diagrams of corroded specimens in comparison with non corroded plain specimens. They reveal faster crack growth rates in corroded specimens during the initial stages of crack propagation, though the diagrams also show much closer agreement for larger cracks. The diagram below indicates that corrosion pits do not exert a significant effect on crack propagation above a crack length of approximately 1mm.

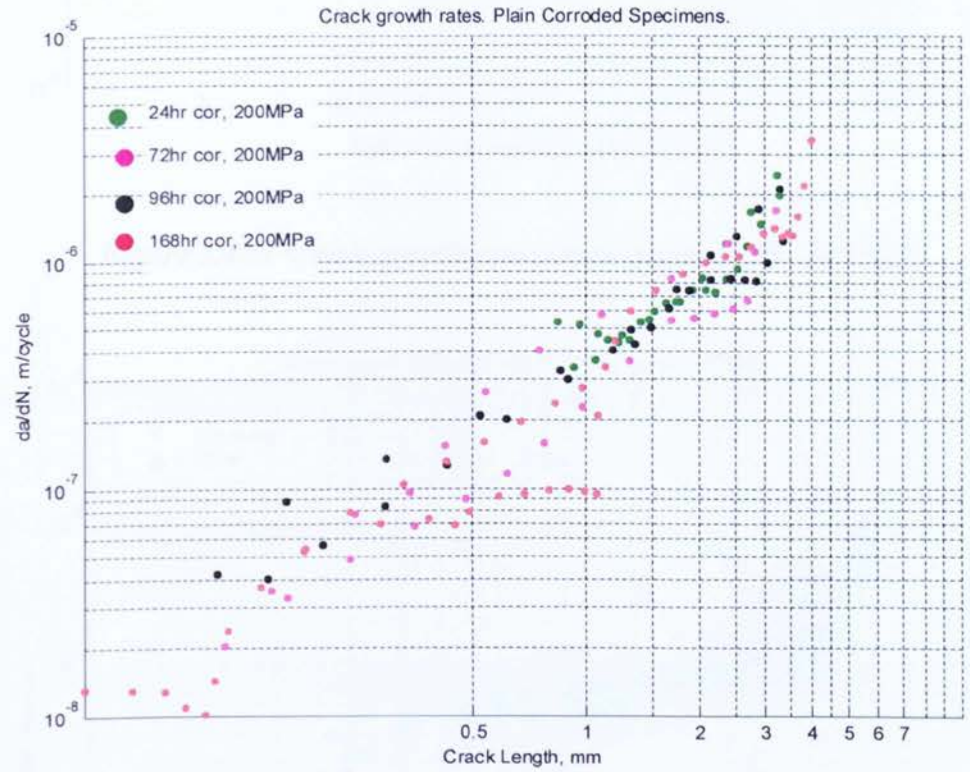

Figure 2.4.10 Crack growth rate versus crack length. 200 MPa

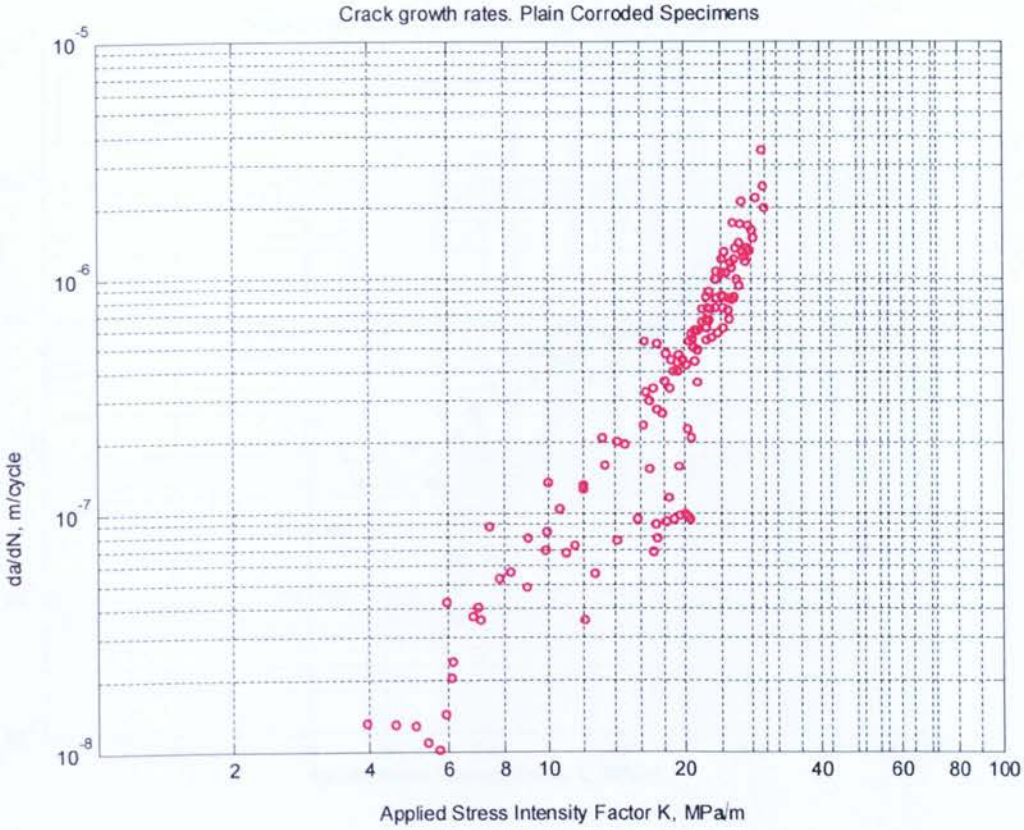

Figure 2.4.11 Crack growth rate versus applied SIF. 200 MPa

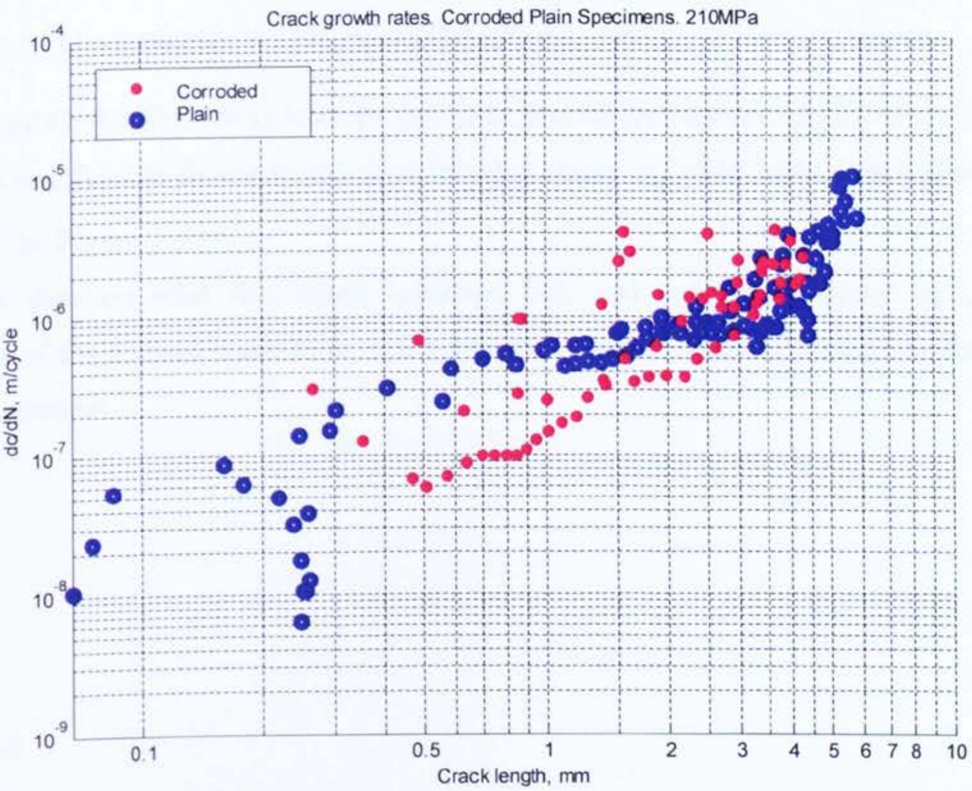

Figure 2.4.12 Crack growth rate versus crack length. Specimens tested at 210MPa

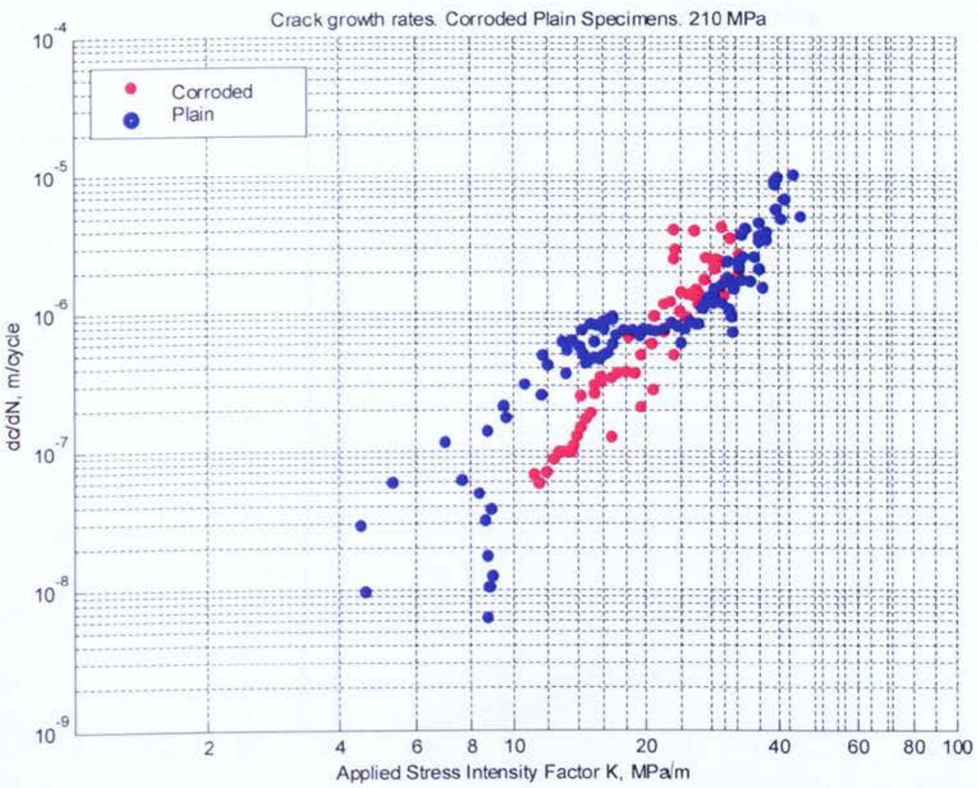

Figure 2.4.13 Crack growth rate versus applied SIF. 210MPa

2.4.3 PLAIN SPECIMENS WITH INTERFERENCE FIT

2.4.3.1 CRACK GROWTH ANALYSIS. PLAIN SPECIMENS WITH INTERFERENCE FIT

3 plain with interference fit specimens were tested at stress σ_{net}=210 MPa. Crack growth diagrams are given in the Figure 2.4.14

Quantitative data on total life, crack initiation life, and crack propagation life, as well as observations of the surface crack form, crack symmetry and pictures of fracture surfaces are given in of the Appendix.

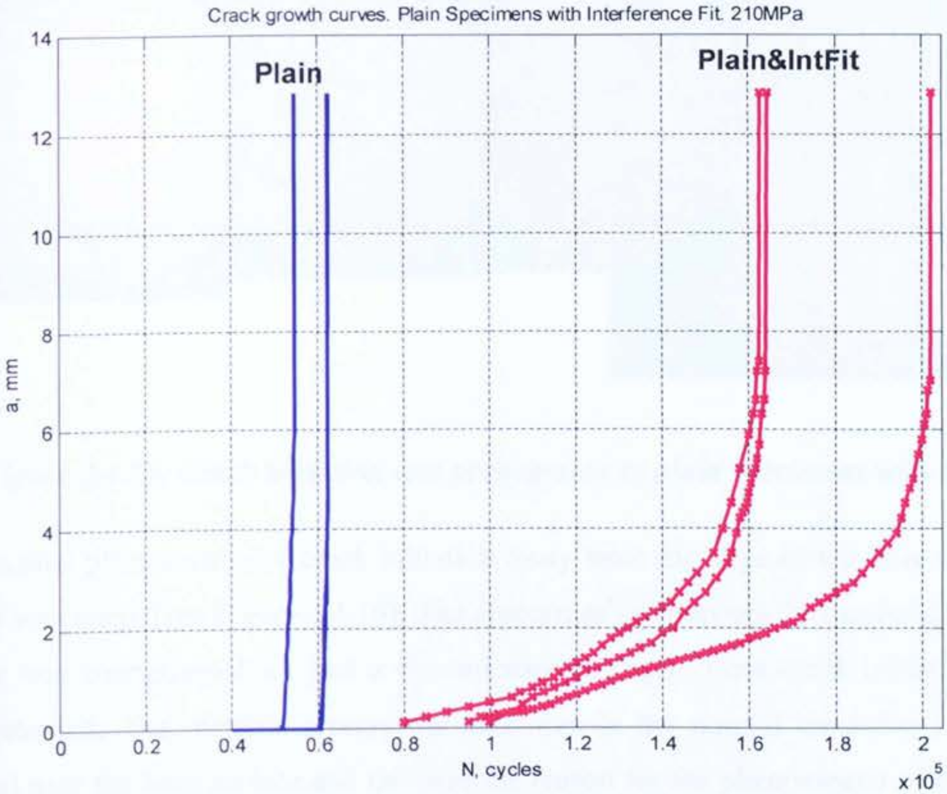

Figure 2.4.14 Crack growth curves. Plain specimens with interference fit

It was be noted that in all cases cracks were assumed to be single asymmetrical cracks, However sometimes cracks initially nucleated at both sides of hole but then the secondary crack was stopped or its propagation was substantially slower than the dominant crack. All cracks did not start in the central section line, supposedly the weakest section, but from the edge of the hole some distance away from the centre line (see Figure 2.4.15).

The weakest section should be the central section. However the inserted oversized titanium pin, which is much harder than Al and not undergoing significant deformation when the specimen is under tensile load may affect this. Under tensile load the hole elongates in the longitudinal direction and contracts in the transverse direction. The pin resists the contraction thus introducing additional compressive stresses in the central section. Hence the weakest section is shifted away from the central section.

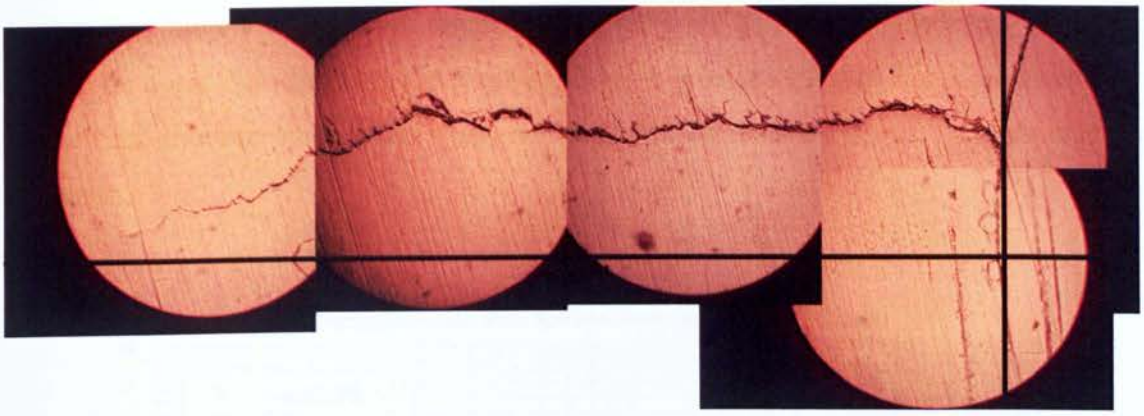

Figure 2.4.15 Crack initiation and propagation in plain specimens with interference fit

The unusual phenomenon of crack initiation away from the edge of the hole was observed in this type of specimen. (see Figure 2.4.16). The amount of interference fit consisted of 1.3% so the bore surface was strengthened for just a few microns in depth. Here crack initiation and propagation were retarded. The material around the hole was in the normal condition i.e. weaker than the material near the bore surface and this was the reason for the phenomenon of crack initiation away from the edge of the hole.

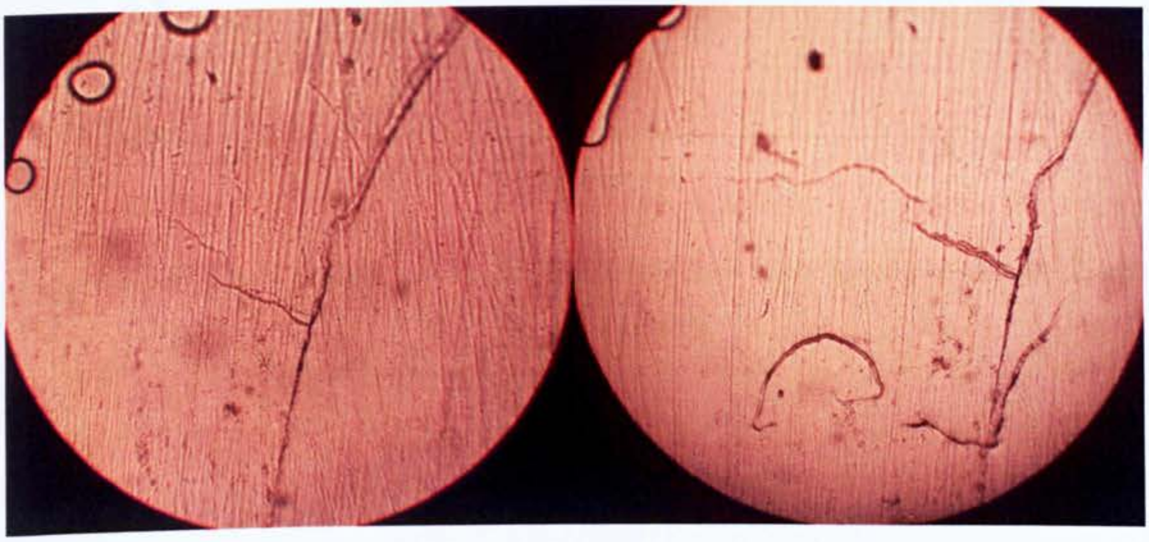

Figure 2.4.16 Phenomenon of pre cracking in plain specimens with interference fit

2.4.3.2 CRACK GROWTH RATE ANALYSIS. PLAIN SPECIMENS WITH INTERFERENCE FIT

To assess the crack growth rate during propagation diagrams of crack growth rate versus crack length versus applied stress intensity factor (see ***Figure 2.4.17***, ***Figure 2.4.18***) were constructed. The diagrams of plain specimens and plain specimens with interference fit show significant retardation of crack growth rate for small cracks in the specimens with interference fit, due to strengthening of the material around the hole. Furthermore, crack growth rate in these specimens was approximately an order of magnitude lower over almost the whole range of crack length. It should be noted that the cracks in these specimens propagated as a corner quarterelliptical crack up to the final fracture while plain specimens without interference fit had through cracks almost from initiation.

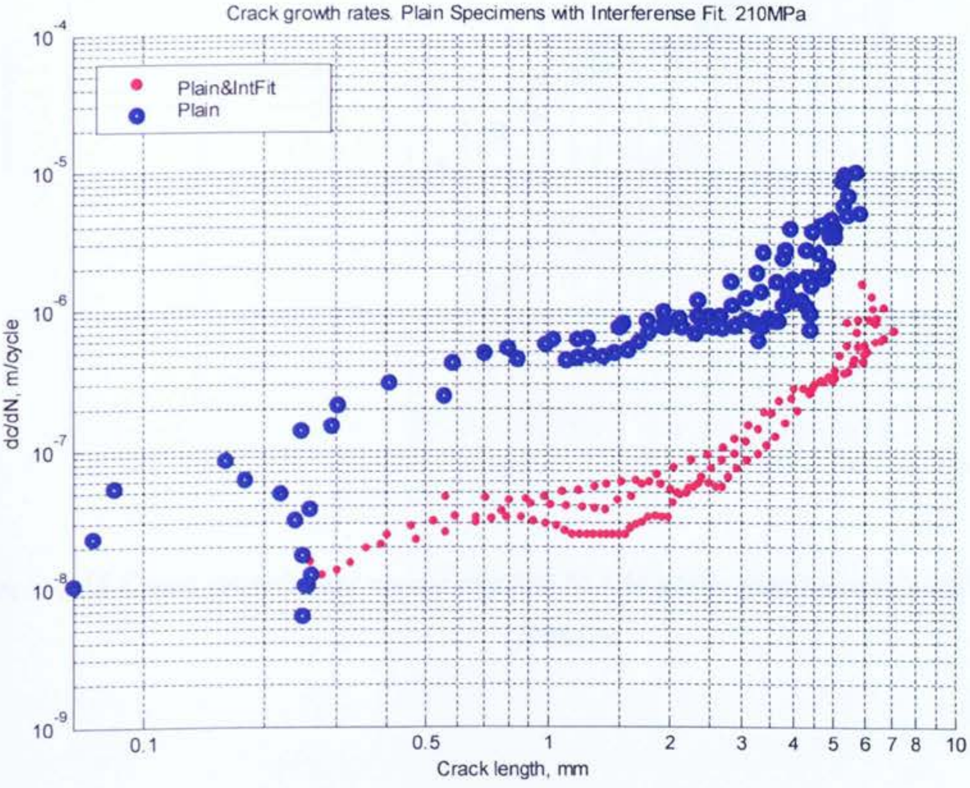

Figure 2.4.17 Crack growth rate versus crack length in plain specimences with interference fit at 210MPa

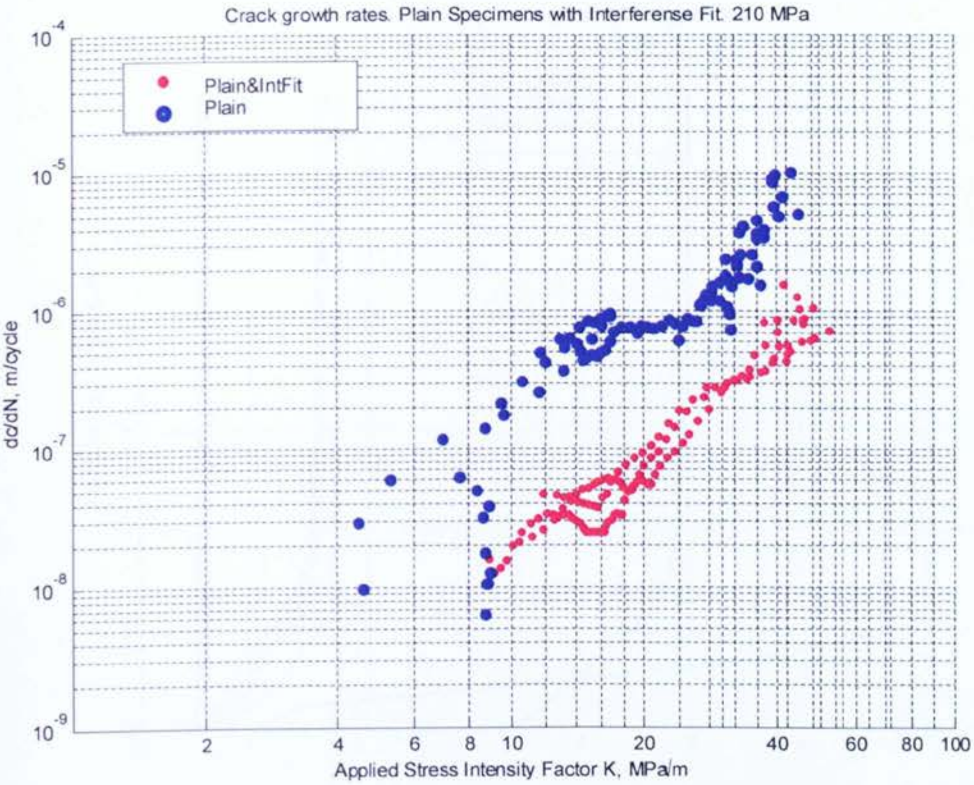

Figure 2.4.18 Crack growth rate versus applied SIF in plain specimences with interference fit at 210MPa

2.4.4 CX SPECIMENS

2.4.4.1 CRACK GROWTH ANALYSIS. CX SPECIMENS

7 CX specimens were tested in total: 2 at a net load of 200 MPa (gross load 160.3MPa) and 5 at a net load of 210 MPa (gross 168.3 MPa). Crack growth diagrams are given in ***Figure 2.4.19***

The figure shows the expected reduction in fatigue life at higher stress levels. Quantitative data on total life, crack initiation life, and crack propagation life, as well as observations of the surface crack form, crack symmetry and pictures of fracture surfaces are given in of the Appendix

The fatigue cracks initiated from the edges of the hole in the central cross section of the specimen. Observation of crack propagation features showed that the left and right branches of the fatigue crack always propagated from both edges of the hole as one dominant crack with a second (lagging) one. In these cases the cracks were assumed to be symmetrical.

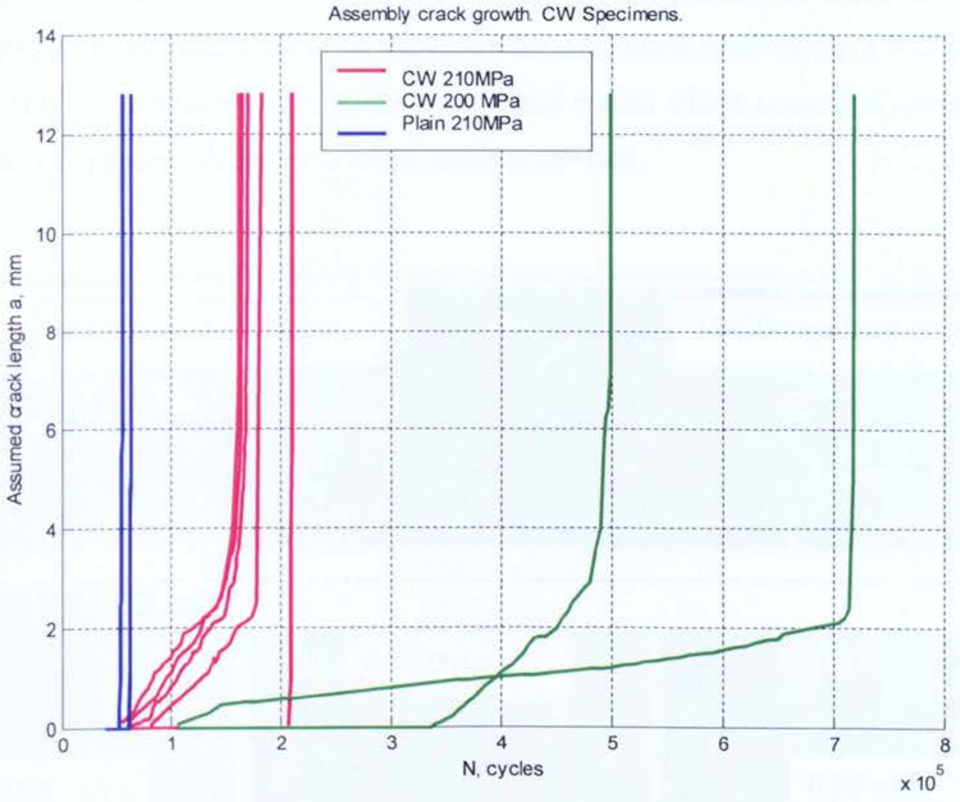

Figure 2.4.19 Crack growth curves. CX specimens.

Crack initiation also often took place by the emergence of two cracks from one edge of the hole (***Figure 2.4.20***). One of these eventually became the dominant crack.

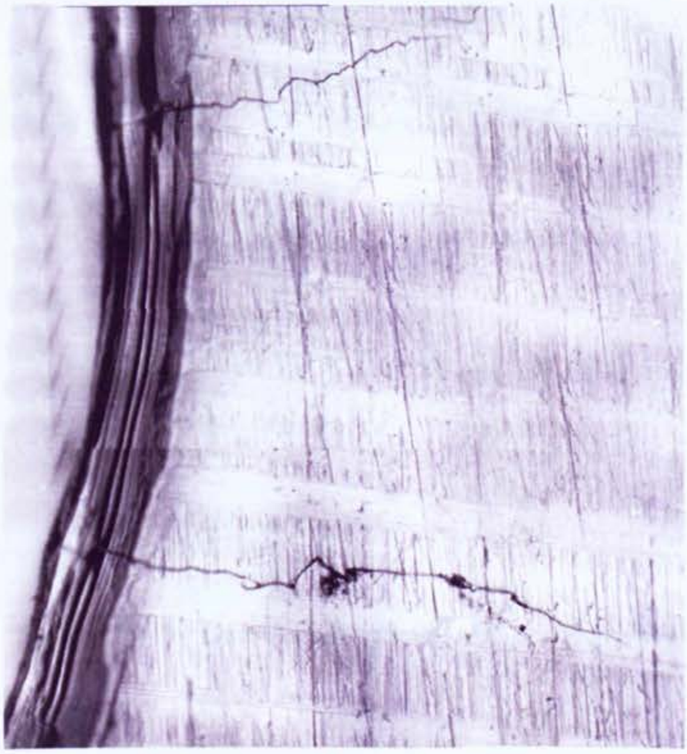

Figure 2.4.20 Two cracks initiating from the hole edge

Pre cracking of material a few microns in front of the tip of the dominant crack was observed (see ***Figure 2.4.21***). This was observed when the tip of the main crack was within 1.0 -3.0 mm from the edge of the hole i.e. approximately in the transitional region where compressive residual stresses created by the CX process change to tension residual stresses.

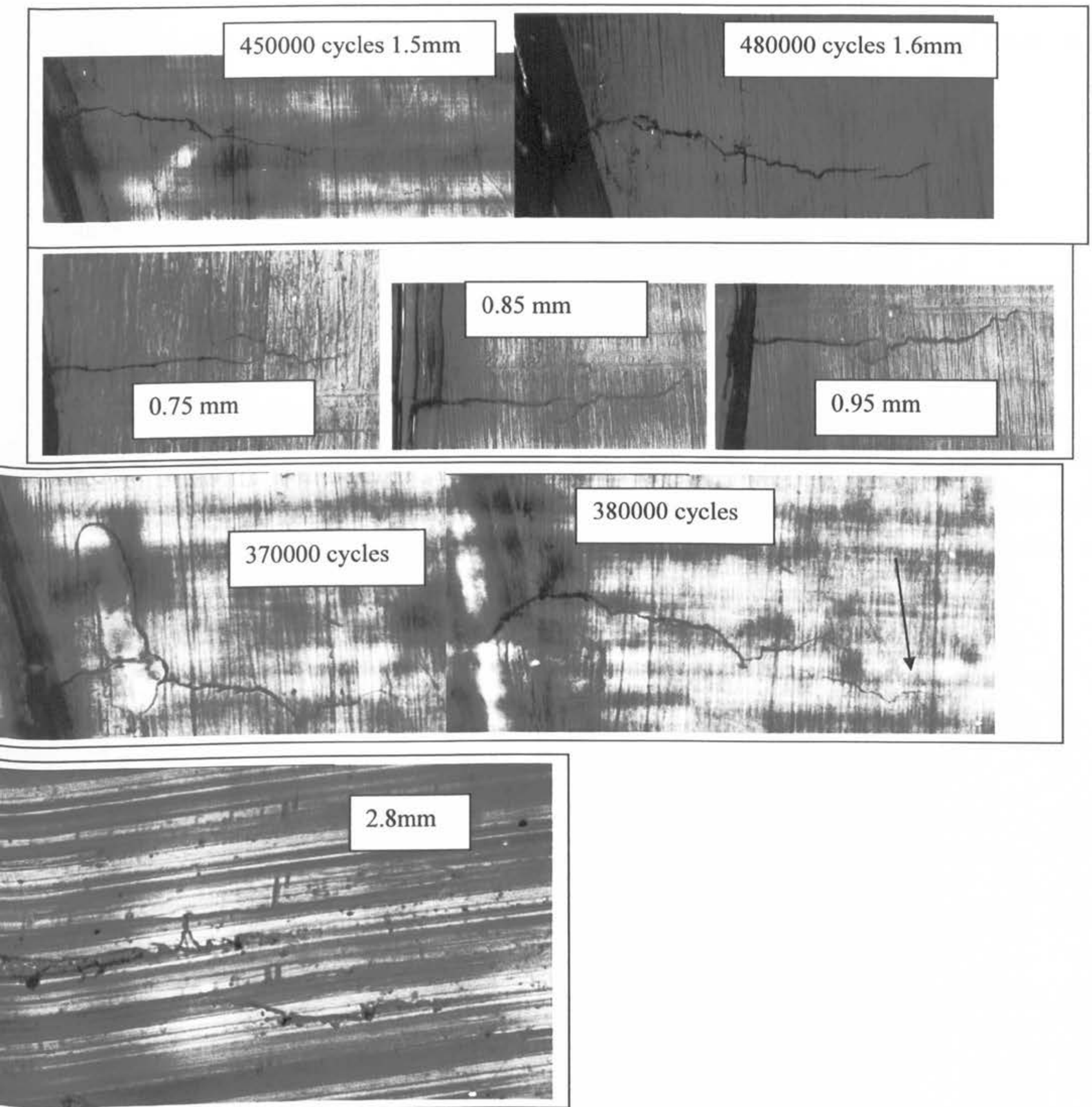

Figure 2.4.21 Emergence of material pre cracking

Possibly, material yielding in the zone of plasticity in front of the crack tip decreases the residual compressive stresses remaining after manufacture of the specimen and encouraged the pre cracking to take place. In addition to this, material may harden or soften with repeated loading which may cause some redistribution of any residual stresses. The effect of pre-cracking does not appear to be related to any material flaws in the specimens.

Analysis of the fracture surfaces left by fatigue crack growth (see fracture surfaces depicted in in appendix) and taking into account available solutions for SIF for similar types of cracks we observed the following crack types:

Symmetrical and asymmetrical through crack

Symmetrical and asymmetrical quarterelliptical corner crack

In the last two cases the ellipse axes relationship a/c were about 1.0-1.5.

Figure 2.4.22 illustrates particular features of cracks growing in CX specimens compared with cracks growing in plain specimens. Figure a) shows a symmetrical crack growing on the inlet side and growing through the thickness to final fracture for a CX specimen. Only one crack – the dominant one, was used for the calculation. Figure b) shows a crack growing in a plain specimen.

Analysing individual crack growth diagrams, it was concluded that virtually all cracks in CX specimens initiated on the inlet side, except in one case (Specimen 26). It confirms that the inlet sides of cold expanded specimens are more vulnerable to crack initiation which suggests there is a smaller compressive residual stress on that side.

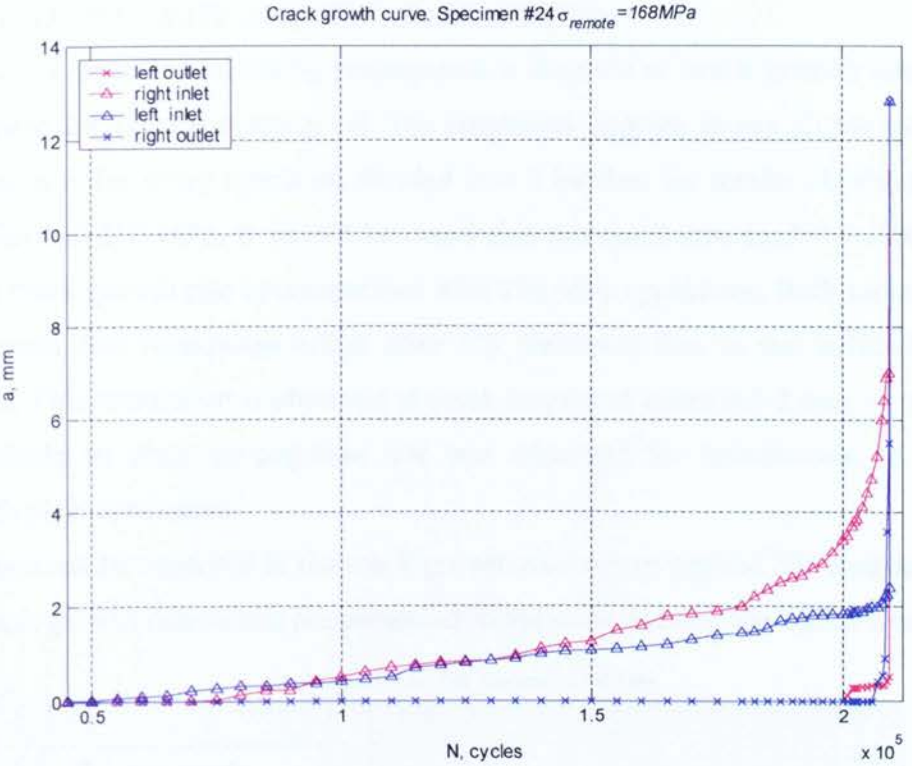

a)

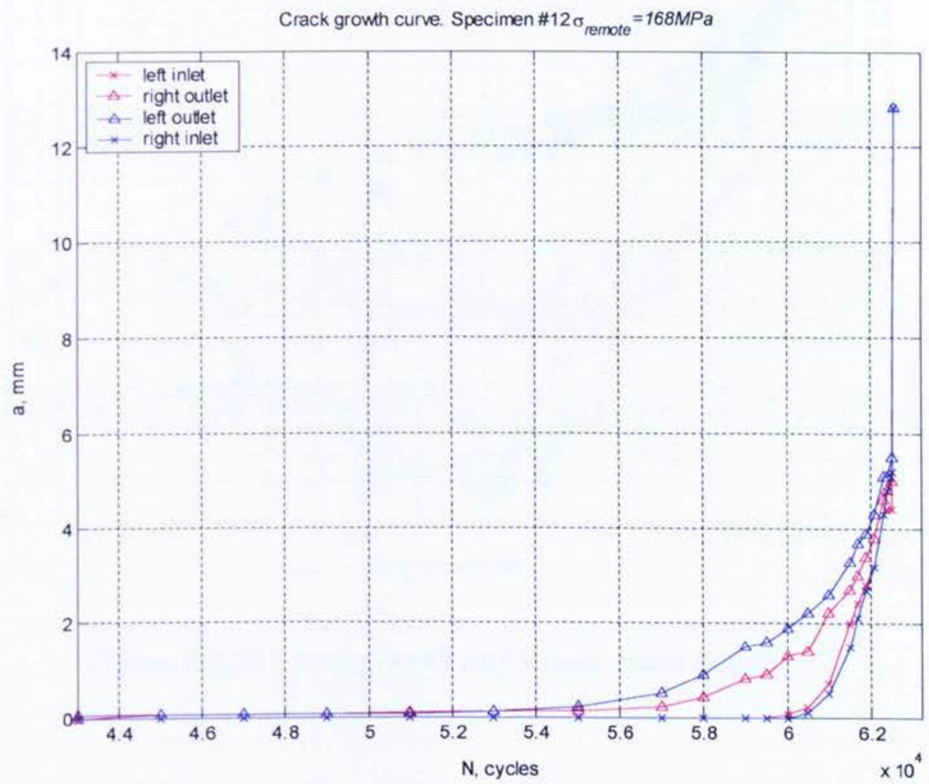

b)

Figure 2.4.22 Typical crack growth diagrams for CX specimens –a) and plain b)

2.4.4.2 CRACK GROWTH RATE ANALYSIS. CX SPECIMENS

To assess the crack growth rate during propagation a diagram of crack growth rate versus crack length (see ***Figure 2.4.23***) was constructed. The combined diagram shows all the individual crack growth rate diagrams for every specimen divided into 2 batches for results obtained at 200 MPa and those obtained at 210 MPa. It should be noted that the specimens loaded at 200 MPa have a clearly reduced crack growth rate in comparison with 210 MPa specimens. Both samples exhibit the same crack growth rate retardation effect after CX treatment due to the induced compressive residual stresses. This retardation is observed at crack lengths of about 0.3-2 mm. A reduction of an order of magnitude in crack propagation rate was observed for interference fit specimens in comparison with plain specimens.

The same features can be observed in the crack growth rate versus applied SIF diagram (see ***Figure 2.4.24***). The crack growth rate results are presented in the same manner for 200MPa and 210MPa.

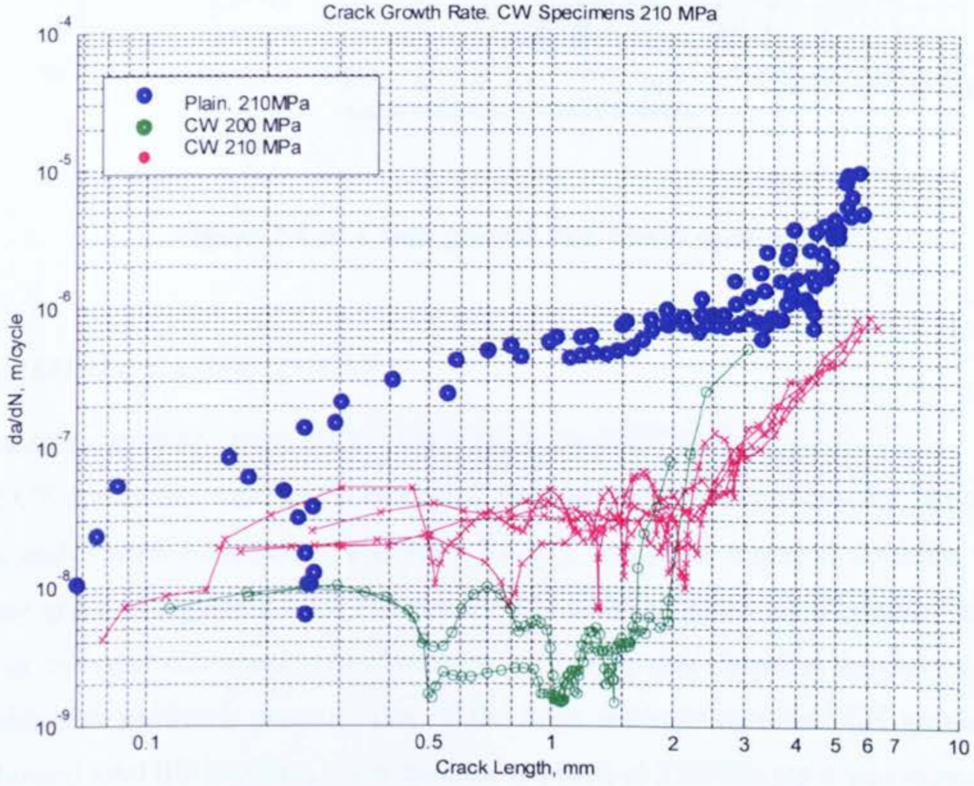

Figure 2.4.23 Crack growth rate versus crack lengthz

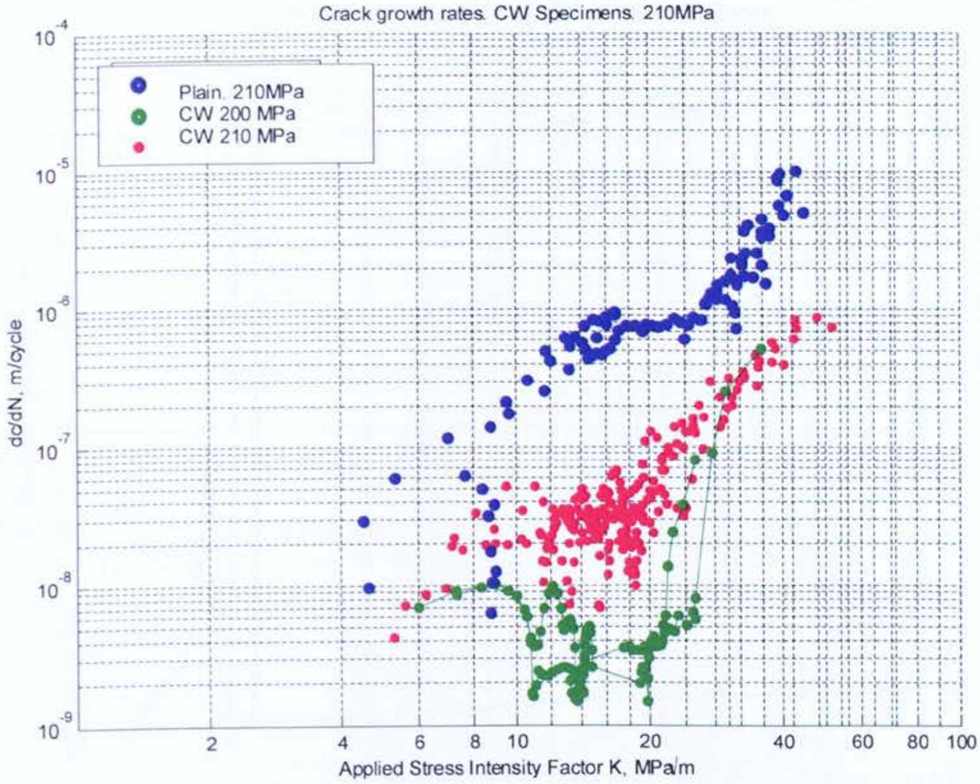

Figure 2.4.24 Crack growth rate versus applied SIF

2.4.5 CORRODED CX SPECIMENS

2.4.5.1 CRACK GROWTH ANALYSIS. CORRODED CX SPECIMENS

4 corroded CX specimens were tested in total. 2 were subjected to corrosion for 72 hours and tested at 210MPa and 2 were subjected to corrosion for 173 hours and tested at 200MPa. Crack growth diagrams are given in ***Figure 2.4.25***. The results shown in the figure reveal improvement in fatigue life even in corroded CX specimens compared with plain non corroded specimens. On the other hand, considerable scatter is present– one of the most severely corroded CX specimens tested at 200MPa showed total life less than plain specimens tested at 210MPa (as it was expected), although another showed greater life than corroded 72 hrCX specimens tested at 210MPa.

Quantitative data on total life, crack initiation life, and crack propagation life, as well as observations of the surface crack form, crack symmetry and pictures of fracture surfaces are given in of the Appendix.

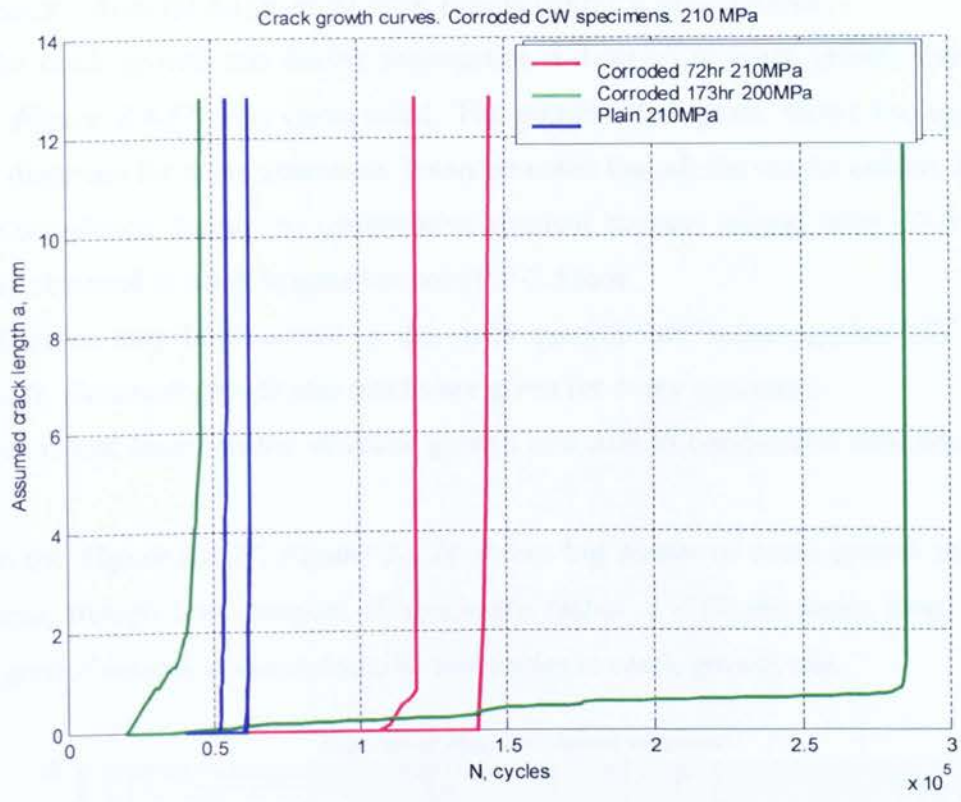

Figure 2.4.25 Crack growth curves. Corroded CX specimens.

A photograph of corrosion pits on the surface near the hole in the specimen is shown in Figure 2.4.26

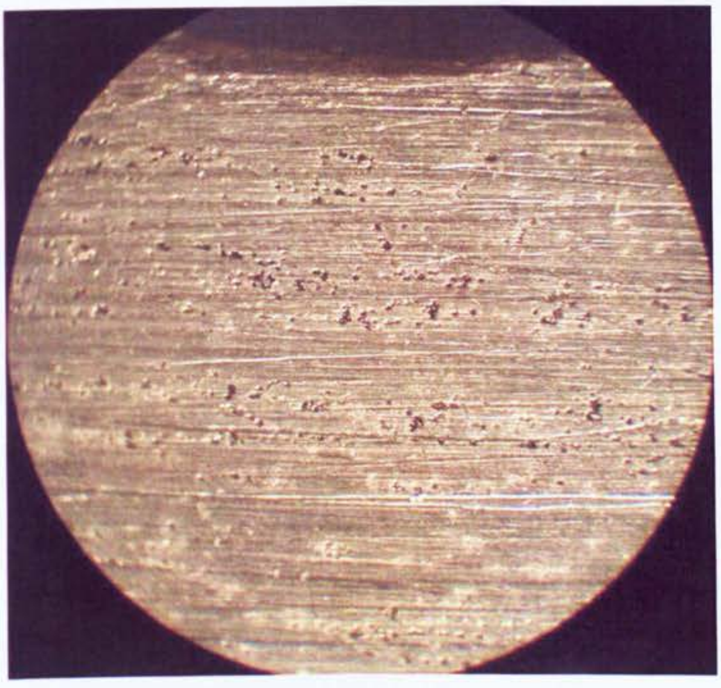

Figure 2.4.26 Typical corrosion pits on the surface of specimens after 72 hrs immersion in 3.5% NaCl solution

2.4.5.2 CRACK GROWTH RATE ANALYSIS. CORRODED CX SPECIMENS

To assess the crack growth rate during propagation a diagram of crack growth rate versus crack length (see ***Figure 2.4.27***) was constructed. The combined diagram shows the individual crack growth rate diagrams for every specimen. It can be noted that all the results exhibit the same crack growth rate retardation due to the compressive residual stresses arising from CX treatment. The retardation is observed at crack lengths between 0.5-2.5 mm.

The same features may be observed in the crack growth rate versus applied SIF diagram (see ***Figure 2.4.28***). The crack growth rate results are given for every specimen.

The diagrams reveal larger scatter of crack growth rate data in comparison with non corroded CX specimens.

Diagrams in the ***Figure 2.4.27***, ***Figure 2.4.28*** shows big scatter of crack growth rate in corroded CX specimens, though both samples of specimens tested at different stress level and subjected different degree of corrosion showed similar tendencies in crack growth rate.

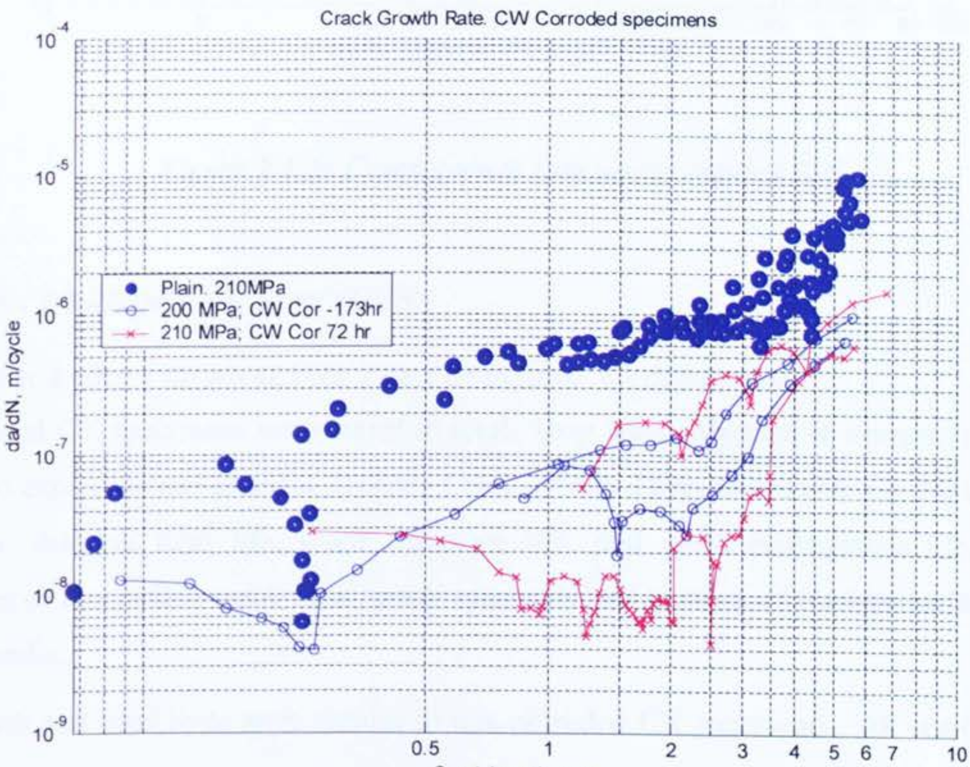

Figure 2.4.27 Crack growth rate versus crack length

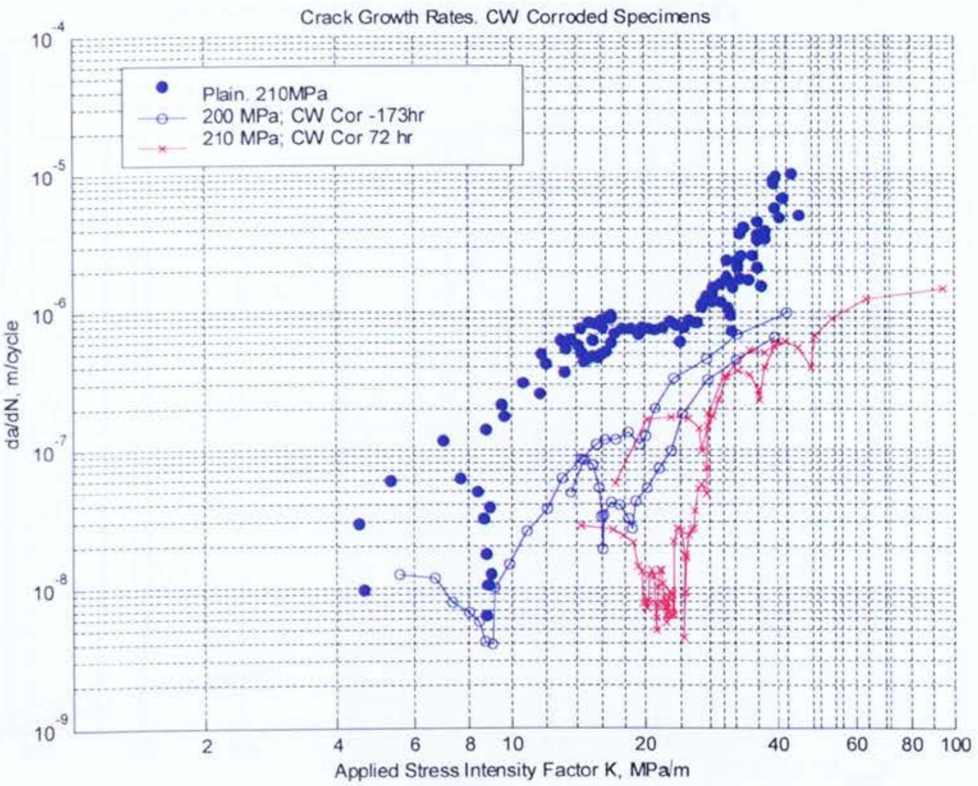

Figure 2.4.28 Crack growth rate versus applied SIF

2.4.6 PRE CORRODED CX SPECIMENS

2.4.6.1 CRACK GROWTH ANALYSIS. PRE CORRODED CX SPECIMENS

3 pre corroded CX specimens were tested in total. They were subjected to corrosion for 72 hours prior to cold expansion and tested at 210MPa Crack growth diagrams are given in ***Figure 2.4.29*** Quantitative data on total life, crack initiation life, and crack propagation life, as well as observations of the surface crack form, crack symmetry and pictures of fracture surfaces are given in in Appendix.

Crack growth and total lives were similar to non corroded CX specimens. All corrosion damage was effectively removed by the reaming procedure during the CX process. Thus damage was eliminated from the area around the hole which is more vulnerable to crack initiation.

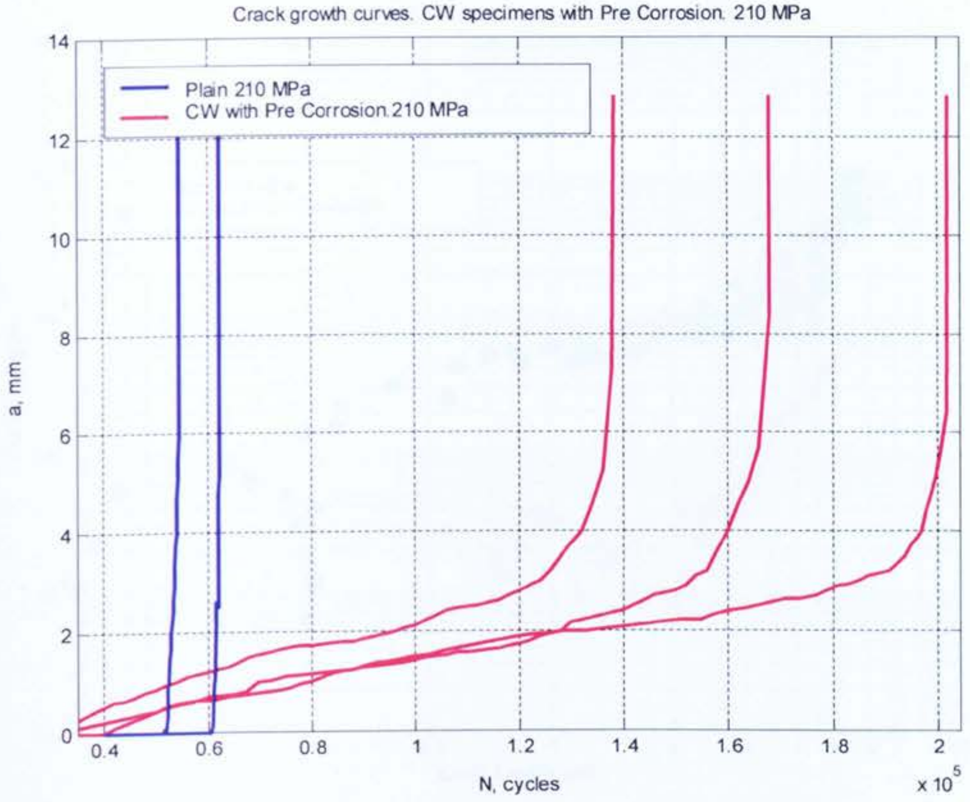

Figure 2.4.29 Crack growth curves. Pre corroded CX specimens.

2.4.6.2 CRACK GROWTH RATE ANALYSIS. PRE CORRODED CX SPECIMENS

To assess the crack growth rate during the crack propagation a diagram of crack growth rate versus crack length (see ***Figure 2.4.30***) was constructed. The combined diagram shows all the individual crack growth rate diagrams of every specimen. These diagrams show the same crack growth rate retardation tendency as before due to compressive residual stresses after CX treatment. The retardation is observed at crack lengths of about 0.3-2.5 mm.

The same features may be observed in the crack growth rate versus applied SIF diagram (see ***Figure 2.4.31***)

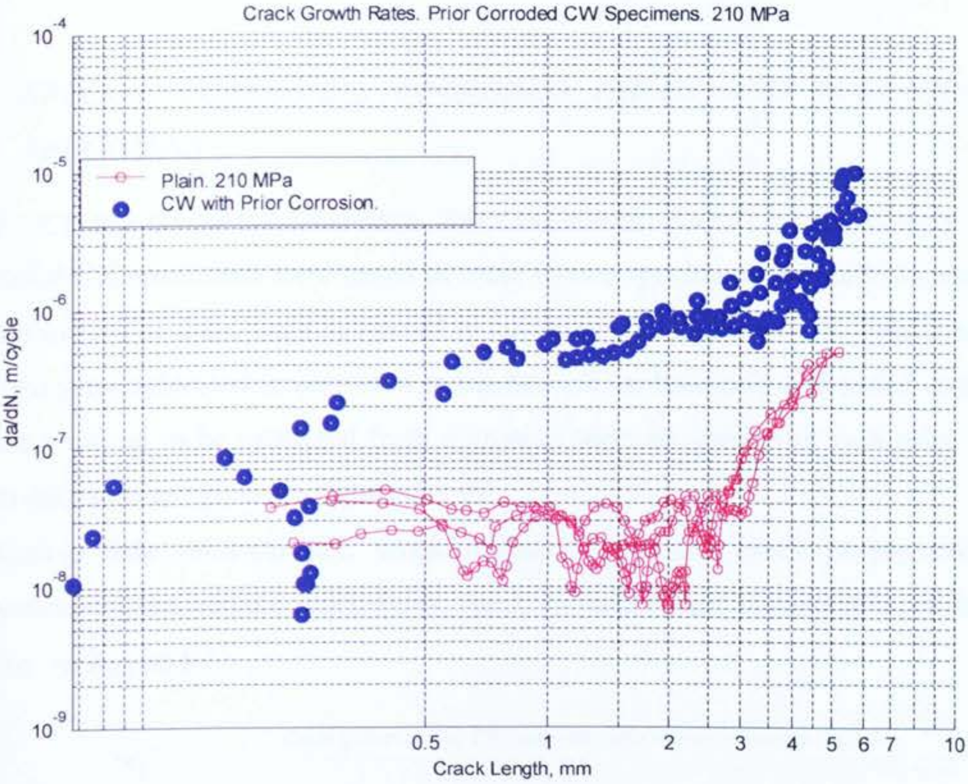

Figure 2.4.30 Crack growth rate versus crack length

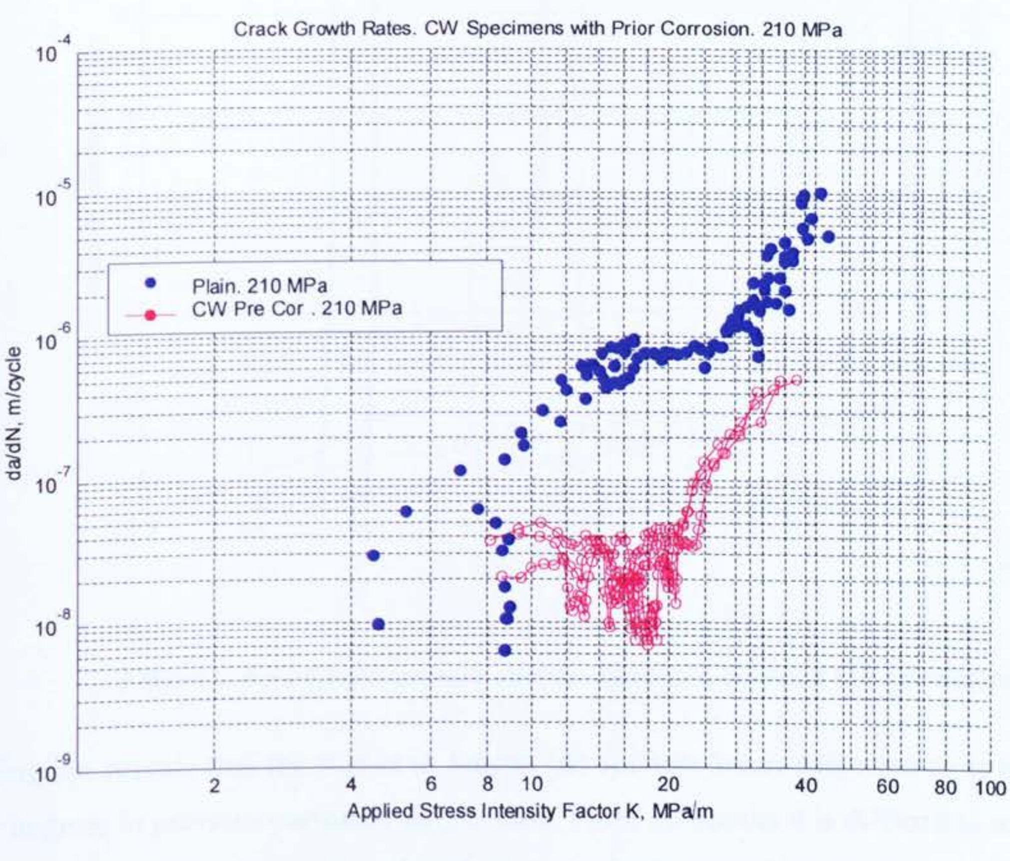

Figure 2.4.31 Crack growth rate versus applied SIF

2.4.7 SPECIAL CORROSION. CORRODED HOLES AND SURFACES OF ONLY CX SPECIMENS

2.4.7.1 CRACK GROWTH ANALYSIS. SPECIAL CORROSION CX SPECIMENS

4 corroded CX specimens were tested in total. In two specimens the surfaces, excluding the bore of the hole of two of them were subjected to corrosion for 72 hours and then tested at 210MPa. The other two were subjected to corrosion in the bore of the hole only and tested at the same stress. The surfaces required to be protected from corrosion were covered with wax prior to exposure. Crack growth diagrams are given in ***Figure 2.4.32***

Quantitative data on total life, crack initiation life, and crack propagation life, as well as observations of the surface crack form, crack symmetry and photographs of fracture surfaces are given in in Appendix

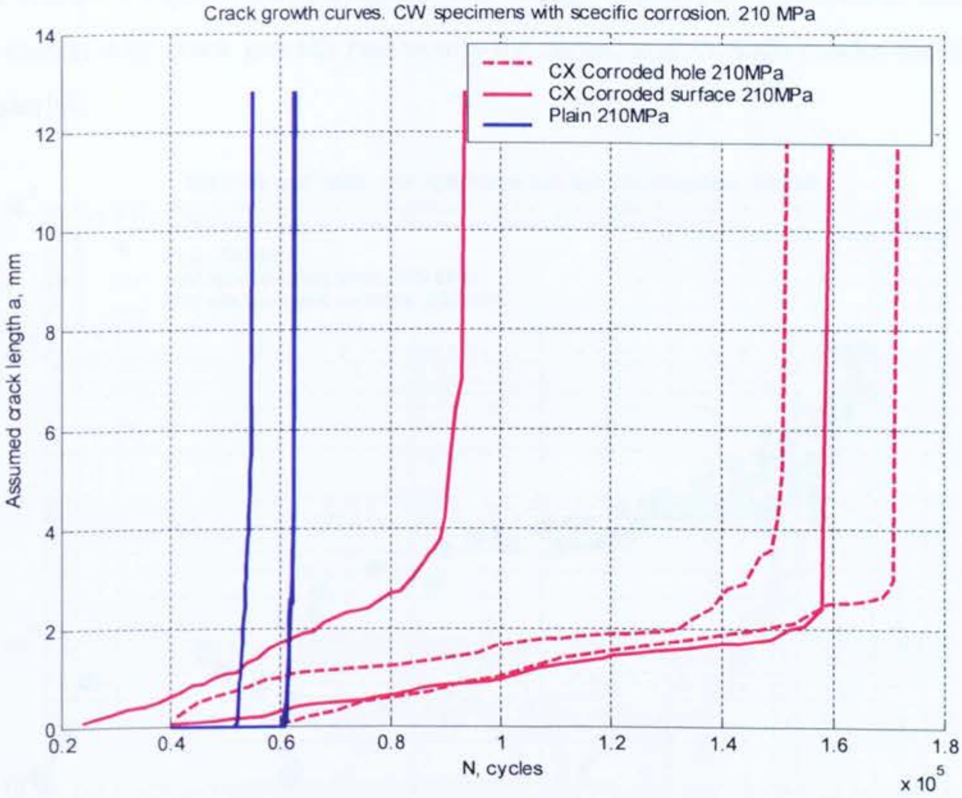

Figure 2.4.32 Crack growth curves. Special Corroded CX specimens.

The diagram reveals that the scatter in fatigue life for specimens subjected to special corrosion is rather large as in previous corrosion fatigue data. From the results it is difficult to assess which type of corrosion, i.e. that on the external surfaces or in the bore of the hole, has a greater influence on crack initiation and propagation.

2.4.7.2 CRACK GROWTH RATE ANALYSIS. SPECIAL CORROSION CX SPECIMENS

To assess the crack growth rate during crack propagation a diagram of CGR versus crack length (see ***Figure 2.4.33***) was constructed. The combined diagram shows all the individual CGR diagrams for each specimen. It can be noted that all results show the same CGR retardation tendency owing to compress residual stresses after CX treatment. This retardation is observed at crack lengths between about 0.5mm to 1.5 mm. It can be noted that CGR in specimens with corroded surfaces is marginally higher than in specimens with corroded holes but from the figure it can be seen that the crack growth rates for these two types of corrosion can be assumed to be approximately equal.

The same is true for the crack growth rate versus applied SIF diagram (see ***Figure 2.4.34***). The crack growth rate results are given for every test specimen. It was noted that cracks in these specimens grew with rather pronounced asymmetry in terms of inequalities of crack branch lengths and the types of cracks formed in the branches. For example, the left crack could propagate as a corner crack while the right crack propagated as a through crack from initiation to final failure. This is the main reason why crack growth rate points for corner and through cracks are so different for the same material.

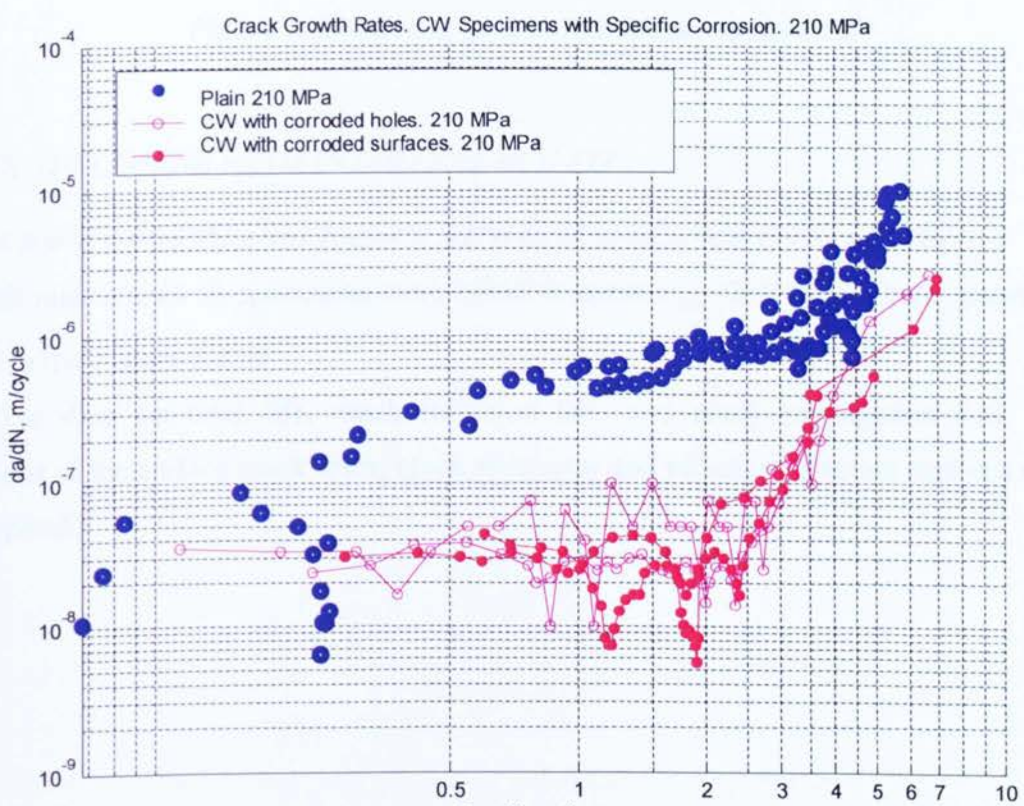

Figure 2.4.33 Crack growth rate versus crack length

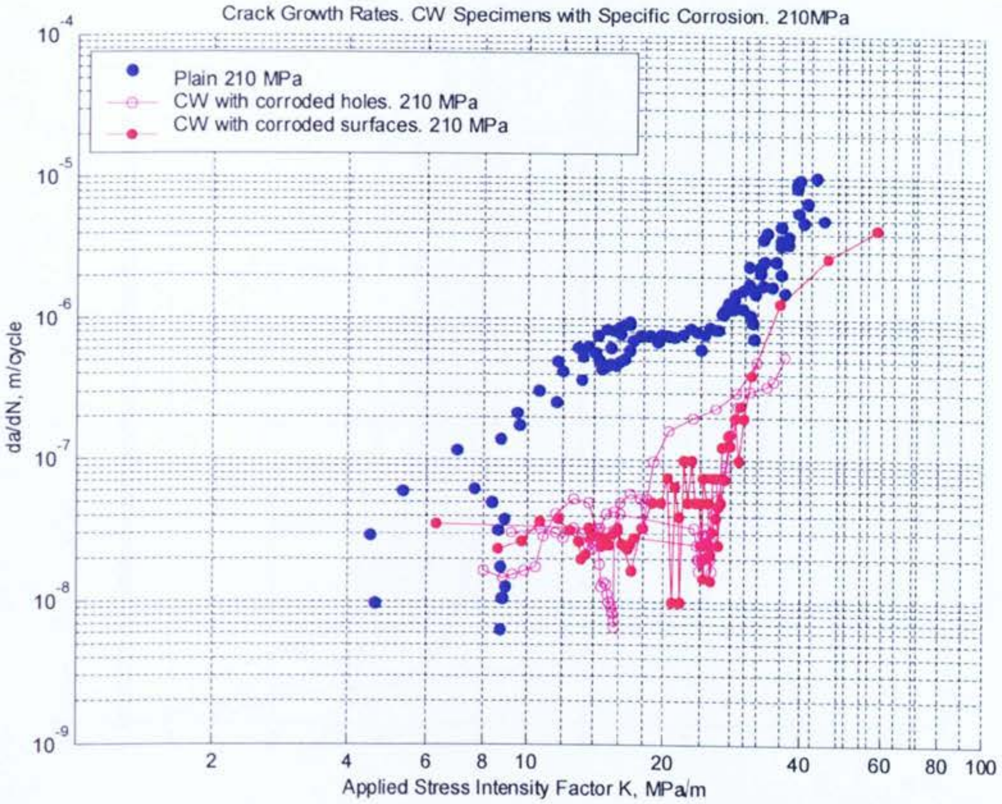

Figure 2.4.34 ***Crack growth rate versus applied SIF***

2.4.8 CX SPECIMENS WITH INTERFERENCE FIT

2.4.8.1 CRACK GROWTH ANALYSIS. CX WITH INTERFERENCE FIT SPECIMENS

6 CX with interference fit specimens were tested at stress σ_{net}=210 MPa. Crack growth diagrams are given in the ***Figure 2.4.35***

Quantitative data on total life, crack initiation life, and crack propagation life, as well as observations of the surface crack form, crack symmetry and picture of fracture surfaces are given in of the Appendix

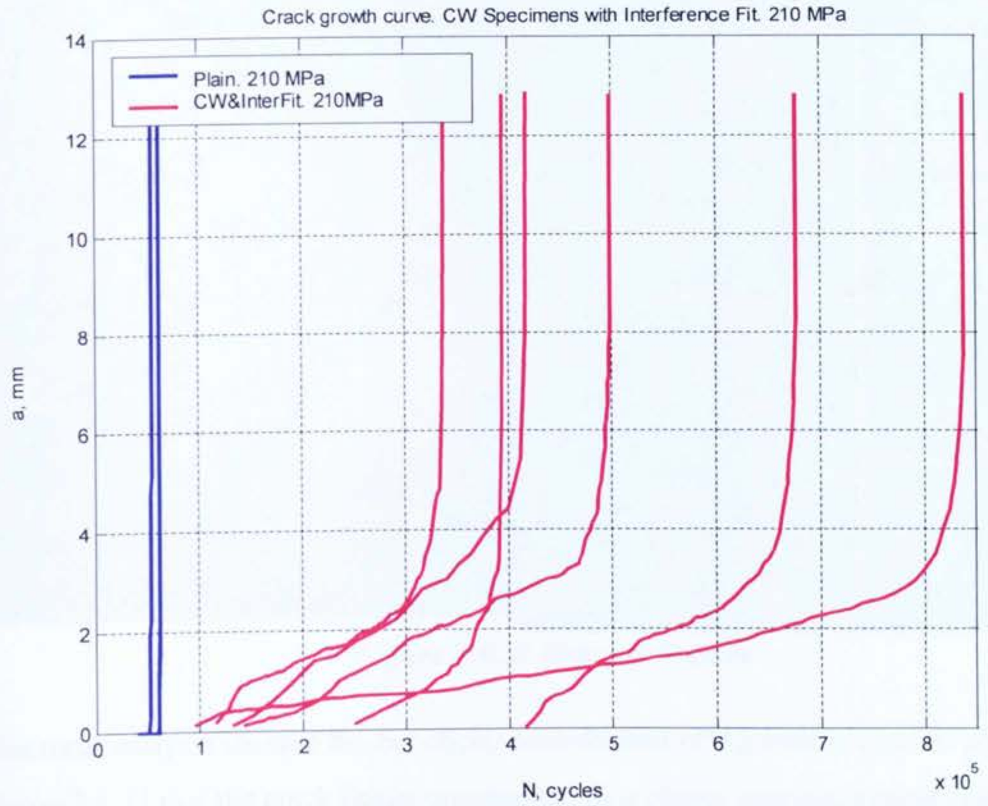

Figure 2.4.35 Crack growth curves. CX with interference fit specimens

It will be noted that in all cases cracks were assumed to be single asymmetrical cracks, though sometimes cracks initially nucleated at both sides of hole but in these cases the secondary crack stopped or its propagation was substantially slower than the dominant crack. All cracks did not start in the central section line, which supposed to be the weakest section, but at the edge if the hole slightly away from of the centre line (see ***Figure 2.4.36***). The weakest section should be at the centre line section but this is influenced by the insertion of the oversized titanium pin. The pin is much harder than Al and has a higher modulus so it doesn't deform as much when specimen is under tensile load. The hole elongates under tensile load in the longitudinal direction and contracts in the transverse direction but the pin resists this contraction thus introducing additional compressive stresses in central section. Hence the weakest section is shifted away from the central section.

In addition it was noted that cracks nucleated on the outlet faces of 4 specimens from the 6 tested. This indicates that a considerable redistribution of residual stresses occurred after the insertion of the pin in the cold expanded hole and following the fatigue load application.

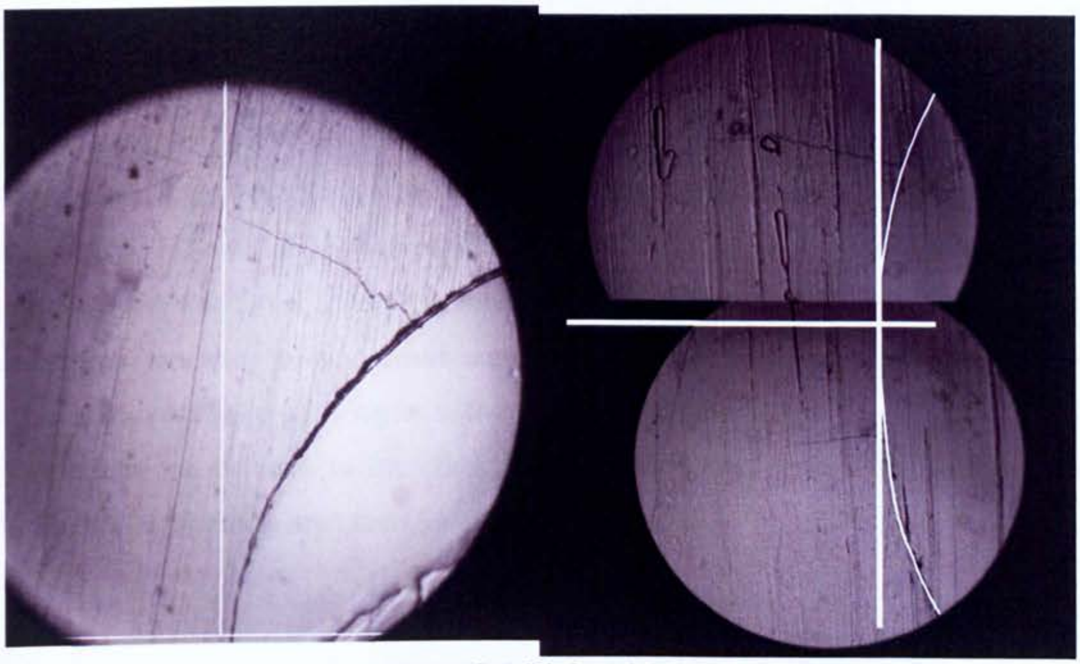

Figure 2.4.36 Crack initiation

Macrofractural analysis showed the beneficial contribution of the interference fit pin. It can be seen from Figure 2.4.37 that the crack began propagating as a corner quarterelliptical crack, but the crack growth rate in the radial direction was considerably faster than through the bore.

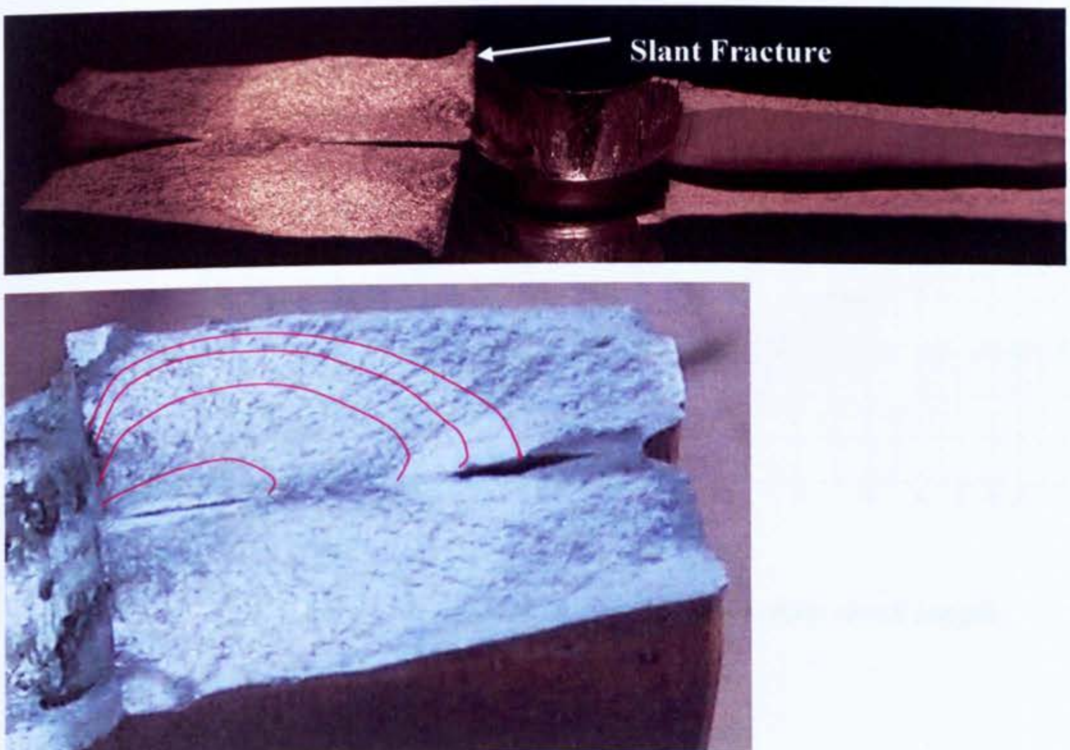

Figure 2.4.37 Macromorphologies of fracture surface in CX specimen with interference fit pin.

Eventually, the part of the crack front propagating along the bore was arrested and continued to grow through the reduced strength area away from the bore. The slant fracture surface at the corner opposite the crack initiation site indicated that the fatigue crack did not penetrate through the thickness along the bore.

2.4.8.2 CRACK GROWTH RATE ANALYSIS. CX WITH INTERFERENCE FIT SPECIMENS

To assess the crack growth rate during the crack propagation a diagram of crack growth rate versus crack length (see ***Figure 2.4.38***) was constructed. The diagram shows individual crack growth rate diagrams for every specimen. It can be noted that not all the results show the same crack growth rate retardation tendency arising from compressive residual stresses after CX treatment. The retardation is observed at crack lengths between about 0.2mm – 3mm.

The same effect can be seen in the crack growth rate versus applied SIF diagram (see ***Figure 2.4.39***). The CGR diagrams are given for every specimen.

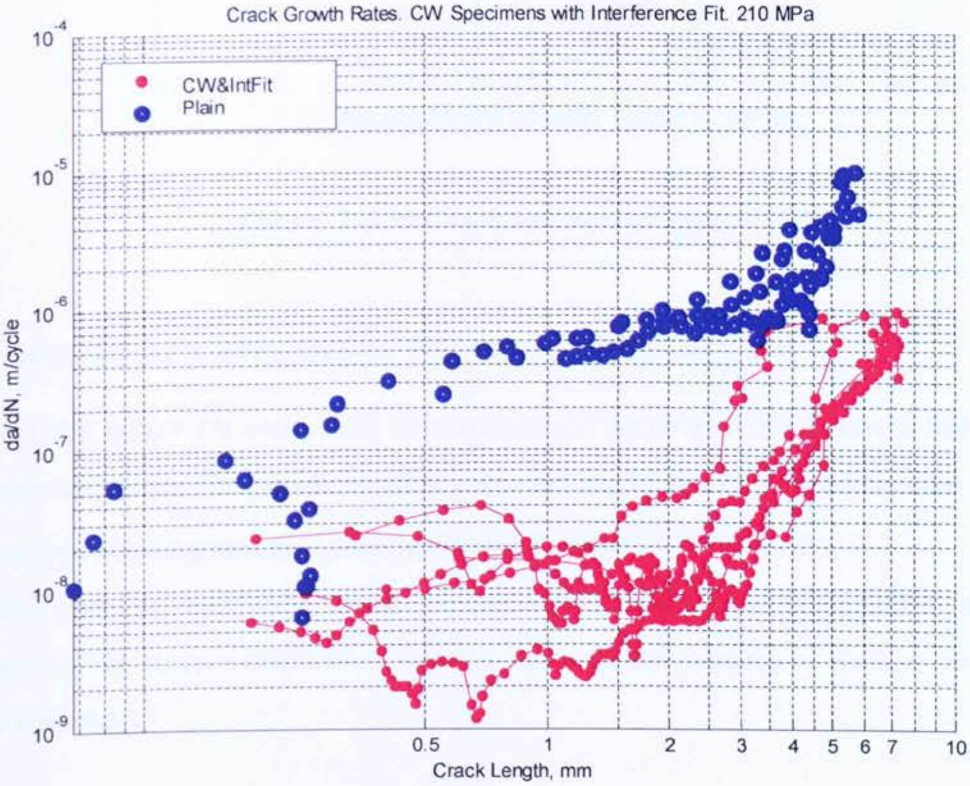

Figure 2.4.38 Crack growth rate versus crack length

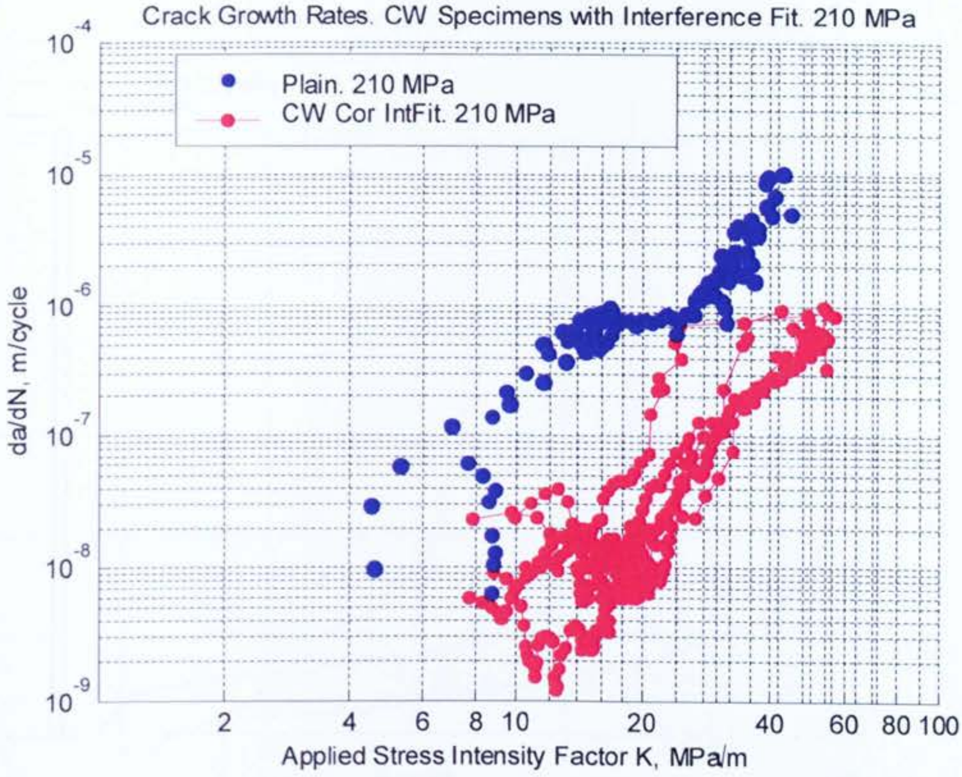

Figure 2.4.39 Crack rate versus applied SIF

2.4.9 CORRODED CX SPECIMENS WITH INTERFERENCE FIT

2.4.9.1 CRACK GROWTH ANALYSIS. CORRODED CX WITH INTERFERENCE FIT SPECIMENS

3 CX with interference fit specimens were corroded for 72 hrs and tested at a net stress σ_{net}=210 MPa. Crack growth diagrams are given in ***Figure 2.4.40***

Quantitative data on total life, crack initiation life, and crack propagation life, as well as observations of the surface crack form, crack symmetry and pictures of fracture surfaces are given in of the Appendix

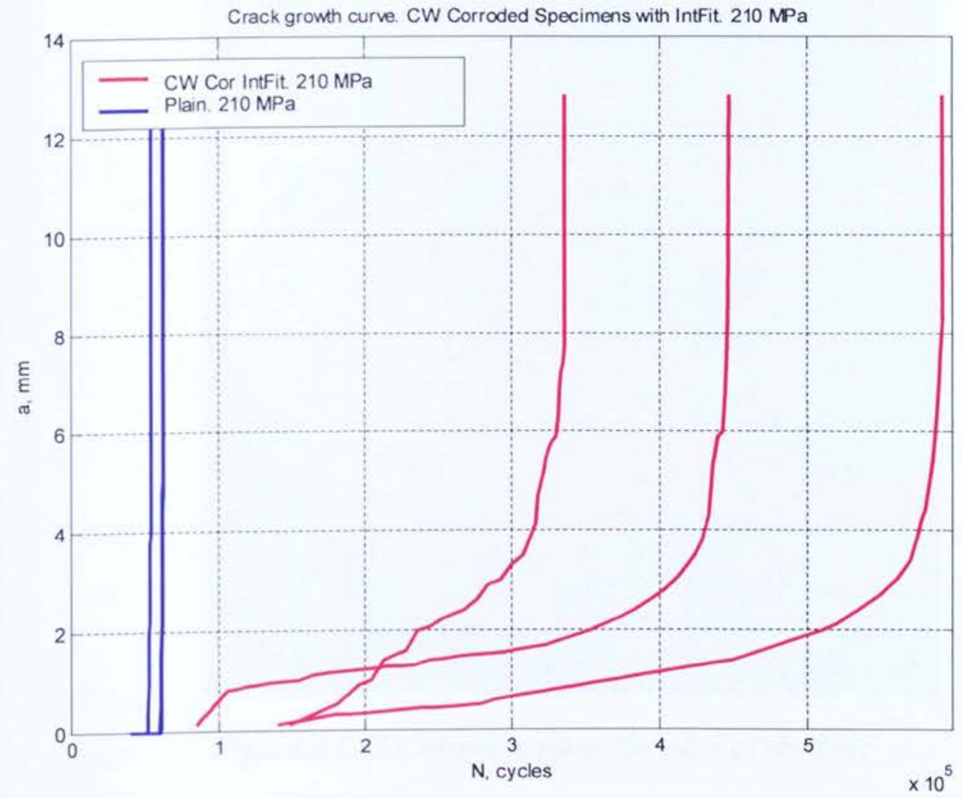

Figure 2.4.40 Crack growth curves. Corroded CX with interference fit specimens

Photographs illustrating corrosion pits at the edge of a hole with a pin are presented in ***Figure 2.4.41***, ***Figure 2.4.42***. The pits acted as initiation sites. **No cracks initiated from corrosion pits away from the hole.** The same tendency of crack initiation at the edge of the hole at some distance from the central line was observed as in all interference fit specimens tested previously. It is to be noted that the corrosion pits at the edge of the hole were quite serious stress concentrators and often cracks were initiated from them in four corners at the same time. Typical pictures of the process are shown in Figure 2.4.43. Initially 4 corner quarterelliptical cracks were initiated but later only one became dominant and the others arrested.

The shape of the cracks is of particular interest. The photograph reveals that the crack grew quicker in the lateral direction and slower in the bore thus forming not an exact quarterelliptical crack front but a shape similar to a quarter of a trefoil petal 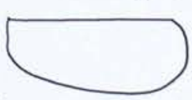 This occurs due to the strengthening of material near the edge of the hole from interference fit effects.

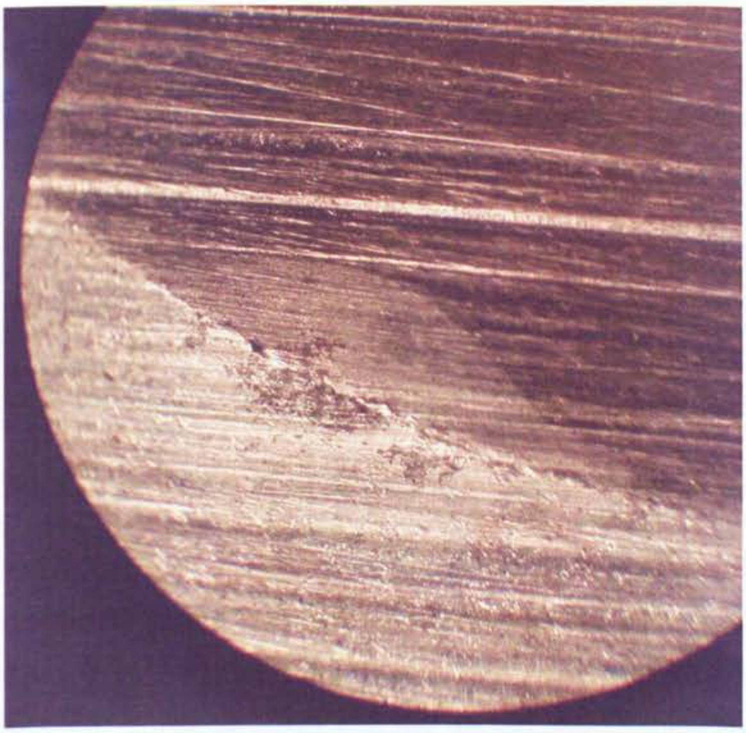

Figure 2.4.41 Corrosion pit at the edge of the hole

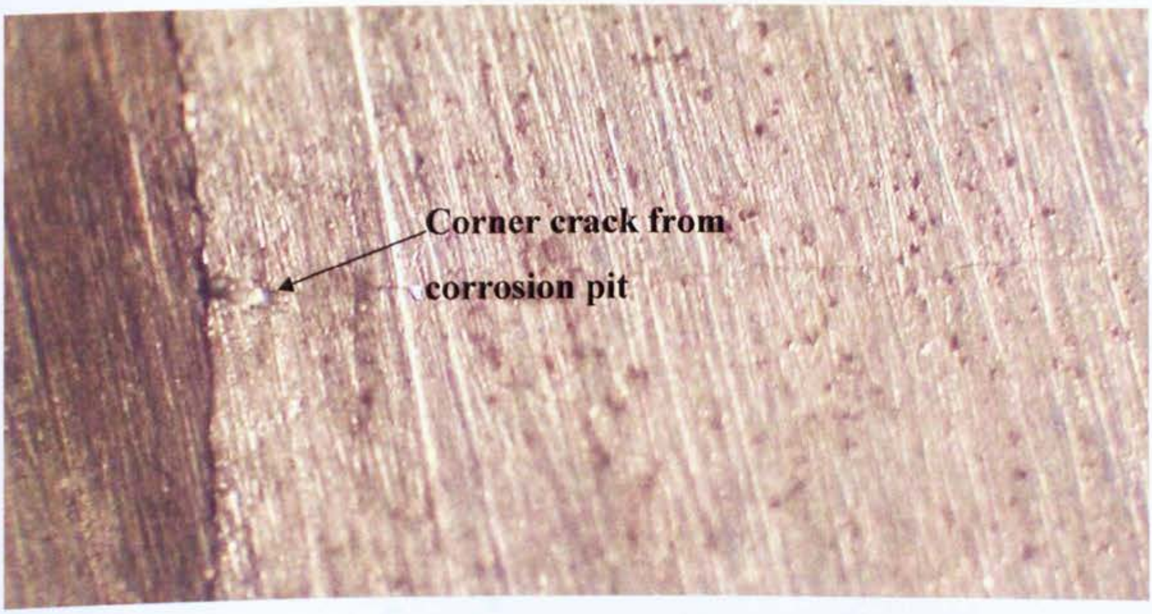

Figure 2.4.42 Crack initiation from a corrosion pit

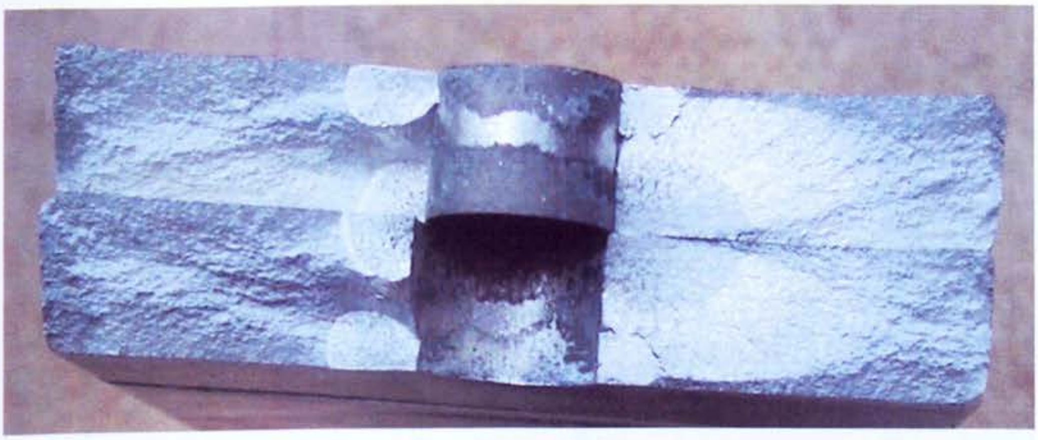

Figure 2.4.43 Crack front shapes in a corroded CX specimen with interference fit

2.4.9.2 CRACK GROWTH RATE ANALYSIS. CX SPECIMENS WITH INTERFERENCE FIT

To assess the crack growth rate during the crack propagation a diagram of crack growth rate versus crack length was constructed. (see ***Figure 2.4.44***) The diagram shows individual crack growth rate diagrams for every specimen. It can be noted that not all the results show the same crack growth rate retardation tendency arising from compressive residual stresses after CX treatment. The retardation is observed at crack lengths between about 0.2mm – 2.5mm.

The same effect can be seen in the crack growth rate versus applied SIF diagram (see ***Figure 2.4.45***).

The diagrams have similar features to previous crack growth rate diagrams

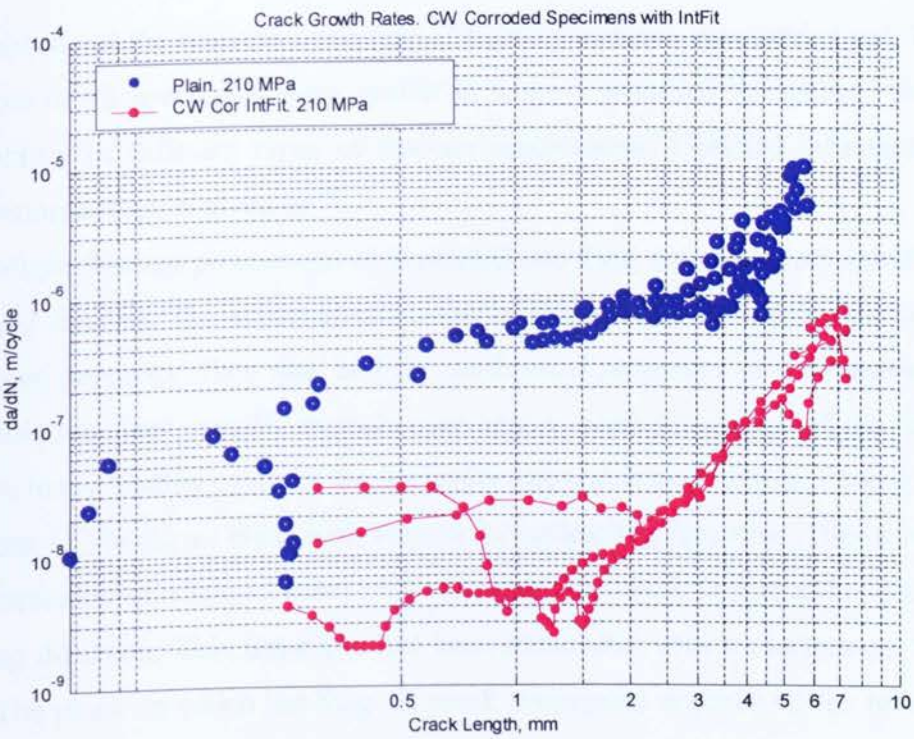

Figure 2.4.44 Crack growth rate versus crack length

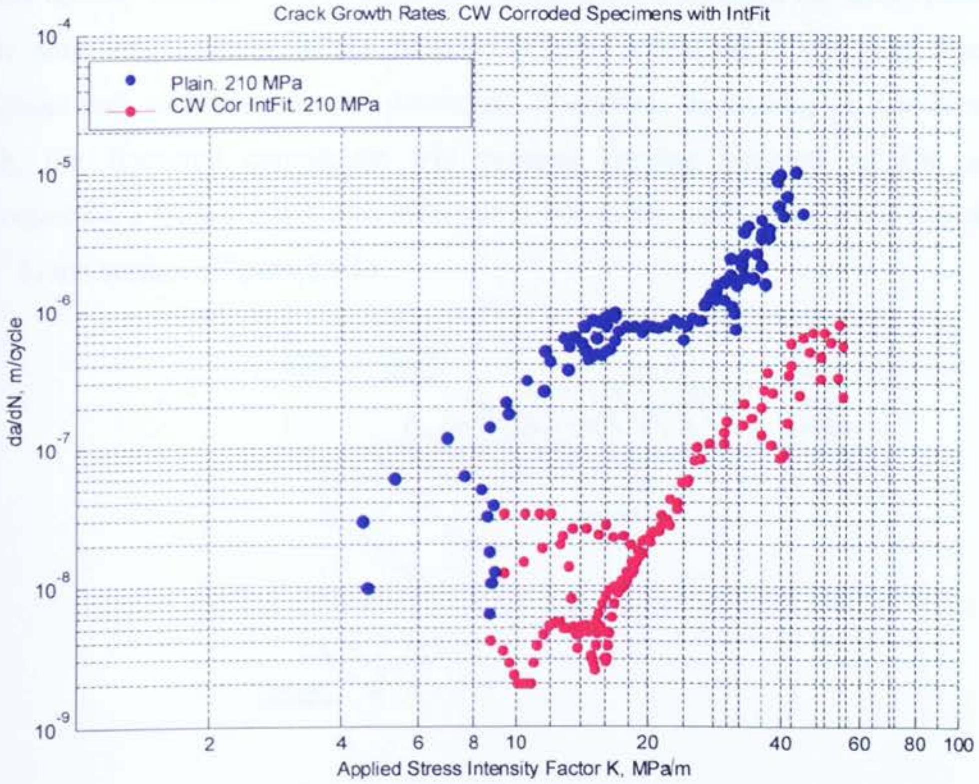

Figure 2.4.45 Crack rate versus applied SIF

2.5 MACROMORPHOLOGIES OF FRACTURE SURFACES

An analysis of the macromorphology of fracture surfaces was carried out. It revealed that fracture surfaces of all specimens were similar in form, a so-called "propeller" shape. This characterises availability of different types of fracture mechanisms. Detailed information on fracture surface macromorphology is given in [105]

The fatigue fracture process can be separated into three regimes: crack initiation, crack propagation, and final fracture. The existence and extent of these stages depends on the applied stress conditions, specimen geometry, flaw size, and the mechanical properties of the material. Stage I, representing the initiation stage, usually extends over only a small percentage of the fracture surface but may require many loading cycles if the nucleation process is slow. Often, Stage I cracks assume an angle of about 45° in the *xy* plane with respect to the loading direction. After a relatively short distance, the orientation of a Stage I crack shifts to permit the crack to propagate in a direction normal to the loading direction. This transition has been associated with a changeover from single to multiple slip. The plane on which the Stage II crack propagates depends on the relative stress state; that is, the extent of plane-strain or plane-stress conditions. When the stress intensity factor range is low (resulting from a low applied stress and/or small crack size), a small plastic zone is developed. When the sheet thickness is large compared to this zone size, plane-strain conditions prevail and flat fracture usually results. With subsequent fatigue crack extension, the stress intensity factor and the plastic zone size increase. When the zone is large compared to specimen thickness, plane-stress conditions and slant fracture are dominant. Therefore, depending on the stress level and crack length, the fractured component will possess varying amounts of flat and slant fracture. Consequently, a fatigue crack may start out at 90° to the plate surface but complete its propagation at 45° to the surface (Figure 2.5.1)

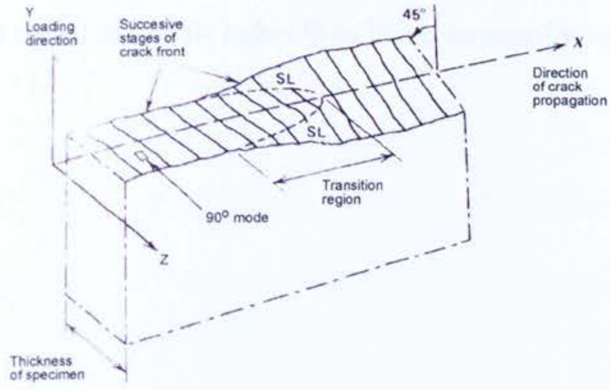

Figure 2.5.1 Transition zone

Alternatively, the crack could propagate immediately at 45° if the plastic zone size to plate thickness ratio were high enough, reflecting plane-stress conditions. It is important to recognize that both unstable, fast-moving cracks and stable, slow-moving fatigue cracks may assume flat, slant, or mixed macromorphologies.

Fracture surfaces of all specimens tested clearly revealed the flat macromorphology during growth of the fatigue crack and slant morphology at final fracture see Figure 2.5.2.

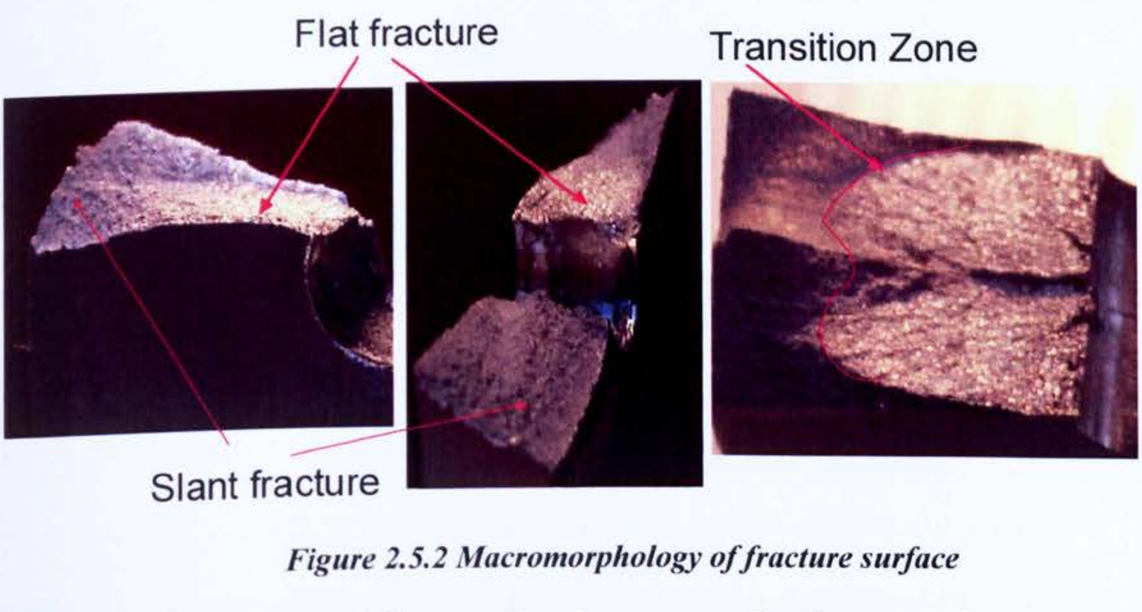

Figure 2.5.2 Macromorphology of fracture surface

Hertzberg refers in to the influence of environment on the fracture mode transition: *It should be noted, however, that a unique relation between the stress state and fracture mode was not observed* *by Vogelesang[219] in 7075-T6 and 2024-T3 aluminum alloys during fatigue crack propagation in aggressive environments. The influence of environment on the fracture mode transition (more flat fracture in corrosive atmosphere than in dry air at the same* ${r_y}/{t}$ *ratio) was believed to be caused by a change in the fracture mechanism.*

Counter to this, the fracture mode transition in the corroded specimens tested at Kingston University was similar to that for non corroded specimens. This may be due to the fact that prior corroded specimens were tested in dry air rather than being exposed to corrosion during testing.

3 ANALYTICAL PART

3.1 CRACK FRONT SIMPLIFICATION

Analysis of the fracture surfaces left by fatigue crack growth (see fracture surfaces depicted in in the Appendix) and taking into account available solutions for SIF for similar types of cracks we observed the following crack types:

- Symmetrical and asymmetrical through crack
- Symmetrical and asymmetrical quarter-elliptical corner crack
- Symmetrical and asymmetrical semi-elliptical crack

In the last two cases the ellipse axes relationship a/c were about 1.0-1.5

Simplification or idealisation of real crack propagation cases was carried out, assuming these three types of cracks. The method of crack identification, depending on orientation of the specimen is shown in Figure 3.1.1.

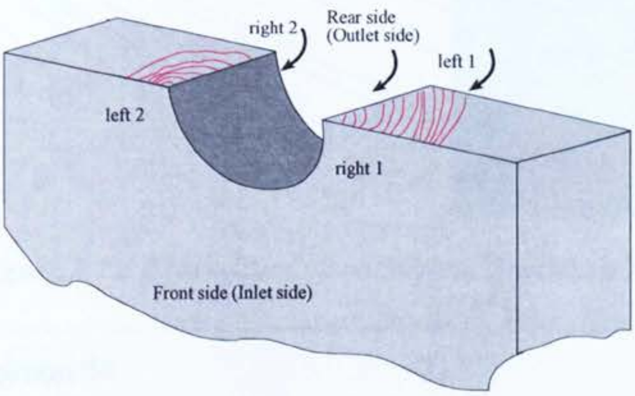

Figure 3.1.1 Cracks identification

The geometry of the crack front lines was quite variable. Some examples of observed crack combinations in one specimen are given in the Figure 3.1.2

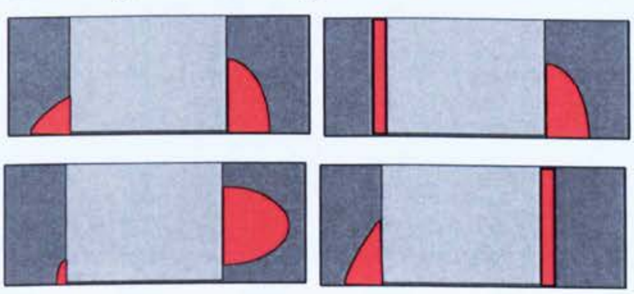

Figure 3.1.2 Variety of virtual geometry of the crack fronts

Let's consider a couple of typical cases of front crack propagation from the hole edge. A simplified visualisation of crack front advance is represented the Figure 3.1.3 and Figure 3.1.5. The straight lines connect points of surface cracks which were observed on both sides of the specimen at same time. The real crack front line can be semi-elliptical, quarter-elliptical or another form of curve, but the following schematic diagram enables us to approximately analyse the type of crack front and the changes taking place during the whole life of the specimen.

The first case corresponds to a plain specimen (№14) without corrosion and without CX treatment.

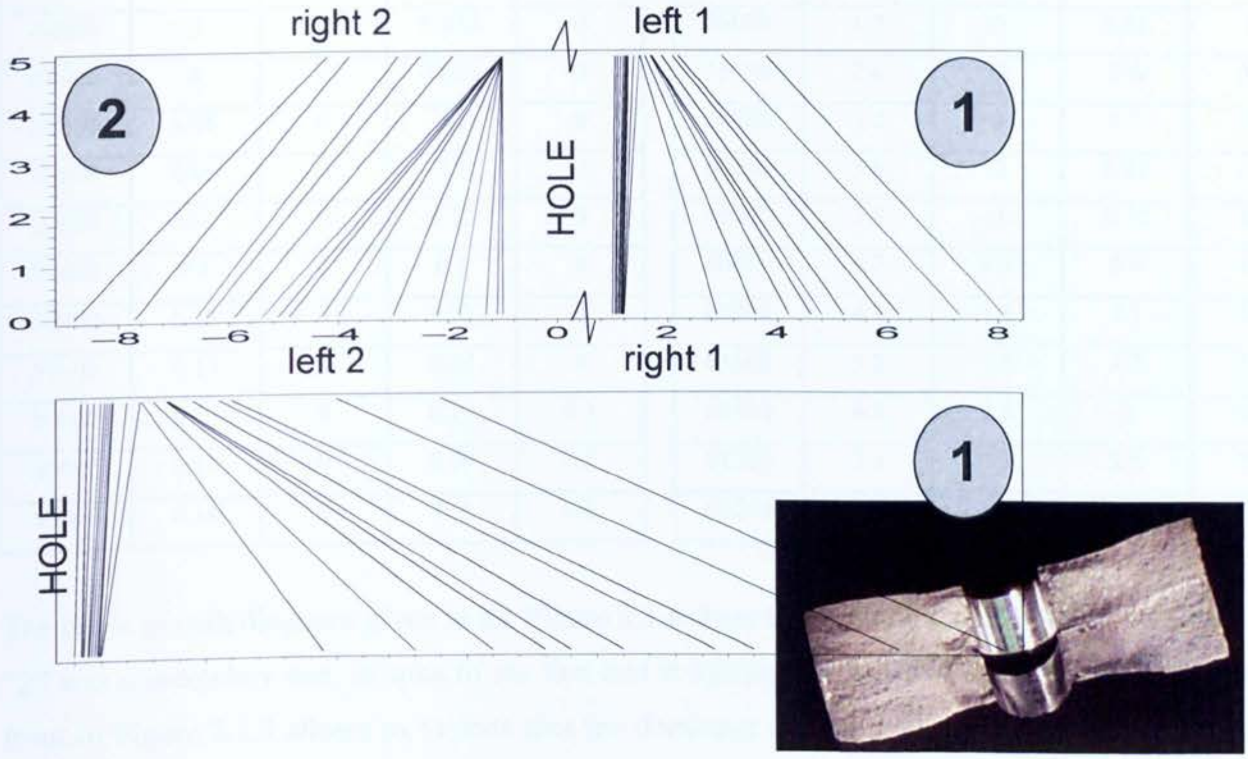

Figure 3.1.3 Crack front visualisation. Specimen №14

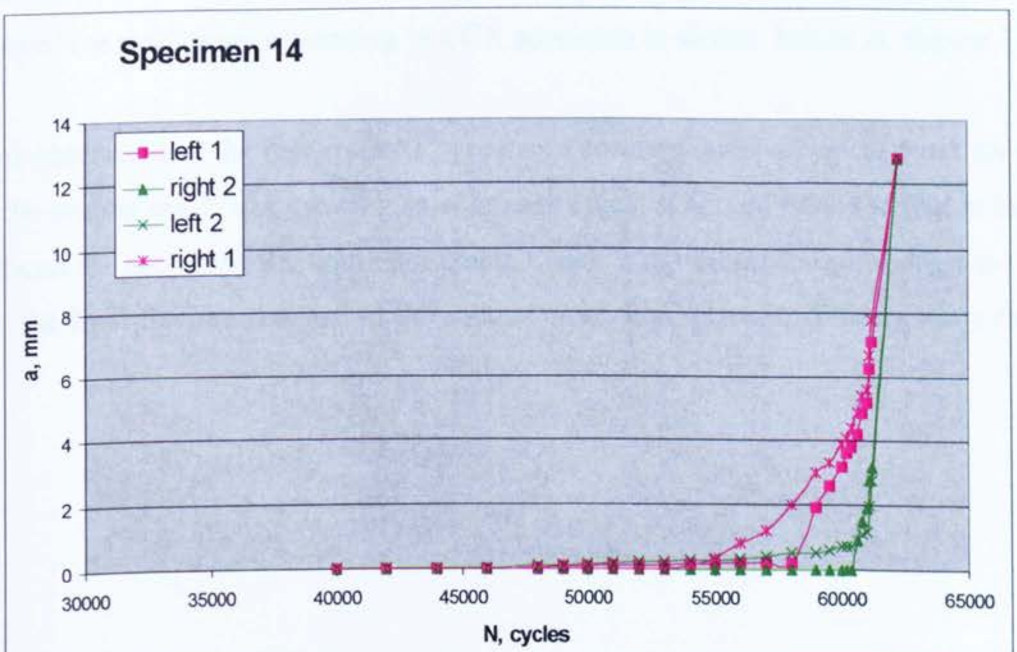

Figure 3.1.4 Crack growth diagrams. Specimen №14

Table 8 Crack Growth Data. Specimen №14

N	Fr_left_1	Fr_right_2	R_left_2	R_right_1
40000	0	0	0.05	0
42000	0	0	0.051	0
44000	0	0	0.052	0
46000	0	0	0.053	0
48000	0.05	0	0.1	0
49000	0.06	0	0.1	0
50000	0.07	0	0.15	0
51000	0.1	0	0.2	0
52000	0.11	0	0.23	0
53000	0.13	0	0.25	0
54000	0.15	0	0.27	0.1
55000	0.17	0	0.29	0.3
56000	0.18	0	0.3	0.8

N	Fr_left_1	Fr_right_2	R_left_2	R_right_1
57000	0.19	0	0.4	1.2
58000	0.2	0	0.5	2
59000	1.9	0	0.51	3
59500	2.6	0	0.6	3.3
60000	3.2	0	0.7	3.9
60200	3.6	0	0.71	4.1
60400	3.8	0	0.72	4.4
60600	4.2	0.9	0.9	4.9
60800	4.9	1.5	1.1	5.4
61000	5.2	1.9	1.2	5.6
61100	6.3	2.8	2	6.7
61200	7.1	3.2	2.8	7.8
62244	12.825	12.825	12.825	12.825

The crack growth diagrams given in the Figure 3.1.4 show that the first crack "1" was dominant and "2" was a secondary one, in spite of the fact that it initiated earlier. The visualisation of the crack front in Figure 3.1.3 allows us to state that the dominant crack propagated as a through crack for most of the life of the specimen while the secondary crack propagated as a quarter-circular corner crack at the same time.

An example of the crack front advancing in a CX specimen is shown below in Figure 3.1.5, Figure 3.1.6 and

Here, it was observed that the first crack "1" grew as a corner quarter-elliptical crack for most of its life while the second crack was growing as a through crack. It should be noted that in this case it is rather difficult to determine the dominant crack. Crack 1 started much earlier than the second but just before the final fracture the size of the second crack had grown to 3 times more than the first one.

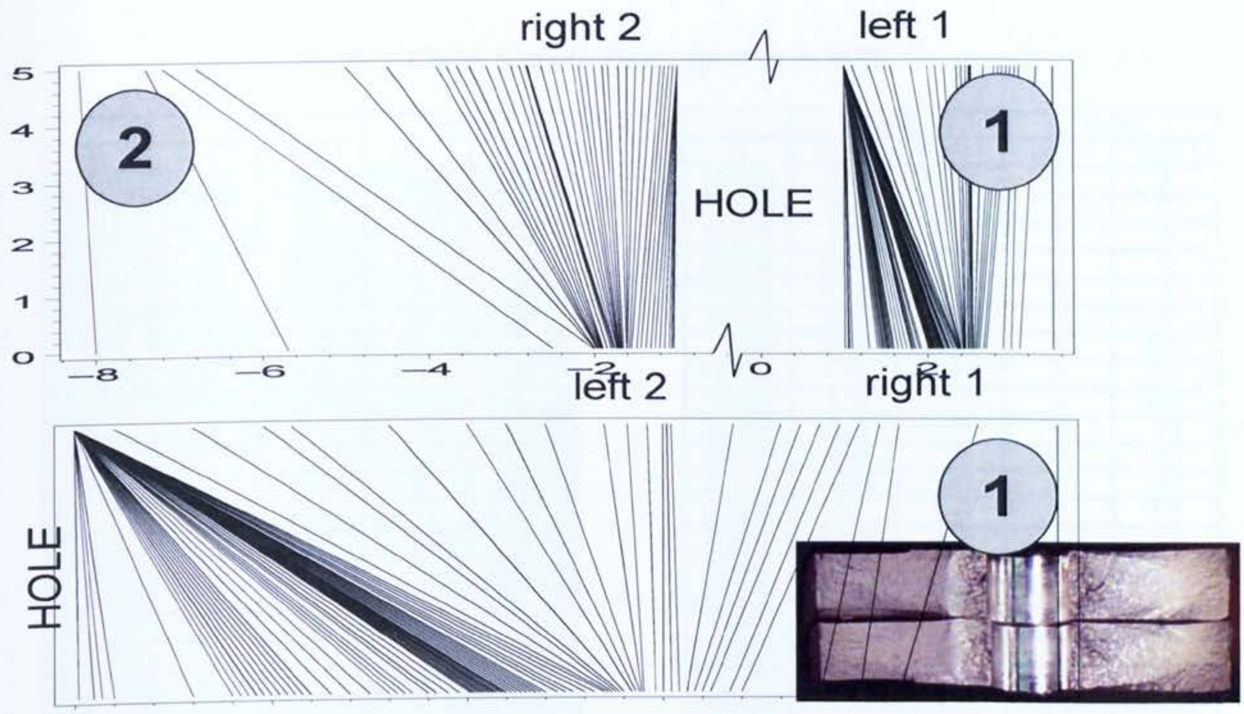

Figure 3.1.5 Crack front visualisation. Specimen №25

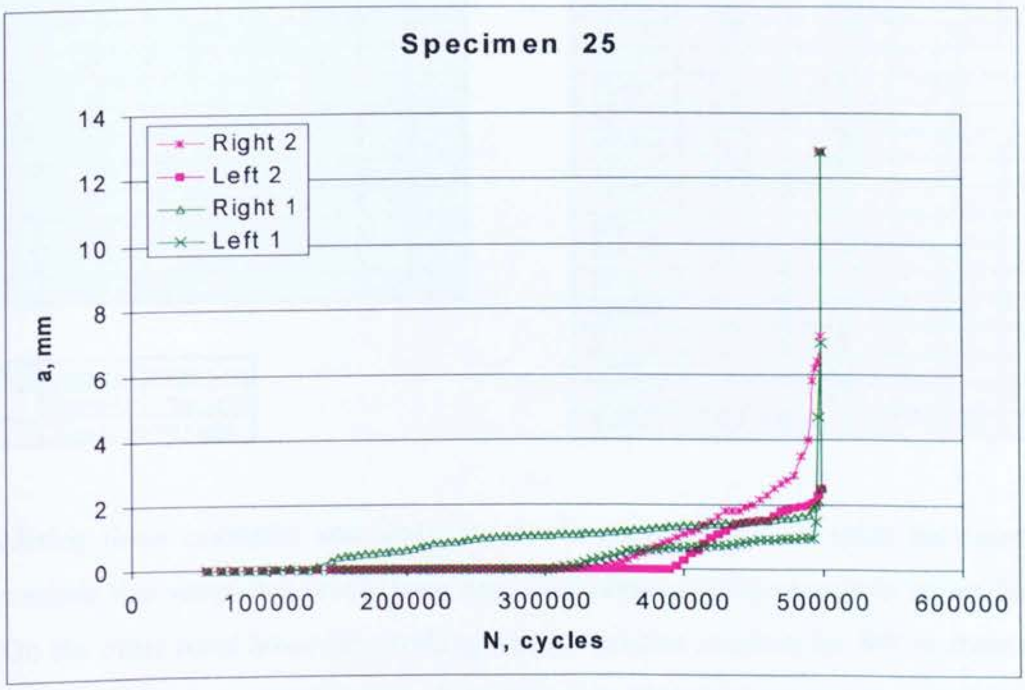

Figure 3.1.6 Crack growth diagrams. Specimen №25

Table 9 Crack Growth Data. Specimen №25

	Inlet		outlet	
N	Left 2	Right 1	Left 1	Right 2
105000	0	0.05	0	0
115000	0	0.07	0	0
125000	0	0.01	0	0
135000	0	0.1	0	0
145000	0	0.3	0	0
150000	0	0.4	0	0
155000	0	0.42	0	0
160000	0	0.44	0	0
165000	0	0.46	0	0
170000	0	0.48	0	0
175000	0	0.5	0	0
180000	0	0.52	0	0
185000	0	0.54	0	0
190000	0	0.56	0	0
195000	0	0.58	0	0
200000	0	0.6	0	0
205000	0	0.65	0	0
210000	0	0.7	0	0
215000	0	0.75	0	0
220000	0	0.8	0	0
225000	0	0.82	0	0
230000	0	0.84	0	0
235000	0	0.86	0	0
240000	0	0.9	0	0
245000	0	0.92	0	0
250000	0	0.95	0	0
255000	0	0.98	0	0
260000	0	1.0076	0	0
265000	0	1.015	0	0
270000	0	1.023	0	0
275000	0	1.031	0	0
280000	0	1.038	0	0
285000	0	1.046	0	0
290000	0	1.054	0	0
295000	0	1.062	0	0
300000	0	1.069	0	0
305000	0	1.076	0	0
310000	0.05	1.085	0	0
315000	0.07	1.092	0	0
320000	0.1	1.1	0	0
325000	0.156	1.1125	0	0
330000	0.212	1.125	0	0
335000	0.27	1.1375	0	0
340000	0.325	1.15	0	0.05
345000	0.38	1.1625	0	0.1
350000	0.44	1.175	0	0.15
355000	0.49	1.1875	0	0.2
360000	0.55	1.2	0	0.3
365000	0.575	1.23	0	0.4
370000	0.6	1.25	0	0.5
375000	0.605	1.27	0	0.6
380000	0.61	1.3	0	0.7
385000	0.65	1.325	0	0.83
390000	0.67	1.35	0	0.9
395000	0.68	1.36	0.1	1
400000	0.69	1.37	0.3	1.1
405000	0.7	1.38	0.48	1.18
410000	0.71	1.39	0.55	1.25
415000	0.72	1.4	0.8	1.38
420000	0.73	1.42	1	1.5
425000	0.75	1.43	1.1	1.63
430000	0.76	1.44	1.2	1.8
435000	0.78	1.445	1.35	1.81
440000	0.8	1.45	1.41	1.82
445000	0.85	1.48	1.46	1.9
450000	0.9	1.5	1.5	2
455000	0.91	1.52	1.51	2.15
460000	0.92	1.54	1.52	2.3
465000	0.93	1.56	1.68	2.5
470000	0.95	1.58	1.8	2.65
475000	0.96	1.6	1.85	2.78
480000	0.97	1.62	1.9	2.9
485000	0.99	1.67	1.95	3.5
490000	1	1.7	2	4
493000	1.01	1.9	2.05	5.8
495000	1.5	2	2.1	6.2
497000	4.7	2.1	2.3	6.4
499000	7	2.5	2.5	7.2
499438	12.825	12.825	12.825	12.825

(green)	Symmetry Through Crack
(yellow)	Symmetry Corner Crack
(pink)	Single Corner Crack

Considering these examples and analysing the fracture surfaces of other specimens we can conclude that simplified crack types suggested above are the exception rather than the rule. On the other hand however, working out the precise solution for SIF in these cases will lead to excessive complication. It is therefore proposed to use the available SIF solutions for the further data processing and carry out comparative investigations into different SIF solutions to avoid possible underestimation of crack growth rate prediction.

3.2 COMPARISON OF THE DIFFERENT SIF SOLUTIONS APPLIED FOR THE SIMPLIFIED CRACK GROWTH DATA OF ONE SPECIMEN.

We'll consider three approaches with approximation.

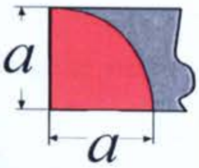

1. The most rough estimation is when we assume that the crack is symmetrical, and growing as only a quarter-circular, or only a semi-circular crack from initiation until it reaches the plate thickness. Afterwards it continues to grow as a through crack to final fracture.
   In the case of the formation of a through crack from the initiation, the crack is assumed as a symmetrical through crack until final fracture. This case can be considered to be a "Rough Estimation".

It is assumed that the crack was symmetrical and simplified crack size determined as:

$$a = \frac{a_{1fs} + a_{1rs}}{2} + \frac{a_{2fs} + a_{2rs}}{2} \qquad (3.2.1)$$

here a_{fs} - crack length for front surface; a_{rs} - crack length for rear surface.

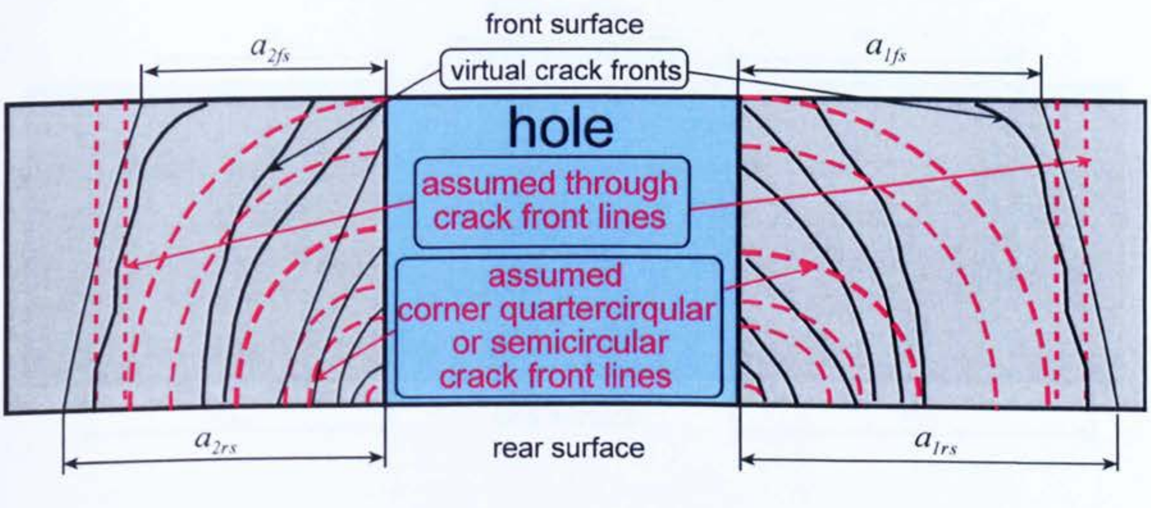

Figure 3.2.1 Schematic visualization of crack front assumption for "Rough Estimation"

The SIF solutions for quarter-circular corner or semicircular cracks are used until the crack reaches a depth equal to the thickness of the specimen and becames a through crack. From that point the corresponding through crack solution was used (see Figure 3.2.1). Therefore, diagrams for quarter-circular corner and semicircular cracks are combined with through crack solutions.

In this case, crack growth features are virtually ignored. If the crack is symmetrical and quarter-circular for instance, it will be estimated virtually by one SIF solution for quarter-circular cracks! The thickness of the plate used is 5 mm and the critical crack size in these tests is about the same, therefore the probability of a through crack appearing is small, perhaps just one or two measurement points before final fracture.

A decision about the type of crack is made clear by observation of the fracture surface and the Crack Growth Diagram.

2. A more exact approach is to assume the crack is symmetrical and quarter-elliptical(circular) or of semi-elliptical(circular) form from initiation until cracks appear on the opposite sides of the plate, Following this (assuming 4 cracks appear) they grow as a through crack to final fracture.

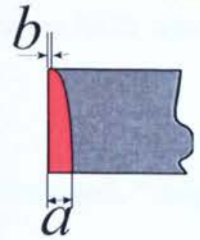

   In the case of a through crack forming at initiation, the crack is assumed to be a through crack until final fracture.

This may be referred to as a "Recommended Estimation", i.e. a mean between "Rough" and "Precise" estimations.

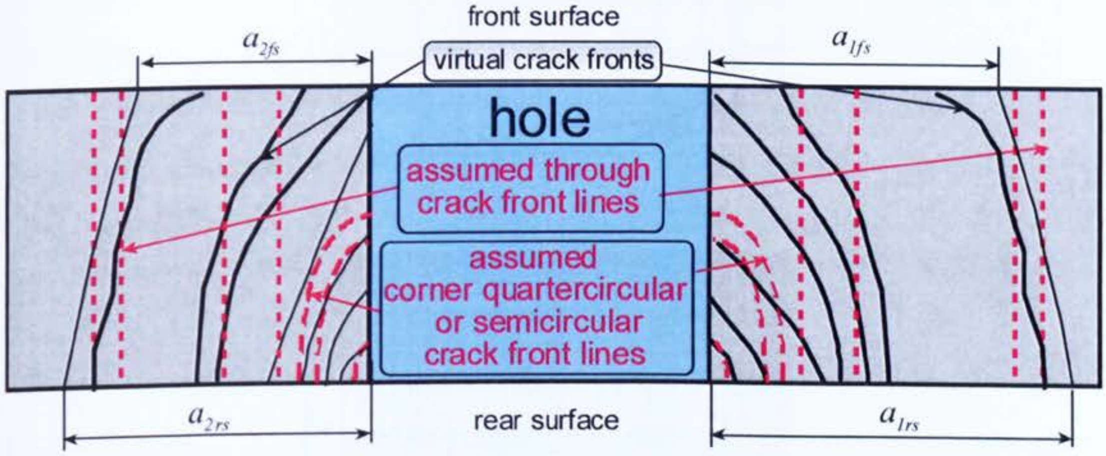

Figure 3.2.2 Schematic visualization of crack front assumption for "Recommended Estimation"

The Crack Growth Rate Diagrams for quarter-circular corner and semi-circular cracks are combined with a through crack solution. In this case, all crack measurements are taken into account and the crack is assumed to be symmetrical and quartercircular, and will be estimated by a suitable SIF solution for quarter-circular cracks until the moment when two through cracks are seen to be propagating from both sides of the hole! The role of the through crack in this case increases in significance. In this case a decision about the type of crack to be considered is made by observation of the fracture surface and Crack Growth Diagram.

3. The third type of estimation is referred to as "Precise Estimation" The difference from the previous variant is that only the initial growth of a single crack is taken into account. After a crack appears on the opposite side of the hole the solutions for symmetrical cracks were used.

There are advantages and disadvantages for each of the suggested estimation methods. Their applicability may be evaluated by an example of one typical specimen №25 which has been examined previously.

"Rough estimation"

The experimental crack growth curves for each of the cracks and the averaged, "rough estimation", curve are shown in Figure 3.2.3.

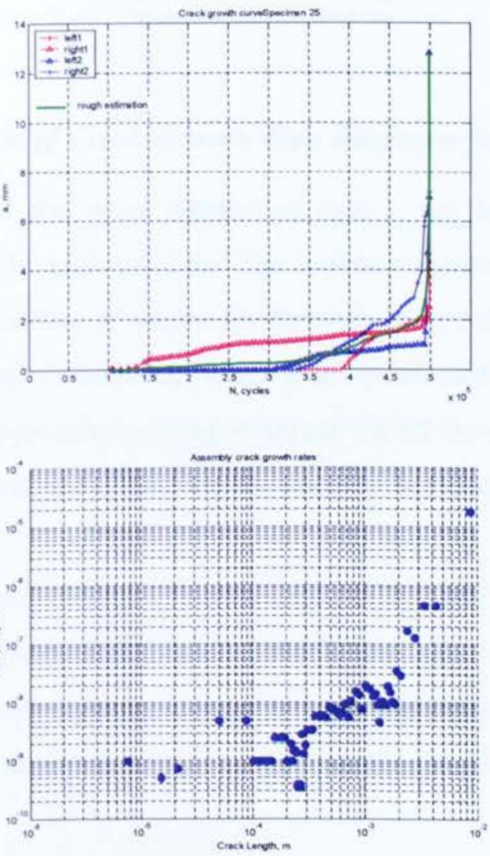

Figure 3.2.3 Crack Growth Diagram and Crack Growth Rate versus Crack Length Diagram for Specimen 25

Using the SIF solutions and crack growth rate data computed for the three assumed crack growth models, the Crack Growth Rate Diagrams given in Figure 3.2.4 were determined

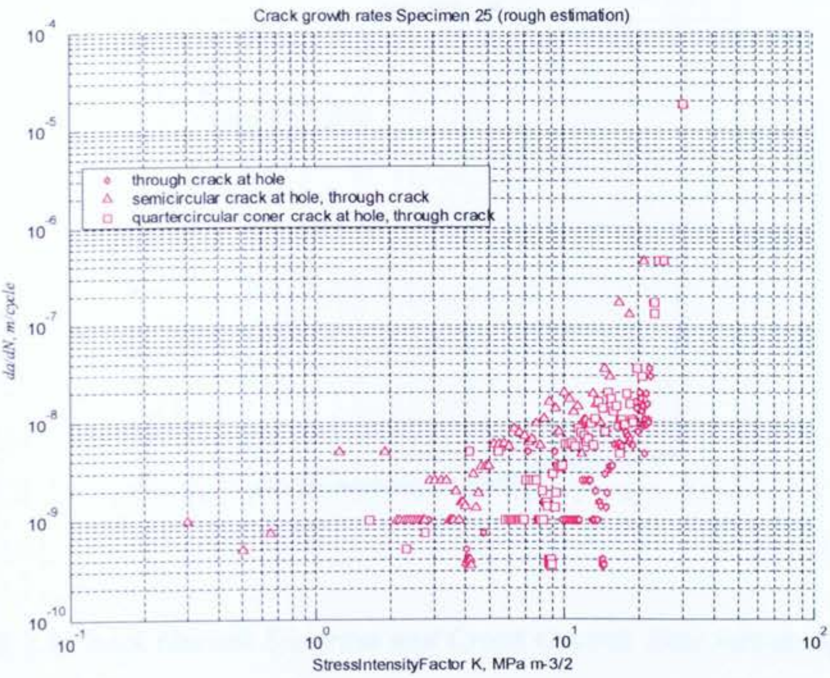

Figure 3.2.4 Comparison of Crack Growth Rate Diagrams for different SIF solutions

The diagram shows that the most dangerous case - the largest magnitude of SIF, corresponds to the through crack solution. The lowest magnitude of SIF is for a quarter-circular corner crack. Therefore, if we use the through crack solution in our calculations it would result in a conservative estimate. It can also be inferred from the diagram that the use of a non-simplified approach applying solutions for all the different types of cracks in one specimen, would produce CGR curves located between the through crack and quarter-circular solutions.

"Recommended estimation"

For the "recommended estimation", crack growth data were divided into two types of crack: Symmetrical Quarter-circular Corner Cracks and Symmetrical Through Cracks. The crack growth curves obtained after averaging are shown in Figure 3.2.5

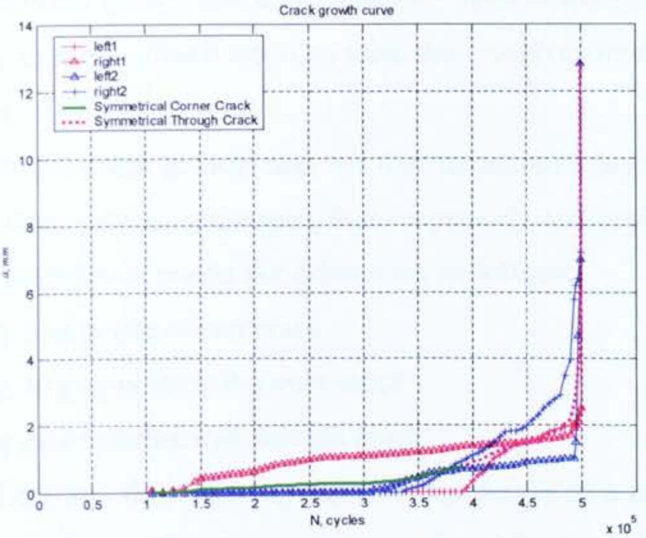

Figure 3.2.5 Crack Growth Diagram and Crack Growth Rate versus. Specimen 25

Crack growth rate data for "recommended estimation" with "rough estimation" methods are shown in Figure 3.2.6

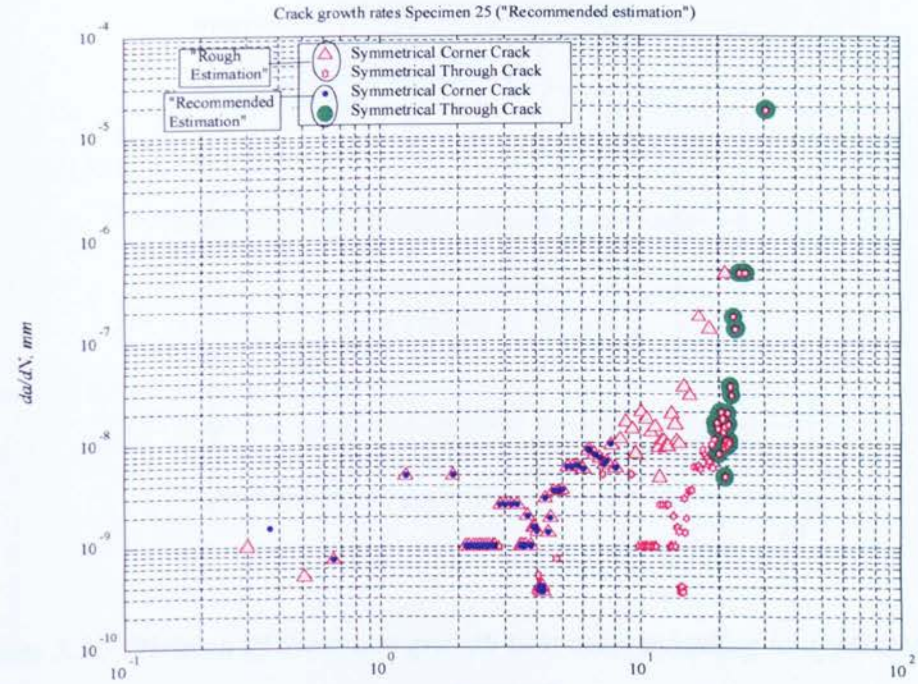

Figure 3.2.6 Comparison of the "Recommended " and "Rough Estimation " in CGR diagrams. Specimen 25

It is to be noted that crack growth rate data from the "recommended estimation " method corresponds closely to crack growth rate data from the "rough estimation" method.

"Precise Estimation"

For this we consider the crack growth data for four measured cracks more precisely. By dividing them into three groups, processing them separately and applying the appropriate SIF solutions the categories of cracks considered are as follows:

Data corresponding to a single corner crack

Data corresponding to a symmetrical corner crack

Data corresponding to a symmetrical through crack

The Figure 3.2.7 illustrates these three groups. A step occurs at a point where a "Single Corner Crack" changes into a "Symmetrical Corner Crack", caused by unequal growth of the branches of the crack. The "Symmetrical Corner Crack" solution averages the crack sizes of both branches. On changing to the "Symmetrical Corner Crack" solution, the length of the secondary crack branch is not as large as the initial one and the average of the two branches is taken. Hence at this point the crack size falls.

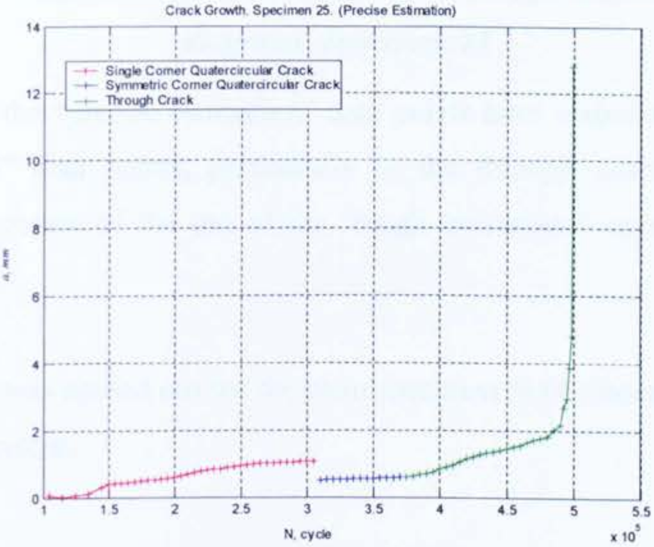

Figure 3.2.7 Division of the crack growth into corresponding to applicable solutions intervals

Using the applicable SIF solutions and crack growth rate data computed from assumed crack growth data, the Crack Growth Rate Diagrams are presented in Figure 3.2.8. This crack growth rate data was compared with the same data obtained for "rough estimation" of corner and through cracks, as given previously (see Figure 3.2.8).

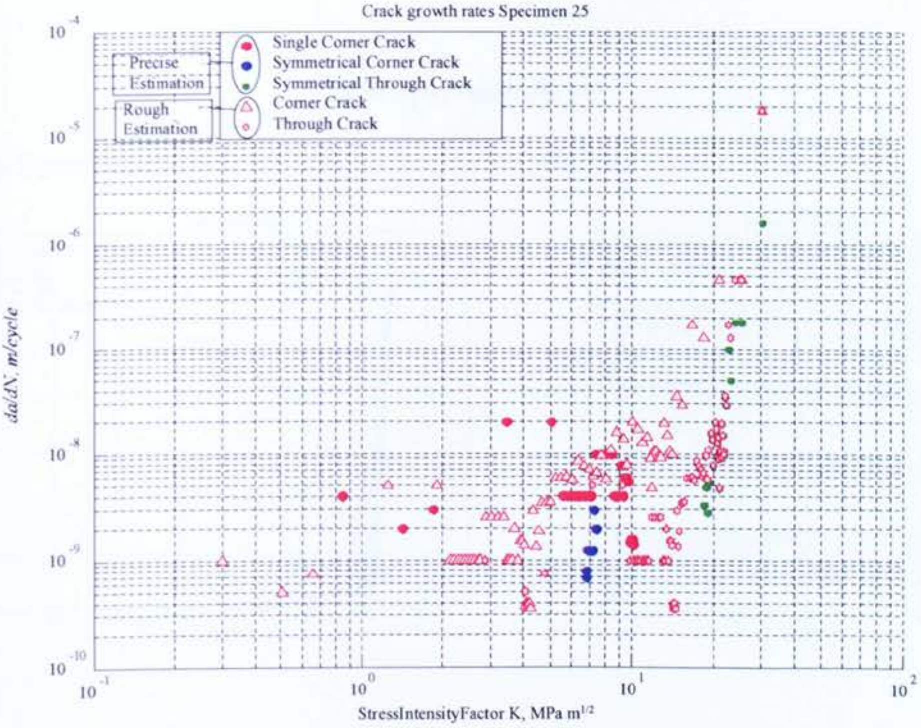

Figure 3.2.8 Comparison of the "Precise " and "Rough Estimation " in CGR diagrams. Specimen 25

It is apparent that the "precise estimation" data points have a similar distribution to the "rough estimation" data points, particularly in the through crack region. This fact confirms the correctness of the use of the "rough estimation" approach for the larger crack region.

The same analysis was carried out for the plain specimen №14 discussed previously. The results are shown below.

Plain Specimen № 14

"Rough Estimation"

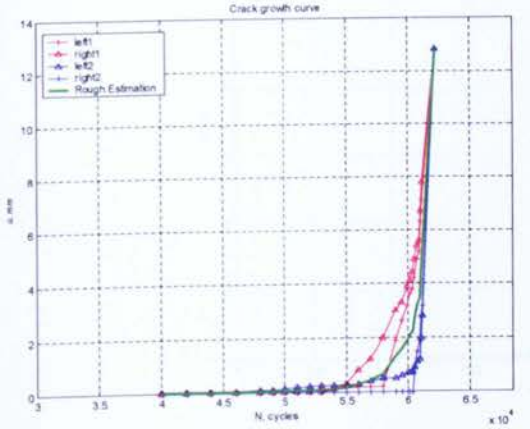

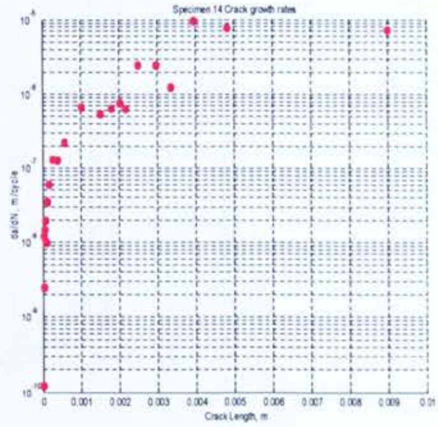

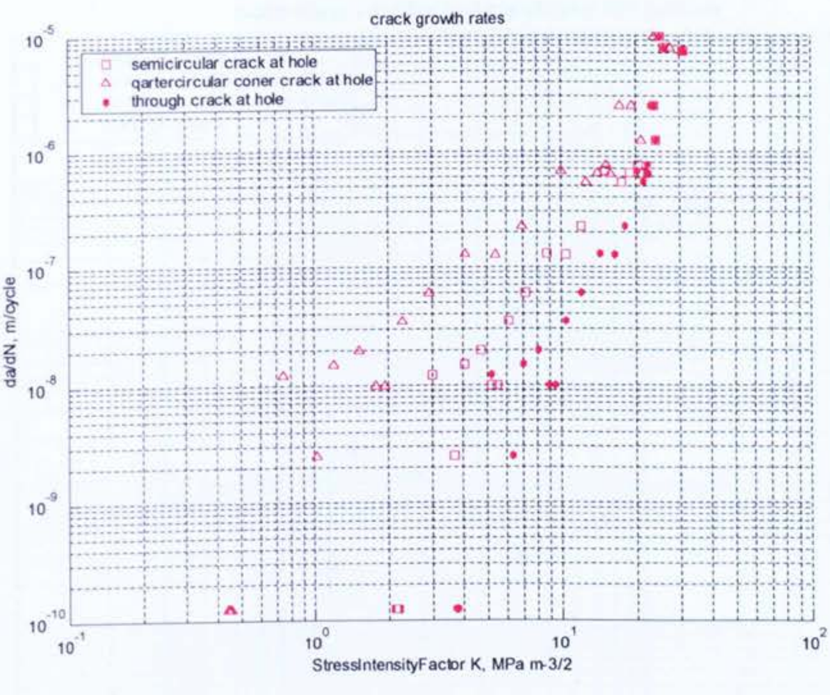

Figure 3.2.9 "Rough Estimation " in CGR diagrams. Specimen 14

"Recommended Estimation"

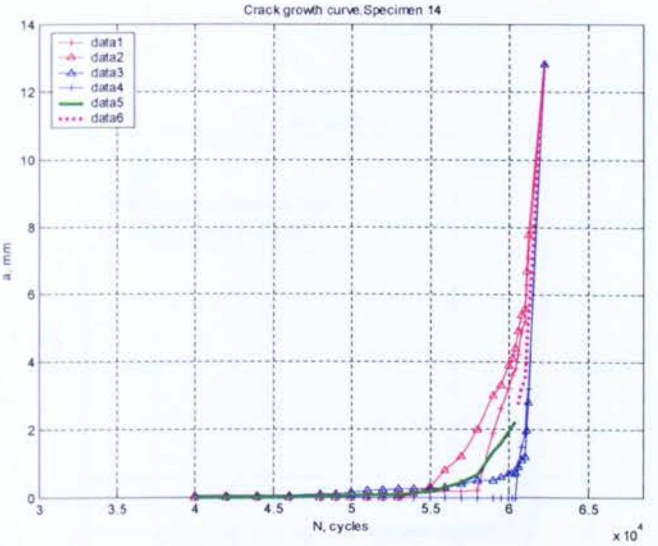

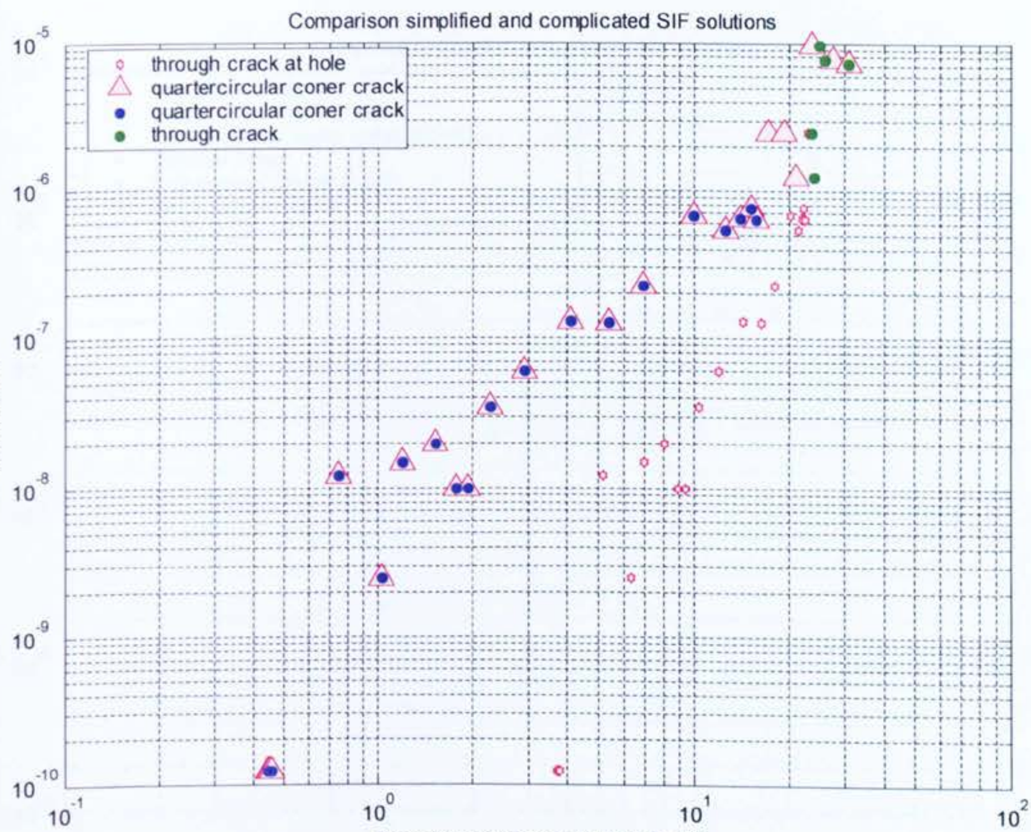

Figure 3.2.10 Comparison of the "Recommended " and "Rough Estimation "methods in CGR diagrams. Specimen 14

"Precise Estimation"

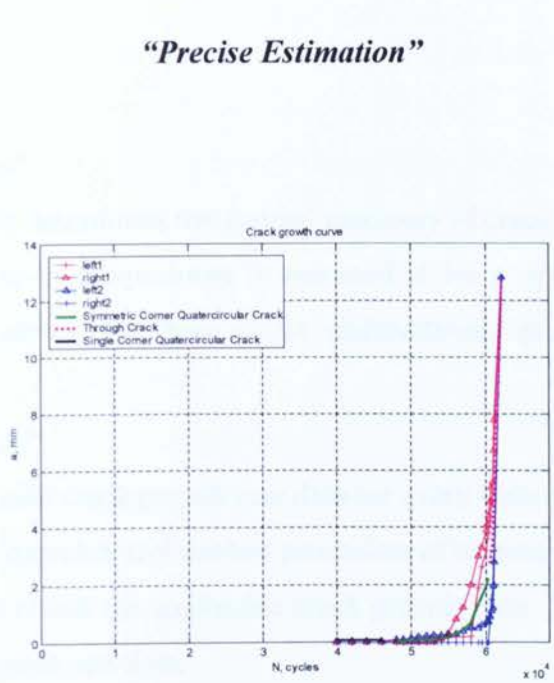

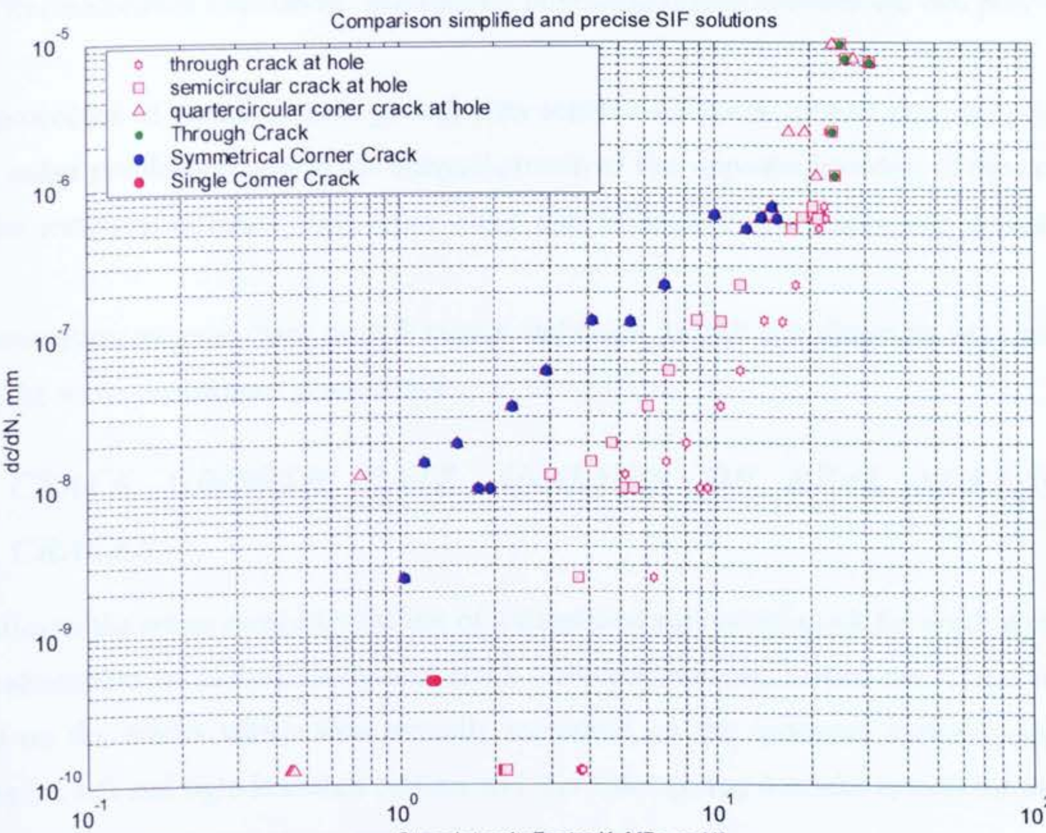

Figure 3.2.11 Comparison of the "Precise " and "Rough Estimation "methods in CGR diagrams. Specimen 14

3.2.1 SUMMARY

- "Rough Estimation"

Rough estimation only determines the general tendency of crack growth rate.

The dominant crack in each specimen is assumed to be a symmetrical through crack which does produce errors, but these errors underestimate growth rate which favours safety.

- "Precise Estimation"

The application of precise crack growth rate data for every type of propagating crack.

This requires a rather complex and unclear procedure of selecting available SIF solutions for each crack type to obtain the applicable crack growth data. This tends to increase the scatter of the crack growth rate data.

- "Recommended Estimation"

The "Recommended Estimation" is a method producing results between the two previous ones

The procedure of creating crack growth data suitable for crack growth rate analysis is often rather problematic due to the unequal growth of two opposite branches of the crack and the variety of different crack types which may be present in one specimen during its life.

All subsequent average crack growth curves and crack growth rate diagrams were made using the recommendations given above.

3.3 CRACK GROWTH RATE ANALYSIS OF REAL SURFACE CRACKS

To estimate the errors caused by the use of a simplified equivalent crack for crack growth rate calculations an analysis of the real crack measurements was carried out. These were based on the cracks which were actually measured on the specimen surfaces during testing i.e. left and right branches on face and rear sides giving 4 cracks in total for every specimen. Just two assumptions were made as follows:

When a crack grew through the specimen it was automatically assumed to become a through-thickness crack with a straight crack front irrespective of its real crack front configuration.

All cracks were considered to be symmetrical cracks, excluding cases where cracks were completely asymmetric for the total life of the specimen. This assumption makes the analysis conservative as this is effectively the worst case scenario.

In the overwhelming majority of cases, crack propagation was symmetrical with the following observations:

- Initiation of corner cracks on the opposite hole edges occurred after a rather long time interval.
- Their growth through the thickness as corner cracks and the formation of through-thickness cracks also occurred after a rather long time interval.

It was noted that in case of the plain specimens (non cold expanded) an initial corner crack grew through the thickness faster than in the CX specimens. In the CX specimens, the through cracks were quite often formed just before the final fracture or did not appear at all. This situation caused big differences in the quantity of crack measurements which contained samples of different crack branches. Some of them contained 60 points but others only 2-3 points.

Different methods of crack growth rate determination were used for the processing of crack length data as follows:

Crack measurement data containing:

less than 5 points was processed by intersection method (2 points method),

less than 6 points - by 3 points polynomial method

and more than 7 points – by 5 points polynomial method

When the SIF for corner crack was computed, parametrical angle φ was accepted 0° corresponding to face surface.

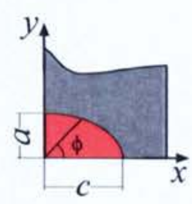

Comparisons between the crack growth rate diagrams constructed for real and simplified cracks are shown in Figure 3.3.1 - Figure 3.3.3. These figures show the differences in behaviour between examples of plain specimens, pure CX specimens and CX specimens with interference fit. Looking at the approach using the simplified equivalent crack formation, it is apparent why the equivalent crack seems to be underestimated compared to a real one. The equivalent crack is an averaged value of two unequal branches of the crack. Therefore, simplified calculations of crack growth rate are displaced towards smaller crack lengths relative to real cracks.

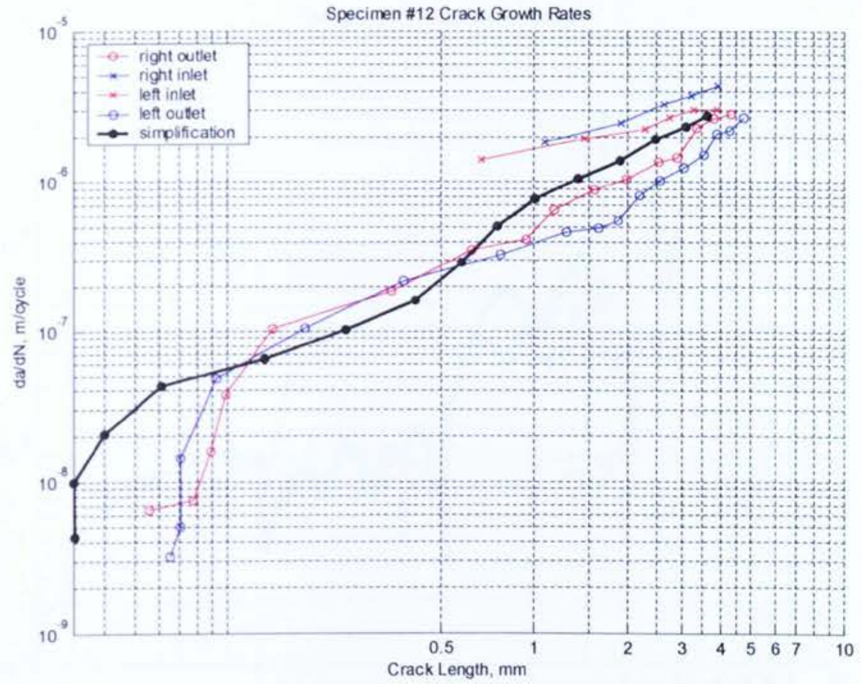

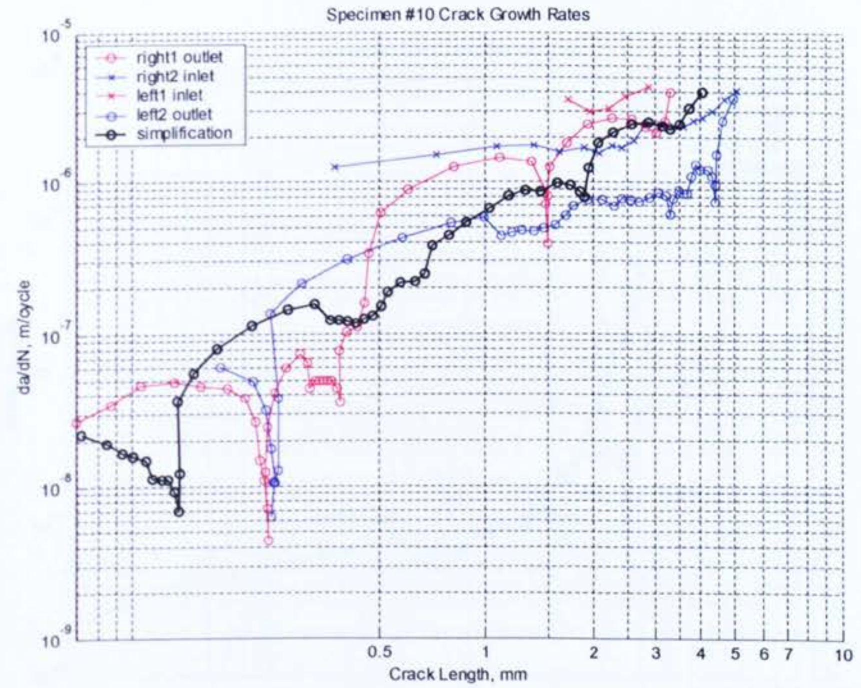

Figure 3.3.1 Comparison between crack growth rate diagrams built by real and simplified cracks by an example of plain specimens

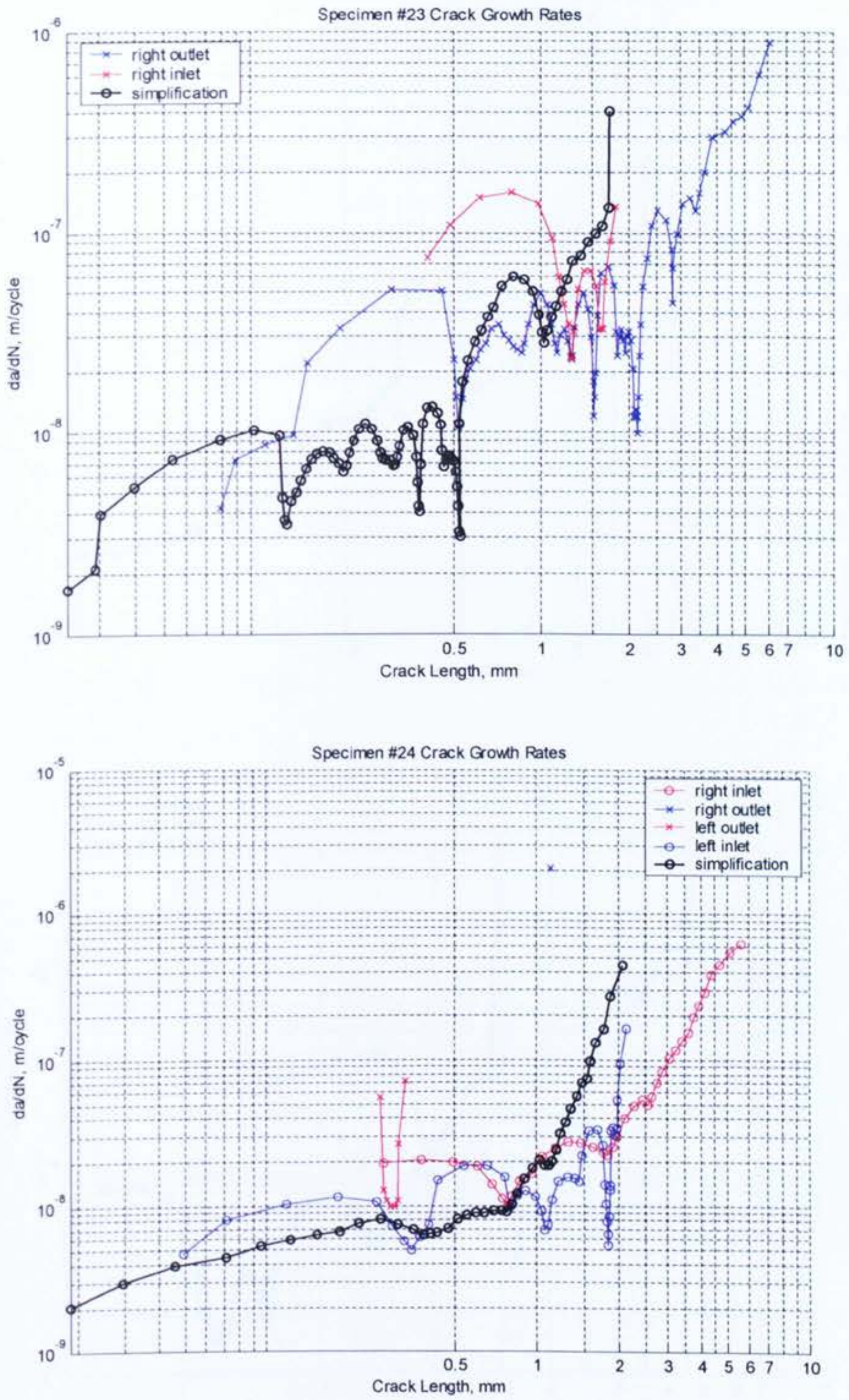

Figure 3.3.2 Comparison between crack growth rate diagrams constructed from simplified crack forms for the CX specimens

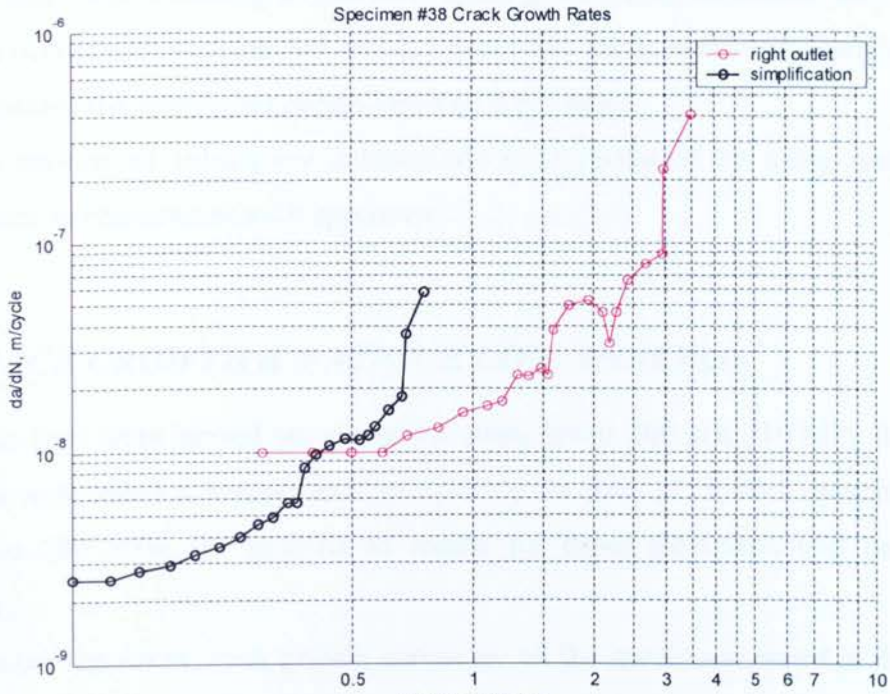

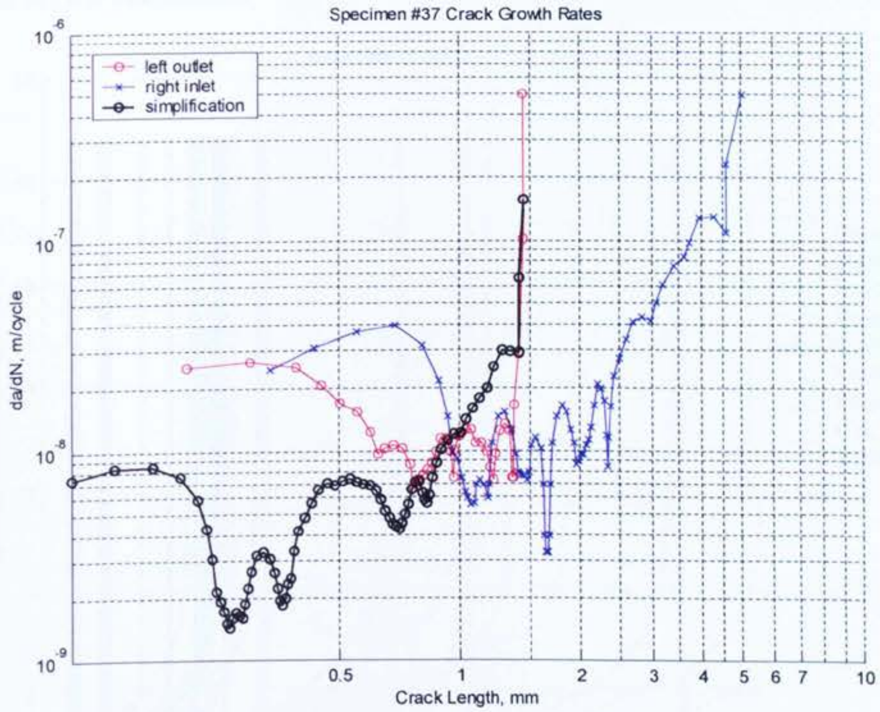

Figure 3.3.3 Comparison between crack growth rate diagrams for real and simplified cracks in an example of a CX specimen with interference fit

It will be noted that according to this data, crack growth rate retardation caused by cold expansion occurs within an interval of 1-2.5 mm while the method using equivalent crack values indicated the retardation occurs between 0.5-1 mm.

For these reasons all subsequent calculations were produced by using one dominant surface crack to characterise each specimen.

3.4 CRACK GROWTH & FATIGUE LIFE ANALYSIS

The fatigue tests were carried out at two net stress levels 200 and 210 MPa. Most of the specimens were tested at a stress level of 210MPa. In order not to lose experimental data obtained at 200 MPa, the analysis of results for these specimens will be presented separately.

A composite diagram of crack growth curves for all the specimens tested at ***210MPa*** are given in the ***Figure 3.4.1***. The final crack length was within a range of 6-8 mm before the failure for all the specimens.

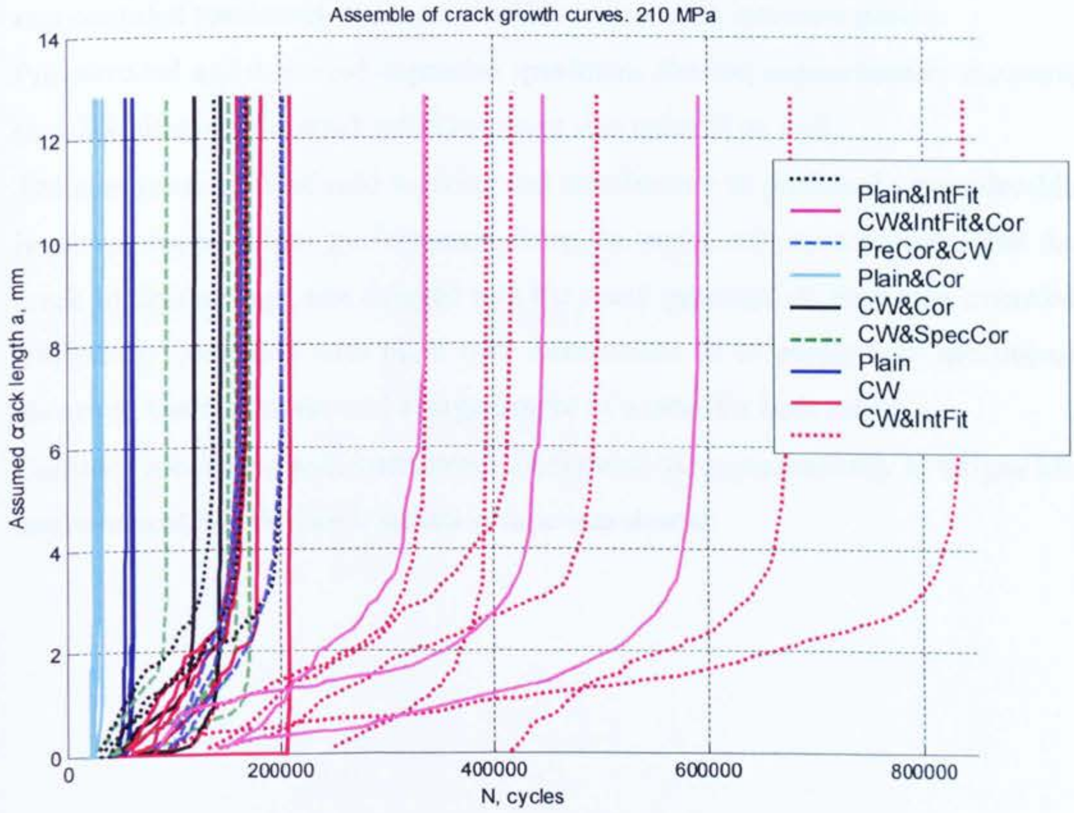

Figure 3.4.1 Assembly of crack growth curves for specimens tested on 210MPa

Individual quantitative data on crack initiation and propagation life produced in the comparative diagram ***Figure*** *3.4.2*. Based on the fact mentioned above that CW specimens with post corrosion had similar behaviour to CW specimens with specific corrosion they were combined as one sample in the chart.

Qualitative analysis of the chart gives the following results

- the minimum total fatigue life was shown in corroded plain specimens and the maximum by CW specimens with interference fit. The results for the CW IF specimens show a massive improvement compared to all other specimen conditions.
- Interference fit in plain specimens extends total fatigue life by approximately the same amount as hole cold working. Crack initiation in the specimens with interference fit is delayed in comparison with CW specimens. Crack propagation in CW specimens is extended more than propagation in specimens with interference fit
- Specimens corroded after cold expansion revealed a reduction in life compared to non corroded specimens due to a reduction in the crack initiation period.
- Pre corroded and then cold expanded specimens showed approximately the same total life although the crack initiation stage was reduced as well.
- The combined effect of cold working and interference fit produced a considerable improvement in fatigue performance. Even the worst test result revealed that the crack initiation stage was delayed and the crack propagation time was extended sufficiently compared with plain with interference fit or purely CW specimens. However, test results showed a large degree of scatter for both stages.
- Corroded specimens with interference fit showed the same tendency in fatigue life improvement, but the crack initiation time was shorter.

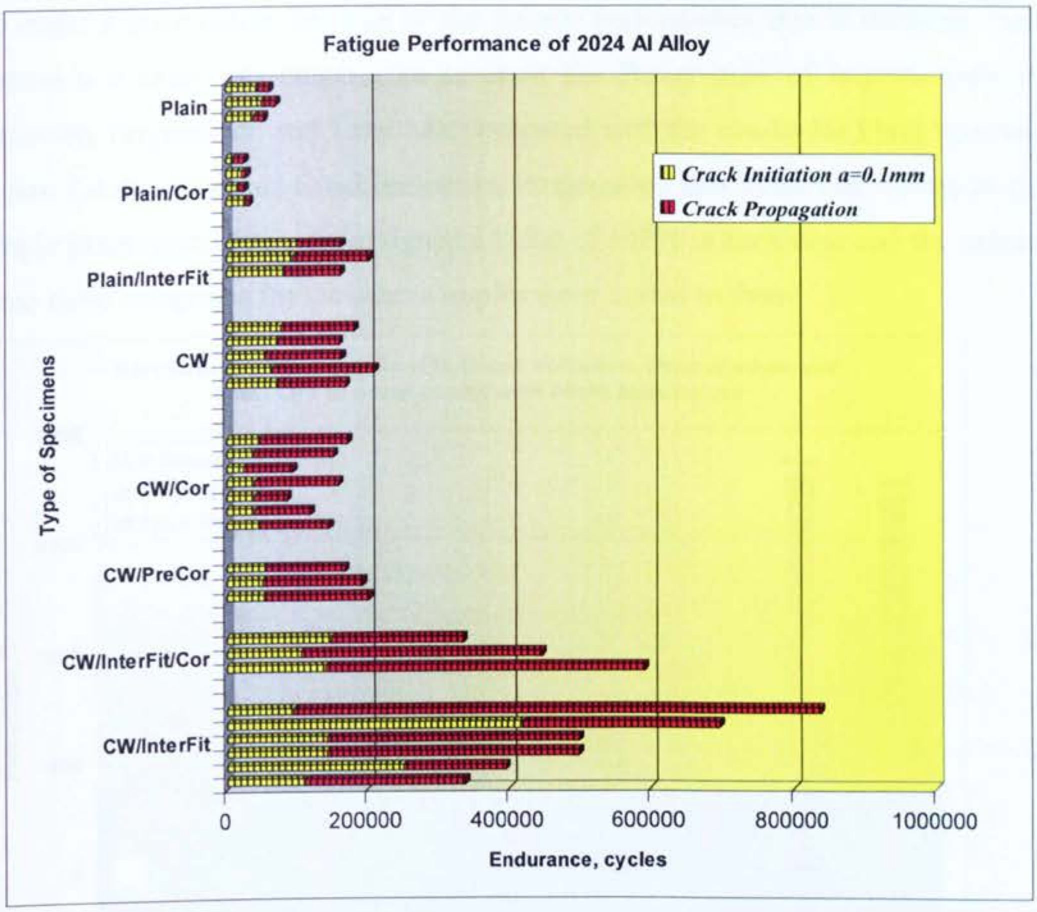

Figure 3.4.2 Quantitative comparison of crack initiation and propagation periods for individual specimens at $\sigma_{net} = 210MPa$

Figure 3.4.3 shows averaged quantitative data for crack initiation and propagation life and visually demonstrates the results of the qualitative analysis given above.

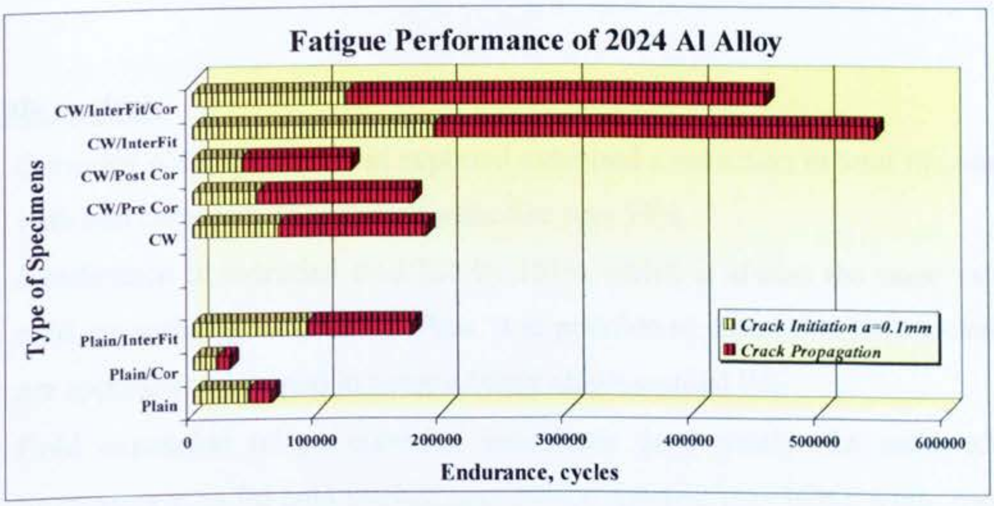

Figure 3.4.3 Average quantitative data on crack initiation and propagation life for specimens tested at $\sigma_{net} = 210MPa$

To make a quantitative analysis of the fatigue performance due to different methods of treatment a chart was constructed to show the Percentages of Improvement in Crack Initiation, Propagation and Total Life compared with the results for Plain Specimens (see Figure 3.4.4). Averaged Crack Initiation, Propagation and Total Life values in cycles for simple plain specimens were assigned a value of 100% in each case and the values for the same three categories for the other samples were scaled to them.

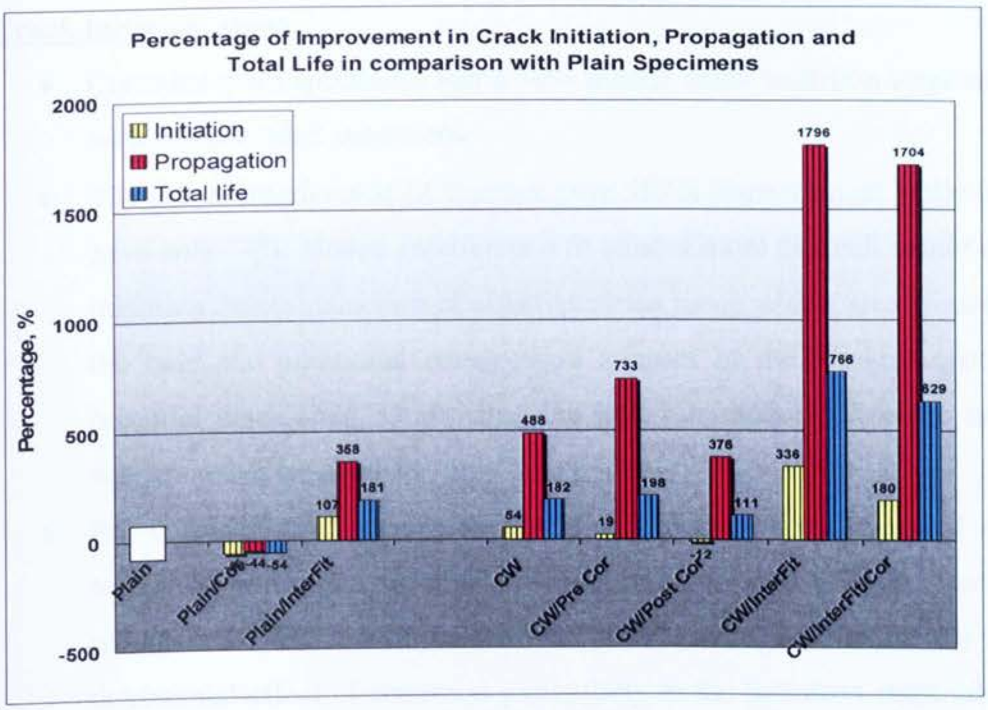

Figure 3.4.4 Average quantitative data on crack initiation and propagation life for specimens tested at $\sigma_{net} = 210 MPa$

Total life analysis

- Corroded plain specimens as expected exhibited a reduction in total life compared with non corroded. The average reduction was 54%
- Interference fit extended total life by 181% which is almost the same value that cold expansion gave (182%). Thus, it is possible to assert that both technologies are approximately equal in terms of their effect on total life
- Cold expansion of pre-corroded specimens gave nearly the same total life improvement as for cold worked uncorroded specimens (+16%), while specimens corroded after cold expansion showed a reduction in total life (-81%). This confirms the detrimental effect of corrosion in the bore of the hole. It should be

noted that cold working of the hole after corrosion will remove all corrosion damage in the hole.

- The combined effects of cold working of a fastener hole together with the insertion of an interference fit fastener gives a considerable improvement in total life (766% for non corroded and 629% for the corroded condition).

Crack initiation stage

- Corroded plain specimens had a 54% shorter crack initiation stage in comparison with non corroded specimens
- The use of interference fit fastener gave 107% improvement while cold working gave only 54%. Hence, interference fit creates more difficult conditions for crack initiation due to reduction of effective stress range within area around the bore of the hole and additional compressive stresses in the weakest central line (the potential crack line) by resisting the hole contraction when the specimens are subjected to.a tensile load.
- Pre corroded CW specimens revealed a slight improvement of + 19% only compared with plain specimens, while post corroded CW specimens showed a reduction of 12% in comparison with plain specimens. This clearly indicated the detrimental effect of corrosion particularly in the initiation stage when corrosion pits at the edge of the hole act as stress concentrators and hence potential sites for crack initiation.
- The combined effects of cold working and interference fit increases the number of cycles until crack initiation (by 366% for non corroded and by 180% for corroded specimens). These results confirm the conclusion made previously of the serious influence of corrosion on the crack initiation process. It should be noted that there is a significant improvement in crack initiation life from the use of the combined technology in comparison with using pure interference fit or pure cold working alone.

Crack Propagation

- Corroded plain specimens had 44% reduction in the crack propagation stage compared with non corroded specimens.
- The crack propagation stage was extended by 358% by the use of an interference fit fastener

- Cold expansion extended the crack growth stage by 488% in pure CW specimens and by 733% in pre corroded CW specimens. This unexpected difference is attributed to scatter.
- Post corroded CW specimens gave a smaller improvement as expected, but this was still at the same level as plain specimens with an interference fit fastener.
- The most dramatic effect in extending the crack propagation stage was achieved with a combination of cold work and interference fit technology which increased it by more than 1700% for both non corroded and corroded specimens.

Similar conclusions can be made for specimens tested at 200 MPa. ***Figure 3.4.5*** shows a considerable increase in crack growth time due to cold expansion (17 times for pure CX and 4.7 times for CX & COR specimens) for CX specimens and an increase in the initiation period (2.5 times) for pure CX specimens.

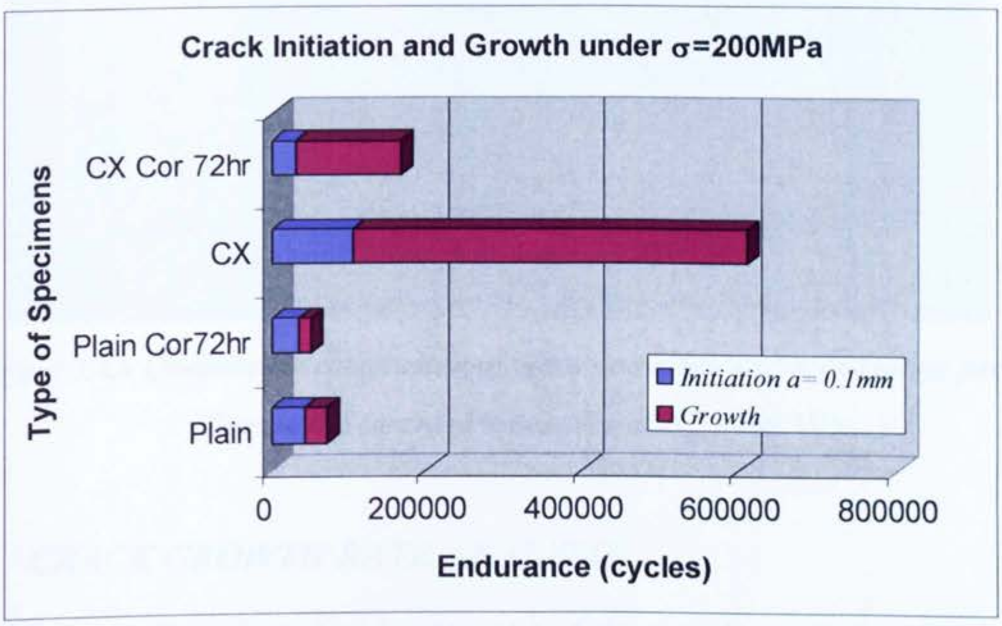

Figure 3.4.5 Average quantitative data on crack initiation and propagation life of specimens tested at σ_{net}=200 MPa

The foregoing experiments included tests of plain specimens subjected to corrosion exposure for times of- 24, 72, 96, or 168 hours followed by testing at 200 MPa. It is of interest to show their gradual reduction in fatigue performance with increasing time of exposure to corrosion. ***Figure 3.4.6*** illustrates this process. Obviously, total life must be reduced when corrosion time increases. This is depicted in the diagram. It should be noted there is a large scatter in fatigue life for corroded specimens as noted previously. From the diagram it can be seen that the average lives for specimens subjected to 24hr corrosion exposure almost equal those for 96hr corrosion exposure and the results for 72hr exposure even exceed those for 24h exposure. It can be seen that the reduction in the total fatigue life can be attributed mainly to the reduced number of cycles for the crack initiation phase whereas the period of crack propagation is reduced by a much smaller amount. More precisely, the relationship between crack initiation time and crack propagation time for 72, 96, and 168 hr corrosion exposure is 2.2, 1.0, and 0.7 .respectively

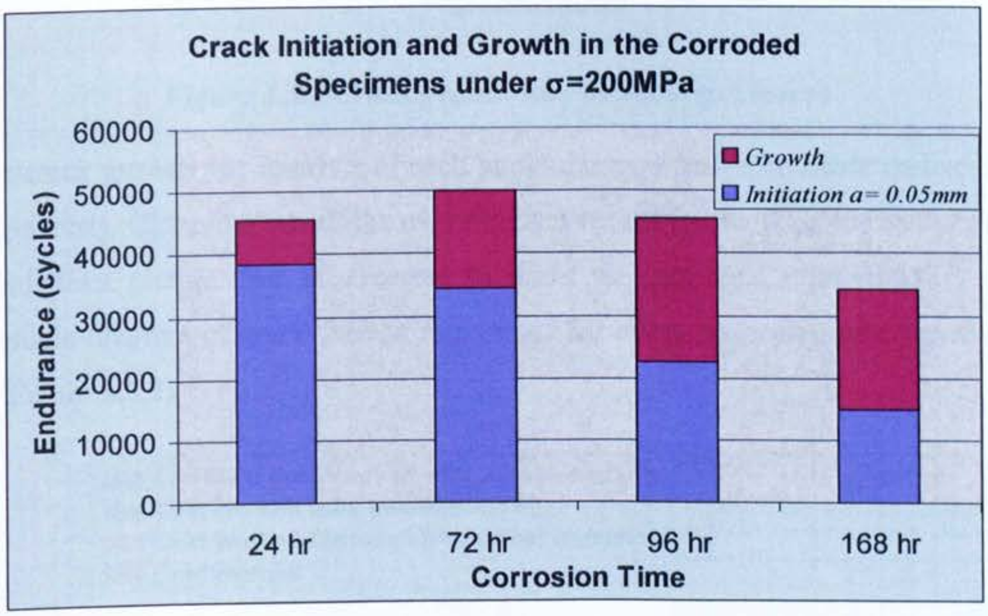

Figure 3.4.6 Quantitative comparison of crack initiation and propagation periods of lives in the corroded specimens at σ_{net} =200 MPa

3.5 CRACK GROWTH RATE ANALYSIS.

To define the effect of a material treatment on fatigue crack growth we should compare the relationship between crack growth rate and *applied SIF* for specimens with and without the treatment. Although this approach may be overly simplistic, it does allow us to identify changes in crack growth rates for similar external loading conditions and similar crack geometries.

First of all, plain specimens were chosen as standard of comparison. The crack growth rates obtained were was compared with ESDU data and showed good agreement (see Figure 3.5.1).

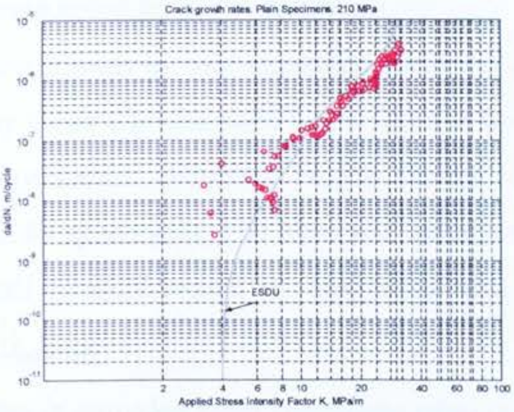

Figure 3.5.1 Crack growth rate in plain specimens

Brief crack growth rate analysis of each particular case had been made earlier in Section Fatigue tests. Gathering the all the experimental results in one diagram would give rather an indistinct picture. For this reason, to make the graphical representation clearer, a schematic diagram of crack growth rate trends for every particular case was constructed (see Figure 3.5.2).

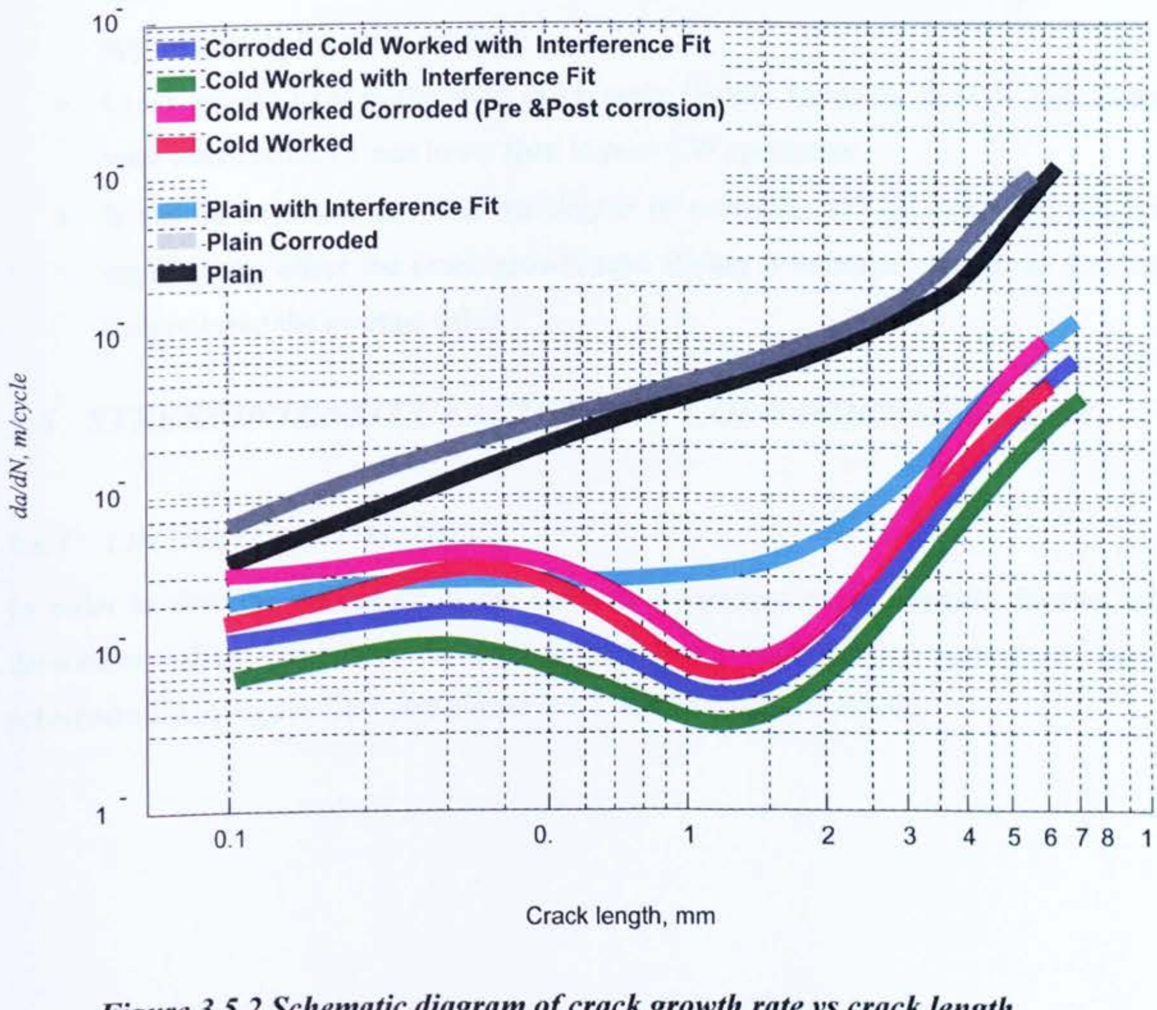

Figure 3.5.2 Schematic diagram of crack growth rate vs crack length

The following features were noted from this diagram.

- Fatigue crack growth rates in cold-expanded and specimens with interference fit were substantially lower than for plain holes. Even at longer surface crack lengths cold-expanded specimens exhibited much lower crack propagation rates compared with plain specimens. The observed reduction in fatigue crack growth rate was the result of an increased σ_{op} compared with plain hole specimens, as Lacarac et. al [220] showed.
- Crack growth rates in corroded plain specimens were higher than in non corroded specimens, especially in short cracks range
- All cold expanded specimens showed a tendency to a reduction in crack growth rate at a distance of 1-2 mm from the hole, while plain specimens with interference fit demonstrated almost a constant crack growth rate up to this point.
- Crack growth rates for all CW specimens with and without interference fit together with crack growth rates for plain specimens with interference fit revealed similar behaviour in the larger crack range (above 1mm). These diagrams have approximately the same gradient.
- Crack growth rates in the short crack range (below 1mm) for the CW specimens with interference fit was lower than in pure CW specimens.
- It should be noted that that the degree of corrosion (72 hr exposure) did not significantly affect the crack growth rate. Rather it increased scatter of the data than reduced the average value.

3.6 STRESS INTENSITY FACTOR FOR COLD WORKED HOLES

3.6.1 LINEAR SUPERPOSITION

In order to describe the nature of the crack face pressure stress intensity factors, and demonstrate their generality, the well known linear superposition procedure shown schematically in Figure 3.6.1 and Figure 3.6.2 will be briefly reviewed.

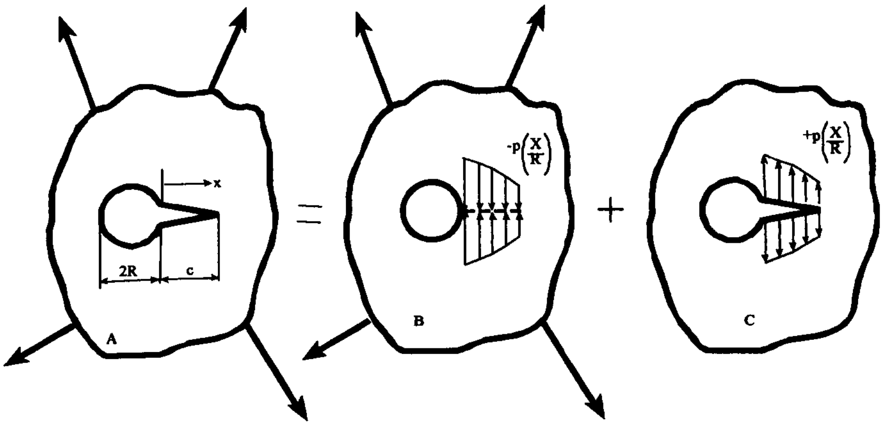

Figure 3.6.1 Schematic of linear superposition showing equivalence between remote load and crack face pressure stress intensity factor.

As indicated in Figure 3.6.1, a cracked body subjected to arbitrary elastic loading (member A) can be resolved into two components (B and C). Member B consists of the uncracked geometry loaded as in case A. A stress free line is introduced along the desired crack plane by cancelling the resulting hoop stress through application of $-p(x/R)$. Here x is the distance measured from the edge of the hole (its radius is ,) and $p(x/R)$ is the hoop stress distribution along the crack plane caused by loading the unflawed member. Since the crack plane is now stress free, a crack can be introduced. Member C consists of the cracked body loaded along the crack faces with the pressure $+p(x/R)$. By superposition, the stress intensity factor for member A is the linear sum of the stress intensity factors for members B and C

$$K_A = K_B + K_C \tag{3.6.1}$$

Now, since the crack plane in member B is stress free, $K_B = 0$, and $K_A = K_C$. Thus, the stress intensity factor for the original problem is identical to that for a crack loaded with the unflawed hoop stress distribution.

If the crack face pressure is defined in terms of a polynomial expansion, it is possible to obtain a "general" solution in terms of the polynomial coefficients. This latter point is demonstrated by the superposition described in Figure 3.6.2, where

$$p(x/R) = A_0 + A_1(x/R) + A_2(x/R)^2 + \cdots \tag{3.6.2}$$

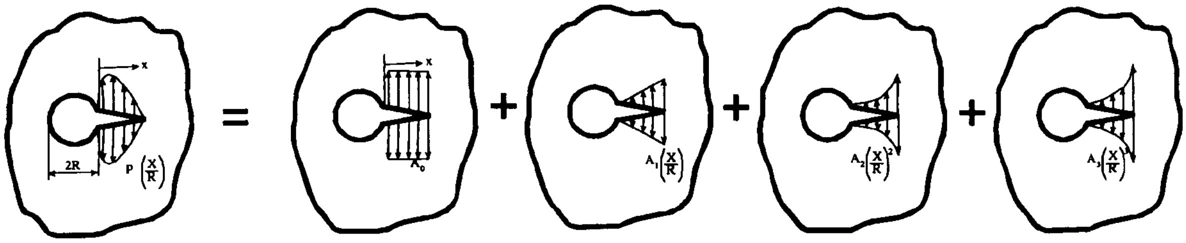

Figure 3.6.2 Schematic of crack face pressure problem resolved into components represented by a polynomial expansion for $p(x/R)$

$$K_I = K_0 + K_1 + K_2 + \ldots = \sum K_n \qquad (3.6.3)$$

Here K_I is the mode-one stress intensity factor for the complete crack face loading (equivalent to the original stress intensity factor for member A in Figure 3.6.1), and the K_n are the stress intensity factors due to the individual pressure terms $A_n(x/R)^n$ in the expansion for $p(x/R)$.

Assuming the principle of superposition:

$$K_{eff} = K_{applied} + K_{residual} \qquad (3.6.4)$$

for any given crack length and geometry. K_{eff} is the effective net stress intensity factor, $K_{applied}$ is the stress intensity factor for the same crack with the remote, applied stress only and $K_{residual}$ is the change in stress intensity due to the presence of the residual stresses.

For a crack growing either completely or partially within a residual stress field the SIF is generally calculated using either the weight function [221,222] or Green's function [223] technique (both of which rely on the principle of superposition). While the two methods are closely related, from an application point of view, they are distinctly different. The weight function method, as defined by Bueckner and Rice, requires knowledge of the crack opening displacement profile for some reference loading condition. The Green's function method, on the other hand, is based on the body's response to a unit point load (hence the term Green's function). In general, given an arbitrary stress distribution and the Green's function for the crack / geometry being analyzed, the corresponding SIF is found by integrating the product of the normalized stress distribution and the Green's function over the crack area.

The two crack configurations considered in this study were a through thickness crack and a quarter-elliptical corner crack at a hole in a plate of finite width and thickness. Calculation of the SIF was based on the weight function methods presented below.

3.6.2 EFFECTIVE SIF FOR THROUGH CRACKED FASTENER HOLES STRENGTHENED BY COLD EXPANSION.

According to Rice(221), knowing the SIF K_I and the displacement field $u_I(x,a)$ for a cracked body under a symmetrical loading (reference case), we may obtain the Mode I weight function in the co-ordinate system given in Figure 3.6.3 from :

$$h(x,a) = \frac{E'}{K_I}\frac{\partial u_I(x,a)}{\partial a} \qquad \textbf{(3.6.5)}$$

where $E' = E$ (Young modulus, 71.4GPa) for the case of plane stress and $E' = E(1-\nu^2)$ for the plain strain.

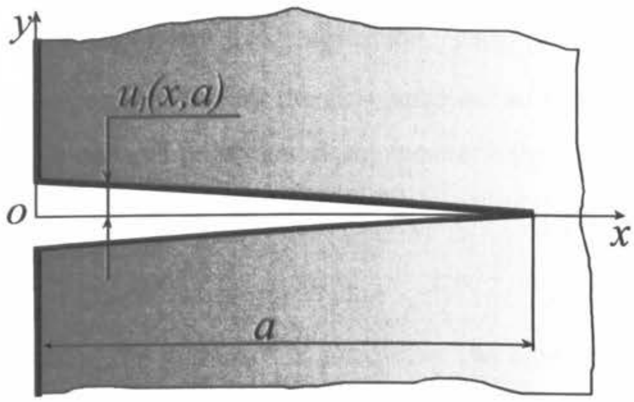

Figure 3.6.3 Co-ordinate system for weight function equations

Once the weight functiona are determined for a given geometry, then the SIF for any other loading system applied to the same cracked body can be calculated by

$$K = \int_0^a \sigma(x)\cdot h(x,a)dx = \frac{E'}{K_I}\int_0^a \sigma(x)\cdot\frac{\partial u_I(x,a)}{\partial a}dx \qquad \textbf{(3.6.6)}$$

In ***(3.6.6)*** $\sigma(x)$ are the stress values on the crack line that appear in the uncracked body due to the loading for which the SIF is calculated.

The equations for the stress intensity factor for plate containing central hole and asymmetrical or symmetrical through thickness cracks under tension, eq. ***(3.6.7)***, were taken from [224]

$$K_I = \sigma\sqrt{\pi a}F(\lambda) \qquad (3.6.7)$$

Newman's calibration factors (approximation of Bowie solution) :

for an asymmetric crack

$$F_{\rightarrow}(\lambda) = 0.707 - 0.18\lambda + 6.55\lambda^2 - 10.54\lambda^3 + 6.85\lambda^4$$

for a symmetric crack

$$F_{\leftrightarrow}(\lambda) = 1 - 0.15\lambda + 3.46\lambda^2 - 4.17\lambda^3 + 3.58\lambda^4$$

where $\lambda = \dfrac{r}{r+a}$;

The solution was not accompanied by expressions of the crack face displacements. In order to be able to apply the weight function technique in this case, the approach of Petroski and Achenbach [225] was used. These authors used the well-known expression for the displacement around the crack tip in an infinite cracked plate

$$u_y(a,x) = \frac{4K}{E'}\left(\frac{a-x}{2\pi}\right)^{1/2} \qquad (3.6.8)$$

where $K_I = \sigma\sqrt{\pi a}$. Starting from this expression, they propose for the crack face displacements a series expansion having the first term in the form given by (3.6.8),and the other terms tend to be zero while approaching the crack tip

$$u(x,a) = \sum_n C_i(a)^{\frac{1}{2}-n}(a-x)^{\frac{1}{2}+n} \qquad (3.6.9)$$

From this series expansion, the authors [225] used only the first two terms, written in the form

$$u_I(a,x) = \frac{\sigma}{E'\sqrt{2}}\left[4F\left(\frac{a}{r}\right)a^{\frac{1}{2}}(a-x)^{\frac{1}{2}} + G\left(\frac{a}{r}\right)a^{-\frac{1}{2}}(a-x)^{\frac{3}{2}}\right] \qquad (3.6.10)$$

where $F\left(\dfrac{a}{r}\right)$ and $G\left(\dfrac{a}{r}\right)$ are functions of the crack length and characteristic dimension.

The function $F\left(\dfrac{a}{r}\right) = K/\sigma\sqrt{\pi a}$ can be calculated from the solutions for the stress intensity factor taken from eq. ***(3.6.7)*** and $G\left(\dfrac{a}{r}\right)$ is obtained from eq.***(3.6.6)*** written for the reference case $K = K_{Ir}$ (self-consistency). In this case, the following expression is obtained

$$K_I = E'\int_0^a \sigma_r(x)\cdot\frac{\partial u_I(x,a)}{\partial a}dx, \qquad (3.6.11)$$

$\sigma_r(x)$ being the crack line stress in the reference case. Integrating this equation with respect to a yields:

$$K = \int_0^a [K_I(a+r)]^2 d(a+r) = E'\int_0^a \sigma_r(x)\cdot\partial u_I(x,a)dx \qquad (3.6.12)$$

Introducing *(3.6.10)* in *(3.6.12)*, and using the known values of the reference stress intensity factor it is possible to obtain an equation in which $G\left(\frac{a}{r}\right)$ is the only unknown. Solving this equation [225]:

$$G\left(\frac{a}{r}\right) = \frac{\left[I_1(a) - 4F(a/r)\sqrt{a}\cdot I_2(a)\right]\sqrt{a}}{I_3(a)}, \qquad (3.6.13)$$

with

$$I_1(a) = \pi\sqrt{2}\sigma\int_0^a F^2\left(\frac{a+r}{r}\right)\cdot(a+r)d(a+r), \qquad (3.6.14)$$

$$I_2(a) = \int_0^a \sigma_r(x)\cdot(a-x)^{1/2}dx, \qquad (3.6.15)$$

$$I_3(a) = \int_0^a \sigma_r(x)\cdot(a-x)^{3/2}dx. \qquad (3.6.16)$$

Once the weight function is known, then the stress intensity factor can be determined from eq. *(3.6.6)* for any other loading case $\sigma_r(x)$, as

$$K = \frac{E'}{K_{Ir}}\int_0^a \sigma(x)\cdot\frac{\partial u_I(x,a)}{\partial a}dx = \qquad (3.6.17)$$

$$= \frac{\sigma}{K_{Ir}\sqrt{2}}\int_0^a \sigma(x)\cdot\frac{\partial}{\partial a}\times\left[4F\left(\frac{a}{r}\right)a^{\frac{1}{2}}(a-x)^{\frac{1}{2}} + G\left(\frac{a}{r}\right)a^{-\frac{1}{2}}(a-x)^{\frac{3}{2}}\right]dx$$

For applying eq. *(3.6.5)* to determine the weight function, the expression for the crack face displacements should be derived in the form given by relation *(3.6.10)*. The coefficient $G\left(\frac{a}{r}\right)$ was calculated according to eqs *(3.6.13)- (3.6.16)* where the expression $\sigma_r(x)$ of the stress distribution on the crack line was determined as for unflawed hole loaded with remote tension σ (accepted for example 200MPa). The radial stress σ_r along a radial line located at an angle $\theta = \pi/2$ to the loading axis (the crack line) is given by (226) and written in the co-ordinate system from Figure 3.6.3 as

$$\sigma_r(x) = \sigma(x)_{ApLoad} = \frac{\sigma}{2}\left[2 + \left(\frac{r}{z+r}\right)^2 + 3\left(\frac{r}{x+r}\right)^4\right] \qquad (3.6.18)$$

In addition to the radial stress, the residual stresses caused by cold expansion are present in the narrow area around the hole.

Experimental Residual Stress values for the outlet side after cold expansion were taken from different sources. Some experimental results for residual stress distributions due to cold expansion are presented below in the table and its graphical representation in Figure1.11.4.

D. Stefanescu and all "The effect of high compressive loading on residual stresses and fatigue crack growth at cold expanded holes [227]	AL 7050 T76, t=5mm, d=9.52mm, Cold Expansion 4%
V.D.Lacarac, A.A.Garcia-Granada, D.J.Smith, M.J.Pavier "Prediction of the growth rate for fatigue cracks emanating from cold expanded holes "[228]	Al 2650 , t=6mm, d=6.31, Cold Expansion 4%
M. Priest PhD thesis, M. Priest and all (30)	2024 t=8mm,d=6.35mm (DRA, X-ray) 2024 t=8mm,d=6.35mm,exit (X-ray,Priest) 2024 t=8mm,d=6.35mm,entrance (X-ray, Priest) 2024 t=6mm,d=6.35mm,entrance (X-ray, Priest) 2024 t=6mm,d=6.35mm,exit (X-ray,Priest) 2024 d=30 mm (Sach method)

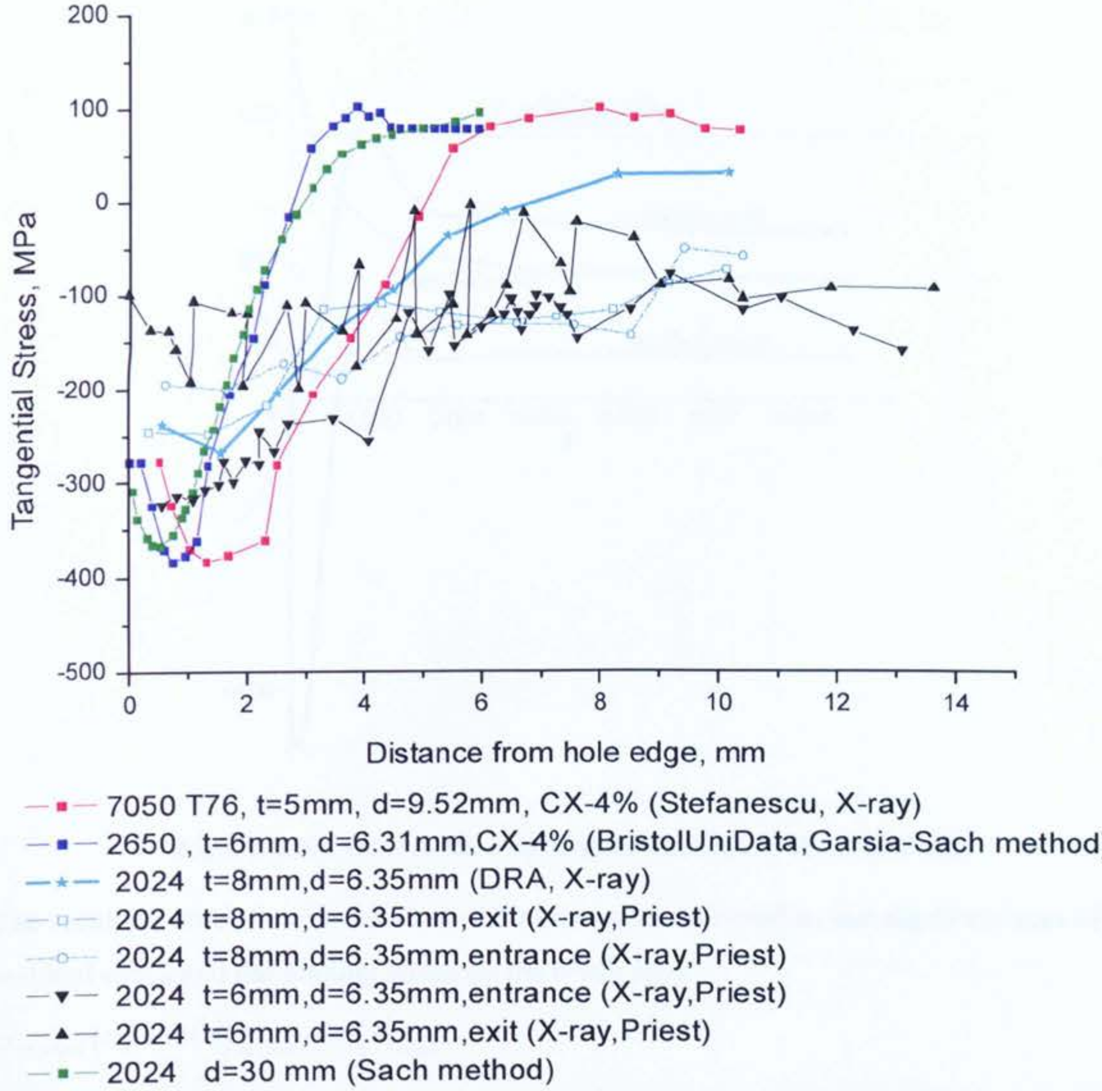

Figure 3.6.4 Experimental results of residual stresses due to cold expansion

As an example, experimental data on Al 2650 were taken for assessment of their influence on effective SIF. The data were approximated by the function shown below:

$$\sigma(x)_{resid} = A_0 + A_1 \exp\left(-\frac{(x - A_2)}{A_3}\right)\sin(A_4 x + A_5), \qquad (3.6.19)$$

where x – distance form the hole edge

The Figure 3.6.5 shows the distribution of radial and residual stresses and their resultant.

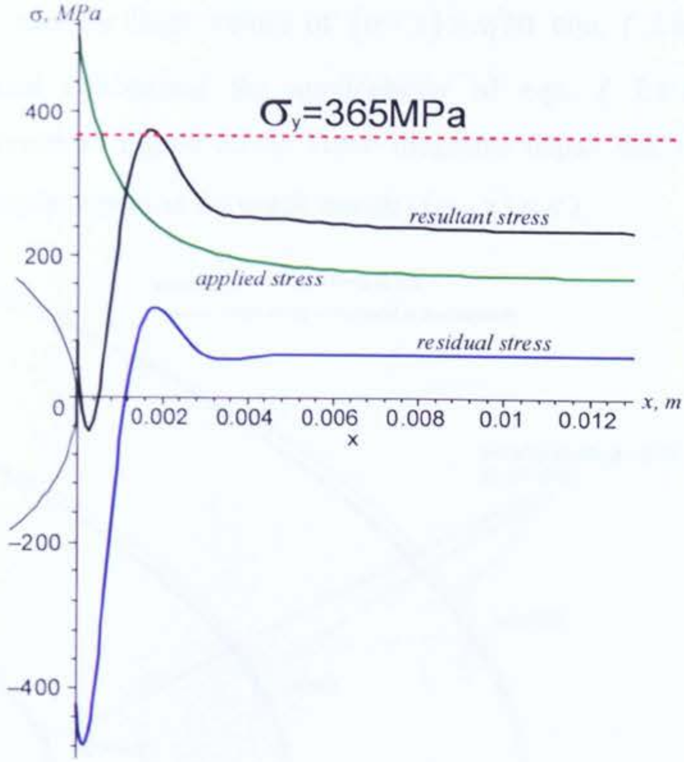

Figure 3.6.5 Distribution of stresses acting on the crack line

The resultant crack face pressure distribution was considered as the algebraic sum of the residual stress and the loading stress on the crack face:

$$\sigma_{resultant}(x) = \sigma(x)_{ApLoad} + \sigma(x)_{resid}$$

Two approaches were used in displacement function determination. The first one was taken from [229], who in their turn reference to [225]. These produce the equation ***(3.6.10)*** given above.

The second approach was taken from [230] who refer to [231]. They give the following equation:

$$u_I(a,x) = 4\frac{K_B}{H}\left(\frac{a-x}{2\pi}\right)^{1/2} \qquad \textbf{\textit{(3.6.20)}}$$

where $H = E$ for plane stress or $H = E/(1-\nu^2)$ for plane strain;

In our case, most of the fatigue crack propagation took place under plain strain conditions characterised by flat fracture surface, while final fracture was under plain stress conditions with slant fracture surfaces.

$K_B = \sigma\sqrt{\pi a}F_B\left(\frac{a}{r}\right)$ - Bowie solution for plate with a hole under tension.(*reference case*)

It is said in [230] that for large values of $(a-x) > a/10$ eqn. ***(3.6.20)*** loses validity; nothing was found concerning the applicability of eqn. ***(3.6.10).*** The solutions considered are shown in Figure 3.6.6. These diagrams depict the shape of one of the crack faces and displacement at the crack mouth ($(a-x) = a$).

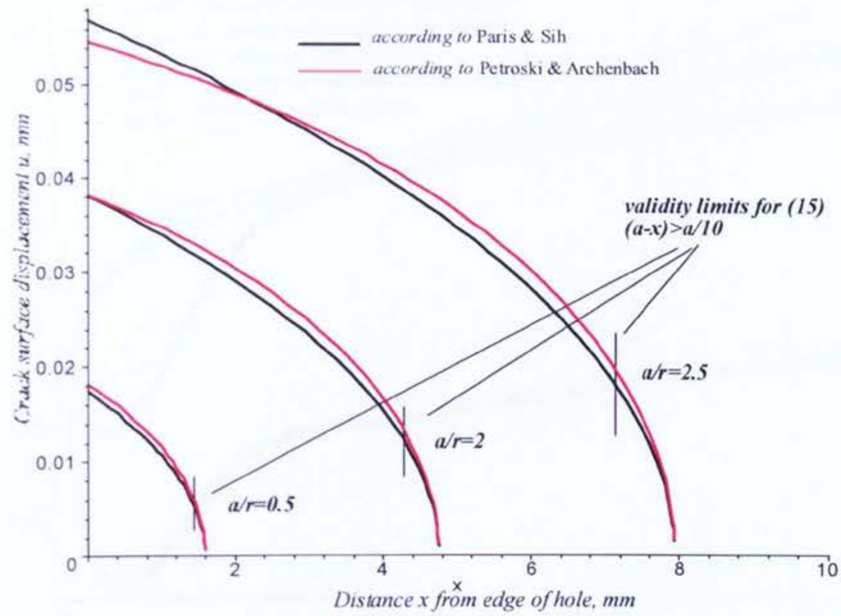

Figure 3.6.6 Crack surface profiles for symmetrical crack solution (Bowie solution, reference case)

It should be noted that the disagreement between the solutions is negligible and we can use both of them in the further calculations.

After determining the displacement variation in the reference case, the stress intensity factor can be calculated for the residual stress loading.

Analysis of the SIF

The following SIF solutions were considered:

- SIF according to Bowie solution (*reference case*) $K_B = \sigma\sqrt{\pi a}F_B\left(\dfrac{a}{r}\right)$
- Effective SIF without alllowing for cold work $K_{Eff} = \dfrac{E'}{K_B}\displaystyle\int_0^a \sigma_r(x)\cdot\dfrac{\partial u_I(x,a)}{\partial a}dx$
- Residual SIF $K_{residual} = \dfrac{E'}{K_B}\displaystyle\int_0^a \sigma_{residual}(x)\cdot\dfrac{\partial u_I(x,a)}{\partial a}dx$
- Resultant SIF $K_{resultant} = K_{Eff} + K_{residual} = \dfrac{E'}{K_B}\displaystyle\int_0^a \sigma_{resultant}(x)\cdot\dfrac{\partial u_I(x,a)}{\partial a}dx$

The solutions are given in the Figure 3.6.7. Comparing the SIF solutions accounting different approaches to displacement function, it is clear that the both approaches are very similar and eligible for further use

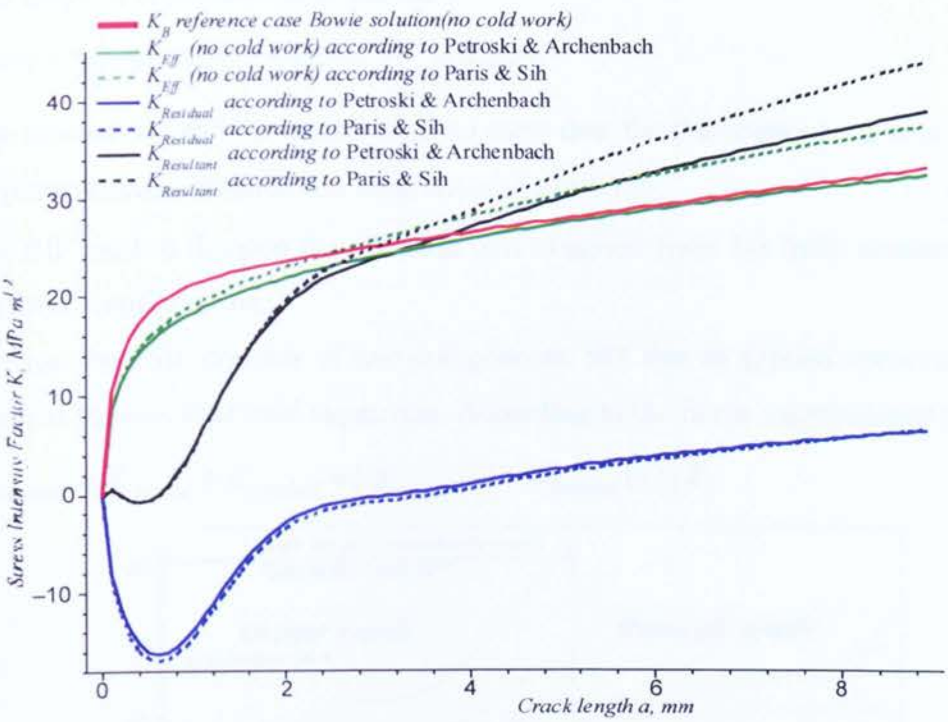

Figure 3.6.7 Stress Intensity Factors for a cold expanded hole

3.6.3 SIF FOR CORNER CRACK FASTENER HOLES STRENGTHENED BY COLD EXPANSION.

Mode I Stress Intensity Factors K_1 given in [159]

Two-Symmetric Corner Cracks – The empirical stress intensity factor equation for a two-symmetric Quarterelliptical Corner Crack at a hole in a finite plate) subjected to tension is shown in Figure 1.7.7.

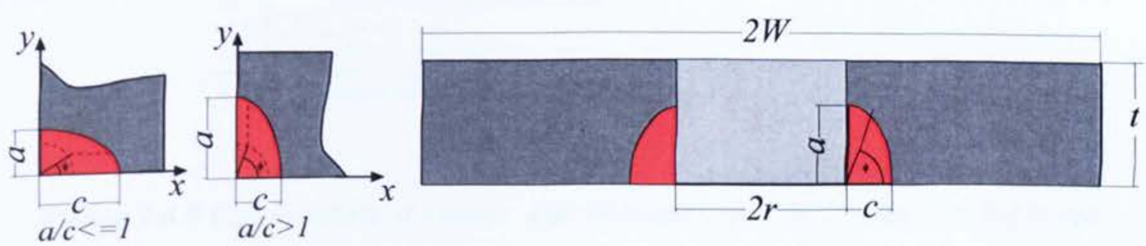

Figure 3.6.8 Corner Crack at a hole and coordinate system used to determine parametric angle

$$K_1 = \sigma\sqrt{\pi\frac{a}{Q}}F_{ch}\left(\frac{a}{c},\frac{a}{t},\frac{r}{t},\frac{r}{W},\frac{c}{W},\phi\right) \quad (3.6.21)$$

The range of applicability for the SIF :

$$\varphi = 0 \div \pi/2, a/t < 1, a/c = 0.2 \div 2, R/t = 0.5 \div 1,$$

The solution is valid for crack length no more than the thickness i.e. up to $a = t$!

A quartercircular solution has been chosen ($a/c = 1$).

The SIF used to develop the equation was obtained from 3D finite element analysis for the crack configuration.

The resultant SIF consists of two components: SIF due to applied stress and SIF due to residual stresses after cold expansion. According to the linear superposition principle

$$K_{Resultant} = K_{ApLoad} + K_{Residual} = \left(\sigma_{ApLoad}(x) + \sigma_{Residual}(x)\right)K_1$$

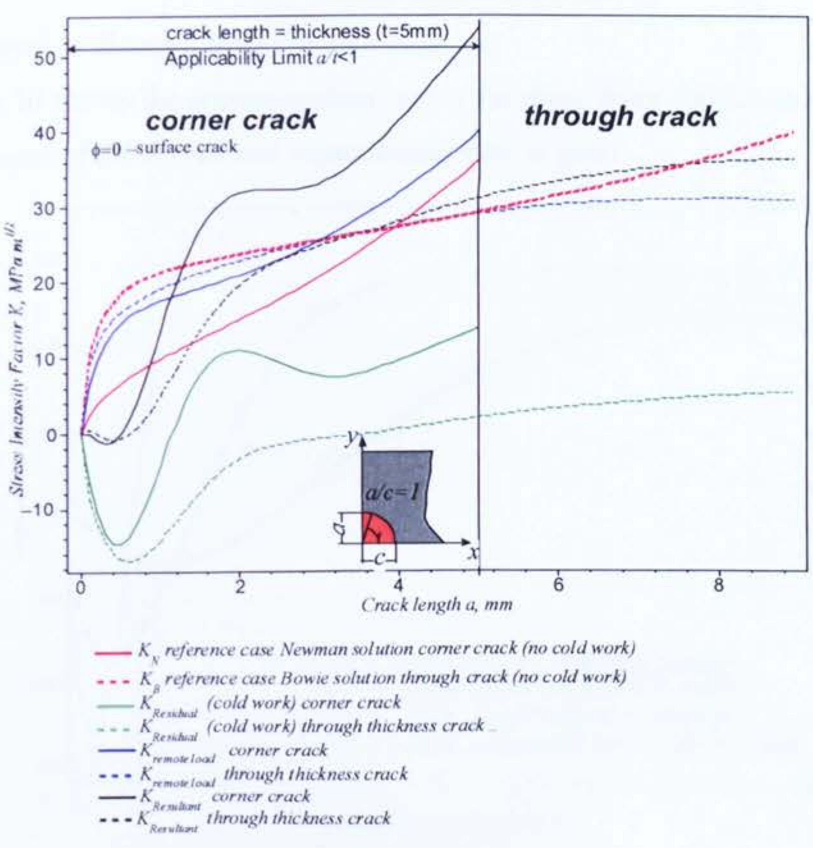

Figure 3.6.9 Combination of corner and through crack SIF acting during crack growth

Figure 1.11.9 shows combination of corner and through crack SIF acting during crack growth. The gap between the SIF solutions for the corner and through crack can be explained by the very rapid transformation of the corner crack into a through crack.

3.6.4 THE INFLUENCE OF DIFFERENT EXPERIMENTAL RESIDUAL STRESS DISTRIBUTIONS ON THE SIF SOLUTION

Experimental Residual Stress distribution data on the outlet side after cold expansion taken from different sources were given previously in the Figure 3.6.4.

As an example, experimental data on Al 2650 (BristolUniData, Garsia-Sach method), Al 2024 (DRA, X-ray), Al 2024 (Sach method) were taken for assessment of their influence on effective SIF. The data were approximated by the function:

$$\sigma_{resid}=A_0+A_1\exp(-\frac{(x-A_2)}{A_3})\sin(A_4x+A_5),$$

where x equal to distance from the hole edge

Figure 3.6.10 shows the approximation curves for these three chosen cases. It is clear that the agreement of the curves and experimental data is good.

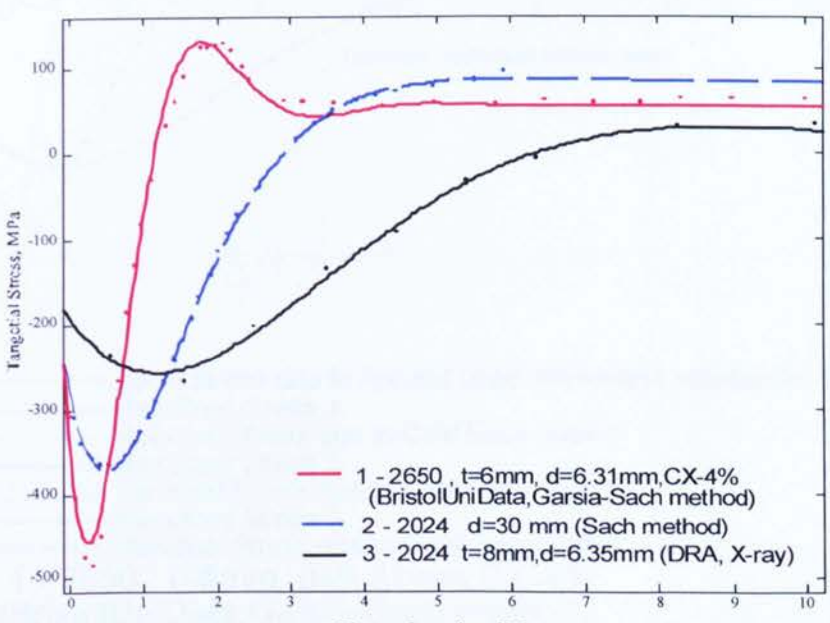

Figure 3.6.10 Approximation of different experimental data on residual stress distribution with function

Figure 3.6.11 shows the distribution of local, residual stresses and resultant stresses according to 3 different sets of experimental data

Figure 3.6.12 shows the distribution of local, residual and resultant SIF according to the 3 considered cases.

According to the superposition principle given previously $K_{Resultant} = K_{ApLoad} + K_{Residual}$

Newman's SIF solution for a corner crack was used for further calculations. Bowie's solution for a through crack is given as a reference case

The initial experimental data of residual stress distribution is seen to make a significant contribution to SIF distribution.

That is why care must be taken in the determination of residual stress distribution.

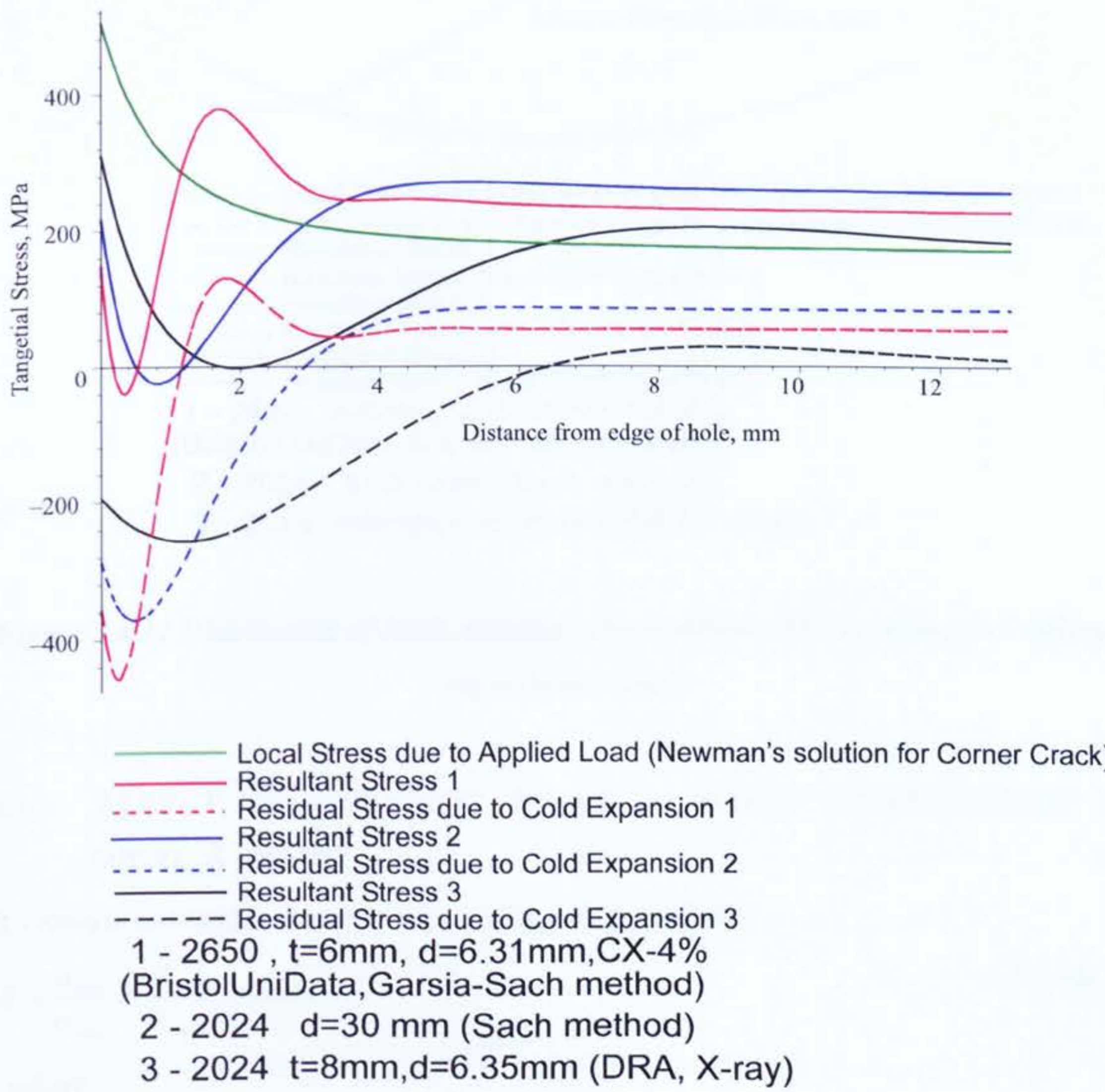

Figure 3.6.11 Distribution of local, residual stresses and resultant stresses according to 3 different experimental data

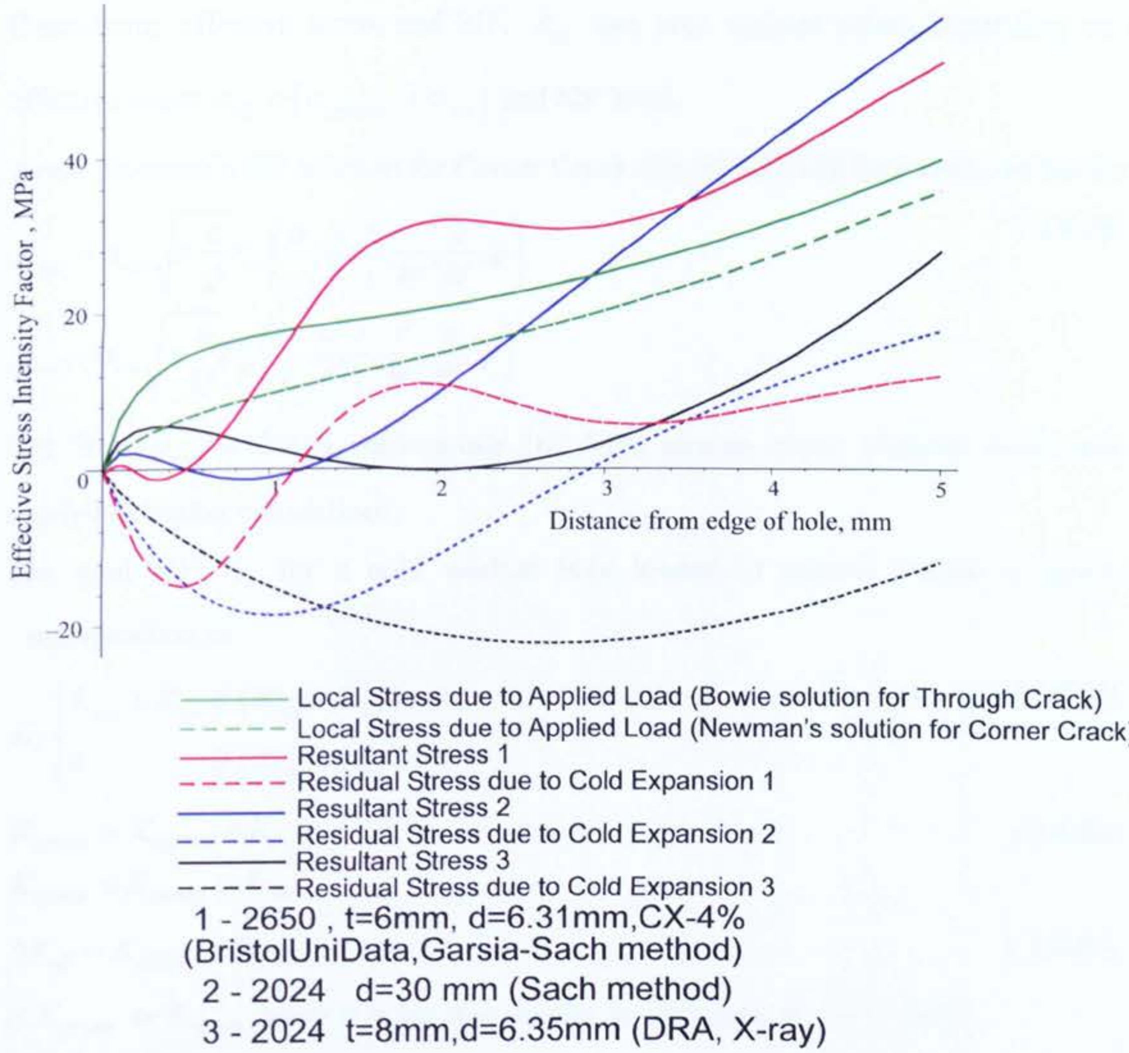

Figure 3.6.12 Distribution of local, residual and resultant SIF according to 3 different experimental data

3.6.5 EFFECT OF DIFFERENT RESIDUAL STRESS DISTRIBUTIONS ON LOCAL R RATIO

R - ratio is constant in terms of remote applied stress of SIF.

$$R = \frac{\sigma_{\min}}{\sigma_{\max}} = \frac{K_{I\min}}{K_{I\max}} = const \qquad (3.6.22)$$

, where

$$K_I = \sigma_{app}\sqrt{\pi\frac{a}{Q}}F_{ch}\left(\frac{a}{c},\frac{a}{t},\frac{r}{t},\frac{r}{W},\frac{c}{W},\phi\right) \qquad (3.6.23)$$

Considering effective stress and SIF, R_{eff} can take various values depending on the effective stress $\sigma_{eff} = \left(\sigma_{app\,local} + \sigma_{res}\right)$ and SIF level.

Terms: Newman's SIF solution for Corner Crack at hole only will be considered further

$$K_{app} = \sigma_{app}\sqrt{\pi\frac{a}{Q}}F_{ch}\left(\frac{a}{c},\frac{a}{t},\frac{r}{t},\frac{r}{W},\frac{c}{W},\phi\right) \qquad (3.6.24)$$

$$K_{res} = \sigma_{res}\sqrt{\pi\frac{a}{Q}}F_{ch}\left(\frac{a}{c},\frac{a}{t},\frac{r}{t},\frac{r}{W},\frac{c}{W},\phi\right)$$

Net Stress σ_{app}=210MPa corresponds 168 MPa remote stress. Remote stress will be applied in further calculations.

The total SIF K_I for a cold worked hole loaded in remote tension is given by superposition as

$$K_I\begin{cases} K_{app} + K_{res} & if\left(K_{app} + K_{res}\right) > 0 \\ 0 & if\left(K_{app} + K_{res}\right) \le 0 \end{cases} \qquad (3.6.25)$$

$$K_{eff\,\max} = K_{app\,\max} + K_{res} \qquad (3.6.26)$$

$$K_{eff\,\min} = K_{app\,\min} + K_{res}$$

$$\Delta K_{eff} = K_{eff\,\max} - K_{eff\,\min} \qquad (3.6.27)$$

If $K_{eff\,\max}$ or $K_{eff\,\min}$ appear to be less than zero they are assumed to be equal to zero.

$R_{eff} = \dfrac{K_{eff\,\min}}{K_{eff\,\max}}$ ***; Assume that $R_{eff} = 0$ if $\Delta K_{eff} = 0$ (i.e. the crack does not grow)***

3 different residual stress distributions given in Figure 3.6.10 were considered.

The ΔK_{eff} and R_{eff} relationships were from DRA.

$K_{app\max}$, $K_{app\min}$ (not taking into account Residual Stresses due to CW) with constant R=0.1 are marked as blue lines in the $\Delta K_{eff}\left(a\right)$ diagram (these reference lines are a blue solid line for $K_{app\max}$ and a blue dashed line for $K_{app\min}$). The range of ΔK_{eff}, taking into account CW Residual Stresses, shown in the figure as the area between the upper red dash dot line and the lower dotted red line. Since the portion of the stress range below zero is ignored, the true values of ΔK_{eff} are in reality the upper red dash dot line.

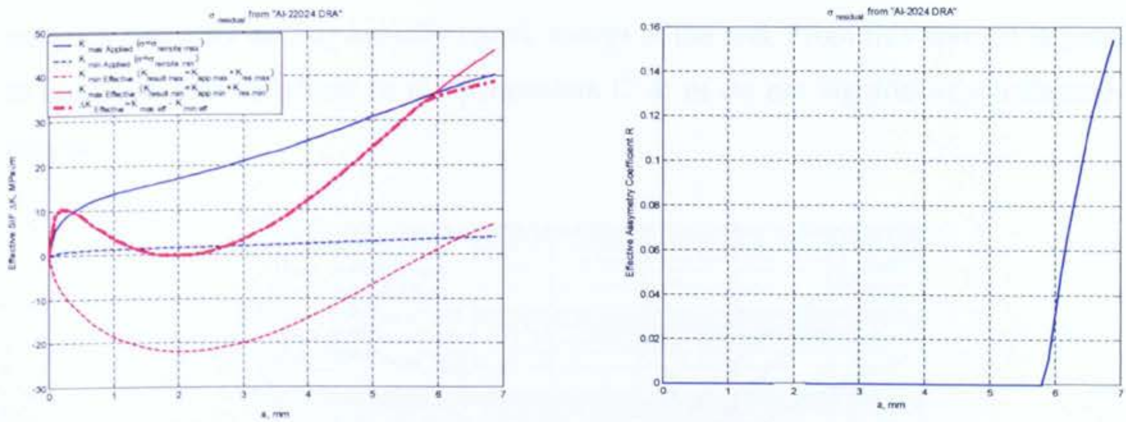

Figure 3.6.13 Effective SIF according Residual Stress Distribution from DRA

Apparently ΔK_{eff} equals $K_{eff\,\max}$ within the whole range of the crack length where $K_{eff\,\min}$ is below zero. Thus the coefficient $R_{eff} = 0$ or <0 within the same range for the same reason. It increases only when $K_{eff\,\min}$ is above zero. The diagram shows that if $K_{app\,\max}$ > 0 over the whole range of crack lengths the crack will grow continuously with the rate of propagation only changing due to variations in the function of ΔK_{eff}.

Using the Paris Crack Growth Rate equation $\frac{da}{dN} = C\left(\Delta K_{eff}\right)^m$, we can model the Crack Growth Rate curves. ESDU gives the following values of the parameters C & m for 3 ranges of Crack Growth Rate range and three R values:

Table 10 C and m parameters from ESDU

	R		0.005	0.5	0.65
Range da/dN	10^{-6} - 10^{-5}	C_3	**7.30 10^{-12}**	**5.00 10^{-14}**	
		m_3	**4.7**	**6**	
	10^{-7} - 10^{-6}	C_2	**1.90 10^{-11}**	**1.70 10^{-11}**	**1.60 10^{-12}**
		m_2	**3.7**	**4**	**5.2**
	10^{-8} - 10^{-7}	C_1	**5.20 10^{-13}**	**1.80 10^{-11}**	**5.40 10^{-12}**
		m_1	**5.2**	**4**	**4.7**

In the case of DRA data, $R_{eff} \leq 0$ within the most important crack length range i.e. up to 6mm. From this dasta Crack Growth Rate diagrams for C & m values corresponding to all the ranges of *da/dN* with an R value =0.005 (see Table 10)were used to assess their influence on the curve.

The diagram below gives the modelled curves obtained from ΔK_{eff} and $K_{eff\max}$. They coincide precisely as they actually equal, except at the end. From this view, it is possible to conclude that variations in the parameters C & m do not significantly influence the curves.

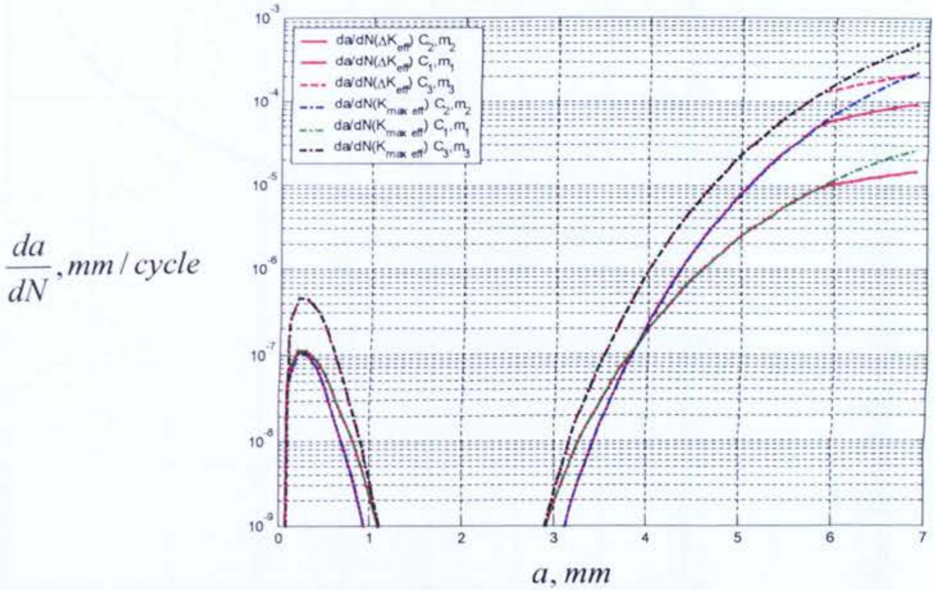

Figure 3.6.14 Effective and nominal crack growth rate curves

To evaluate the behaviour of $\Delta K_{eff}(a)$, $R_{eff}(a)$ for other possible σ_{res} distributions, similar diagrams were produced as given below. It is certain that the shape of $R_{eff}(a)$ is determined by the form of $\sigma_{\text{resultant}}(a)$. Modelling results of the various cases considered showed that the R_{eff} variation was between 0 and 0.4.

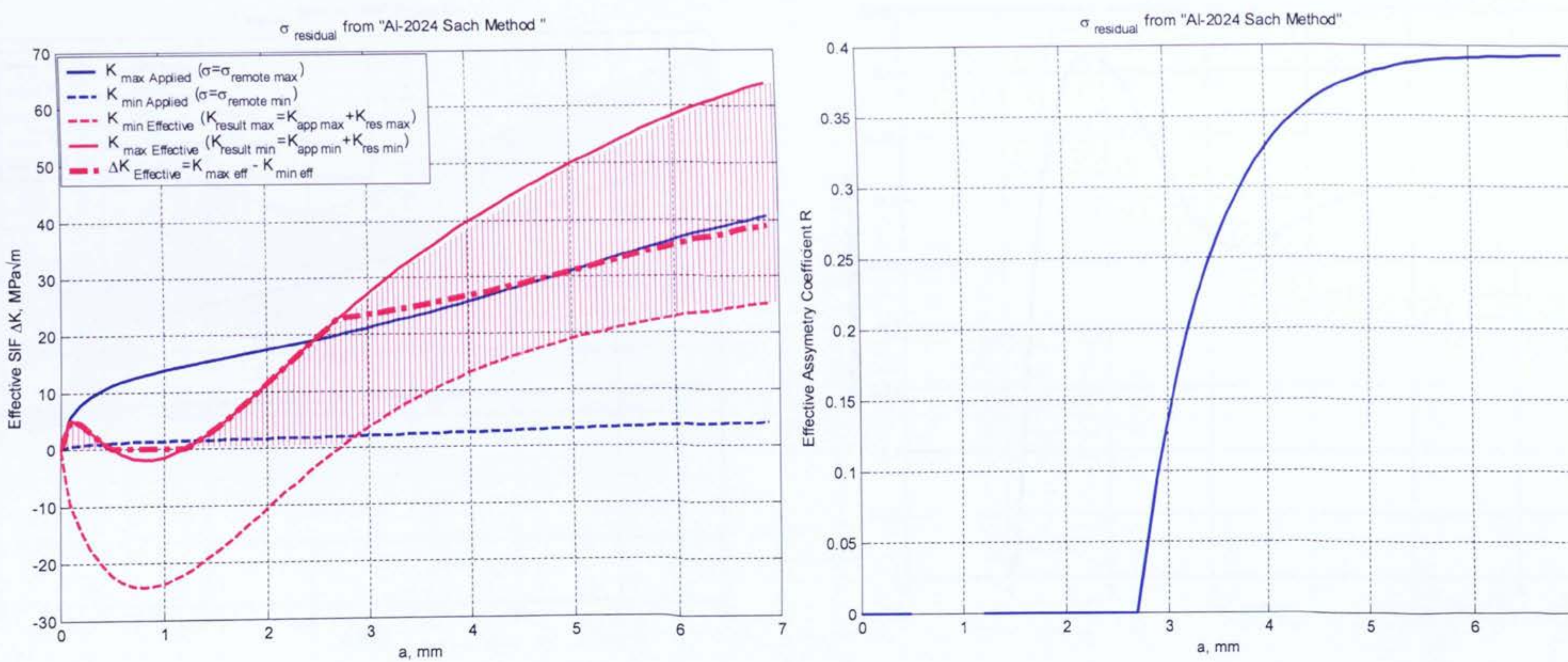

Figure 3.6.15 Effective SIF according Residual Stress Distribution from Sach Method

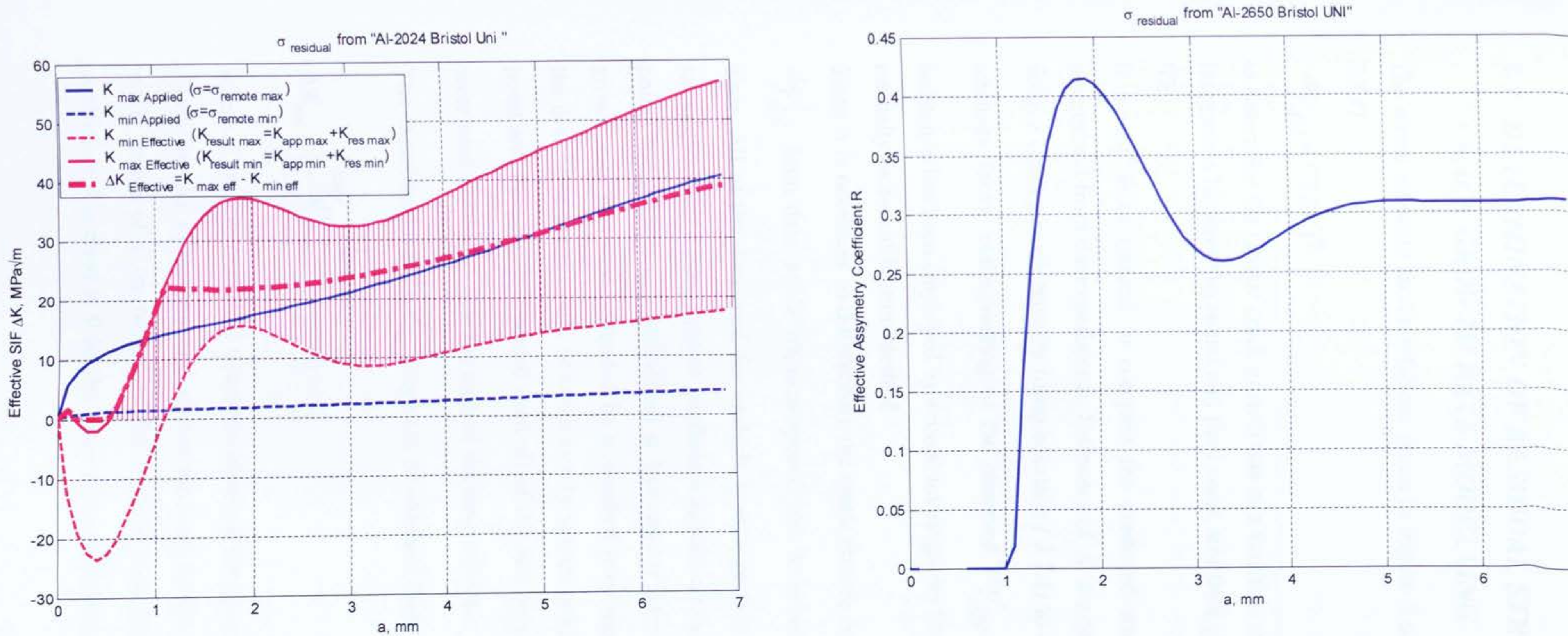

Figure 3.6.16 Effective SIF according Residual Stress Distribution from Bristol Universitet

3.7 DETERMINATION OF RESIDUAL STRESS DISTRIBUTION AND CRACK GROWTH RATE MODELLING.

The stress intensity factor solutions given in Figure 3.6.12 may be used with equation *(3.7.1)*

$$da/dN = C(\Delta K)^m \qquad (3.7.1)$$

to determine the fatigue crack growth rate as a function of crack length.

Integration between the initial and final crack size then gives the total fatigue crack growth life.

It would be of interest to compare the predicted stress intensity factors with values determined from the experiments. Estimates of K are readily obtained from the measured fatigue crack growth rates by using equation *(3.7.1)* to compute the cyclic range in stress intensity factor corresponding to the observed da/dN. This fatigue crack growth rate technique has been employed by several investigators [15, 21-23] as an experimental stress intensity factor calibration method.

Since it is necessary to differentiate the crack growth curves to obtain K, computation of da/dN from data $a(N)$ requires special care to prevent magnification of experimental error. All of the data used for analysis here were first smoothed by a simple averaging technique. Next a least squares parabola was passed through a set of seven successive data points and crack lengths calculated at four regular intervals over the range of the set. The growth rate was then computed by a standard least squares formula which approximates the derivative at the centre of seven evenly spaced points. The set was then advanced one point and the process repeated until all of the data were used. Slightly different formulas were used for da/dN near the ends of the range of data.

The experimental SIF ΔK_{exp} range can be obtained from *(3.7.1)*

$$\Delta K_{exp} = \left(\frac{da/dN}{C} \right)^{\frac{1}{m}}, \qquad (3.7.2)$$

where C, m are empirical constants obtained for specimens with a known K. They are characteristics of material and are not functions of the geometry of the specimens. In this work, values of C, m were used for Al 2024 from ESDU (see Table 10). Assuming the coefficient R is close to 0 for the range of crack lengths measured, we may use ESDU data for this alloy at R=0.005 so the parameters over the Crack Growth Rate Ranges *should* be similar to those measured experimentally.

Fatigue crack growth rates were computed as a function of crack length by this procedure for the 3 plain and 3 cold worked specimens tested at 210 MPa. One dominant crack in each specimen was selected then their $a(N)$ data were subjected to further analysis. Cracks in the plain specimens were assumed to be through thickness cracks and those in the cold worked specimens to be corner cracks. Corresponding SIF solutions were used for SIF prediction. Calculations of experimental $\Delta K_{\exp}$ were then made by eq. ***(3.7.2)*** and are summarized in Figure 3.7.1 as the collection of experimental data points.

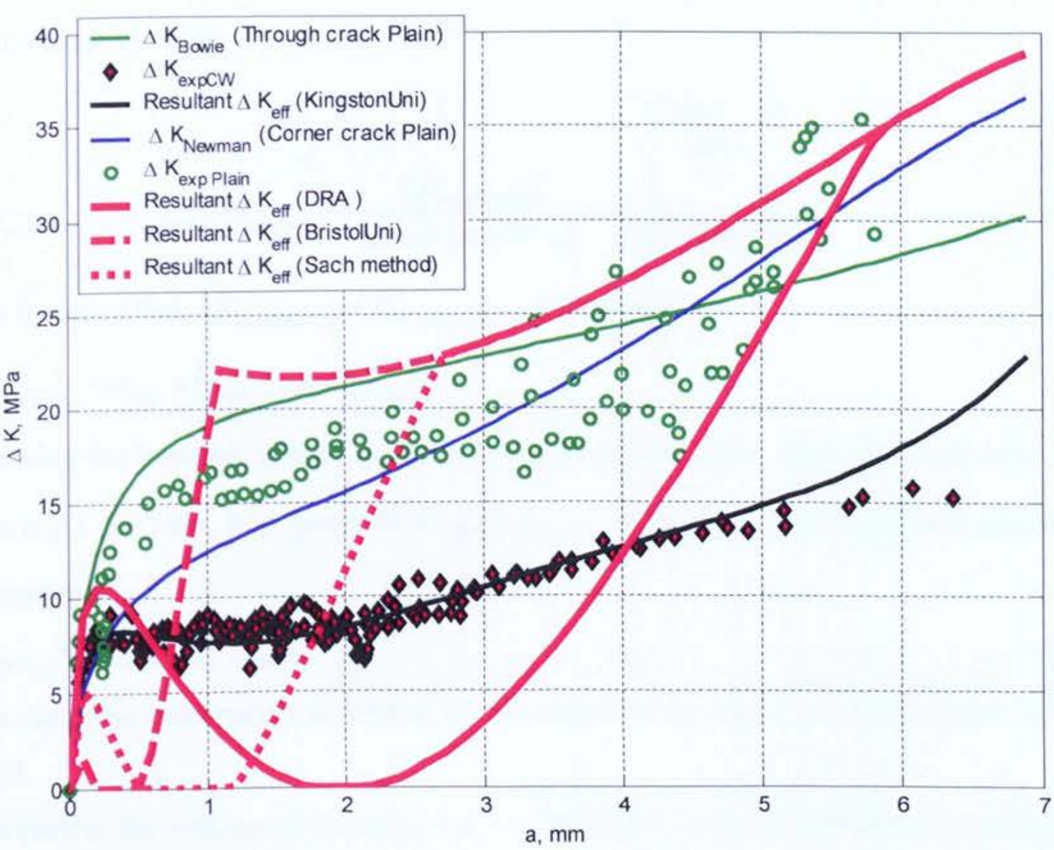

Figure 3.7.1 Comparison of predicted and experimental SIF for plan and cold worked specimens tested at 210 MPa

It was found that ESDU parameters C_3 & m_3 for the range da/dN=10^{-5} - 10^{-6} mm/cycle (see Table 10) did not match the experimental crack growth data obtained in the specimens. The figure above gives $\Delta K_{\exp Plain}$ points obtained through ESDU parameters C & m where C_3 and m_3 were replaced by the C_2 and m_2 values given in the table.

There is a distinct difference between the experimental points for plain and cold worked specimens. The residual stresses reduced the level of the effective stress causing a reduction in the SIF. This is why experimental data for CW specimens with corner cracks does not coincide with effective ΔK_{Newman} for corner cracks in non CW specimens. These latter points are plotted on the diagram as a reference (blue line). The diagram gives resultant ΔK_{eff} curves according to the various residual stress distributions obtained experimentally. It is obvious that none of them satisfied the experimental data which means that the residual stress distribution in our CW specimens is rather different from those considered above.

Assuming the relevance of the following equation

$\Delta K_{\text{experimental}} = \left(\sigma_{applied} + \sigma_{residual}\right)\sqrt{\pi a}F(a,t,W...)$, we can determine the resultant stress distribution by using

$$\Delta\sigma_{\text{resultant}} = \left(\sigma_{applied} + \sigma_{residual}\right) = \frac{\Delta K_{\text{experimental}}}{\sqrt{\pi a}F(a,t,W...)} = \frac{\left(\frac{da/dN}{C}\right)^{\frac{1}{m}}}{\sqrt{\pi a}F(a,t,W...)} \qquad \textit{(3.7.3)}$$

$R \leq 0$ means that $\Delta K_{\text{experimental}} = K_{\max \text{experimental}}$ and hence

$\Delta\sigma_{\text{resultant}} = \sigma_{\max} = \left(\sigma_{applied} + \sigma_{residual}\right)$.

Knowing the function of local stress distribution at hole under applied remote load $\sigma_{applied}$ (see eq. (3.6.18)), it is possible to get $\sigma_{residual}$ distribution through crack growth rate assessment.

$$\sigma_{residual} = \sigma_{\max \text{resultant}} - \sigma_{applied} \qquad \textit{(3.7.4)}$$

The diagrams constructed according to the equations ***(3.7.3)***, ***(3.7.4)*** are given in Figure 3.7.2

Comparing the calculated residual stress distribution with that obtained experimentally given in Figure 3.6.11, the discrepancy is apparent. All points of distribution are located at a level substantially below zero even at a large distance from the hole where the residual stress would be expected to be about zero. The evaluated points of residual stress distribution were approximated with a cubic polynomial expression:

$$\sigma_{residual} = Ax^3+Bx^2+Cx+D \qquad \textit{(3.7.5)}$$

This is presented in Figure 3.7.2.

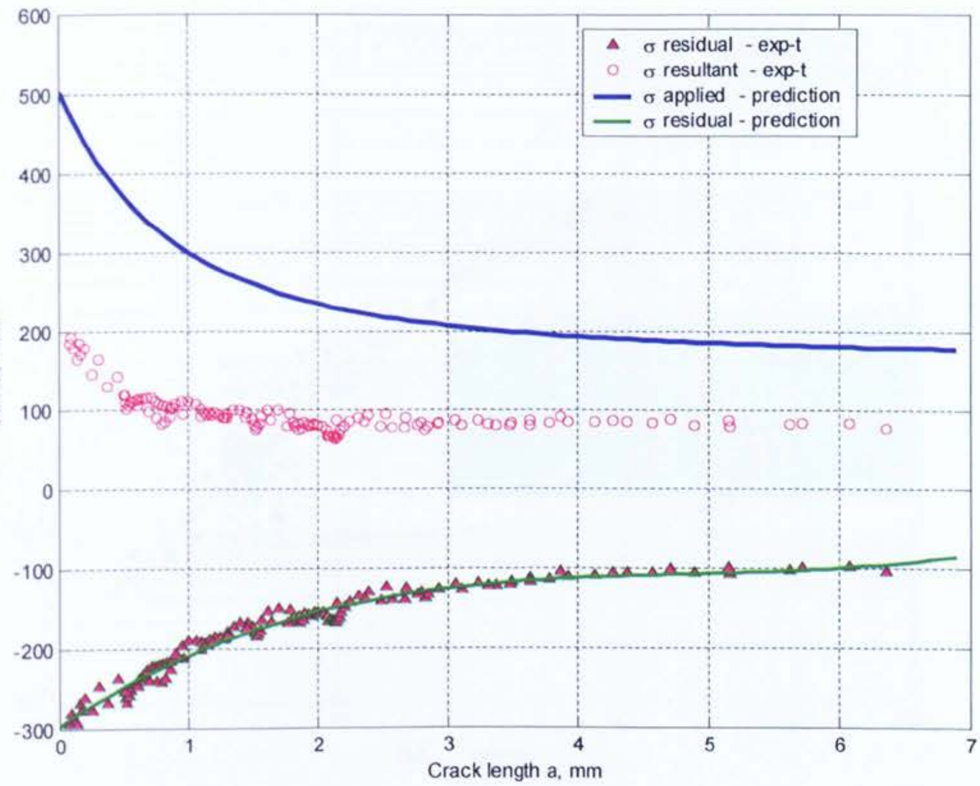

Figure 3.7.2 Distributions of Residual and Resultant Stresses obtained through crack growth rate assessment

The experimental SIF points of $\Delta K_{\exp CW}$ given in Figure 3.7.1 can be predicted from the function of ΔK_{eff}. The predicted ΔK_{eff} values using this approximation are presented in the same figure (black line).

From the standard Paris equation $\frac{da}{dN} = C\left(\Delta K_{eff}\right)^m$ by substituting the $\sigma_{residual}$ expression

(3.7.5)

$$\frac{da}{dN} = C\left(\Delta\left(\sigma_{app} + \sigma_{res}\right)\sqrt{\pi a}F\left(a, W.t...\right)\right)^m$$

and using parameters C, m used previously corresponding to Crack Growth Rate Ranges given in Table 10 from ESDU, predicted Crack Growth Rate Curves were compared with experimental data (Figure 3.7.3 - Figure 3.7.4).

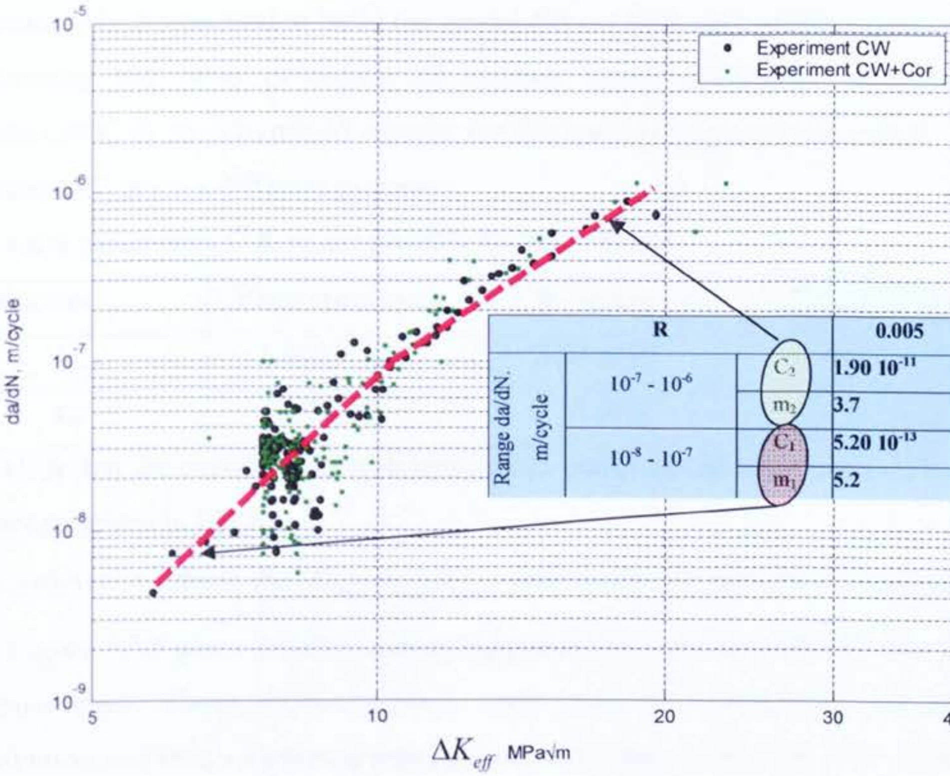

Figure 3.7.3 Crack Growth Rate da/dN vs ΔK_{eff}

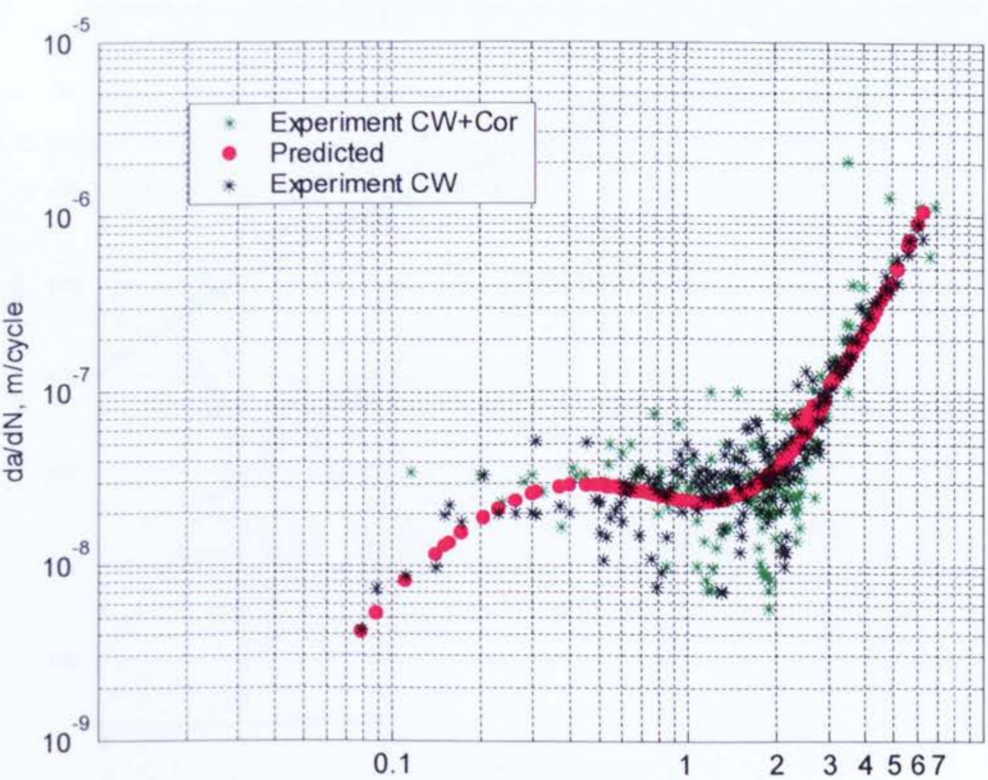

Figure 3.7.4 Crack Growth rate model.

The agreement in Crack Growth Rate data is good, though the Residual Stress Distribution obtained, which was used to build the model did not look very credible (see Figure 3.7.2). Performing the same procedure of residual stress distribution derivation but with parameters C & m determined exactly for the specimens tested (so called "valid C & m parameters") gives a different picture.

The valid parameters C & m are given in the table below

Parameters	Plain specimens	CW Specimens		ESDU data
C	1.605×10^{-12}	5.83×10^{-13}		1.9×10^{-11}
m	4.028	3.805		3.7

It is clear that the experimentally determined C parameter shows a large difference to the C parameter given in ESDU.

This difference affects the $K_{\exp}, \sigma_{\exp}, \sigma_{resid}$ and finally the analytical solution for resultant SIF. Figure 3.7.5 gives Residual Stress Diagrams obtained from ESDU data and valid C & m parameters. These approximations were used for calculations of resultant stress distribution and then substituted into the analytical solution for SIF. The different in Stress Distributions obtained by the two methods is also shown in Figure 3.7.6.

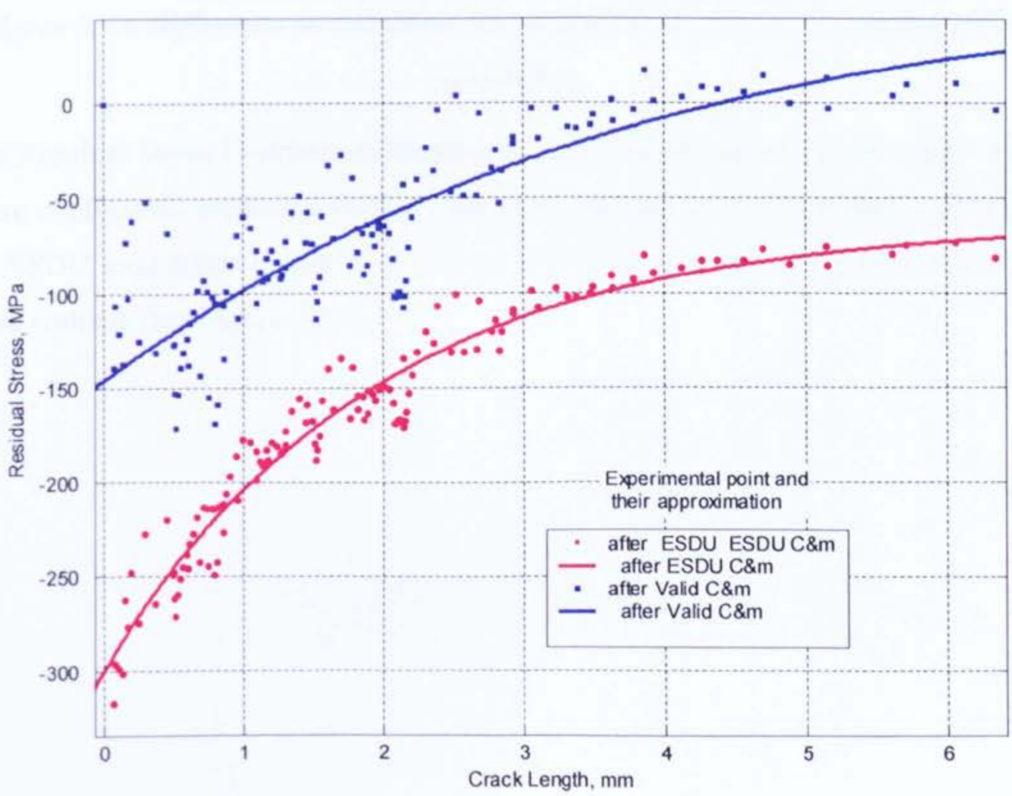

Figure 3.7.5 Difference in Residual Stress Distribution caused by different C&m parameters.

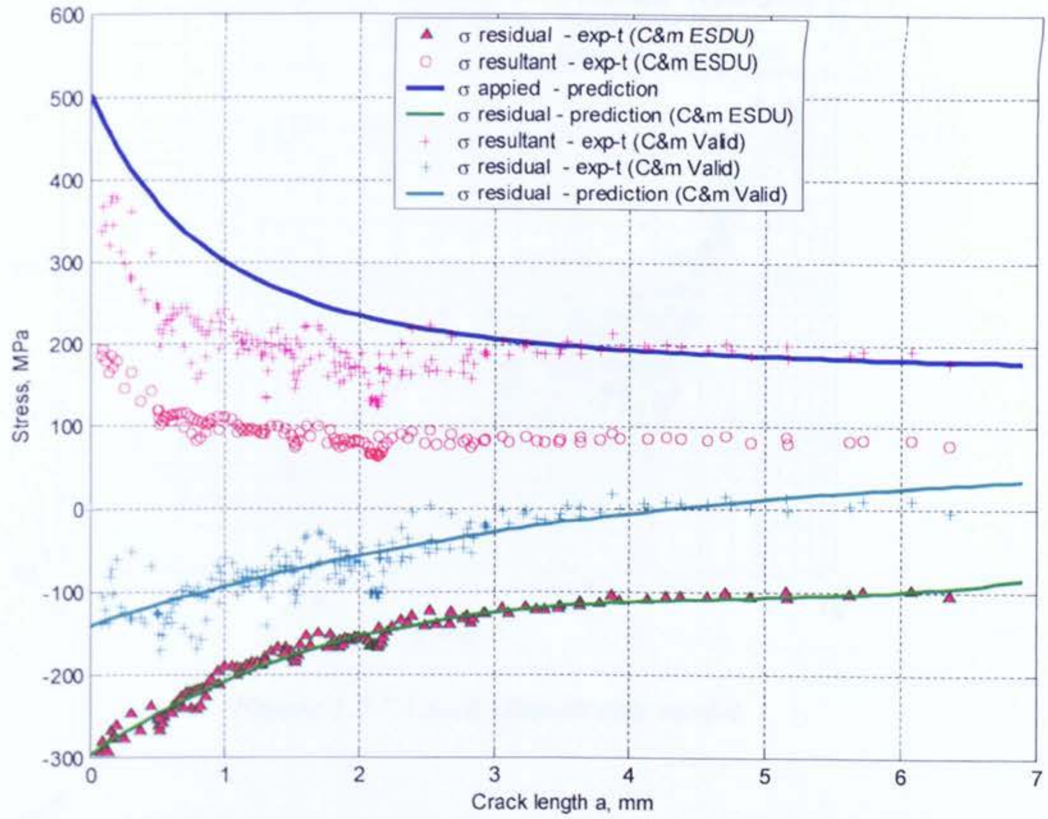

Figure 3.7.6 Difference in Resultant Stress Distribution caused by different C&m parameters.

The Residual Stress Distribution obtained by using experimental da/dN values and "valid" C&m coefficients predicts a similar Crack Growth Rate to those obtained previously using the ESDU model(See Figure 3.7.7, Figure 3.7.8) but the level of Residual Stresses looks more realistic (see Figure 3.3.6).

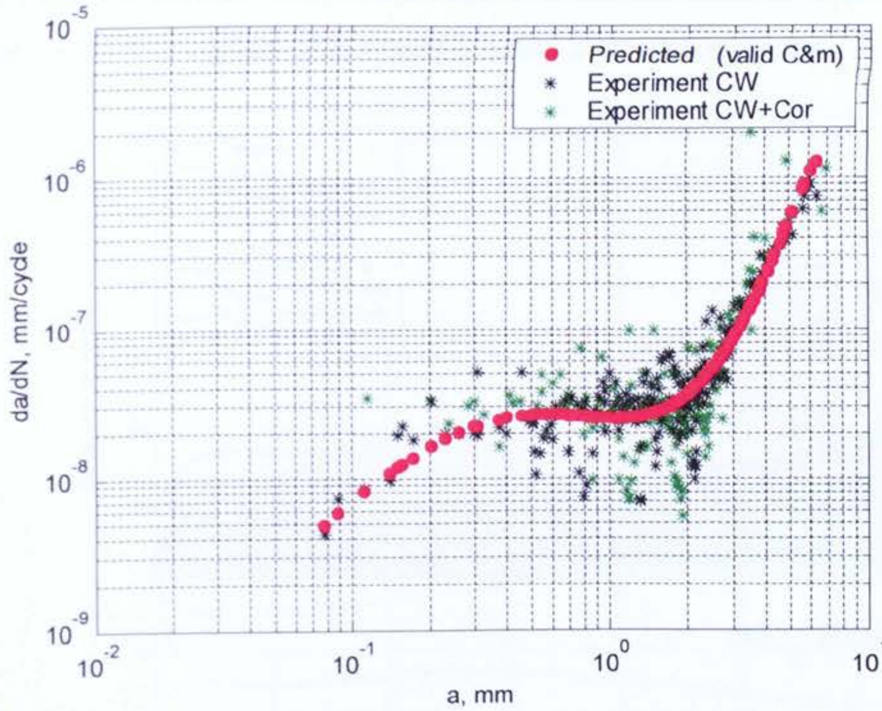

Figure 3.7.7 Crack Growth rate model.

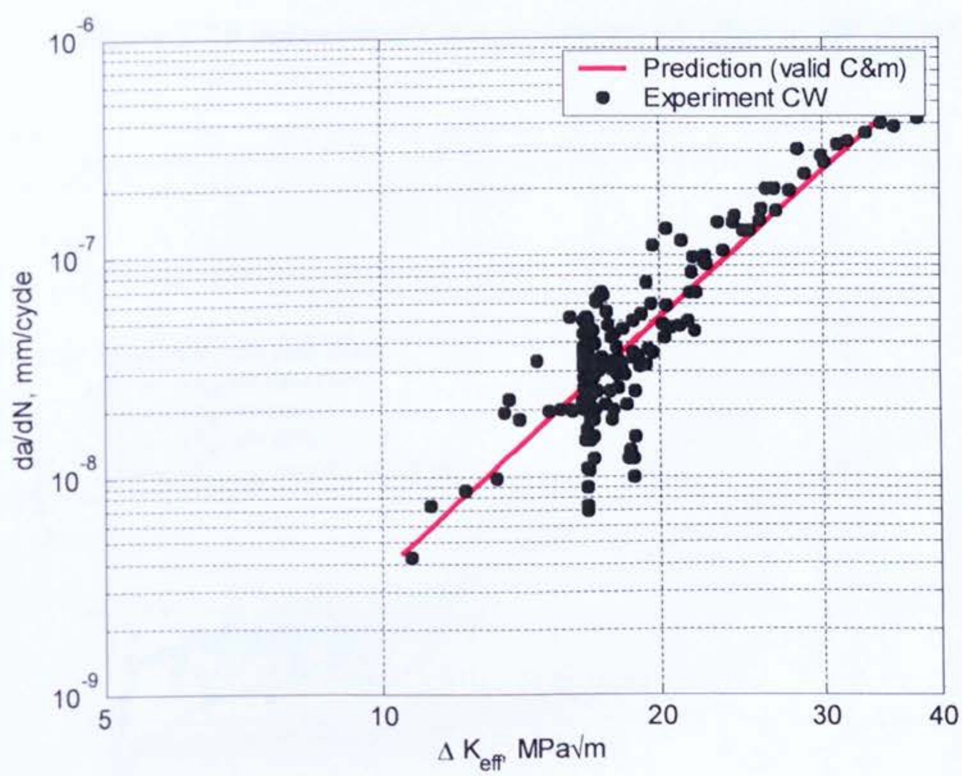

Figure 3.7.8 Crack Growth Rate vs ΔK_{eff}

The effect of ESDU and "Valid" C&m parameters on SIF distribution was considered. Figure 3.7.9 compares resultant SIF distributions derived from residual stress distributions obtained by the use of different *C&m* values. It is clear that if we use **"valid"** C&m

parameters it indicates that the contribution of residual stress in reducing SIF values is less than ESDU data implies. This situation is also illustrated in Figure 3.7.10.

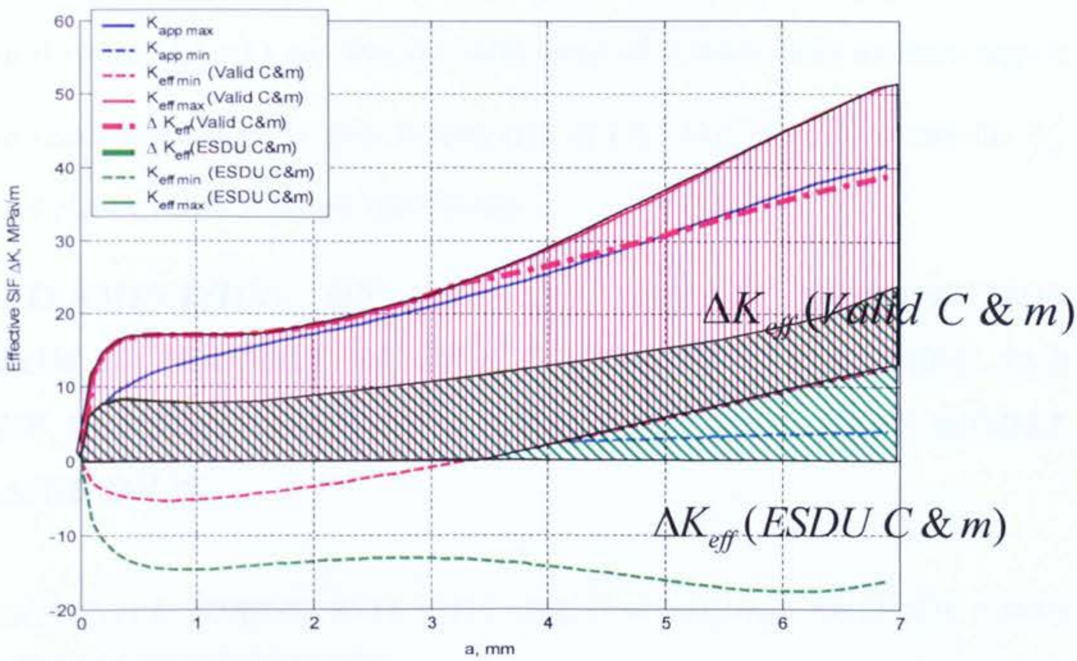

Figure 3.7.9 Influence of C&m parameters on effective SIF distribution

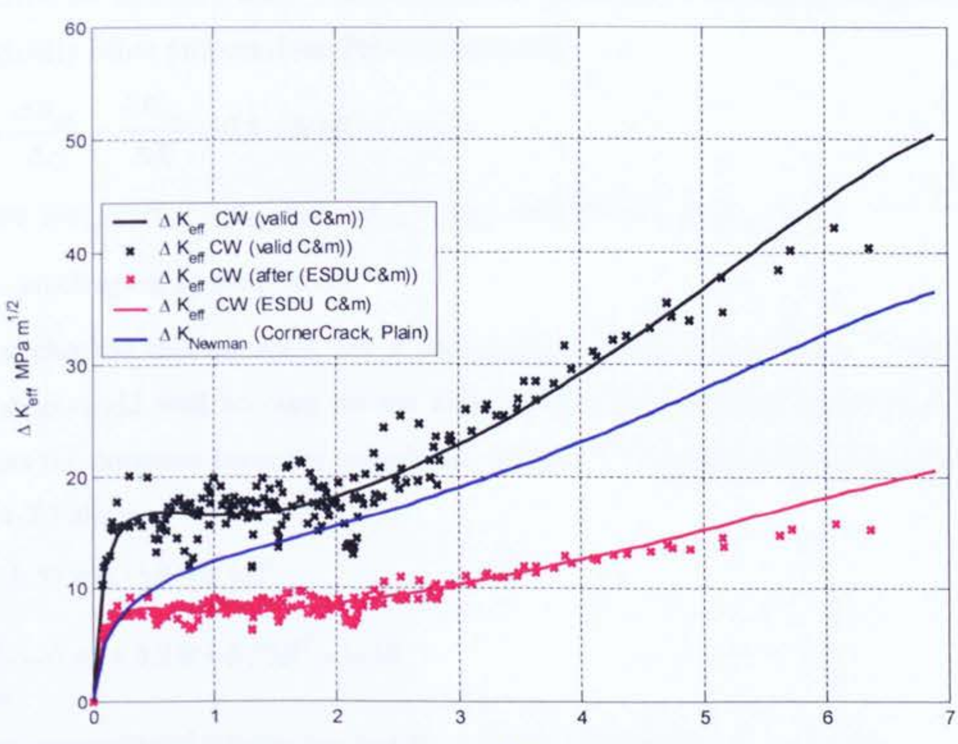

Figure 3.7.10 SIF distribution obtained from "valid" C&m and from ESDU data

Two models ("**ESDU**" and "**Valid**") are being used. We have to choose which one is more realistic.

It should be noted that all analytical calculations were conducted assuming quartercircular symmetrical cracks ($a/c = 1$) and that the valid range of distance from the hole edge is limited to 5mm (thickness of the plate is 5mm (see eq. (1.7.19)). If we try to vary the a/c relation, the picture will be changed significantly.

3.8 DETERMINATION OF OPENING STRESS DISTRIBUTION FROM EXPERIMENTAL CRACK GROWTH RATE DATA AND THE CONSTRUCTION OF A CRACK GROWTH RATE MODEL BASED ON IT.

3.8.1 EFFECTIVE STRESS INTENSITY FACTOR RANGE DERIVED FROM OPENING STRESS VALUES

Elber [232] suggested that the governing parameter for characterising fatigue crack growth is the effective SIF, ΔK_{eff}. This parameter takes into account crack opening and is able to describe an effective local stress range, the parameter controlling fatigue crack growth. Originally Elber proposed for 2024-T3 material:

$$U = \frac{\Delta\sigma_{eff}}{\Delta\sigma} = \frac{\Delta K_{eff}}{\Delta K} = 0.5 + 0.4R$$

where $\Delta\sigma_{eff} = \sigma_{\max} - \sigma_{op}$, $\Delta\sigma = \sigma_{\max} - \sigma_{\min}$, and $R = \sigma_{\min}/\sigma_{\max}$.

σ_{op} - crack opening stress level.

Elber checked this equation. for R values from -0.1 to 0.7. Schijve [233] showed that this equation could well account for the effect of R if R is positive. However, for negative R values the equation becomes unrealistic. Schijve [233] proposed the following equation for 2024-T3 alloy:

$$U = 0.55 + 0.35R + 0.1R^2 \qquad \text{or} \qquad \textit{(3.8.1)}$$

$$\frac{\sigma_{op}}{\sigma_{\max}} = 0.45 + 0.2R + 0.25R^2 + 0.1R^3$$

From experimental fatigue test results on 2024-T3 Ibrahim [234] suggested

$$\left(\frac{\sigma_{op}}{\sigma_{\max}}\right)_{R=0} = 0.5\left(1-\frac{\sigma_{\max}}{\sigma_y}\right)^{1/2} \quad (3.8.2)$$

$$\frac{\sigma_{op}}{\sigma_{\max}} = \left(\frac{\sigma_{op}}{\sigma_{\max}}\right)_{R=0} (1-R)^2 + R \quad for\ R \geq 0$$

$$\frac{\sigma_{op}}{\sigma_{\max}} = \left(\frac{\sigma_{op}}{\sigma_{\max}}\right)_{R=0} \left(1-\left(\frac{\sigma_{\min}}{\sigma_y}\right)^2\right)^2 + R \quad for\ R \leq 0$$

where σ_y yield stress of the material (365 MPa for 2024-T3)

The solutions are presented in the comparison diagram ***Figure 3.8.1***. Only Schijve's and Ibrahim's solutions will be used for further analysis since they gave theoretical results closer to those found in their fatigue test experiments. For our test conditions and material properties the solutions give, for plain specimens, σ_{op} =79 and 66 MPa respectively.

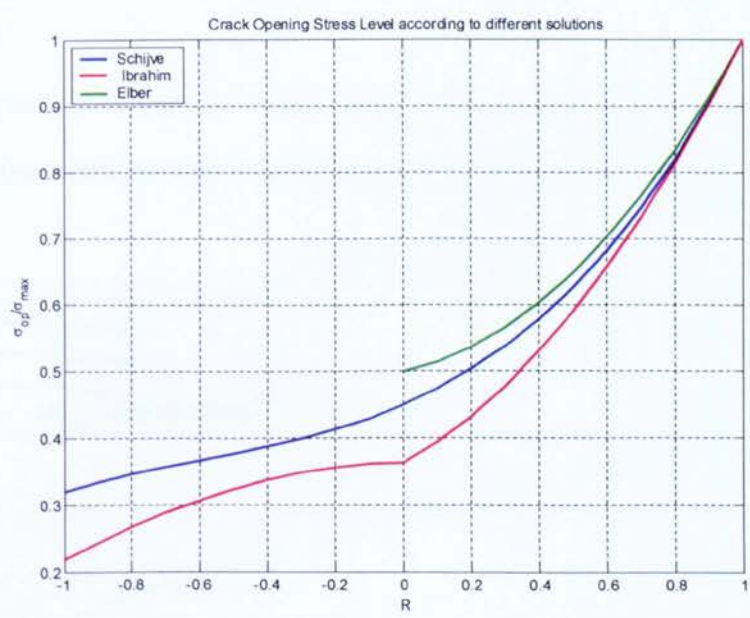

Figure 3.8.1 Crack Opening Stress level – different solutions.

$$\Delta\sigma_{eff} = \sigma_{\max} - \sigma_{op} \text{ and hence } \begin{cases} \Delta K_{eff} = \Delta\sigma_{eff}\sqrt{\pi a}F_{ThroughCrack}(a,W,t...) \\ \Delta K_{eff} = \Delta\sigma_{eff}\sqrt{\pi a}F_{CornerCrack}(a,W,t...) \end{cases}$$

Lacarac et al. [220] showed that the measured crack opening stress level for CW hole specimens of Al 2650 was found to be quite independent of R ratios as observed for plain holed specimens. Measured values were however substantially higher in CW hole specimens (see ***Figure 3.8.2***)

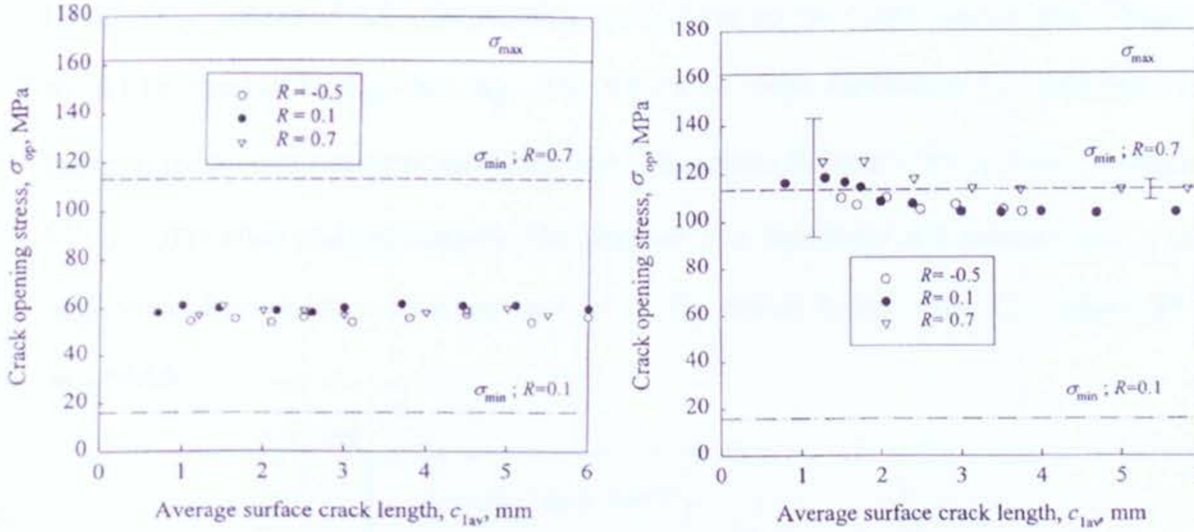

Figure 3.8.2 Crack Opening Stress - Independence of R ratio.

Based on these observations we can assume that σ_{op} for crack in Al 2024 will have the same behaviour.

$\Delta K_{eff}(a)$ diagrams according to Schijve and Ibrahim were produced for plain and CW specimens together with real experimental points ΔK_{exp} (see ***Figure 3.8.3***).

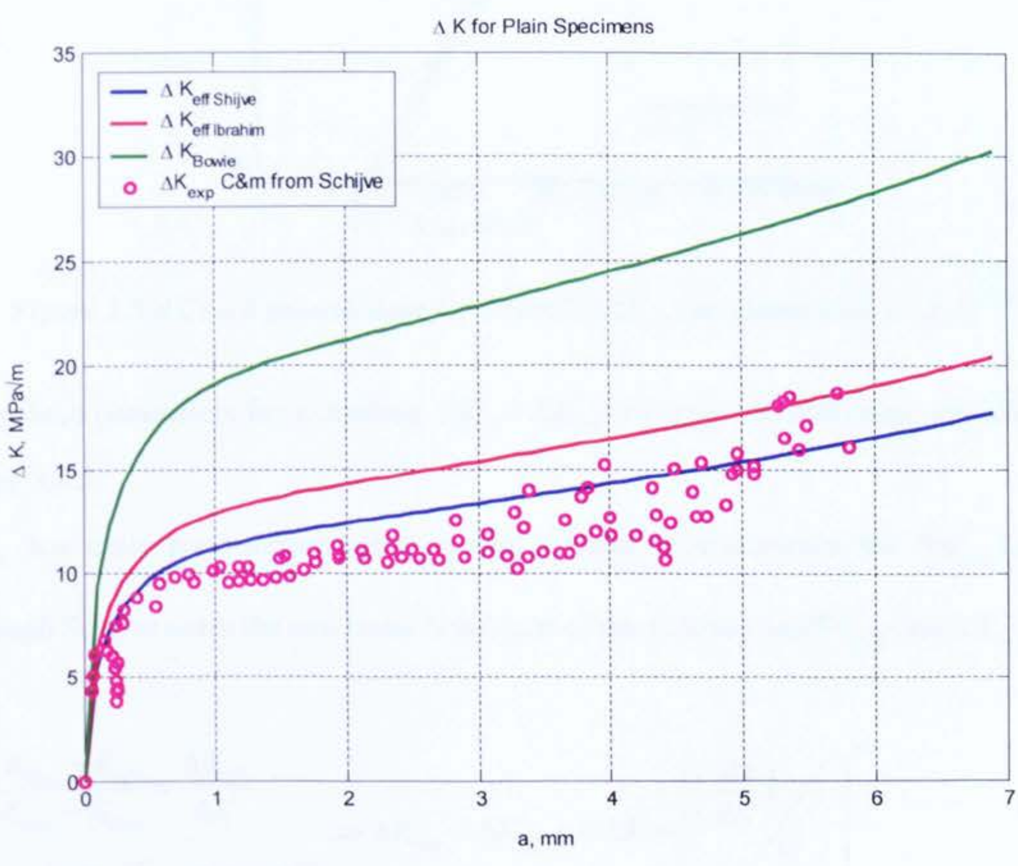

Figure 3.8.3 ΔK_{eff} for plain specimens with a through crack.

Using ΔK_{eff} instead of ΔK , the parameters C and m for the Crack Growth Rate Diagram should be changed to C_{eff} and m_{eff} . The values for these parameters for 2024 were not found in the literature review, thus they were taken from Schijve's $\frac{da}{dN}(\Delta K_{eff})$ diagram [233] for 2024 alloy plain specimens. The diagram was digitalised and parameters C_{eff} and m_{eff} were derived by a least squares fit. The values found were C_{eff} **=1.25 10^{-11}, m_{eff} =4.65.**

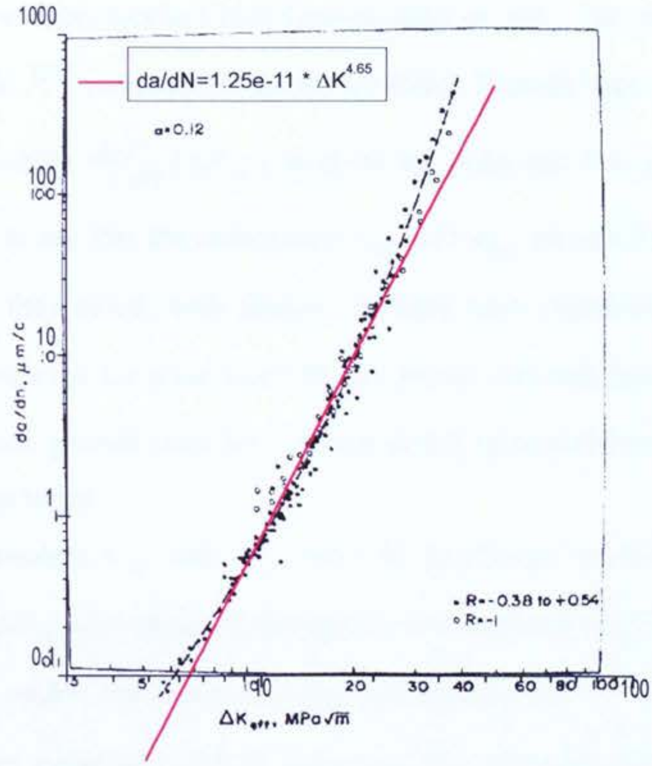

Figure 3.8.4 Crack growth data for 2024-T3 ΔK_{eff} calculated with (3.8.1) [233]

Using these parameters for extracting $\Delta K_{eff} = \Delta K_{exp}$ we have the following data shown in ***Figure 3.8.3***

ΔK_{exp} has quite good agreement assuming a linear approximation for $\frac{da}{dN}(\Delta K_{eff})$. Although Schijve notes the non linear behaviour of the function $\log \frac{da}{dN}(\log \Delta K_{eff})$.

$$U = \frac{K_{\max} - K_{op}}{K_{\max} - K_{\min}} = \frac{\Delta K_{eff}}{\Delta K}$$
$$\frac{da}{dN} = C(\Delta K_{eff})^m = C(U\Delta K)^m \quad \Rightarrow \Delta K_{\exp} = \Delta K_{eff} = U\Delta K = \left(\left(\frac{da}{dN}\right) \Big/ C \right)^{1/m} \qquad \textbf{\textit{(3.8.3)}}$$

According to ***(3.8.3)***, $\Delta K_{\exp}$ including the function *U*.

"Nominal" Crack Growth Rate model

$$\frac{da}{dN} = C\left(\Delta K_{nom}\right)^m \text{ (C\&m from ESDU)}$$

"Effective" Crack Growth Rate model

$$\frac{da}{dN} = C_{eff}\left(\Delta K_{eff}\right)^{m_{eff}} \quad (\Delta K_{eff} = U_{Schijve}\Delta K)$$

Figure 3.8.5 displays work of "nominal " and "effective" models for crack growth rate vs crack length in comparison with experimental data for plain specimens.

No data was found with respect to Crack Growth Rate vs ΔK_{eff} for cracks in CW holes in Al2024. Lacarac et.al. (220) produced diagrams for Crack Growth Rate vs ΔK_{eff} for Al2650 (see ***Figure 3.8.7***), where ${}^{da}\!/_{dN}\left(\Delta K_{eff}\right)$ is given for plain and CW specimens. From the diagram, it possible to say that the parameters C_{eff} and m_{eff} are similar for both plain and CW specimens. As they noted, with fatigue cracking rates expressed in terms of ΔK_{eff} similar trends are observed for plain and CW specimens. Nevertheless, for a given ΔK_{eff}, the experimental crack growth rates for cold-expanded specimens were lower than crack growth rates for plain holes.

Assuming that parameters C_{eff} and m_{eff} for CW specimens are the same as for plain specimens $\Delta K_{\exp} = \Delta K_{eff}$ was obtained through the same procedure ***(3.8.3)***, with the same C_{eff} =1.25e-11, m_{eff}=4.65. The results are shown in ***Figure 3.8.8***

ΔK_{eff} obtained from equation ***(3.8.3)*** was used for experimental results obtained at Kingston University on CW specimens and these are plotted in ***Figure 3.8.8***. As can be seen these plots occur at significantly lower stress intensity range levels than the $\Delta K_{eff\ Schijve}$ plots for plain specimens.

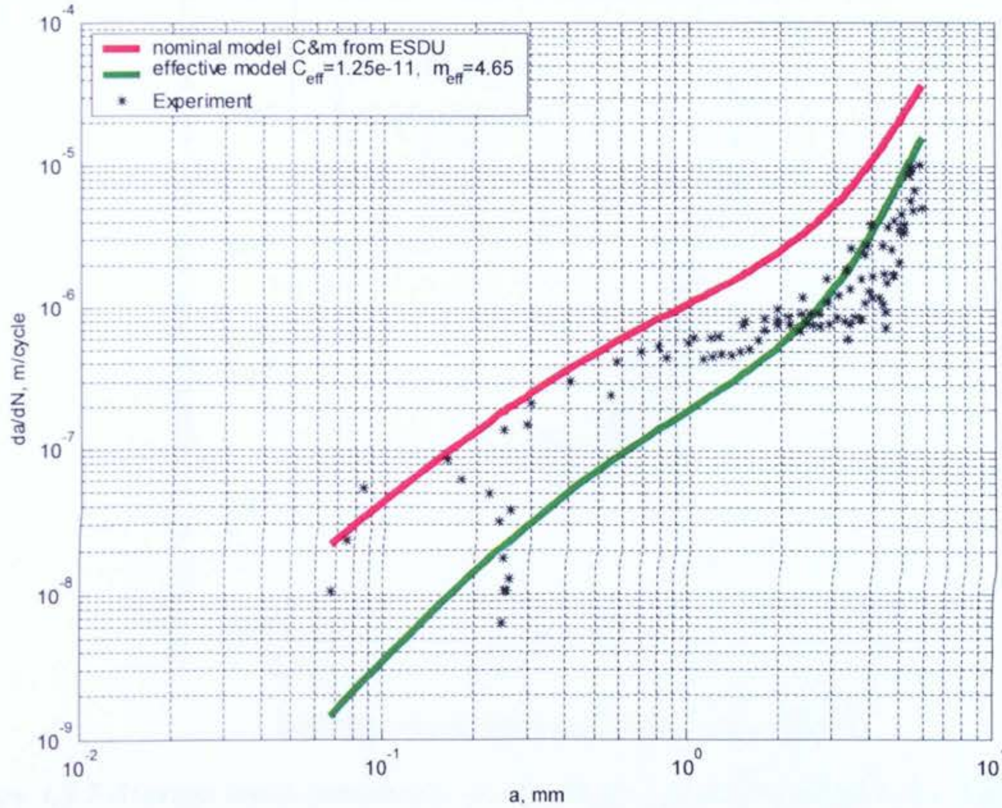

Figure 3.8.5 Crack Growth Rate: Experimental data and models. Plain Specimens

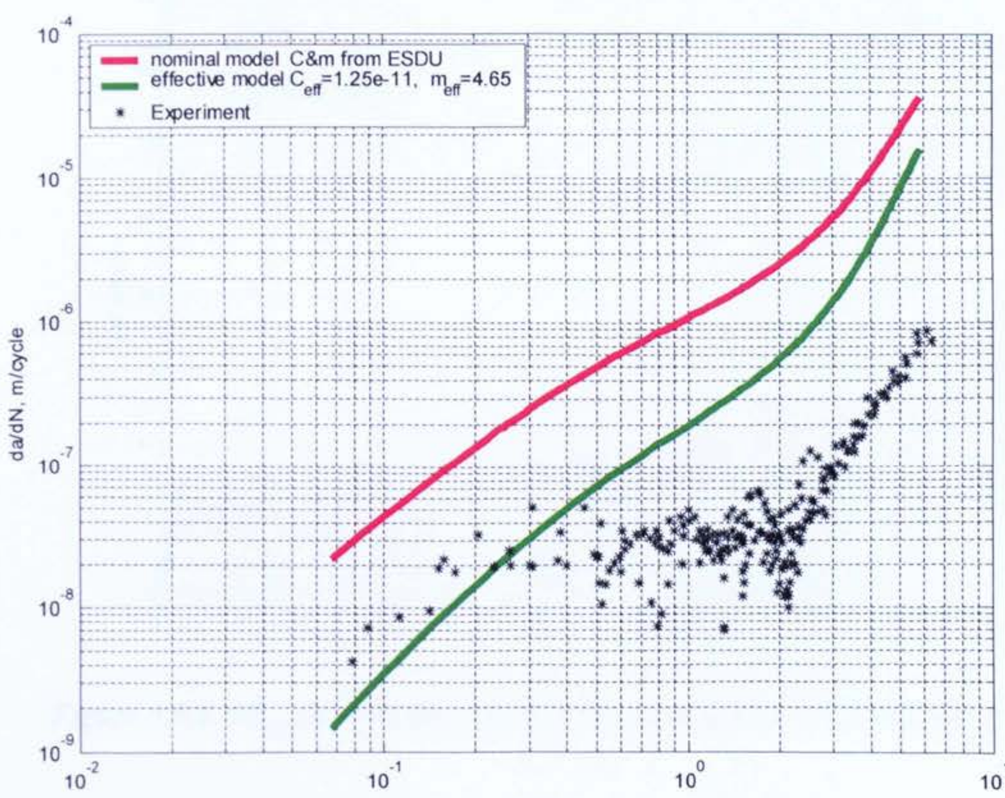

Figure 3.8.6 Crack Growth Rate: Experimental data and models. CW Specimens

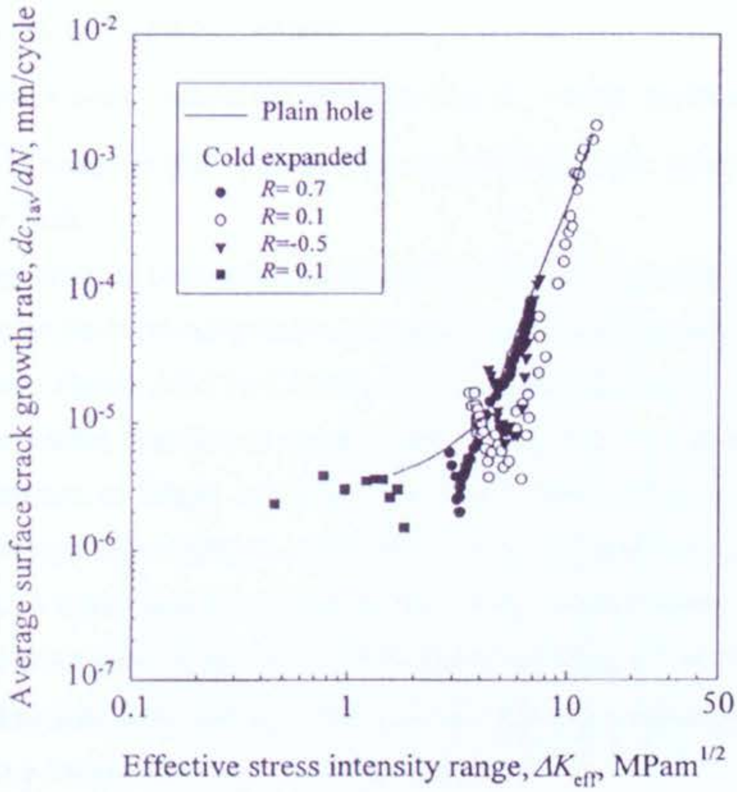

Figure 3.8.7 Average crack growth rate in specimens containing plain and CX holes for Al2650 (220)

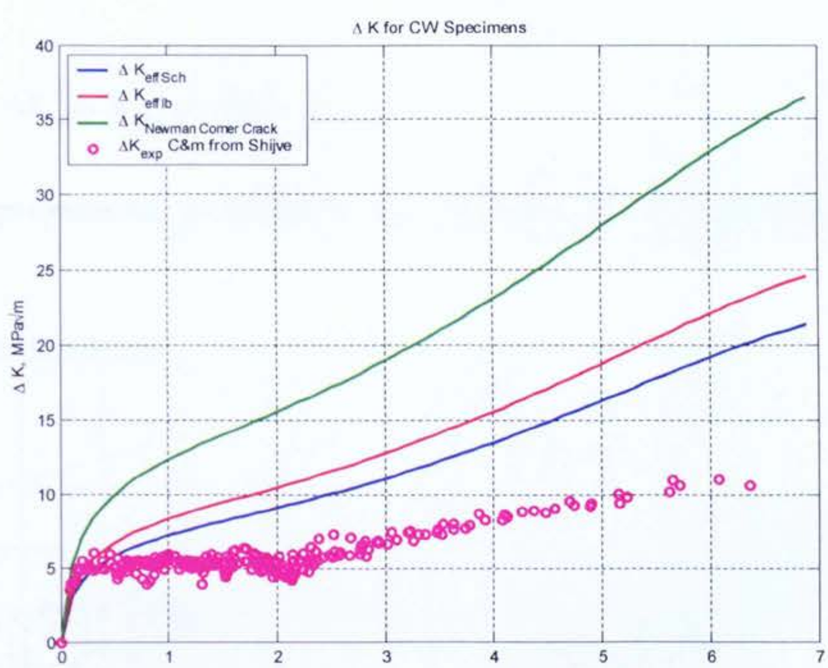

Figure 3.8.8 ΔK_{eff} for CW specimens with corner crack. CW specimens

3.8.2 OPENING STRESS DERIVATION

All of these diagrams were constructed assuming that σ_{op}=const. However in discussion, ***Lacarac et al.*** **.** [220] recognise that opening stress values change with crack length.

According to their work:

The crack opening stress in cold-expanded specimens was a measure of the remote stress required to overcome the local compressive residual stress associated with cold expansion. The results shown in ***Figure 3.8.2*** for CX specimens illustrate that the crack opening stress was a slightly decreasing function of crack length, irrespective of applied load ratio. In contrast, the difference in fatigue crack growth rates between plain and cold-expanded specimens was strongly dependent on crack length. This occurred for both alloys and for various R values. A more detailed picture of the crack opening stress was obtained by assuming that the crack growth rate in a cold-expanded specimen was associated with an effective stress intensity factor range. This assumed that the fatigue crack growth rate shown in Fig . 6 is a characteristic curve for the material, where

$$\frac{da}{dN} = C\left(\Delta K_{eff}\right)^{m} \qquad \textbf{\textit{(3.8.4)}}$$

With $\Delta K_{eff} = K_{\max} - K_{op}$, inverting Eq.(3.8.4) , and rearranging gives,

$$K_{op} = K_{\max} - \Delta K_{eff} = K_{\max} - \left(\frac{da}{dN} \Big/ C \right)^{\frac{1}{m}} \qquad \textbf{\textit{(3.8.5)}}$$

Graphical representations of calculated K_{op} for plain and CW specimens are given in Figure 3.8.9.

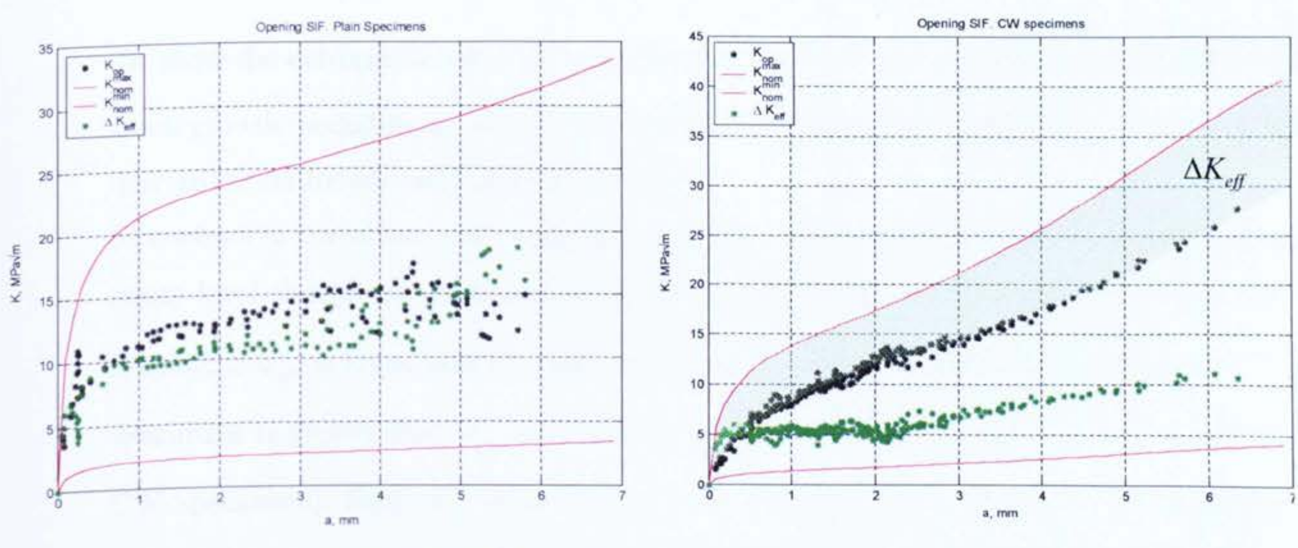

Figure 3.8.9 K_{op} ***distribution for Plain and CW specimens***

Using $K_{op} = \sigma_{op}\sqrt{\pi a}F_{Corner/ThroughCrack}(a,W,t...)$ then allows determination of the crack opening stress, where

$$\sigma_{op} = {K_{op}}\Big/{\sqrt{\pi a}F_{Corner/ThroughCrack}(a,W,t...)} \qquad (3.8.6)$$

Calculated crack opening stresses σ_{op} are in good agreement with the prediction from Schijve (3.8.1) for plain specimens. It can be stated that both samples have approximately the same level σ_{op}^{Shijve} = 79MPa. However the results for corroded specimens are placed somewhat lower than Schijve's prediction. This indicates that corrosion impaired the fatigue performance of the material hence the opening stresses were reduced (see ***Figure 3.8.10*** a).

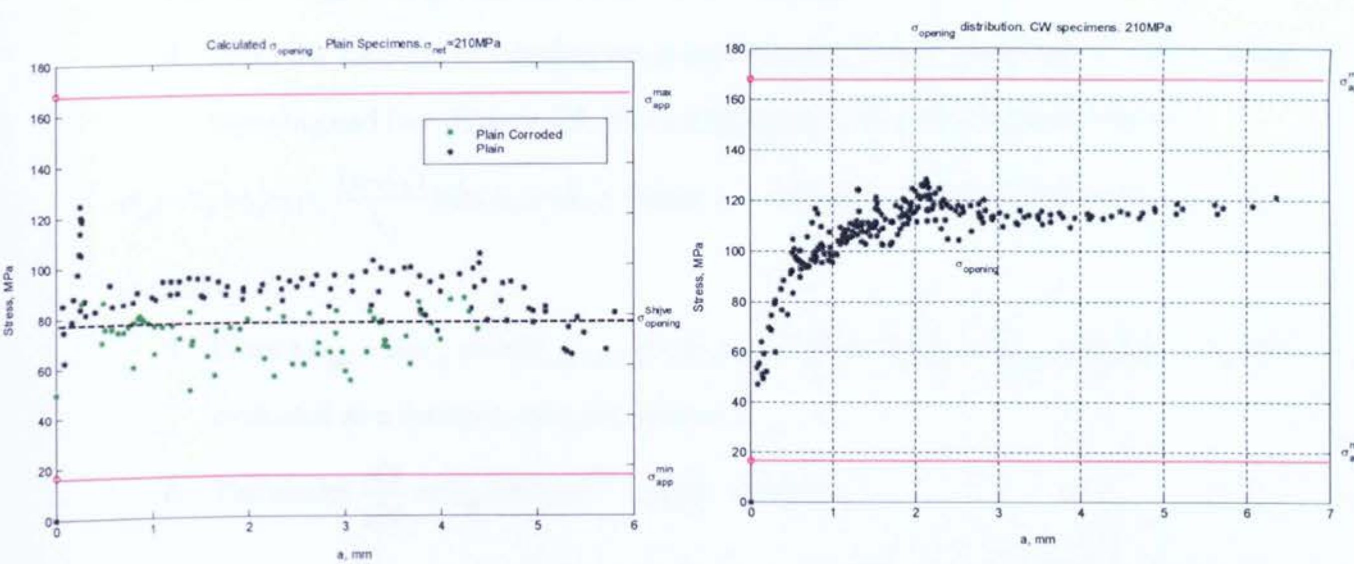

a ***b***

Figure 3.8.10 Crack opening stress. a -Plain and Plain Corroded Specimens; b – non corroded CW specimens

To show the detrimental effect of corrosion the σ_{op} level was assumed to be 65 MPa for crack growth modelling as used for the Nesterov effective crack growth rate model (3.8.3) derived earlier for corroded plain specimens.

In contrast to corrosion, cold working strengthens the material and increases the opening stress level though the treatment makes the σ_{op} distribution non uniform. For the CW specimens σ_{op} is lower than for plain specimens if a<0.5mm. For a>0.5mm σ_{op} for CW specimens is greater than σ_{op} for the plain specimens (hence the slower crack growth in CW specimens). Peak σ_{op} is at a =2 mm in CW specimens, with σ_{op} approximately constant for a>3mm, where it is about 1.5 times the Schijve value. The trends for the CW specimens appear similar to those for 2650 alloy in Figure 1.1.3 (no data was given for a<1mm).

3.8.3 CRACK GROWTH RATE MODEL FOR CW SPECIMENS

The model was constructed as follows:

1. From ***Figure 3.8.4*** and ***Figure 3.8.7*** effective parameters C&m applicable to plain and CW specimens were obtained. $\frac{da}{dN}=C_{eff}\left(\Delta K_{eff}\right)^{m_{eff}}$
2. From eq. ***(3.8.3)*** $\Delta K_{eff}=\Delta K_{\exp}$ was obtained
3. From $K_{\max}-\Delta K_{eff}$ K_{op} was determined (see ***Figure 3.8.9***)
4. From the function of opening stress (not constant!) eq.***(3.8.6)*** the σ_{op} distribution was obtained (see ***Figure 3.8.10***) and approximated by the function below:

$\sigma_{op}=A_0+A_1\exp(-\frac{(x-A_2)}{A_3})\sin(A_4x+A_5)$ where x – distance form the hole edge, A_0-A_5 - constants.

5. From $\Delta K_{eff}=\Delta\sigma_{eff}\sqrt{\pi a}F_{CornerCrack}\left(a,W,t...\right)$ where $\Delta\sigma_{eff}=\sigma_{\max}-\sigma_{op}\left(a\right)$ σ_{op} was evaluated as a function, not as a constant!
6. The model $\frac{da}{dN}=C_{eff}\left(\Delta K_{eff}\right)^{m_{eff}}$ is now complete.

Individually obtained CGR diagrams of the model $\frac{da}{dN}=C_{eff}\left(\Delta K_{eff}\right)^{m_{eff}}$ for different specimen conditions and approximate opening stress distributions are given in ***Figure 3.8.11*** - ***Figure 3.8.20***. The combined diagram for CGR and the combined diagram for opening stress are shown in Figure 3.8.21 and ***Figure 3.8.23*** respectively for all the specimen conditions considered.

As can be seen from the diagrams the model gave Crack Growth Rate curves which agreed closely with the experimental data. The model takes into account retardation of crack growth due to cold expansion and describes crack growth rate behaviour for different kinds of of the hole preparation. The nominal model for plain specimens (red curves) are provided as a reference to enable the assessment of the benefits of different treatments to the hole. In all cases, the advantages are obvious. The precise description of the experimental data for CGR was possible owing to the acceptance of opening stress as a function, not as a constant as in the case of plain specimens.

If σ_{op} was taken as a constant (but at a higher level than that for plain specimens), it would look like curve for "nominal" model (red curves) but shifted down and it would have good agreement in the larger crack range (above 2mm), though it wouldn't describe the crack growth retardation within specific range of crack length(1-2mm) observed in CX and Interference fit specimens.

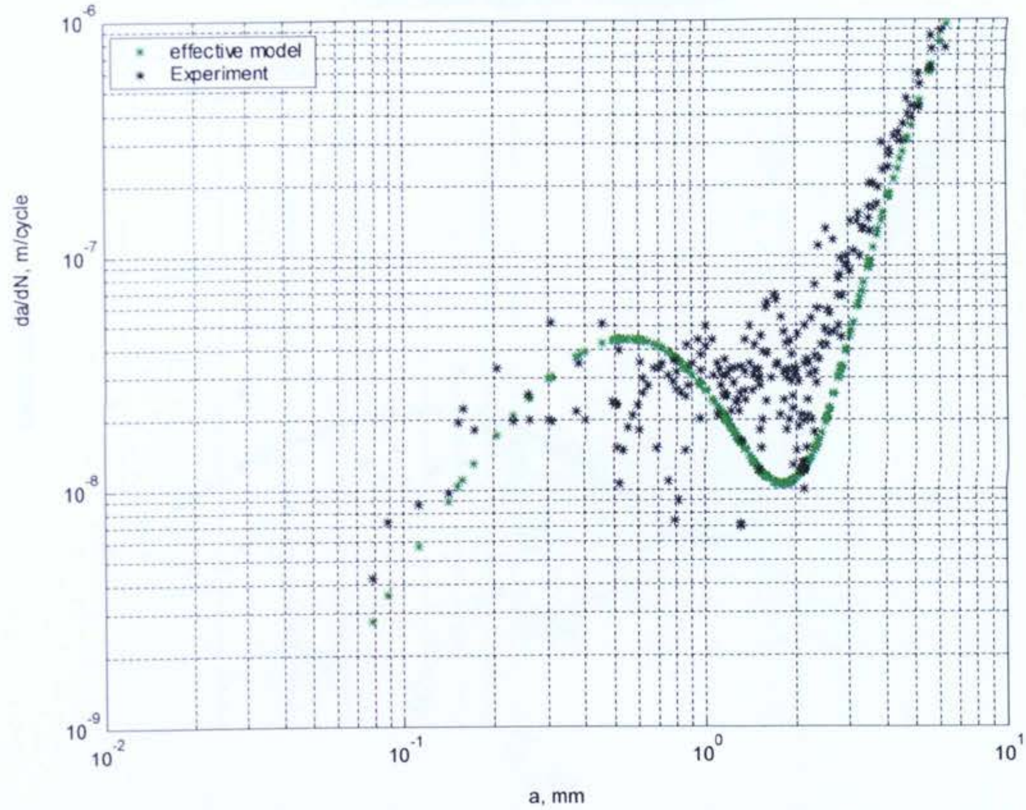

Figure 3.8.11 Crack Growth Rate in CW specimens: model and experimental data

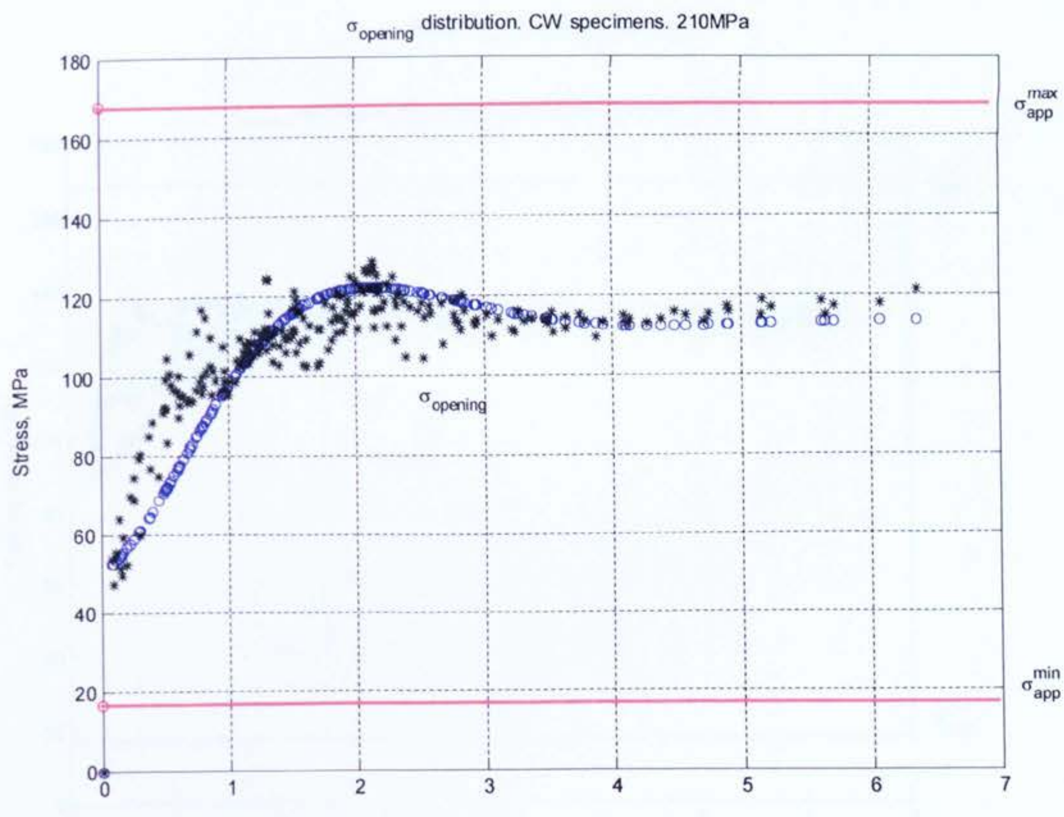

Figure 3.8.12 Opening stress in CW specimens: model and experimental data

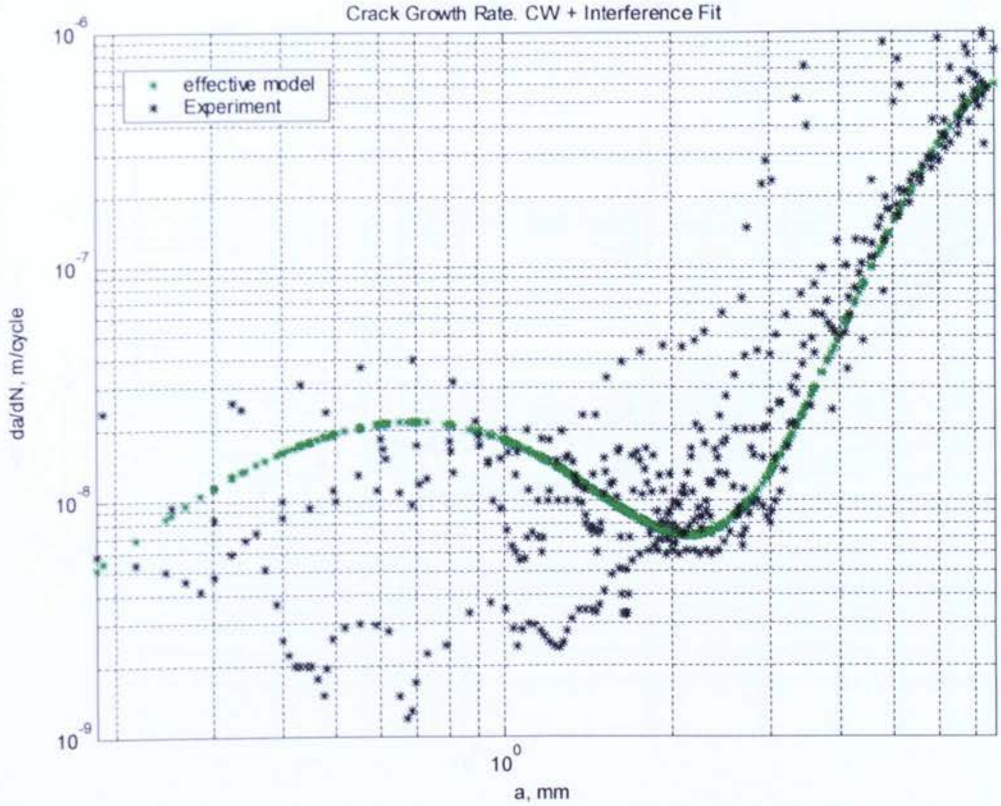

Figure 3.8.13 Crack Growth Rate in CW with Interference Fit specimens: model and experimental data

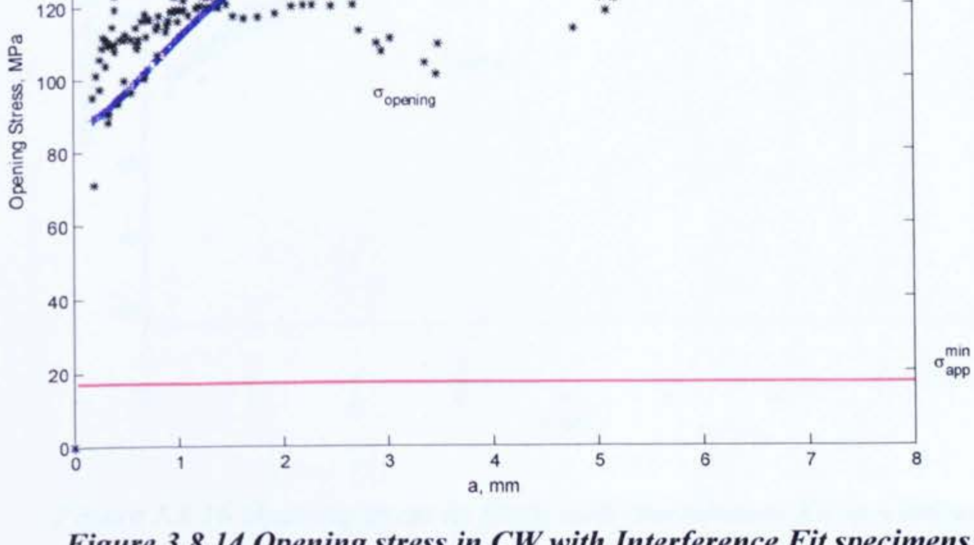

Figure 3.8.14 Opening stress in CW with Interference Fit specimens: model and experimental data

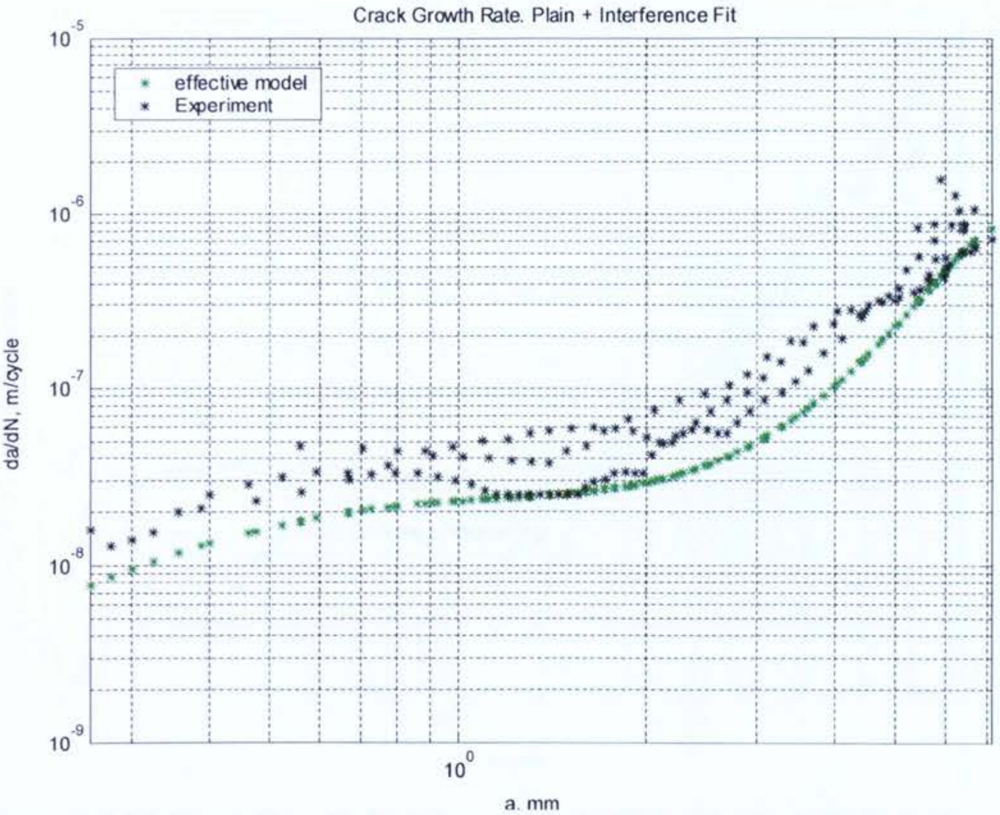

Figure 3.8.15 Crack Growth Rate in Plain with Interference Fit specimens: model and experimental data

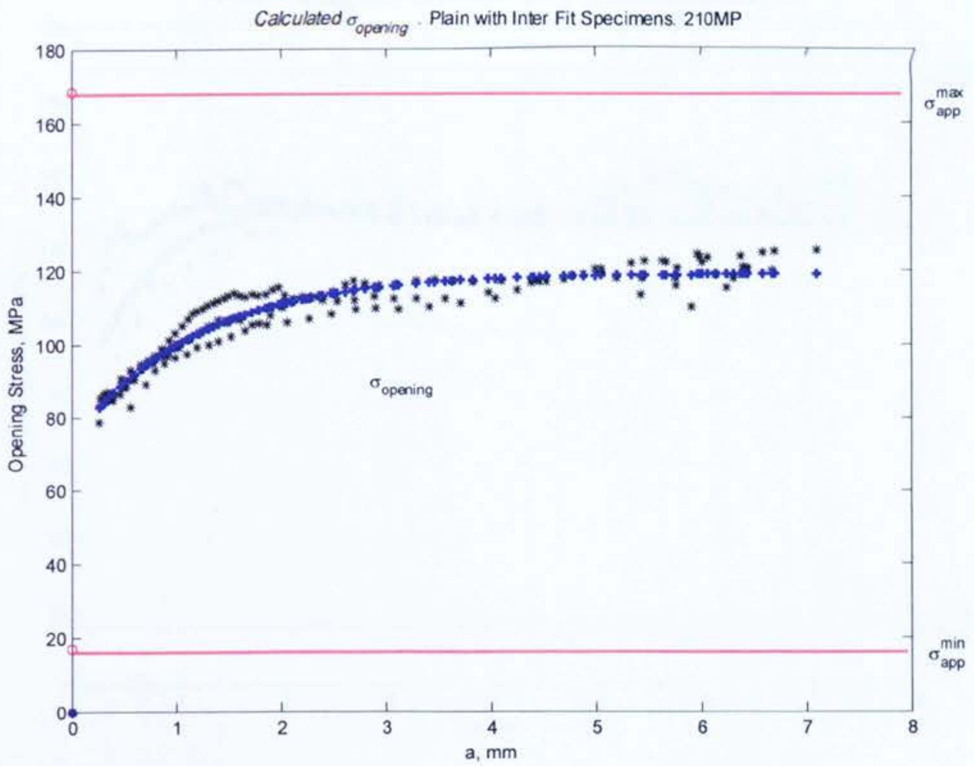

Figure 3.8.16 Opening stress in Plain with Interference Fit specimens: model and experimental data

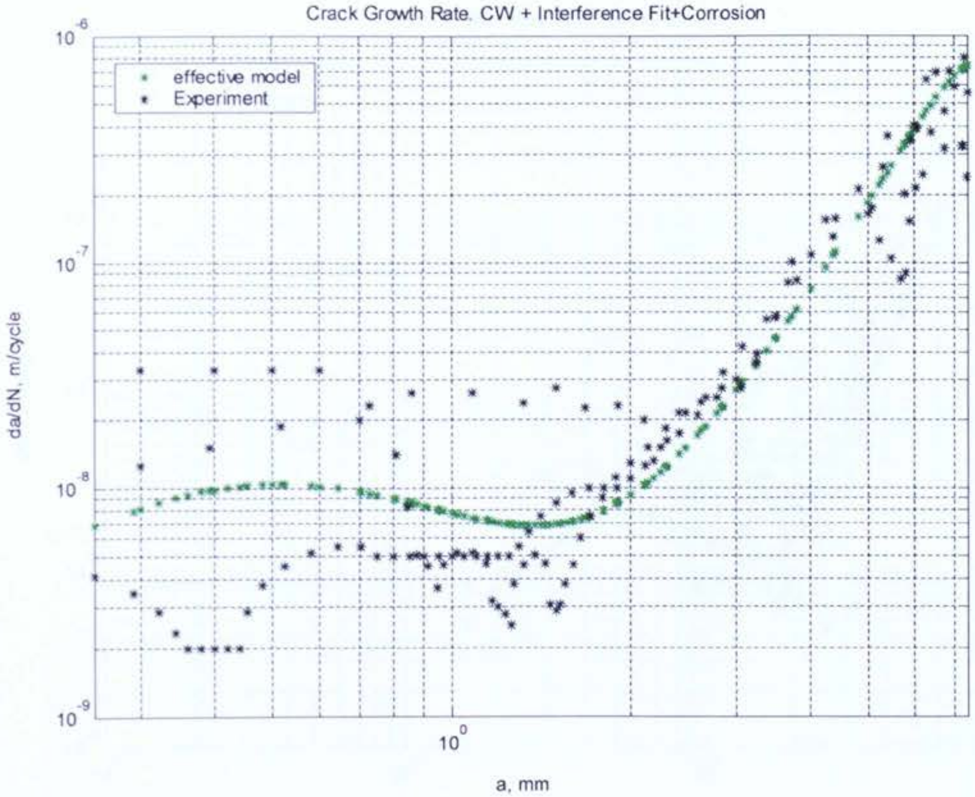

Figure 3.8.17 Crack Growth Rate in corroded CW specimens with Interference Fit : model and experimental data

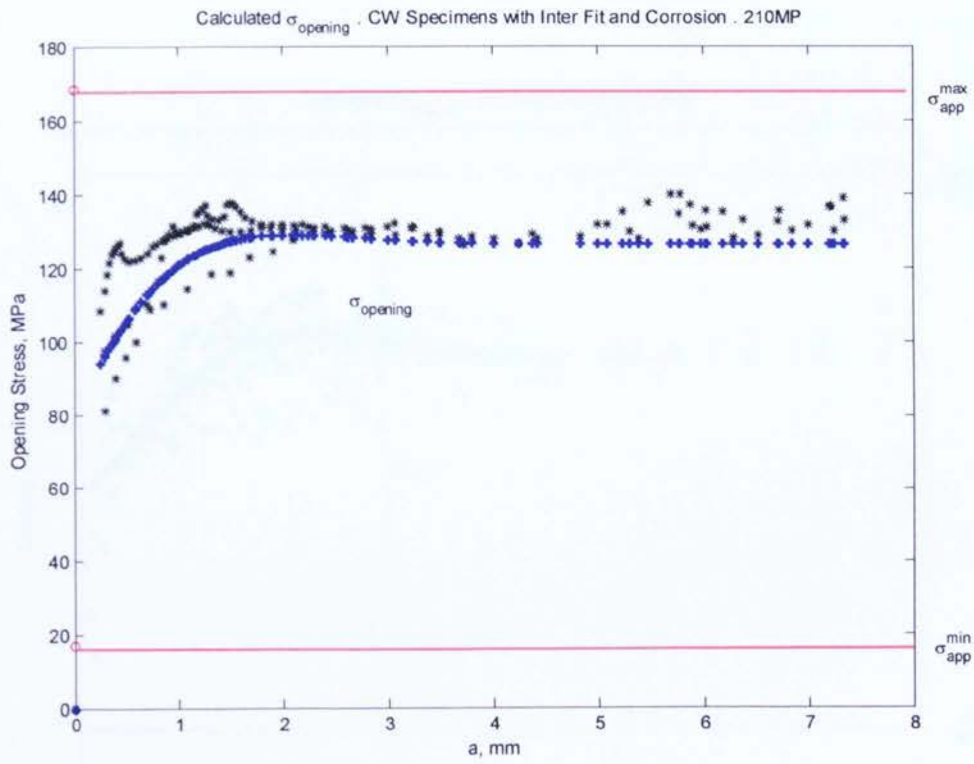

Figure 3.8.18 Opening stress in corroded CW specimens with Interference Fit: model and experimental data

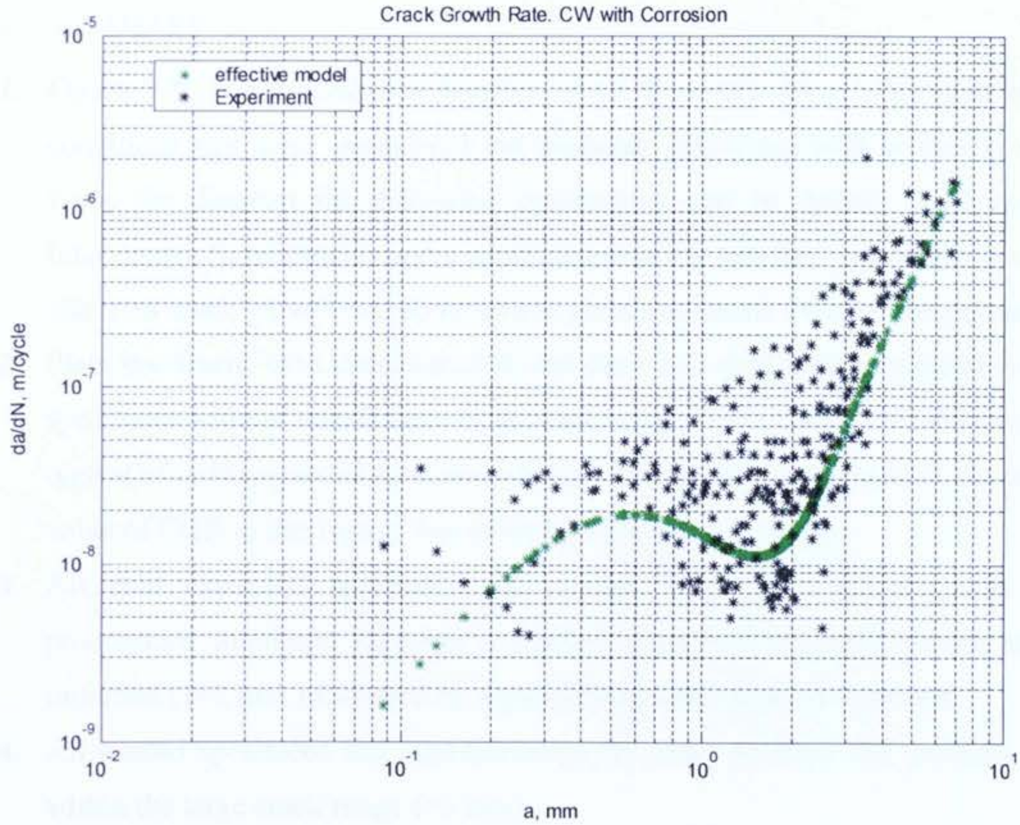

Figure 3.8.19 Crack Growth Rate in corroded CW specimens: model and experimental data

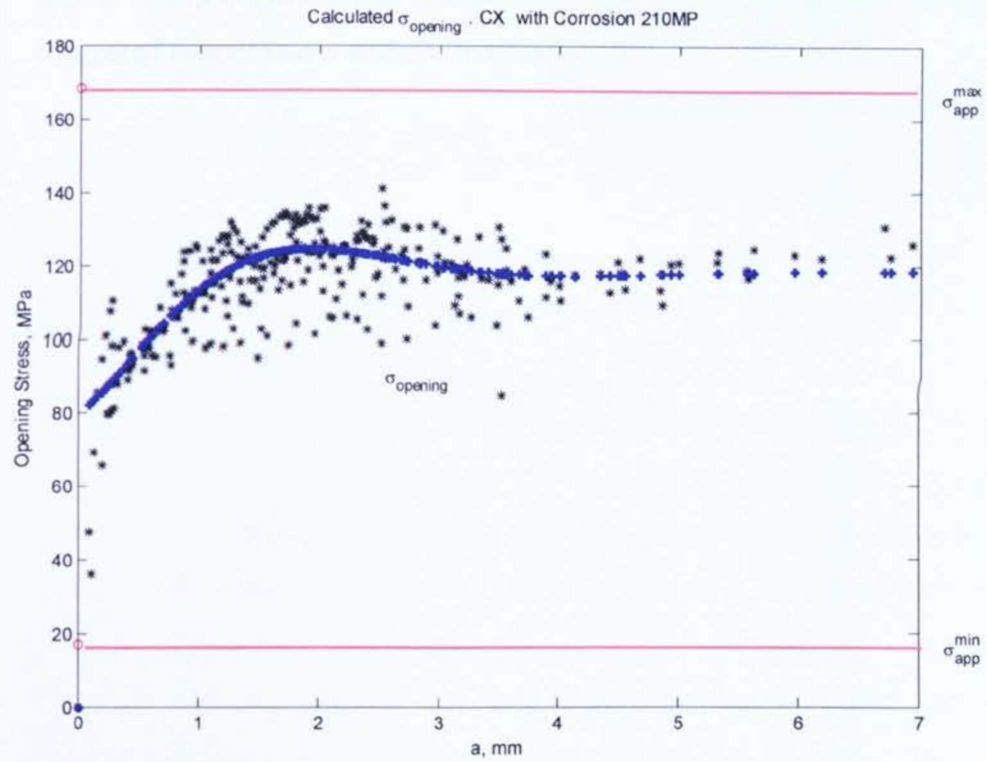

Figure 3.8.20 Opening stress in corroded CW specimens with Interference Fit: model and experimental data corroded CW specimens

3.8.4 SUMMARY

1. Figure 3.8.21 is a combined diagram of CGR models for all the main specimen conditions that were considered but excludes specimens with corrosion damage. From the diagram the following conclusions can be drawn: Cold expansion, Interference fit treatments and a combination of the two have a dramatic retardation effect on crack growth rate compared to plain specimens without these treatments.
2. Plain specimens with interference fit did show a drop in CGR compared with plain specimens without interference fit at crack lengths of 1~2mm. This drop in CGR is typical of cold expanded specimens but for interference fit specimens the minimum value of CGR in this region was an order of magnitude higher.
3. All cold expanded specimens had typical forms of CGR diagrams with a pronounced minimum showing a marked reduction of crack growth rate after initiation (1~2 mm) followed by region of constant crack rate gradient.
4. All treated specimens had approximately the same position and gradient of CGR within the large crack range (>3 mm)
5. CW specimens without Interference Fit had a slightly less marked drop in CGR in comparison with the CW specimens with Interference Fit.
6. CW specimens with Interference Fit had a slightly delayed transition from the region of crack growth rate arrest to the region of crack growth rate acceleration compared to specimens without Interference fit.

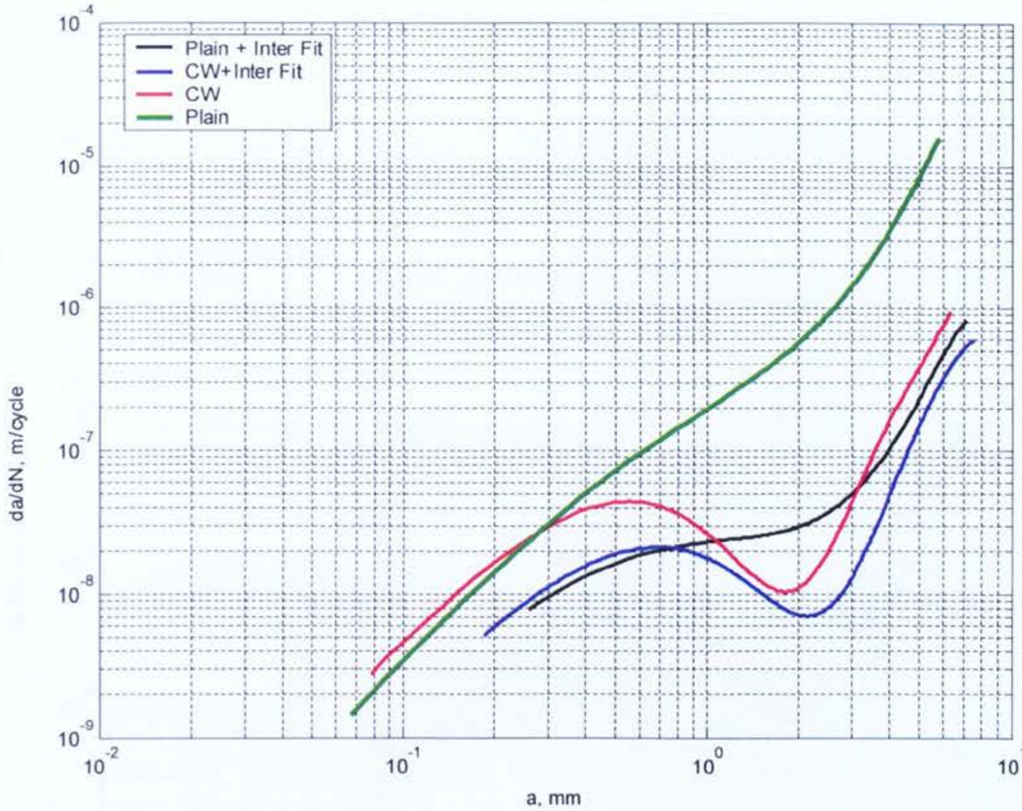

Figure 3.8.21 Crack Growth Rate Modelling. Combined diagram for different conditions

Figure 3.8.22 shows effect of corrosion on the specimens tested in terms of the effective CGR model.

1. From the crack opening stress distribution derived for corroded plain specimens the σ_{op} level was assumed to be 65MPa rather than the 79MPa evaluated through Shijve's equation ***(3.8.1)***. This approach gave the same crack growth rate diagram as for plain specimens but the values were shifted slightly upwards into the range of higher growth rates.
2. Corrosion in pure CW specimens gave a very similar diagram to CW specimens without corrosion though it ought to be higher as for the plain corroded specimens. The reason for this is the very large degree of scatter of experimental crack growth rate data in comparison with non corroded CW specimens. particularly in the small crack length range.
3. Crack growth rate data for corroded CW specimens with Interference fit also showed a large degree of scatter and it would have been expected that the diagram would be shifted up. Also it was noted that there was a shift towards smaller crack

sizes.in the transition point between crack arrest and the following acceleration phase

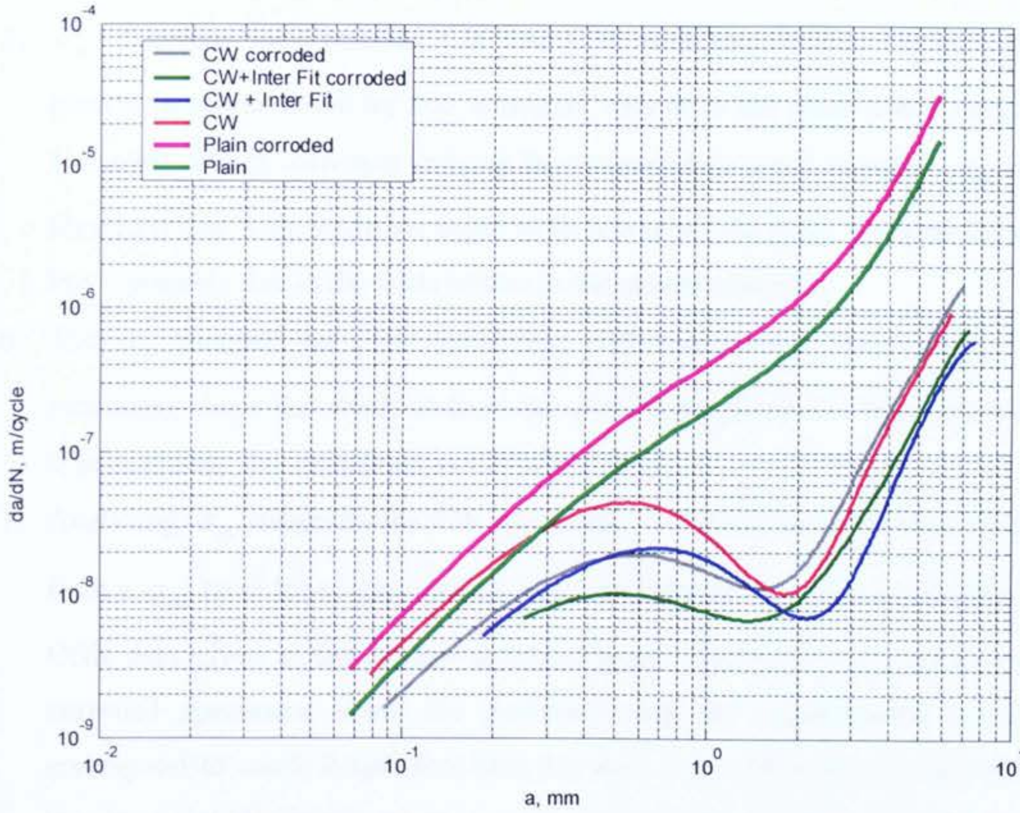

Figure 3.8.22 The effect of corrosion on Crack Growth Rates

As noted previously, the CGR models were determined using crack opening stress functions (as described in section 3.4.2) Approximate functions of crack opening stress are presented in ***Figure 3.8.23*** below. From this diagram the following conclusions can be drawn:

1. All of the σ_{op} vs a (crack length) plots for CW specimens are placed above the plots of σ_{op} vs a for plain specimens over almost the whole crack length range. Though there are exceptions.
2. It is possible to state that all of the σ_{op} diagrams for CW specimens started from approximately the same level as for plain specimens - 80MPa. Thus, at initiation conditions for crack propagation are approximately equal for plain and treated specimens.
3. All the plots for CW specimens have typical hump-like form with a local minimum at 1~2 mm caused by maximal residual stresses in this region.

4. Plots for specimens with CW plus Interference Fit have a less defined hump-like form and an opening stress level approximately 10 MPa higher than pure CW specimens
5. σ_{op} diagrams for Corroded CW and CW with Interference Fit have the same growth trends as those for non corroded, except in the small crack range (about 1~2 mm), where corrosion reduces the resistance to crack growth. σ_{op} diagrams for specimens with corrosion ought to be lower but the plots obtained did not show this – possibly due to the wide scatter in the results obtained.
6. The σ_{op} diagram for Plain specimens with Interference Fit shows a gradually increasing shape that tends to level out a crack length of 3~4 mm where it attains approximately the same level as CW specimens.
7. Analysing σ_{op} diagrams for CW specimens, it can be seen that they tend to start from a σ_{op} level lower than that for plain specimens. σ_{op} data points derived from CGR data given in the ***Figure 3.8.12***, ***Figure 3.8.20*** for CW corroded and non corroded specimens show the tendency with the experimental points which correspond to crack length less than 0.5 mm. It means that crack growth in CW specimens at the initial stages can be more intensive than in plain specimens. Detailed analysis is a problem due to a lack of experimental information for small crack sizes i.e. below 0.5mm.

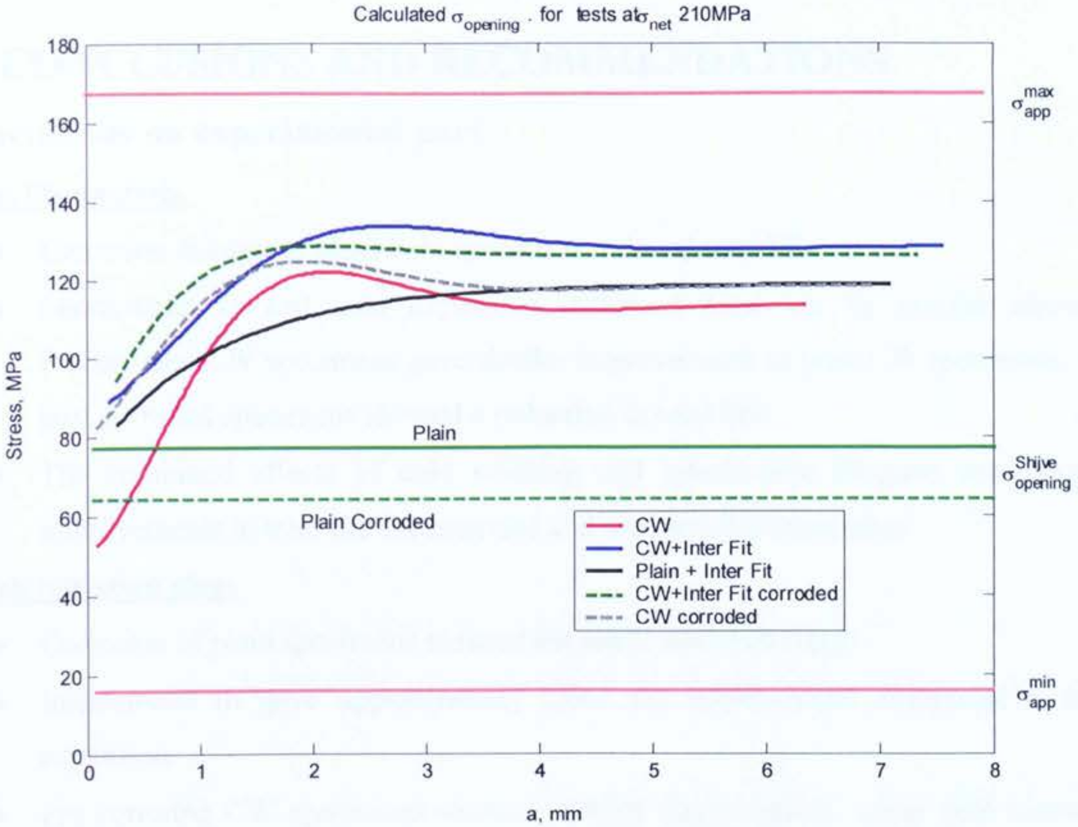

Figure 3.8.23 Opening stress models. Combined diagram.

4 CONCLUSIONS AND RECOMMENDATIONS

Conclusions on experimental part

Total life analysis

- Corrosion damage to plain hole specimens reduced total life
- Interference fit and cold expansion increased total life by similar amounts Precorroded CW specimens gave similar improvements to pure CW specimens, but post corroded specimens showed a reduction in total life.
- The combined effects of cold working and interference fit gave considerable improvements in total life for corroded and noncorroded specimens.

Crack initiation stage

- Corrosion of plain specimens reduced the crack initiation stage.
- Interference fit gave approximately twice the improvement compared to cold expansion
- Pre corroded CW specimens showed a slight improvement, while post corroded CW specimens were slightly worse than plain specimens.
- The biggest delay in crack initiation was achieved from the combined effects of cold working and interference fit..

Crack Propagation stage

- Corrosion of plain specimens reduced the crack propagation stage.
- Interference fit extended the crack propagation stage by a significant amount.
- Cold expansion increased crack growth time in plain and pre corroded specimens..
- Cold expansion of post corroded specimens gave smaller improvements.
- The most greatest effect in extending crack propagation time was achieved from combined cold work and interference fit for both non corroded and corroded specimens.

Crack Growth Rate Analysis

- Fatigue crack growth rates in cold-expanded and specimens with interference fit were substantially lower than for plain holes.
- Crack growth rates in corroded plain specimens were higher than in non corroded, especially in the short crack range.
- All cold expanded specimens showed a reduced crack growth rate at crack lengths in the range 1-2 mm.

- Crack growth rates in the large crack range was similar in all CW specimens with and without interference fit, and in plain specimens with interference fit.
- Crack growth rate for short cracks in CW specimens with interference fit was lower than in pure CW specimens.
- The degree of corrosion (72 hr) did not affect crack growth rate but increased scatter of the data.

Conclusions on analytical part

- Attempts to apply residual stress distribution data obtained by X-ray and Sach's techniques to SIF analysis were not succesful
- Attempts to derive residual stress distribution from experimental crack growth rate data gave non creditable results
- Derivation of Opening stress from experimental crack growth rate data using conception of effective SIF gave quite credible results confirmed by experimental results from other sources
- Crack growth rate models based on the concepts of effective SIF and Opening stress were constructed and applied to all types of specimens tested.
- The results predicted from the models closely agreed with experimental data.
- In summary, the combination of cold expansion and interference fit gave the biggest benefit in terms of overall fatigue performance for fastener holes in 2024 T351 aluminium alloys

RECOMMENDATIONS:

Recommendations for further investigation highlighted as a result of this work are as follows:

1. The experimental results from this work may be used as validation for 3D finite element analysis models for combined cold expansion and interference fit treatments
2. The prediction of stress distribution in specimens derived from experimental data on crack growth rates are areas warranting further investigation.
3. Fatigue tests using TWIST or FALSTAFF should be carried out to simulate real service conditions
4. The present investigation and its further development can be particularly important for the evaluation of inspection intervals and repair requirements relating to fastener holes and the integration of these into maintenance schedules.

APPENDIX

SUMMARY TABLE OF THE PREVIOUS AND PRESENT TEST RESULTS

Specimen Number	σ, MPa	Total Life	Crack initiating life(0.1mm)	crack propagation life	Side of crack initiation	Surface crack form	Crack Symmetry	Fracture surface
Plain specimens								
8	200	72500	-	-	-	quartercircular corner	Symmetrical	
9	200	72713	-	-	-	semicircular middle	Symmetrical	
10	210	54766	40000	14766	-	semicircular middle	Symmetrical	
11	210	71203	50000	21203	-	semielliptical middle	Symmetrical	
12	210	62571	43000	19571	-	semicircular middle	Symmetrical	
13	200	71567	44000	27567	-	semielliptical middle	Symmetrical	
14	200	70200	40000	30200	-	semielliptical middle	Symmetrical	
Plain corroded specimens								
15Cor24hr	200	44333	40000	4333	-	Through thickness	Symmetrical	

16Cor24hr	200	46945	37000	9945	-	semielliptical middle	Symmetrical	
17Cor72hr	200	47908	35000	12908	-	semielliptical middle	Symmetrical	
18Cor72hr	200	52356	34000	18356	-	semielliptical middle	Symmetrical	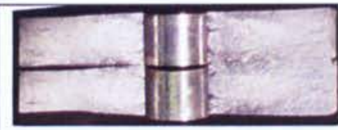
19Cor96hr	200	47497	20000	27497	-	quarterelliptical corner	Symmetrical	
20Cor96hr	200	43793	25000	18793	-	quarterelliptical corner	Symmetrical	
21Cor168hr	200	37718	10000	17718	-	semielliptical middle	Symmetrical	
22Cor168hr	200	40456	20000	20456	-	quarterelliptical corner	Symmetrical	
39PreCor72hr	210	33114	25000	8114			Symmetrical	
40 PreCor72hr	210	26613	10000	16613			Symmetrical	
41 PreCor72hr	210	29291	23000	6291			Symmetrical	
42 PreCor72hr	210	26093	11000	15093			Symmetrical	
Cold Expanded specimens								
23CX	210	169383	60000	109383	inlet	quarterelliptical corner	Symmetrical	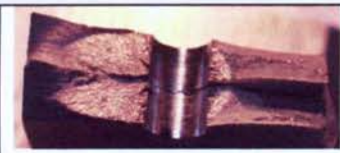
24CX	210	209727	55000	154727	inlet	quarterelliptical corner	Symmetrical	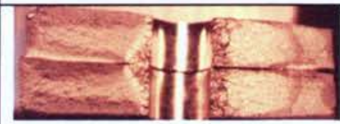

43CX	210	182446	78000	104446	outlet	quarterelliptical corner	Symmetrical	
7CX	210	160574	60000	100574	inlet	quarterelliptical corner	Asymmetrical	
25CX	200	499438	105000	394438	Inlet	semielliptical middle	Symmetrical	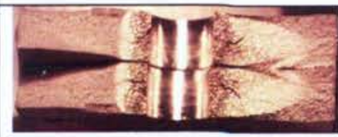
26CX	200	718920	105000	613920	Outlet	quarterelliptical corner	Asymmetrical	
Cold Expanded Corroded specimens								
27CX_cor173h	200	45909	-	-	inlet	ThroughCrack	Symmetrical	
28CX_cor173h	200	285085	20000	265085	inlet	quarterelliptical corner	Symmetrical	
29CX_cor96h	Specimen overloaded							
30CX_cor96h	200	48081	40000	8081	inlet	ThroughCrack	Asymmetrical	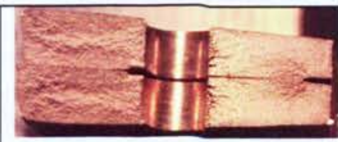
31CX_cor72h	210	145120	65000	80120	inlet	quarterelliptical corner	Symmetrical	
32CX_cor72h	210	119432	74432	45000	inlet	quarterelliptical corner	Symmetrical	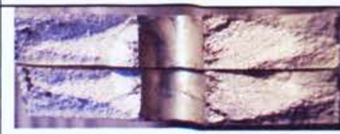

Cold Expanded Surface&Holes Corroded specimens								
33CX_Cor_Surfaces 72h	210	159651	40000	119651	inlet	quarterelliptical corner	Symmetrical	
34CX_Cor_Surfaces 72h	210	93436	23000	70436	inlet	quarterelliptical corner	Symmetrical	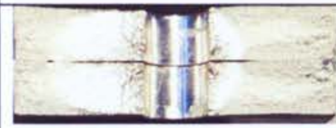
35CX_Cor_Hole 72h	210	151744	37000	114744	inlet	quarterelliptical corner	Symmetrical	
36CX_Cor_Hole 72	210	171920	57000	114920	inlet	quarterelliptical corner	Symmetrical	
Cold Expanded Prior Corrosion specimens								
49 PreCor/CW	210	202208	36000	166208	inlet	quarterelliptical corner	Symmetrical	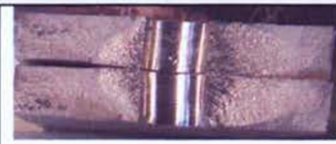
50 PreCor/CW	210	192376	32000	160376	inlet	quarterelliptical corner	Symmetrical	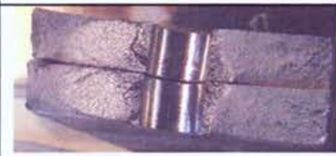
51 PreCor/CW	210	168088	35000	133088	inlet	quarterelliptical corner	Symmetrical	
Cold Expanded & Interference fit Specimens								

37CX_Inter_fit	210	338500	110000	228500	Inlet	quarterelliptical corner	Asymmetrical	
38CX_Inter_fit	210	338500	160000	235728	outlet	quarterelliptical corner	Asymmetrical	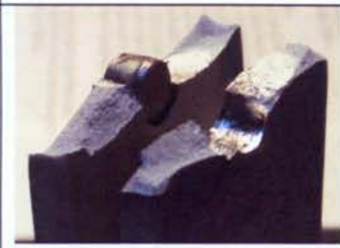
44 CX_Inter_fit	210	501933	**Crack From Outer Corner of the specimen**					
52 CX_Inter_fit	210	498124	136000	362124	Outlet	quarterelliptical corner	Asymmetrical	
53 CX_Inter_fit	210	417406	132000	285406	Outlet	quarterelliptical corner	Asymmetrical	
54 CX_Inter_fit	210	696155	420000	276155	Outlet	quarterelliptical corner	Asymmetrical	
55 CX_Inter_fit	210	837903	95000	742903	Inlet	quarterelliptical corner	Asymmetrical	
Cold Expanded & Interference fit Specimens Post Corrosion								
56CX/IF/PreCor	210	591632	140000	451632	Outlet	quarterelliptical corner	Asymmetrical	
57CX/IF/PreCor	210	447142	85000	362142	Inlet	quarterelliptical corner	Asymmetrical	
58 CX/IF/PreCor	210	336119	148000	188119	Inlet	quarterelliptical corner	Asymmetrical	
Plain Interference Fit Specimens								

45 PL/IntFit	210	162643	80000	82643	Inlet	quarterelliptical corner	Asymmetrical	
46 PL/IntFit	210	202351	95000	107351	Inlet	quarterelliptical corner	Asymmetrical	
47 PL/IntFit	210	164370	100000	64370	Inlet	quarterelliptical corner	Asymmetrical	

LITERATURE

1Campbell, G. S. & Lahery R. A., Survey of Serious Aircraft Accidents Involving Fatigue, Int. J. Fatigue, Vol. 6, № 1 - January 1984.

2 Hardrath, H. F., Structural Integrity In Aircraft, Journal of Testing and Evaluation, JTEVA, Vol. 1, No. 1, Jan. 1973, pp. 3-12.

3 Ozdemir A.T., Cook R., Edwards L. (1995). Residual stress distributions around cold expanded holes. Estimation enhancement and control of aircraft fatigue performance, Vol 2, Pub EMAS, 1995.

4 Cook R and Holdway. P (1993). Residual stresses induced by hole cold expansion. Computer Methods and Experimental Measurements for Surface Treatment Effects. Pub. CMP, Southampton, U.K.

5 Clark G. (1984). Fatigue Crack Growth Through Residual Stress Fields-Theoretical and Experimental Studies on Thick-Walled Cylinders, Theoretical and Applied Fracture Mechanics, 2, p 111-125.

6 Moore T.K. (1978). The Influence of Hole Processing and Joint Variables on the Fatigue Life of Shear Joints, Air Force Materials Laboratory, Wright-Patterson Air Force Base, Ohio, AFML-TR-77-167.

7 Hsu T.M., McGee W.M., Aberson J.A. (1977). Extended Study of Flaw Growth at Fastener Holes, Air Force Flight Dynamics Laboratory, AFFDL-TR-77-83.

8 Schijve J., Jacobs F.A., Meulman A.E. (1978). Flight Simulation Fatigue Tests on Lugs with Holes with Holes expanded According to the Split Sleeve Cold Work Method, NLR TR 78131 U.

9 Petrak G.J., Steward R.P. (1974). Retardation of Cracks Emanating from Fastener Holes, Engineering Fracture Mechanics, 6, pp 275-282.

10 Cassat G.C., Tenclay M.C. (1982). A Comparison of Residual Stresses Around Fastener Holes Produced by Three Different Methods of Mechanical Overstraining. A Fatigue Technology Inc. (FTI) Report (unpublished).

11 Chackherlou T.N., Vogwell J.,The effect of a fastener Hole using a sleeve during cold expansion, Engineering Failure Analysis, v. 10, .2003

12 Fatigue Technology Inc. 2004 (online), retrieved via Explorer. www.fatiguetech.com/coldEX_Split_sleeve.html

13 Clark G. (1991) Modelling Residual Stresses and Fatigue Crack Growth at Cold Expanded Fastener Holes. Fatigue Fract. Eng. Mater. Struct. Vol 14, No 5, pp 579-589.

14 M.A. Landy, R.C. Champoux, FTI Engineering Process Specification FTI, 8108B, 1984, Seattle, USA, Fatigue Technology Inc.

15 Chandawanich N., Sharpe W.N.Jr (1979), Eng. Fract. Mech., 11, p 609.

16 Champoux R.L. (1986), An Overview of Hole Cold Expanded Methods. Fatigue Prevention and Design, EMAS, Wharley, UK.

17 A. Leon, Benefits of split mandrel coldworking, Int. J. Fatigue Vol. 20. No. I. pp. I-X, 1998

18 Finney J.M., Cold Expansion and Interference for Extending the Fatigue Life of Multi-layer Metal Joints. AD-A274 9X2. Department of Defence. Defence Science and Technology Organisation Aeronautical Research Laboratory, Melbourne, Victoria, Australia, 1993.

19 Macherauch E., Kloos K.H. (1987), Origin Measurement and Evaluation of Residual Stresses. In: Macherauch, E. Hauk V., eds Deutsche Gesellshaft für Metalkunde, Germany, p3.

20 Grandt A.F. Jr., Potter R.M. (1979), An Analysis of Residual Stresses and Displacements due to Radial Expansion of Fastener Holes, Air Force Materials Laboratory, Wright-Patterson Air Force Base, Ohio, Technical Report AFML-TR-79-4048.

21 Ozdemir A.T., (1983), Cold Expansion of Fastener Holes, PhD Thesis, Faculty of Technology, The Open University.

22 Cook R, Holdway P., Residual stresses induced by hole cold expansion. In: Computer methods and experimental measurement for surface treatment effects. Great Britain. Computational Mechanics Publications; 1993, p. 90-100.

23 Chang JB., Prediction of fatigue crack growth at cold-worked fastener holes. J Aircraft, 1977; 14, pp. 903-8.

24 Ball DL, Lowry DR, Experimental investigation on the effects of cold expansion of fastener holes. Fatigue Fract Eng Mater Struct 1998, 21, pp. 17-34

25 Su X, Gu M., Yan M., A simplified residual stress model for predicting fatigue crack growth behavior at coldworked fastener holes. Fatigue Fract Eng Mater Struct 1986, 9, pp. 57-64.

26 Sharpe WN., Residual strains around coldworked fastener holes. J Eng Mater Tech 1978; 100, pp. 310-2

27 Poolsuk S., Sharpe W.N., Measurement of the elastic-plastic boundary around cold-worked fastener boles. Trans ASME, J Appl Mech, 1978, 45, pp. 515-20.

28 Link R.E., Sanford R.J., Residual strains surrounding split-sleeve cold expanded holes in 7075-T65 aluminium, J Aircraft 1990;27:599-604.

29 Hermann R. Three dimensional stress distribution around cold expanded holes in aluminium alloys. Eng Fract Mech, 1994, 48, pp. 819-35.

30 Priest M., Poussard C.G., Pavier M.J., Smith D.J., An assessment of residual-stress measurements around cold-worked holes, Exp Mech, 1995, 35, pp. 361-6

31Cloud G., Residual surface strain distribution near fastener holes which are coldworked to various degrees, Wright-Patterson Air Force Base, OH, AFML-TR-78-153; 1978.

32 Cloud G., Measurement of strain fields near coldworked holes, Exp Mech, 1980, 20, pp. 9-16.

33 Edwards L., Ozdemir A.T., Effect of residual stress on fatigue life of cold expanded fastener holes. In: Computer method and experimental measurements for surface treatment effects. Great Britain: Computational Mechanics Publications; 1993. pp. 102-9

34 Van Houtte P., Buyser L.D., (1993), The Influence of crystallographic Texture on diffraction Measurements of Residual Stress, Acta Met. Mat., 41, (2), pp. 323-336

35 Koh S.K., Stephens R.I., (1991), Stress Analysis of an Autofrettaged Thick-Walled Pressure, Vessel Containing an External Groove, Int. J. Pres. Ves. & Piping, 46, pp.95-111

36 Dietrich G., Potter J.M., (1977), Stress Measurements on Cold-Worked Fastener Holes, Adv. in X-Ray Analysis, 20, pp. 321-328.

37 Jongebreur A.A., de Konig A.U., (1983), Results of a Study of Residual Stresses and Fatigue Crack Growth in Lugs with Expanded Holes, NLR MP 83024 U, presented at the 12th ICAF Symposium, Toulouse, 25-27 May, 1983.

38 Noronha P.J., Henslee S.P., Gordon D.E., Wolanski Z.R., Yee B.G.W., (1978), Fastener Hole Quality, Air Force Flight Dynamics Laboratory, Technical Report AFFDL-TR-78-206-Vol 1.

39 Su X., Gu M., Yan M., (1986), A Simplified Residual Stress Model for Predicting Fatigue Crack Growth Behaviour at Coldworked Fastener Holes, Fatigue Fract. Eng. Mater. Struct., 9, (1), pp 57-64.

40 Hermann R., Reid C.N., (1991), Experimental Analysis of the Stress Distribution around Cold-expanded Holes in Thin Sheets, ICRS-3,Tokushima, Japan.

41 Stacey A., MacGillivary H.J., Webster G.A., Webster P.J., Ziebeck K.R.A., (1985), Measurement of Residual Stresses by Neutron Diffraction, Journal of Strain Analysis, 20, (2), pp 93-100.

42 Bonner N.W., (1996), Measurement of Residual Stresses in Thick – Section Welds, PhD thesis, Advanced Engineering Materials Research Laboratory, Department of Mechanical Engineering, University of Bristol, UK

43 Sachs G., (1927), Der Nachweis innerer Spannungen in Stangen and Rohren, Zeitschrift für Metallkunde, 19, pp 352-357.

44 Hauk V., Hotter P., Macherauch E., (1986), Measuring Techniques of Residual Stresses – Present situation and future Aims, Residual Stresses in Science and Technology, E. Macherauch and V. Hauk V., Eds, Proceedings of ICRS 1986, pp. 231-255

45 Ogden W.P., (1991), Detection of subsurface Tensile Stress in an Aircraft Engine Mainshaft Bearing Using Barkhausen Noise, presented at ASM Conference on Practical Applications of Residual Stress Technology, 15-17 May 1991, Indianapolis, IN, USA

46 Lonsdale D., Doig P., Jones G.T., (1989), Magnetic and X-ray Methods of Stress Measurement on Large Components, Proceedings of Stress and Vibration: Recent Developments in Industrial Measurement and Analysis, London, Pub: SIRA

47 Heller M., Carey R.P., (1991), Stress Analysis of Inteference-fit Fastener Holes using a Penalty Finite Element Method, Computers and Structures, 39, (1,2), pp. 73-81.

48 Poolsuk S., Sharpe W.N.Jr., (1978), Measurements of the Elastic-Plastic Boundary around Coldworked Fastener Holes, Transactions of the ASME Journal of Applied Mechanics, 45, pp. 515-520.

49 Poolsuk S., (1977), Measurement of the Elastic-Plastic Boundary around Coldworked Fastener Holes, Phd Thesis, Michegan State University.

50 Sharpe W.N.(1976), Measurement of Residual Strains around Coldworked Fastener Holes, Michegan State University Technical Report AFOSR-TR-77-0020.

51 Sandford R.J., Link R.E., (1989), Holographic Measurement of the Elastic-Plastic Boundary Surrounding Cold-Expanded Holes, Journal of Strain Analysis, 24 (2), pp 103-106.

52 Link R.E., Sanford R.J., (1990), Residual Strains Surrounding Split-Sleeve Cold Expanded Holes in 7075-T651 Aluminium, J. Aircraft, 27 (7), pp. 599-604.

53 Adler W.F., Dupree D.M., (1974), Stress Analysis of Coldworked Fastener Holes, Air Force Materials Laboratory, Wright-Patterson Air Force Base, Ohio, AFML-TR-74-44.

54 Chandawanich N., Sharpe W.N.Jr., (1979), An Experimental Study of Fatigue Crack Initiation and Growth from Coldworked Holes, Engineering Fracture Mechanics, 11 (4), pp. 609-620.

55 Cullity B.D., (1978), Elements of X-Ray Diffraction, 2nd Ed., Addison-Wesley.

56 Noyan I.C, Cohen J.B., (1987), Residual Stress-Measurement by Diffraction and Interpretation, MRE, Springer-Verlag.

57 Hilley M.E., Larson J.A., Jatczak C.F., Ricklefs R.E. (eds), (1971), Residual Stress Measurement by X-Ray Diffraction, SAE Information Report J 784a, Society of Automotive Engineers.

58 Pintschovius L., Macherauch E., Scholtes, B., (1986), Determination of Residual Stresses in Autofrettaged Steel Tubes by Neutron and X-Ray Diffraction, in: Macherauch, E and Hauk, V. (eds.), Residual Stresses in Science and Technology (ICRS 1986), Germany: DGM, pp 159-165.

59 Mesnager R.G., (1919), Compt. Rend., 169, p. 1391

60 Buhler H., (1952), Zeitschrift für Metalkunde, 19, p. 388.

61 C. Poussard, MJ Pavier, DJ Smith, Analytical and finite element predictions of residual stresses in cold worked fastener holes, J. of Strain Analysis, 1995, V.30(4), pp.291-304

62 Armen H, Levy A, Eidinoff HL,Elastic-plastic behavior of cold-worked holes. J Aircraft 1984;21:I93-201

63 Guo W. Elastic-plastic analysis of a finite sheet with a cold-worked hole. Eng Fract Mech 1993;45:857-64.

64 Bernard M, Bai-Quoc T, Burlat M, Effect of re-coldworking on fatigue life enhancement of a fastener hole, Fatigue Fract Eng Mater Struct I992;18:761-75.

65 Banks-Sills L, Dagani E, Eiiasi R, Reinberg E, Schwartzman R., Analysis and testing of surface cold-work procedures applied to notched flat elements, Fatigue Fract Eng Mater Struct 1994;17:1371-81.

66 MJ Pavier, C. Poussard, DJ Smith, Finite Element Modelling of the Interaction of Residual Stress with Mechanical Load for a Crack Emanating from a Cold Worked Fastener Hole, J. of Strain Analysis, 1998, V. 33(4), pp. 275-289

67 MJ Pavier, C. Poussard, DJ Smith, Effect of residual stress around cold worked holes on fracture under superimposed mechanical load, Engng. Fract. Mech., 1999, V63, pp. 751-773

68 Hsu YC, Forman RG., Elastic-plastic analysis of an infinite sheet having a circular hole under pressure, Trans ASME, J Appl Mech 1975;42:347-52

69 Rich DL, Impellizzeri LF., Fatigue analysis of cold-worked and interference fit fastener holes. In: Cyclic stress-strain and plastic deformation aspect of fatigue crack growth. ASTM STP 637. American Society for Testing and Materials; 1977. p. 153-75.

70 Ball DL., Elastic-plastic stress analysis of cold expanded fastener holes. Fatigue Fract Eng Mater Struct, 1995;18:47-63

71 Nadai A., Theory of flow and fracture of solids, New York: McGraw-Hill; 1950.

72 Wang GS., An elastic-plastic solution for a normally loaded center hole in a finite circular body, Int J Press-Vess Piping 1988;33:269-84.

73 Mangasarian OL., Stresses in the plastic range around a normally loaded circular hole in an infinite sheet, Trans ASME, J Appl Mech 1960;27:65-73.

74 Mann J.Y., Jost G.C (1983), Stress Field associated with Interference Fitted and Cold-Expanded Holes. Metals Forum, 6, 43-53.

75 Pell R.A., Beaver P.W., Mann J.Y., Sparrow J.G., (1989), Fatigue of Thick-Section Cold Expanded Holes with and without Cracks, Fatigue Frac. Eng. Mater. Struct., 12, 553-567.

76 Clark G., (1982), Residual Stresses in Swage-Autofrettaged Thick-Walled Cylinders, Report MLR-R-847, DSTO Materials Research Laboratory, Department of Defence, Melbourne, Australia.

77 Cathey WH, Grandt Jr. AF., Fracture mechanics consideration of residual stresses introduced by coldvvorking fastener holes, J Eng Mater Technol 1988; 102:85-91.

78 Z. Wang, X. Zhang, Predicting fatigue crack growth life for cold-worked holes based on existing closed-form residual stress models, International Journal of Fatigue, V.25, pp. 1285-1291(7)

79 Crisfield MA., Essentials. Non linear finite element analysis of solids and structures, v. 1. John Wiley&Sons;1991 [Chapter 6].

80 Budiansky B., An exact solution to an elastic-plastic stress concentration problem. Prikl Mat Phys 1971; 35:40-8

81 Hoffman O., Sachs G., In: Introduction in theory of plasticity for engineers . NewYork; McGraw-Hill; 1953. p.80-95

82 Phillipps J.L., (1974), Sleeve Coldworking Fastener Holes, Technical Report AFML-TR-74-10, Air Force Materials Laboratory, Wright-Patterson Air Force Base.

83 Ozelton M.W., Coyle T.G., (1986), ASTM STP 927, p 53.

84 Buch A., Berkovits A., (1987), The Effects of Cold Expansion on Fatigue Life of AlZn Aluminium Lugs under Manoeuvre Loading.

85Ball D.L. and Doerfler M.T., Experimental and Analytical Studies of Residual Stress Field Evolution and Fatigue Crack Growth at Cold Expanded Holes, 2003 USAF ASIP Conference, Savannah GA, Dec. 2003.

86 Crews J.H. Jr. (1975), Analytical and Experimental Investigations of Fatigue in a Sheet Specimen with an Interference-fit Bolt, NASA TN-D-7926.

87 Lowak H., (1981), Tech. Report, Berict Nr;, FB-157.

88 Champoux R.L., (1986), An Overview of Cold Expansion Methods, Fatigue Prevention and Design, EMAS, Wharley, UK.

89 Gong-Fan S., Yong S., Yan C., (1988), Cold Expanding of Holes Improves Fatigue-Life of Aluminium Alloy Components, Fatigue Prevention and Design.

90 Mann J.Y., Sparrow J.G., Beaver P.W., (1989), Fatigue Characteristics of Joints with Holes Cold-Expanded in a Multilayer Stack, Int. J. Fatigue, 11, (4), pp. 214-220.

91 Ozelton M.W., Coyle T.G., Fatigue Life Improvement y Cold Working Fastener Holes in 7050 Aluminium.

92 Cook R., (1994), Technical Report, DRA/SMC/CR 942021

93 Köbler H.G., Huth H., Schütz D., (1979), Fatigue Life Improvement of Riveted Joints by Coldworking of Precracked Fastener Holes. Extract from the unpublished LBF-Rep No 3913.

94 Pell R.A., Beaver P.W., Mann J.Y., Sparrow J.G., (1989), Fatigue of Thick-Section Cold Expanded Holes with and without Cracks, Fat. Fract. Eng. Mat. and Struct., 12, (6), pp 553-567.

95 Polmear IJ, Pons G, Octor H, Sanchez C, Morton A, Borbridge W, et al. After Concorde: evaluation of an AL-Cu-Mg-Ag alloy for use in the proposed European SST. Mat Sci Forum 1996; 217-222;: 1759-64

96 Throop JF, Thermal relaxation in autofrettaged cylinders. In: Kula E, Weiss V, editors. Proseedings of Residual Stress and Stress Relaxation. 1982: 205-26

97 Fowler. Air Force Materials Laboratory Report, № AFIYX-TR-81-4017. 1981

98 V.D. Lacarac, D.J. Smith, M.J. Pavier, The effect of cold expansion on fatigue crack growth from open holes at room and high temperature, International Journal of Fatigue, V 23, pp. 161-170(10)

99 Hermann R, Moffatt J., (1991), Experiments and Analysis of the Fatigue Life Improvement in Fastener Holes of Aluminium-Lithium Alloy 2091, Proceedings of the Sixth International Al-Li Conference, Germany

100 Chao L, Xiulin Z., (1992), Effects of Cold Expansion of a Hole on Fatigue Crack Initiation Location and Life of an LY12CZ Alloy, Fatigue Fract. Eng. Mater. Struct, 15, (3), pp 241-247.

101 Colon J, Reid C.N (1984), The Effect of Cold -Expanded Holes on the Fatigue Properties of Aluminium Alloy 6082, in: Beevers, C.J (eds.), Fatigue, 11, (4), pp 214-220.

102 Toor P.M., (1976), Crack Emanating from Precracked Coldworked Holes, Engineering Fracture Mechanics, 8, pp 391-395.

103 Won-Kyun Lim, Jin-Sang Yoo and Seung-Yong Choi, The effects of concurrent cold expansion and ring-indentation on the growth of fatigue cracks emanation from circular holes. Department of Mechanical Engineering, Myongji University, Yongin, Kyonggi-do 449-728, Republic of Korea

104T. N. Chakherlou and J. Vogwell, (2004), A novel method of cold expansion which creates near-uniform compressive tangential residual stress around a fastener hole, Fatigue tract Engng Mater Struct 27, 343-351

105 R.W. Hertzberg, Deformation and Fracture Mechanics of Engineering Materials, 4th edition, John Wiley&Sons, Inc., 1996.

106 H.O. Fuchs, R.I. Stephens, Metal Fatigue in Engineering, A Wiley-Interscience Publication John Wiley & Sons, 1980.

107 J. A. Bannantine, J. J. Comer, J. L. Handrock, FUNDAMENTALS OF METAL FATIGUE ANALYSIS, Prentice Hall Endlewood Cliffs, New Jersey, 1990

108 H.M. Westergaard, Trans. ASME, J. Appl. Mech. 61, 49(1939).

109 G.R. Irwin, Handbuch der Physik, Vol. 6, Springer, Berlin, 1958, p.551.

110 P.C. Paris, G.C. Sih, ASTM STP 381, 1965, p30.

111 H. Tada, P. C Paris, and G. R. Irwin, The Stress Analysis of Cracks Handbook, Del Research, Hellertown, PA, 1973.

112 G. C. M. Sih, Handbook of Stress Intensity Factors, Lehigh University, Bethlehem, PA, 1973

113 Y. Murakami, Ed., Stress Intensity Factors Handbook, Pergamon Oxford, 1987.

114 W. F. Brown, Jr. and J. E. Srawley, ASTM STP 410, 1966.

115 C. Feddersen, ASTM STP 410, 1967 p. 77.

116 P. J. E. Forsyth, The Physical Basis of Metal Fatigue, American Elsevier Publishing Co., New York, 1969.

117 Plumbridge W.J, Ryder D.A., (1969), The Metallography of Fatigue, Met. Rev. (136), The Metals and Metallurgy Trust.

118 Thompson N., Wadsworth N.J., (1958), Advanced in Physics, vol. 7, p 72.

119 Schijve J., (1990), Fatigue, Static Tensile Strengths and Stress Corrosion of Aircraft Materials and Structures, TU Delft.

120 Asby M.F., Jones D.R.H., (1980), Engineering Materials, Pergamon Press, Oxford.

121 R. H. Christensen, Fatigue Cracking, Fatigue Damage, and Their Detection, Metal Fatigue, G. Sines and J. L. Waisman, Eds., McGraw-Hill Book Co., New York, 1959, p. 376.

122 P.C. Paris, F. Erdogan, A Critical Analysis of Crack Propagation Laws, Trans. ASME, J. Basic Eng., Vol. D85, 1963, pp. 528-534

123 R.G. Forman, V.E. Kearney and R.M. Engle, Numerical analysis of Crack Propagation in Cyclic Loaded Structure, Trans. ASME, J. Basic Eng., Vol. D89, № 3, 1967, pp. 459-464

124 A. Wöhler, Zeitschrift für Bauwesen 10 (1860)

125 R.E. Peterson, Edgar Marbury Lecture, ASTM, 1962, p. 1.

126 H. F. Hardrath et. al., NASA TN D-210, 1959

127 G. Clark, (1991), Modelling residual stress and fatigue crack growth at cold-expanded fastener holes, Fatigue Fract, Engng. Mater. Struct. Vol.14 №5 pp579-589

128 R.A. Pell, P.W. Beaver, J.Y. Mann and J.G. Sparrow (1989) Fatigue of thick-sections of cold-expanded holes with and without cracks. Fatigue Fract, Engng. Mater. Struct. Vol.12 pp553-567

129 Lin X.B. Smith R.A. Fatigue shape analysis for corner cracks at fastener holes Engineering Fracture Mechanics Vol. 59, No. 1, pp. 73-87, 1998

130 Lin X. B., Numerical simulation of fatigue crack growth. Ph.D. Thesis, The University of Sheffield, UK, 1994.

131 Lin X. B. and Smith R. A., An improved numerical technique for simulating the growth of planar fatigue cracks. Fatigue Fract. Engng Mater. Struct., 1977, 20, 1363-1373.

132 Heckel J. B. and Rudd J. L., Evaluation of analytical solutions for comer cracks at holes. In Fracture Mechanics. Sixteenth Symposium, 1985, ASTM STP 868, pp. 45-64.

133 Perez R., Ray S. K. and Grandt A. F. Jr. Application of a weight function method to predict the fatigue life of corner cracked holes loaded in bending. Engng Fracture Mech., 1987, 28, 283-291.

134 Berkovits, A. and Prinz, D., Growth of parabolic fatigue cracks from flaws at fastener holes. In Fracture Mechanics: Eighteenth Symposium, 1988, ASTM STP 945, pp. 1050-1069.

135 Varfolomeyev I. V., Vainshok V. A. and Krasowsky A. Y. A., Prediction of part-through crack growth under cyclic loading, Engng Fracture Mech., 1991, 40, 1007-1022.

136 Grandt A. F. Jr. and Macha D. E., Digitized measurements of the shape of corner cracks at fastener holes. Engng Fracture Mech., 1983, 17, 63-73.

137 J.R.Snow, A stress intensity factor calibration for corner flaws at an open hole, Tech Rep. AFML-TR-74282, Air Force Materials Laboratory, Wright-Patterton Air Force Base, Ohio (1975)

138 W.T. Kirkby, D.P. Rooke A Fracture Mechanics Study of the Residual Stress of Pin-Lug Specimens. Royal Aircraft Establishment, Farnborough. In: P. Stanley editor, Fracture Mechanics in Engineering Practice, Annual Conference of the Stress Analysis Group of the Institute of Physics held on the University of Sheffield, England, 1976

139 McGowan JJ, Smith CW. Stress intensity factors for deep cracks emanating from the corner formed by a hole intersecting a plate surface. In: Mechanics of crack growth. ASTM STP 590, 1976. p. 460-76

140 Shah RC. Stress intensity factors for through and part-through cracks originating at fastener holes. In: Mechanics of crack growth. ASTM STP 590, 1976. p. 429-59.

141 Smith CW. Jolls M, Peters WH. Stress intensities for cracks emanating from pin-loaded holes. In: Flaw growth and fracture. ASTM STP 631, 1977. p. 190-201.

142 Kullgren TE, Smith FW, Ganong GP. Quarter-elliptical cracks emanating from holes in plates. J Engng Mater Tcchnol 1978;100:144-9.

143 Kullgren TE, Smith FW. Part-elliptical cracks emanating from open and loaded holes in plates. .J Engng Mater Technol 1979:101:12-17.

144. Raju IS., Newman Jr. JC., Stress-intensity factors for two symmetric corner cracks. In: Fracture mechanics, ASTM STP 677, 1979. p. 411-30

145 Rudd JL, Hsu TM, Wood HA. Part-through crack problems in aircraft structures. In: Part-through crack fatigue life prediction, ASTM STP 687, 1979. p. 168-94.

146 Grandt Jr AF, Kullgren TE. Stress intensity factors for corner cracked holes under general loading conditions. J Engng Mater Technol 1981 ;103:171-6.

147 Grandt Jr AF., Kullgren TE., Tabulated stress-intensity solutions for flawed fastener holes. Engng Fracture Mech 1983;18:435-51.

148 Heath BJ, Grandt Jr AF. Stress intensity factors for coalescing and single corner flaws along a hole bore in a plate. Engng Fracture Mech 1984;19:665-73.

149 Schijve J. Comparison between empirical and calculated stress intensity factors of hole edge cracks. Engng Fracture Mech 1985;22:49-55.

150 Alturi SN., Nishioka T., Computational methods for three-dimensional problems of fracture. In: Alturi SN edilor,Compulational methods in mechanics of fracture, 1986. p. 230-87.

151 Newman Jr JC, Raju IS. Stress-intensity factor equations for cracks in three-dimensional finite bodies subjected to tension and bending loads. In: Atluri SN editor, Computational methods in the mechanics of fracture, vol. 2.1986 chap. 9.

152 Berkovils A, Prinz D. Growth of parabolic fatigue cracks from flaws at fastener holes. In: Fracture mechanics: eighteenth symposium. ASTM STP 945, 1988. p. 1050-69.

153 Perez R, Grandt Jr AF, Saff CR., Tabulated stress-intensity factors for corner cracks at holes under stress gradients. In: Surface-crack growth: models, experiments, and structures, ASTM STP 1060, 1990, p. 49-62.

154 Shin CS., The stress intensity of corner cracks emanating from holes. Engng Fracture Mech I990;37:423-36.

155 Shin CS. Some aspects of corner fatigue crack growth from holes. Int J Fatigue J991;13:233—40.

156 Vainshtok VA, Varfolomeyev IV. Stress intensity factor analysis for part-elliptical cracks in structures. Int J Fracture 1990;46:l-24.

157 Guo W. Stress intensity factors for corner cracks at holes subjected to biaxial and pin loads. Engng Fracture Mech 1993;46:473-9.

158 X.B. Lin, R.A. Smith, Stress intensity factors for corner cracks emanating from fastener holes under tension. Engineering Fracture Mechanics 62 (1999) 535-553

159 Newman JC, Raju IS. Stress intensity factor equations for cracks in three-dimensional finite bodies. In: Lewis JC, Sines G, editors. Fracture Mechanics, XIV Symposium, vol. 1, Theory and Analysis, ASTM, 1983, pp. I-238--I-265

160 Grandt AF Jr.. Stress intensity factors for some through-cracked fastener holes. International Journal of Fracture 1975;11(2):283–94.

161 J.C. Newman, Predicting failure of specimens with either surface cracks or corner cracks at holes. NASA TN-D-8244, 1976

162 Bowie, O.L. Analysis of an Infinite Plate Containing Radial Cracks Originating at the Boundary of an Internal Circular Hole. J. Math.&Phys., V.XXXV, №1, Apr. 1956, pp. 60-71

163 R. Hermann, Three-dimensional stress distridution around cold expanded holes in Al alloys, Engng Fract, Mech.,(1994) V48, №6, pp. 819-835,

164 H.F. Hardrath, Structural Integrity in Aircraft, Journal of Testing and Evaluation, V.1, №1, Jan., 1973, pp.3-12

165 C R Smith, Experimental Mechanics 5(8) 19A, 1965

166 D. Broek, The Practical Use of Fracture Mechanics, 1988, pp. 313 -316

167 Tomashov N.D., (1966), Theory of Corrosion and Protection of Metals, The Science of Corrosion, The Macmillan Company, New York.

168 Guilhandis A., (1952), La tenue des alliages légers à la Corrosion Marine, J. Aluminium, 6, n°186, 85-91

169 Pourbaix M. (1963), Atlas d'Equilibre Electrochimiques à 25°C, Ed. Gauthier-Villers, 168-176

170 ASM Handbook Committee (1994), Metals Handbook- 1st Edition, volume 1

171 Reboul M., (1987), Durabilité des Alliages d'Aluminium, Mécanismes de Corrosion, Essais et Remèdes, Mém. Etu. Sci. Rev. Met, nb 2, pp 61-74

172 Desjardins D., Oltra, R. (1987), Introduction à la Corrosion sous Contrainte, Corrosion sous Contrainte- Phénoménologie et Mécanismes, Eds. Scientifiques D. Desjardins and R. Oltra, Eds. Physiques, pp 1-17

173 Gruhl W. (1978), The Stress Corrosion Behaviour of High Strength Al-Zn-Mg Alloys, Aluminium, vol. 54, pp 323-325

174 Landolt D., (1993), Fissuration sous Contrainte, Traité des Matériaux, Corrosion et Chimie de Surfaces des Métaux, Ed. Presses Polytechniques et Universitaires Romandes, vol. 12, pp 413-462

175 Speidel M.O., (1984), Hydrogen Embrittlement and Stress Corrosion Cracking of Aluminium Alloys, Hydrogen Embrittlement and Stress Corrosion Cracking, Eds. Gibala, R.H Hehemann, ASM, pp 271-295

176 Berman L.,(1970) NADC, Report Nb NADC-ST-7007

177 Shaffer, Sebastiani J.C, Rosenfield M.S, Ketchan S.J., (1968), Journal of Materials, vol 3, pp 400-424

178 Rebiere M., (1989), De la Corrosion sous Contrainte à la Fatigue-Corrosion; Mécanismes d'Amorçage des Fissures dans les Alliages Al-Zn-Mg et Al-Li-Cu, Thèse de l'Institut Polytechnique de Grenoble

179 Foley R.T (1986), Localized Corrosion of Aluminium Alloys- A Review, Corrosion, NACE, vol. 42, No 5

180 Huddle R., (1956) Proc. 1st Intern. Conf.. Peaceful Uses Atom. Energy, 9, 403

181 Streicher M., (1956), J;Electrochem. Soc., 103, 375

182 Brennert S., Jernkont. Ann, 119, 281 (1935); Korr. Metallsch, 12, 46 (1936)

183 Perryman E.C.W., (1953), J. Metals (5), p 911

184 Edeleanu C., Evans, U.R, (1951), Trans. Far. Soc, 47, 1121

185 Pryor M.J., (1971), Corrosion Science, (11), p 463

186 Brock A.J., Wood, G.C (1967), Electochim. Acta, 12, p 395

187 Breen A.J., Wood G.C., Unpublished Work

188 Beck A.F., Heine M.A., Keir D.S., Van Rooyen D., Pryor M.J., (1962), Corrosion Science, (2), 133.

189 Berzins A., Lowson R.T., Mirams, K.J (1977), Aust. J. Chem., vol. 30, p 1891

190 Videm K., (1974), Kjeller Report nb. KR-149, Institute for Atommenergi

191 Kawano L., Baba N., Tajima S., (1972), Denki Kagaku, vol. 40, pp 29 and 632

192 Konno H.B., Kobayashi S., Takahashi H., Nagayama M., (1982), Corrosion Science, vol. 22, p 913

193 Wood G.C., Sutton W.H., Richardson J.A., Riley T.N.K, Malherbe A.G., (1974), Localized Corrosion, NACE-3, Staehle, R.W, Brown, B.F, Kruger, J., Agrawal, A.K, Eds., National Association of Corrosion Engineers Houston, Texas, pp. 526-546

194 Klein G., (1966), J. Electrochem. Soc, (113), p 349

195 Johnson W.K., (1971), Recent Developments in Pitting Corrosion of Aluminium, Br. Corros. J., Vol 6, pp 200-204

196 Hübner W., Wranglén G., (1965),Current corrosion research in Scandinavia, Kemian Keskusliito, r.y, Helsinki, Finland

197 Pearson E.C., Huff H.J., Hay R.H., (1952), Can. J. Techno. (30), p 311

198 Perryman, E.C.W (1953), J. Metals (5), p 911

199 Metzer M. & Intrater, (1953), J. Metals (5), p 821; Nature (174), p 547 (1954)

200 Basset G.A, Edeleanu C., (1960), Phil. Mag., (5), p 1217

201 Augustynski J., (1978), Passivity of Metals, Frankenthal, R.P, Kruger, J., Eds. Electrochemical Society, Pennington, New Jersey, p 989

202 Fouroulis Z.A, Thubrikar, J. Electrohem. Soc, vol. 122, p1296 (1975)

203 Stirrup B.N, Hampson, N.A, Midgeley I.S, J. Appl. Electrochem, vol 5, p229 (1975)

204 Johannson G., Acta Chem. Scand., vol 16, p403 (1962)

205 Foley R.T, Nguyen T.H., J. Electrochem. Soc., Vol 16, p 464 (1982)

206 Lorking K.F, Mayne E.O., J. Appl. Chem (London), vol 11, p 170, (1961)

207 Lorking K.F., Mayne E.O., Brit. Corr J., vol 1, n° 5, p181 (1966).

208 Porter F.C, Hadden, S.E., (1953), J. Appl. Chem., 3, 385

209 Hoar T.P, (1947), Disc. Far. Soc., 1, 299

210 Hagyar T., Santhiapillai J.R., (1959), J.Appl. Chem., 9, 323

211 Davies D.E., (1959), J. Appl. Chem, 9, 651

212 Pryor M.J., Keir D.S., (1955), J. Electrochem. Soc., 102, 605

213 Churchill J.R., (1939): Trans. Electrochem. Soc., 76, 341

214 Roikh J.L., Ordynskaya, V.V., (1961), Zhur. Prikl. Khim, 34, 1979

215 Aziz P.M., (1953), Views on the Mechanism of Pitting Corrosion of Aluminium, Corrosion- NACE, vol 9, pp 85-90

216 Breen A.J, Wood G.C, Unpublished Work

217 ASTM, Standard Test Method for Measurement of Fatigue Crack Growth Rates, 1996, E647-95, American Society for Testing and Materials.

218 FTI Tooling Catalogue (1990).

219 L.B. Vogelesang, Report LR-286, Delft, The Netherlands, 1979

220 V. Lacarac, D.J. Smith, M.J. Pavier, M. Priest Fatigue crack growth from plain and cold expanded holes in aluminium alloys, Int. J. of Fatigue, 22 (2000), pp. 129-203

221 J.R. Rice, Some remarks on Elastic Crack-Tip Stress Fields, Int. J. Of Solids and Structures, 8,6 June (1972), 751-758

222 Bueckner, H.F., A Novel Principle for the Computation of Stress IntensityFactors, Z. Angew. Math. Meek, Vol. 50, No. 9, 1970, pp. 529-546.

223 Cartwright, D.J. and Rooke, D.P., Green's Functions in Fracture Mechanics, Fracture Mechanics: Current Status, Future Prospects, R.A. Smith, ed., Pergamon, Toronto, 1979, pp. 91-123

224 J.C. Newman, Jr. Predicting failure of specimens with either surface cracks or corner cracks at holes. NASA TN D-8244, 1976..

225 Petroski H.J. and Archenbach J.D., (1978), Computation of the weight function from a stress intensity factor. Engng. Fract. Mech. 10, 257-266.

226 S. Timoshenko and J.N. Goodier, Theory of Elasticity, 3rd edition, McGraw-Hill Book Company

227 D. Stefanescu and all, The effect of high compressive loading on residual stresses and fatigue crack growth at cold expanded holes, J. Strain Analysis, V38, №5

228 V.D.Lacarac, A.A.Garcia-Granada, D.J.Smith, M.J.Pavier, (2004), Prediction of the growth rate for fatigue cracks emanating from cold expanded holes, Int. J. of Fatigue, 26, pp 585-595

229 P.M.G.P.Moreira, P.F.P. de Matos, S.T. Pinho, S.D. Pastrama, P.P. Camanho, P.M.S.T. de Castro, The residual stress intensity factors for cold-worked cracked holes: technical note, Fatigue Fract. Engng. Mater. Struct. (2004)

230 Grandt AF Jr.. Stress intensity factors for some through-cracked fastener holes. International Journal of Fracture 1975;11(2):283–94.

231 P.C. Paris and G.C. Sih, Stress Analysis of Cracks, Fracture Toughness Testing and Its Applications, ASTM STP 381, (1965) 30-81

232 W. Elber , The significance of crack closure, ASTM STP 486, pp. 230-242 (1971)

233 Schijve J., Some formulas for the crack opening stress level, Engng Fract Mech, V. 14, pp.461-465, 1981

234 Ibrahim FK. The effect of stress ratio, compressive peak stress and maximum stress level on fatigue behaviour of 2024-T3 alu-minium alloy. Fatigue and Fracture of Engineering Materials and Structures 1989;12(1):1–8